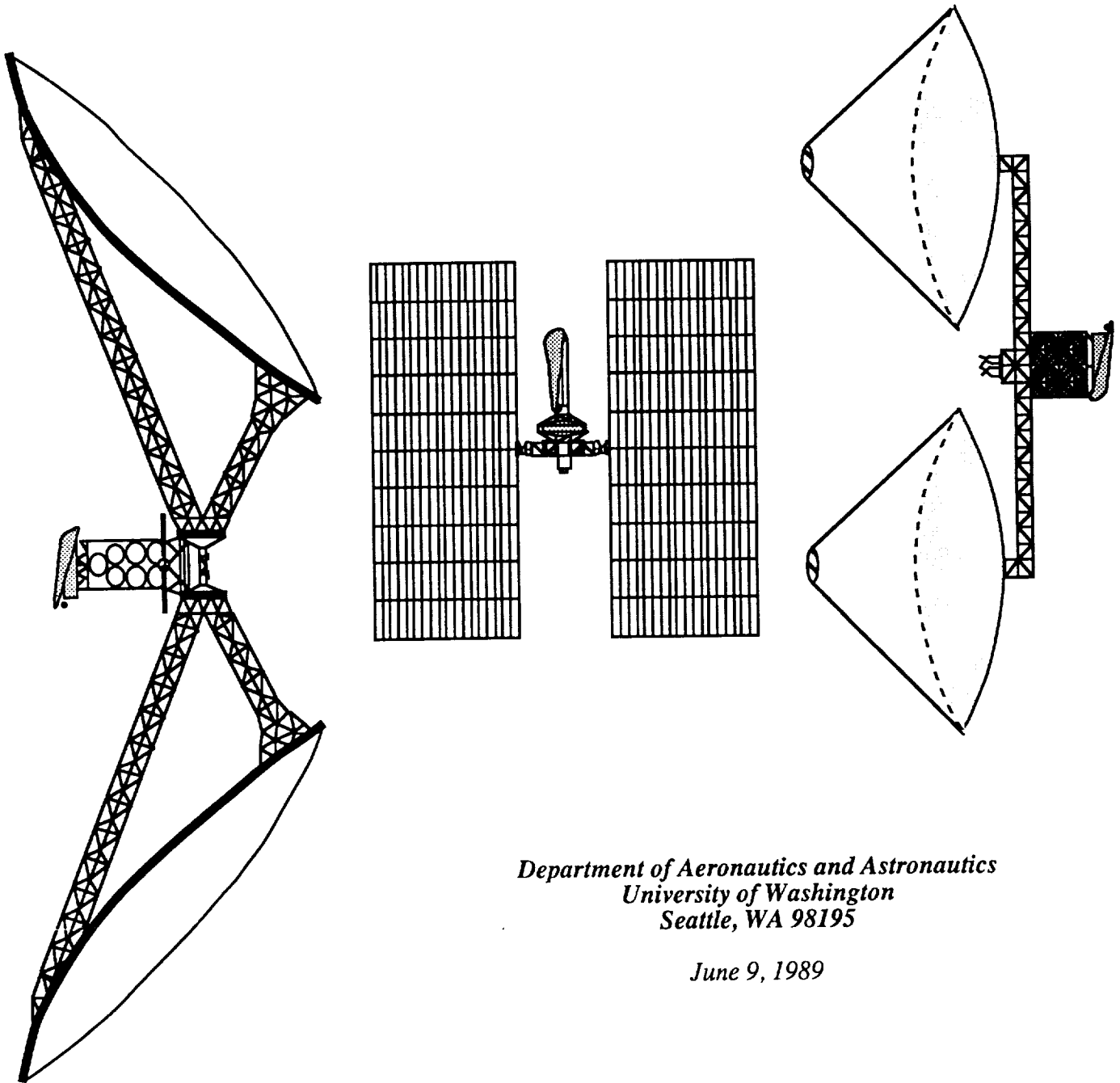


ADVANCED SOLAR-PROPELLED CARGO SPACECRAFT FOR MARS MISSIONS 297P

FINAL REPORT

Spacecraft Systems Design, AA420/499D
NASA/USRA University Advanced Design Program



*Department of Aeronautics and Astronautics
University of Washington
Seattle, WA 98195*

June 9, 1989

(NASA-CR-186218) ADVANCED SOLAR-PROPELLED
CARGO SPACECRAFT FOR MARS MISSIONS Final
Report (Washington Univ.) 297 p CSCL 22B

N90-25164

Unclas
63/18 0253805

ADVANCED SOLAR-PROPELLED CARGO SPACECRAFT FOR MARS MISSIONS

FINAL REPORT

Spacecraft Systems Design, AA 420/499D
NASA/USRA University Advanced Design Program

Prepared By:

Jacqueline Auzias de Turenne	Neil Phelps
Mark Beall	Amy Prochko
Joseph Burianek	Michael Rhodes
Anna Cinniger	Terri Schmitt
Barbrina Dunmire	Jeffrey Slostad
Eric Haberman	Ronald Teeter
James Iwamoto	Johnny Thorpe
Stephen Johnson	Thai Tran
Shawn McCracken	Tad Unger
Melanie Miller	Jay Wornath

Faculty Advisors:

Adam P. Bruckner

Abraham Hertzberg

*Department of Aeronautics and Astronautics
University of Washington
Seattle, Washington 98195*

June 9, 1989

ABSTRACT

At the University of Washington, three concepts for an unmanned, solar powered, cargo spacecraft for Mars support missions have been investigated. These spacecraft are designed to carry a 50,000 kg payload from a low Earth orbit to a low Mars orbit. Each design uses a distinctly different propulsion system: a solar radiation absorption (SRA) system, a solar-pumped laser (SPL) system, and a solar powered magnetoplasma-dynamic (MPD) arc system.

The SRA directly converts solar energy to thermal energy in the propellant through a novel process developed at the University of Washington. A solar concentrator focuses sunlight into an absorption chamber. A mixture of hydrogen and potassium vapor absorbs the incident radiation and is heated to approximately 3,700 K. The hot propellant gas exhausts through a nozzle to produce thrust. The SRA has a specific impulse of approximately 1,000 s and produces a thrust of 2,940 N using two thrust chambers.

In the SPL system, a pair of solar-pumped, multi-megawatt, CO₂ lasers in sun-synchronous Earth orbit converts solar energy to laser energy. The laser beams are transmitted to the spacecraft via laser relay satellites. The laser energy heats the hydrogen propellant through a plasma breakdown process in the center of an absorption chamber. Propellant flowing through the chamber, heated by the plasma core, expands through a nozzle to produce thrust. The SPL has a specific impulse of 1,260 s and produces a thrust of 1,200 N using two thrust chambers.

The MPD system uses indium phosphide solar cells to convert sunlight to electricity, which powers the propulsion system. In this system, the argon propellant is ionized and electromagnetically accelerated by a magnetoplasma-dynamic arc to produce thrust. The MPD spacecraft has a specific impulse of 2,490 s and produces a thrust of 100 N.

Various orbital transfer options are examined for these concepts. In the SRA system, the mother ship transfers the payload into a very high Earth orbit and a small auxiliary propulsion system boosts the payload into a Hohmann transfer to Mars. The SPL spacecraft releases the payload as the spacecraft passes by Mars. Both the SRA powered spacecraft and the SPL powered spacecraft return to Earth for subsequent missions. The MPD propelled spacecraft, however, remains at Mars as an orbiting space station. A patched conic approximation was used to determine a heliocentric interplanetary transfer orbit for the MPD propelled spacecraft. All three solar-powered spacecraft use an aerobrake procedure to place the payload into a low Mars parking orbit. The payload delivery times range from 160 days to 873 days (2.39 years).

PREFACE

The Department of Aeronautics and Astronautics at the University of Washington has been a participant in the NASA/USRA University Advanced Design Program since its inception in 1985. From the beginning, student involvement in this space design activity has been integrated as much as possible with the faculty's NASA-funded research program. This synergism has been highly beneficial both to the design course and to the research. The choice of design topic, for example, has on several occasions been motivated by the results of our research projects and, conversely, the basic research program carried out by the faculty has benefited from the recognition of the practical problems of design as they reflect back through the program.

Our course structure is aimed at exposing the students to a design situation which is "real world" as much as possible within the University framework. In addition, the course undertakes the responsibility of teaching the students those aspects of space engineering and science which would be needed for a general capability in the field of space systems. Students are taught the fundamentals of reentry physics, nuclear and solar power systems, space structures and thermal management, as well as selected topics on advanced propulsion systems and orbital mechanics. The design problems expose the students to situations in which they must understand the complete systems dependence of structural components, thermal components, and environmental constraints particular to space.

The current course offering consists of two 10-week academic quarters (Winter and Spring). The first course (AA420, Space Systems Design - typical enrollment 35-45 students) is initially structured as a formal lecture/discussion series which meets 5 hrs/week. Formal lectures by the instructors and presentations by guest lecturers from industry and NASA provide the students with the fundamental background they need to carry out their design studies. By the second week of the quarter, the students are divided

into design teams whose responsibility is to address specific subsystems of the overall design. As the design progresses, more and more time is devoted to in-class discussions of the students' work. A teaching assistant supported by NASA/USRA funds works with the students and helps the instructors with project management. The results of the design study are presented at the end of the quarter in the form of formal written reports, one by each of the design groups.

The Spring Quarter offering (AA499D - Independent Studies in Space Systems Design) is intended to refine and advance the design developed during the Winter Quarter and to address key unresolved problem areas. Participation in this class is elective; typically, about half of the AA420 students sign up for this offering. Those who do are usually the most capable and motivated students in the department. The class meets formally three hours a week in group discussion format. Early in the quarter the students are encouraged to submit papers on their projects to the AIAA Region VI Student Conference. In all cases to date, the reactions of the judges to the quality of our students' papers has been very favorable. Since the inception of the NASA/USRA program our students have garnered several awards in the undergraduate division of the competition. At the end of the Spring Quarter the students submit a single final report on the overall design and make an oral presentation at the annual NASA/USRA Advanced Design Summer Conference.

Under the NASA/USRA program our students have examined various problems relating to the critical needs of space prime power and propulsion. The choice of these topic areas reflects the historical emphasis on space power and propulsion in the research carried out by the faculty involved in the program. For example, in 1985 the problem of providing space prime power for the post-space station era was explored, and a unique solar dynamic power module capable of powering either roving or orbital space factories was designed. A central feature of the module was the use of the liquid droplet radiator for heat rejection, a concept developed earlier at the University of Washington under separate

NASA funding. In 1986 the design of a multimewatt nuclear space power system for lunar base applications was undertaken. A novel variation of the liquid droplet heat rejection system for use in a gravitational field was developed for this power system and the results published at the 1987 Symposium on Space Nuclear Power Systems, Albuquerque, NM. In 1987 and 1988 an engineering design study of a mass launcher system based on the ram accelerator concept developed at the University of Washington was carried out. This work, coupled with the results of parallel NASA-funded investigations of this concept, was presented at the 1987 IAF Congress, Brighton, England, and at the AIAA/ASME/SAE/ASEE 24th Joint Propulsion Conference, Boston, MA, in 1988.

The design topic chosen for the current academic year is solar propulsion of a cargo-carrying spacecraft to Mars. This space freighter is intended to be launched in support of a manned mission to that planet. Three different approaches have been investigated: solar-electric propulsion, solar-pumped laser propulsion, and solar thermal propulsion based on the high temperature flowing gas radiation receiver concept developed at the University of Washington under a separate NASA grant. Our students have responded to the design challenges with enthusiasm and creativity, encouraging us to plan follow-up studies of some of the concepts presented here.

A.P. Bruckner
Research Professor

A. Hertzberg
Professor

June 9, 1989

ACKNOWLEDGEMENTS

The members of the design teams for the three solar powered spacecraft presented in this report would like to take this opportunity to express their deep appreciation to Professor Adam Bruckner and Professor Abraham Hertzberg of the Department of Aeronautics and Astronautics for their countless hours of counsel and advice concerning all aspects of a solar powered spacecraft and its travel to Mars.

We would also like to extend our gratitude to Professor Tom Mattick, also from our Department of Aeronautics and Astronautics, for his invaluable assistance in the development of the flowing gas radiation heater, the design of the solar-pumped laser, as well as the transmission of the laser beam; Keith McFall, graduate student in the Department of Aeronautics and Astronautics at the University of Washington, for his assistance in the development and implementation of a computer program for a one-dimensional temperature profile within the flowing gas radiation heater.

Thanks are also due to Professor Robert Brooks of the Department of Nuclear Engineering for his assistance in the research and development of the laser-powered thruster; Walter Christiansen of the Department of Aeronautics and Astronautics for his contributions to the design of the solar-pumped laser system; Bob Soals of the Technical Sales Support, CVI Corporation, for his assistance in optical surface materials research; Ted Kopf and Curtis Clevan of the Jet Propulsion Laboratory for their advice and expertise concerning various laser aiming and tracking schemes; and John Hedgepeth of Astro Research for his assistance in structural materials and coatings for space structures.

We would also like to extend our gratitude to Dr. Tom Piverato of the Jet Propulsion Laboratory and Dr. Karl Faymon of the NASA Lewis Research Center for their assistance in the design of the MPD propulsion system; Irving Weinberg, also of the NASA Lewis Research Center, Paul Stella of the Jet Propulsion Laboratory, and Professor William Potter of the Electrical Engineering Department at the University of Washington for

their aid in the development of the solar arrays, power conditioning systems, and the circuitry behind the power supply components; Professors Keith Holsapple and K. Y. Lin of our Department of Aeronautics and Astronautics, and Martin Mikulas of the NASA Langley Research Center for their assistance in the development of a support structure for the solar arrays and the mainframe of the spacecraft; Stephen Paris of Boeing Aerospace for his donation of a Runge-Kutta integration program for orbital analysis; and lastly, R. J. Cassady of Rocket Research Co. for his insightful information on the applicability of an MPD propulsion system.

Our study of aerobraking procedures could not have been completed without the generous assistance of Professor Scott Eberhardt, of our Department of Aeronautics and Astronautics; Michael Tauber, Carol Davies, Gene Mennes, and Chul Park of the NASA Ames Research Center; and Bob Maraia of the Johnson Spaceflight Center.

An additional note of thanks goes to the design team members Jacqueline Auzias de Turenne, Mark Beall, Barbrina Dunmire, Melanie Miller, and Ronald Teeter, whose diligence and hard work played a vital role in the success of this report; Anna Cinniger, our chief editor, for her demands and deadlines which contributed to the completion of this report; and the members of our winter quarter Space Design class of the 1988 academic year for their contributions during the initial development stages of all three concepts.

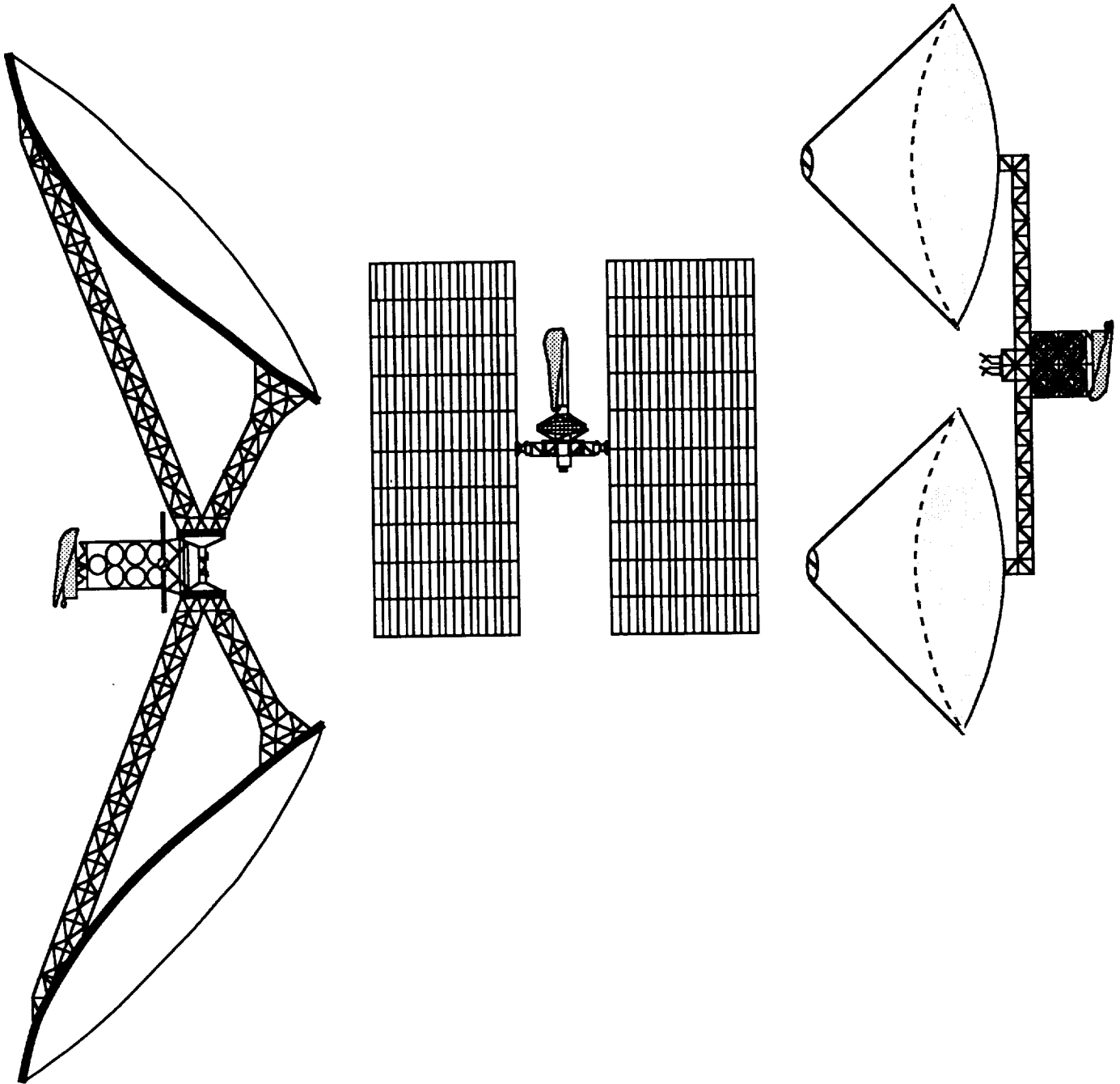
Finally, we would like to express our deep appreciation to NASA and USRA for their support of the University of Washington in the Advanced Design Program since its inception. Special thanks are due to Jack Sevier, Director, and Carol Hopf, Deputy Director, USRA Educational Programs, John Alred, Manager of the NASA/USRA Advanced Design Program, and Barbara Rumbaugh, Senior Project Administrator of the Advanced Design Program. We are also deeply indebted to Karl Faymon, of the NASA Lewis Research Center, who was our "center mentor", providing us with important literature, data and advice, and presented a topical seminar at the University. Last but not least we would like to thank Andrew Berschauer, graduate teaching assistant, for his help and contributions throughout the duration of the project.

TABLE OF CONTENTS

ABSTRACT	i
PREFACE	iii
ACKNOWLEDGEMENTS.....	vi
I. INTRODUCTION	1
REFERENCES.....	5
II. SOLAR RADIATION ABSORPTION PROPELLED SPACECRAFT	6
INTRODUCTION	7
PROPULSION THEORY	12
SOLAR OPTICS.....	20
DESIGN OF SPACECRAFT	27
ORBITAL MECHANICS.....	66
CONCLUSION	76
NOMENCLATURE	77
REFERENCES.....	80
III. SOLAR PUMPED LASER PROPELLED SPACECRAFT	84
INTRODUCTION	85
PROPULSION SYSTEM.....	88
LASER AND ASSOCIATED OPTICAL SYSTEM	107
SPACECRAFT RECEIVER SYSTEM	122
SPACECRAFT DESIGN.....	126
ORBITAL MECHANICS.....	134
CONCLUSION	144
NOMENCLATURE	146
REFERENCES.....	149

IV. MAGNETOPLASMA DYNAMIC PROPELLED SPACECRAFT.....	153
INTRODUCTION	154
THE MPD THRUSTER	155
POWER SUPPLY	172
SPACECRAFT CONFIGURATION AND STRUCTURE	183
ORBITAL MECHANICS.....	197
CONCLUSION.....	208
NOMENCLATURE	210
REFERENCES.....	213
V. CONCLUSION	217
VI. APPENDICES	221
APPENDIX A: Aerobraking at Mars.....	222
APPENDIX B: Mathematical Model of Thermal Characteristics in Thruster Chamber	246
APPENDIX C: Analytical Methods Used in the Design of the MPD Propelled Spacecraft Structure.....	252
APPENDIX D: Numerical Trajectory Calculation Programs.....	258

I. INTRODUCTION



I. INTRODUCTION

Jacqueline Auzias de Turenne
Amy Prochko
Stephen Johnson

With the renewed interest in planetary exploration, the United States has been considering a manned Mars mission. Such a mission should be different from the Apollo mission to the Moon in that it should establish the initial elements of a long-term outpost which would be utilized and expanded by subsequent manned missions over a period of several decades. A substantial amount of supplies and equipment will be needed. As we have learned from the Skylab, Salyut, and Mir long duration manned Earth-orbital missions, long term exposure to zero gravity has adverse effects on human physiology; thus, the transfer time for a manned Mars mission should be as short as possible. To facilitate a rapid transfer, all supplies and equipment not essential to the crew need to be transported on a separate cargo vehicle. The substantial payload masses envisioned for such a mission will require the utilization of advanced propulsion systems capable of specific impulses well in excess of the levels characteristic of chemical propulsion systems. Nuclear-thermal, nuclear-electric, and solar-electric propulsion schemes, the latter two involving ion propulsion, have been suggested for such missions during the past three decades [1].

Students at the University of Washington have designed three new approaches for an Earth to Mars cargo transport utilizing solar energy for propulsion. Mission assumptions include that the U. S. manned space station is operational and that the vehicle components are transported to low Earth orbit (LEO) by the space shuttle and assembled by a crew from the space station. The payload consists of supplies and equipment with a mass of 50,000 kg, which is within the range of the payload masses that have been considered by others. The cargo ferry would be launched long before the manned mission, so that the

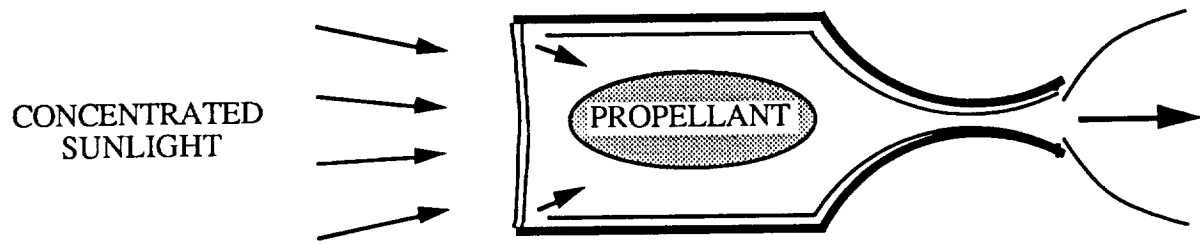
success of the supply mission can be ascertained before the manned mission begins its journey. The three concepts include a solar radiation absorption (SRA) propulsion system, a solar-pumped laser (SPL) propulsion system, and a solar-powered magneto-plasmadynamic (MPD) propulsion system. All three concepts offer specific impulses well in excess of those achievable by chemical propulsion systems.

The SRA propulsion system (Fig. I-1a) employs direct conversion of solar energy to thermal energy in the propellant using a novel process developed at the University of Washington [2]. Solar energy is concentrated using erectable reflectors and is directed through a sapphire window into an absorption chamber. Hydrogen propellant, seeded with an alkali metal (potassium), absorbs the incident radiation, and the heated propellant exhausts through a nozzle to produce thrust.

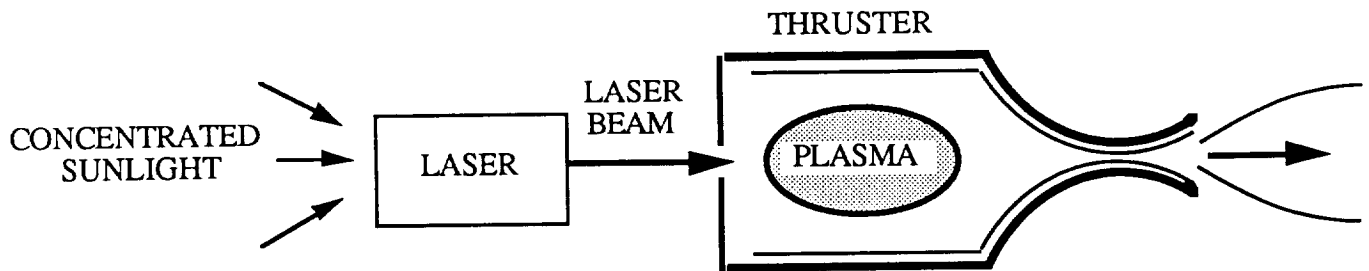
In the SPL propulsion system (Fig. I-1b), the thruster aboard the cargo vessel is powered by a remote Earth-orbiting laser system. The laser itself is powered by concentrated solar radiation using a blackbody pumping concept capable of 15% efficiency [3]. The laser beam is transmitted to the spacecraft, where the energy is focussed into an absorption chamber where the hydrogen propellant is heated through a plasma breakdown process. The heated propellant expands through a nozzle to produce thrust.

The MPD propulsion system (Fig. I-1c) uses advanced solar cell technology (indium phosphide) to convert sunlight to electricity, which powers the magneto-plasmadynamic propulsion system. In this system, the argon propellant is ionized in a diffuse electric arc and electromagnetically accelerated to produce thrust.

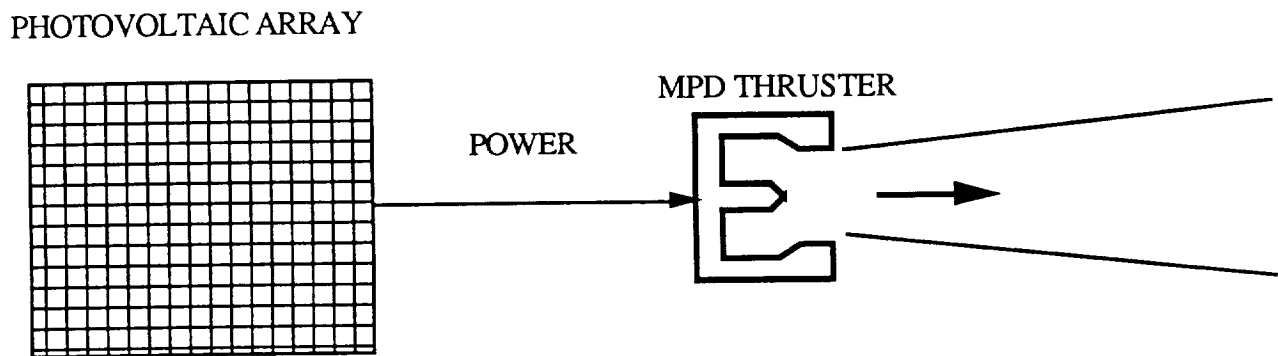
This report presents the three propulsion systems separately. Within each propulsion system section is a review of the propulsion theory, a description of the spacecraft structure, a summary of the orbital mechanics particular to each propulsion design, and a summary of the key elements and performance characteristics.



a) Solar Radiation Absorption Thruster



b) Solar Pumped Laser Thruster System



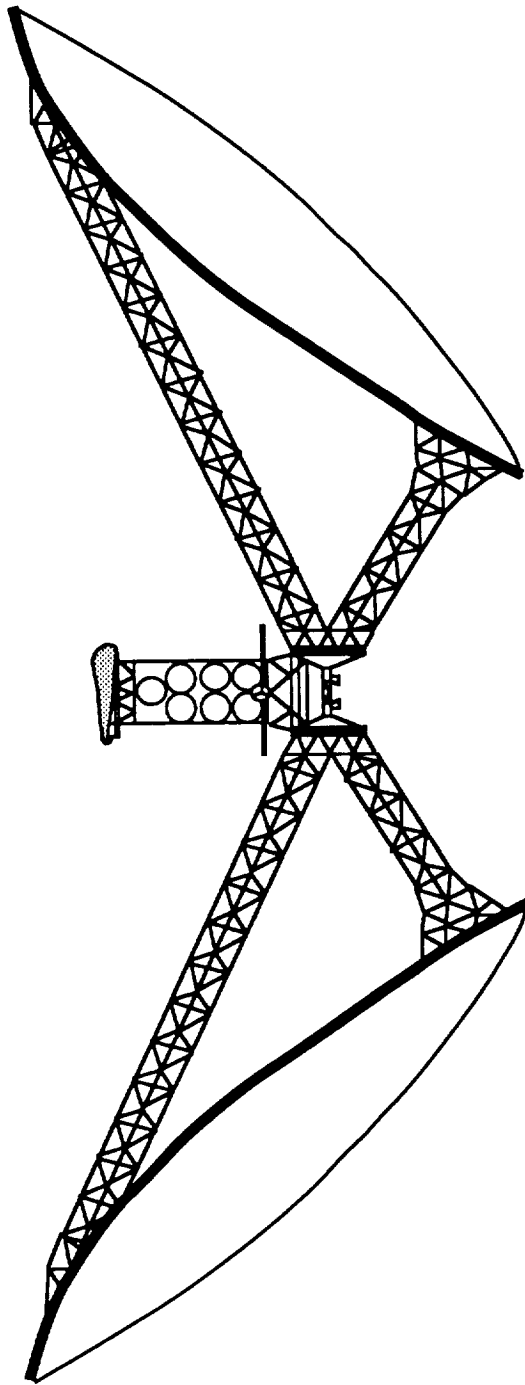
c) Magnetoplasmadynamic Thruster System

Figure I-1. Schematic of the Three Solar Propulsion Concepts Considered.

REFERENCES

1. Sutton, G., and Ross, D., Rocket Propulsion Elements, John Wiley & Sons, New York, 1976.
2. Mattick, A.T., et al., "High Temperature Solar Photon Engines", Reprinted from the Journal of Energy, Vol. 3, No. 1, pp. 30-39, Jan.-Feb., 1979.

II. SOLAR RADIATION ABSORPTION PROPELLED SPACECRAFT



INTRODUCTION

Mark Beall
Ronald Teeter
Thai Tran

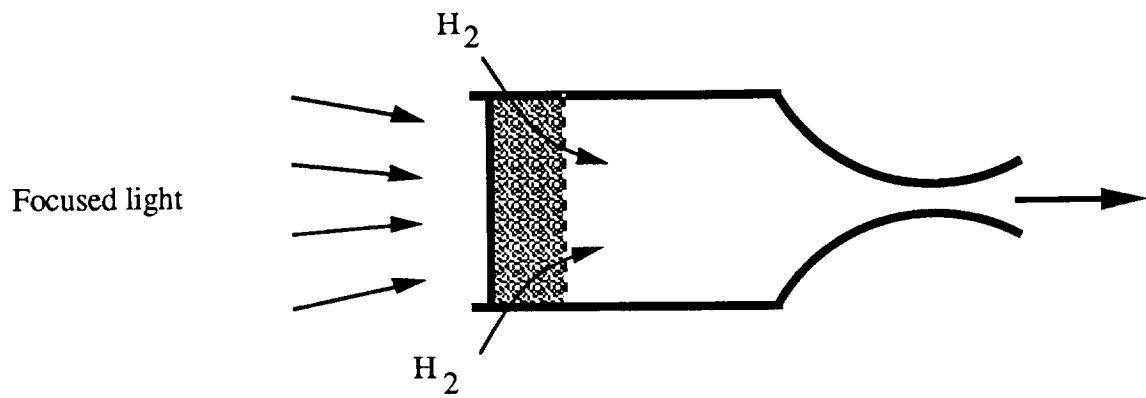
The Solar Radiation Absorber (SRA) propulsion system was designed to use a flowing gas volume absorber to directly convert solar energy to thermal energy in the propellant [1]. The propellant is then exhausted through a nozzle to provide the thrust and specific impulse necessary to deliver the payload to Mars. The flowing gas volume absorber was conceived at the University of Washington by Mattick, et al. [2] in 1979. Since then further research and experimental work by Rault [3] has led to greater understanding of the energy transfer mechanisms and verification of the enhanced efficiency. K. McFall is currently expanding the numerical simulation to two dimensions. The flowing gas volume absorber has the advantage of direct energy absorption since the energy is not transformed into an intermediate form (eg. mechanical or electrical) or converted to another wavelength (eg. lasers, microwaves, etc.). In addition, the direct absorption of radiant energy by the propellant avoids some of the limitations of earlier solar thermal propulsion systems [4].

Past efforts to couple solar radiation to a working fluid have concentrated on two concepts: surface absorbers and particulate volume absorbers. The surface absorber, shown schematically in Fig. II-1a, is the simplest method to transfer radiant solar energy to the fluid since the energy is absorbed by a heat exchanger surface or in a black-body cavity. In this concept broadband radiant energy is absorbed and heats a solid surface. This heat energy is transferred by conduction and convection to the working fluid (propellant) which is exhausted through a nozzle to produce thrust. Although this method has been used in terrestrial power production, it is not currently suitable for space propulsion since maximum allowable material temperatures (and therefore propellant temperatures) result in low specific impulses. In addition, Mattick, et. al. have shown that the efficiency of the

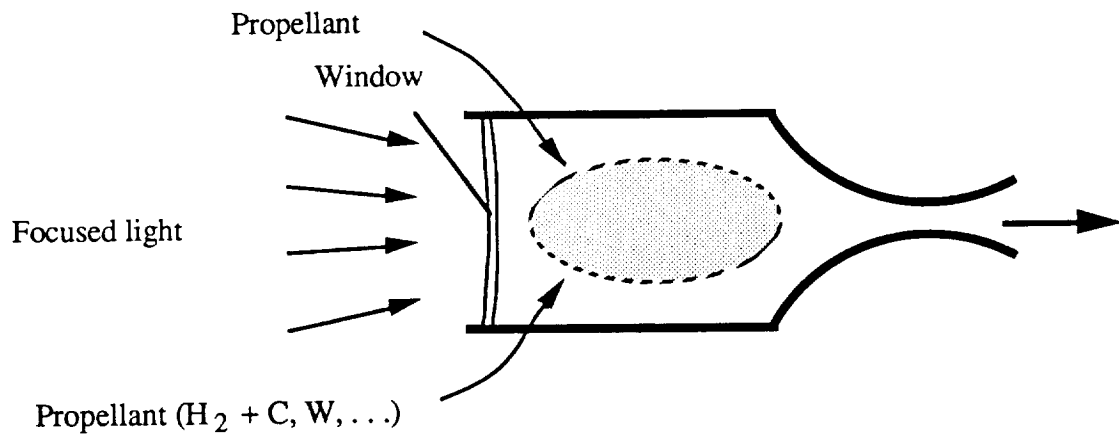
surface absorber declines rapidly with increasing temperatures [2]. Even with future high temperature material developments the low efficiency of surface absorbers will preclude their use for space propulsion. The particulate volume absorber, see Fig. II-1b, is more complex concept than the surface absorber. In this concept, a propellant gas (hydrogen) is seeded with a cloud of broadband absorbing solid particles. The particles absorb the incident solar energy and transfer their heat energy to the hydrogen through conduction and convection. The heated particulate seeded hydrogen propellant is exhausted through a nozzle to produce thrust. The particulate volume absorber, like the surface absorber, is not well suited for space propulsion. The particulate mass excessively increases the molecular weight of the propellant which decreases the specific impulse. Also, even for very small particles the energy transfer from particles to gas is very slow, requiring long residence times and thus long thrust chambers. In addition, the problems of reduced receiver efficiency due to deposition of particles on the window and performance losses due to nozzle throat erosion have yet to be solved.

In the SRA thruster, shown schematically in Fig. II-1c, radiant energy is transferred through a transparent window to the propellant gas contained inside a pressurized absorption chamber. This energy is absorbed volumetrically by the gas as it travels from the front (window end) to the back (nozzle end) of the chamber, thus raising the enthalpy of the propellant. Proper selection of the propellant gas enables the cooler gas in the vicinity of the window to absorb the reradiated energy from the hotter gas deeper inside the chamber. This radiation trapping results in a higher receiver efficiency, as shown in Fig. II-2, since the power loss due to reradiation is characterized by the temperature of the cool gas near the window, while the temperature for propulsive use is the peak temperature of the hot gas near the nozzle. This higher temperature results in higher exit velocities and larger specific impulses. Since no heat transfer through solid materials is required to heat the propellant, the operating temperature and propulsion performance can be increased.

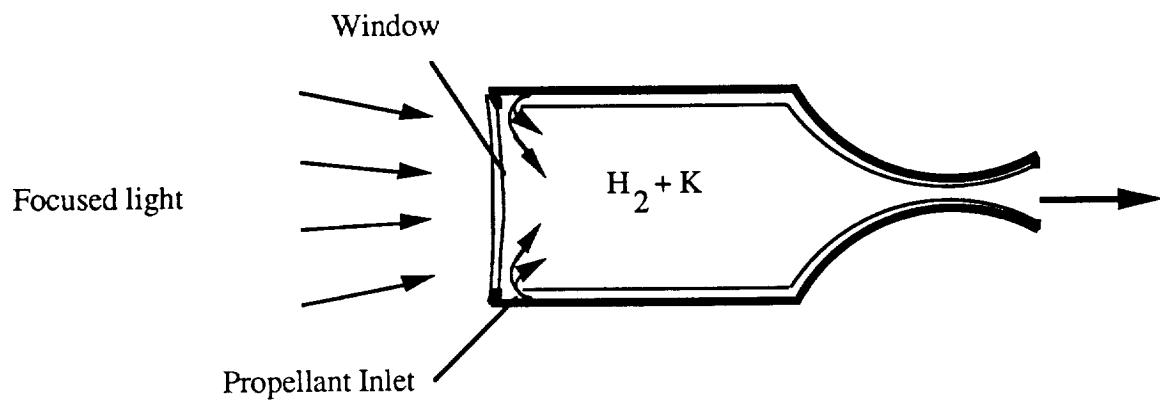
The following sections outline the design of a spacecraft using the SRA propulsion concept. First, the theory behind the flowing gas volume absorber is summarized. Next, the optical system that provides the power for the propulsion system is discussed. The actual design of each of the components of the spacecraft is then given, concentrating on the thruster, the structure for the optical system and the propellant storage system. Finally, the orbital mechanics for the Mars cargo delivery mission are discussed.



a) Surface Absorber



b) Particulate Volume Absorber



c) Flowing Gas Volume Absorber

Figure II-1. Variations of Solar Thermal Propulsion Concepts.

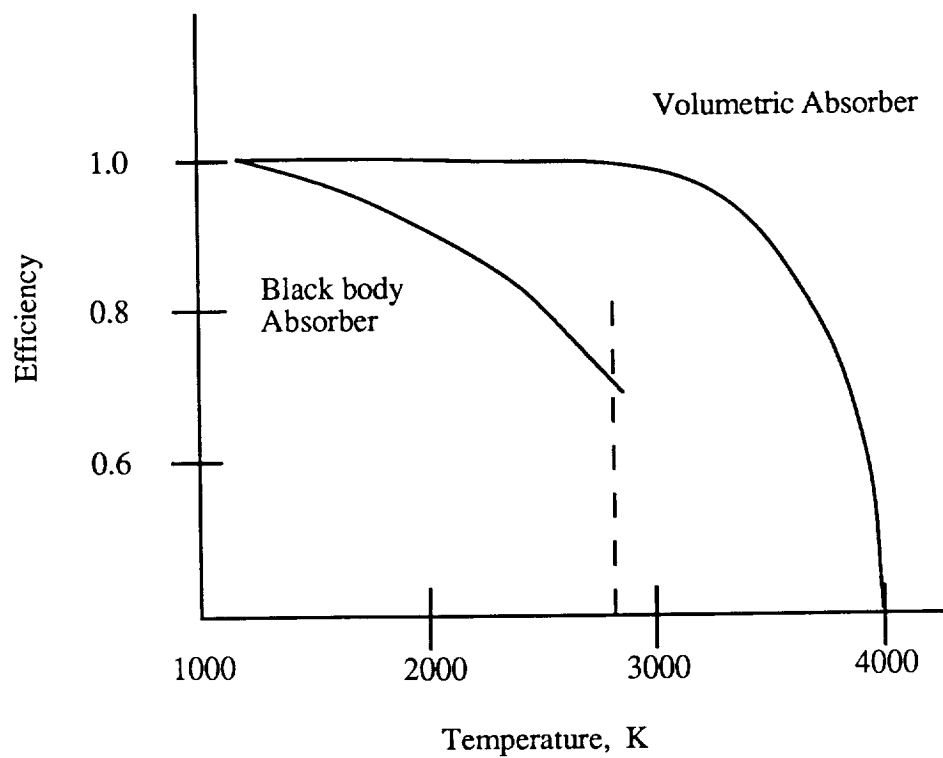


Figure II-2. Efficiency of Volume Absorption Compared to Black Body Absorption, for Solar Concentration Ratio of 8000 [4].

PROPULSION THEORY

Ronald Teeter

MATHEMATICAL MODEL

A one-dimensional model, developed by A. T. Mattick, is used to predict the performance of the flowing gas volume absorber [1]. This model, shown in Fig. II-3 is one dimensional, and includes only axial radiative heat transfer and convection. It also assumes that the radiation enters through a perfectly transparent window. A porous, grey back wall is assumed to be separated from the window by a distance d . The window transmits concentrated solar radiation with intensity, I_s , and the back wall radiates with emissivity, ϵ , at a temperature, T_w . In addition, constant pressure, inviscid, non-heat conducting, and constant heat capacity ideal gas flow is assumed. The absorption characteristics of the flowing gas are specified with respect to wavelength. Mattick reduced the necessary energy and heat transfer equations to,

$$\rho_m u C_p [T(x) - T_o] = 2\pi \int_0^\infty dv \left\{ \int_0^1 \mu I_v(0, \mu) [1 - e^{-\tau_v/\mu} + \rho F(\tau_v, \mu)] d\mu \right. \\ \left. + \int_0^1 \alpha_v(x') I_{vb}(T(x')) [G(\tau_v, \tau'_v) + \rho H(\tau_v, \tau'_v)] dx' \right. \\ \left. + \frac{\epsilon}{2} I_{vb}(T_w) C(\tau_v) \right\} \quad (II-1)$$

where,

$$C(\tau_v) = 2[E_3(\tau_{v0} - \tau_v) - E_3(\tau_{v0})]$$

$$F(\tau_v, \mu) = \begin{cases} \exp[(\tau_v - 2\tau_{v0})/\mu] - \exp(-2\tau_{v0})/\mu & \text{(specular reflection)} \\ \exp(\tau_{v0})/\mu C(\tau_v) & \text{(diffuse reflection)} \end{cases}$$

$$H(\tau_v, \tau'_v) = \begin{cases} E_2(\tau_{v0} - \tau_v - \tau'_v) - E_2(2\tau_{v0} - \tau'_v) & \text{(specular reflection)} \\ E_2(\tau_{v0} - \tau_v - \tau'_v) - E_2(2\tau_{v0} - \tau'_v) & \text{(diffuse reflection)} \end{cases}$$

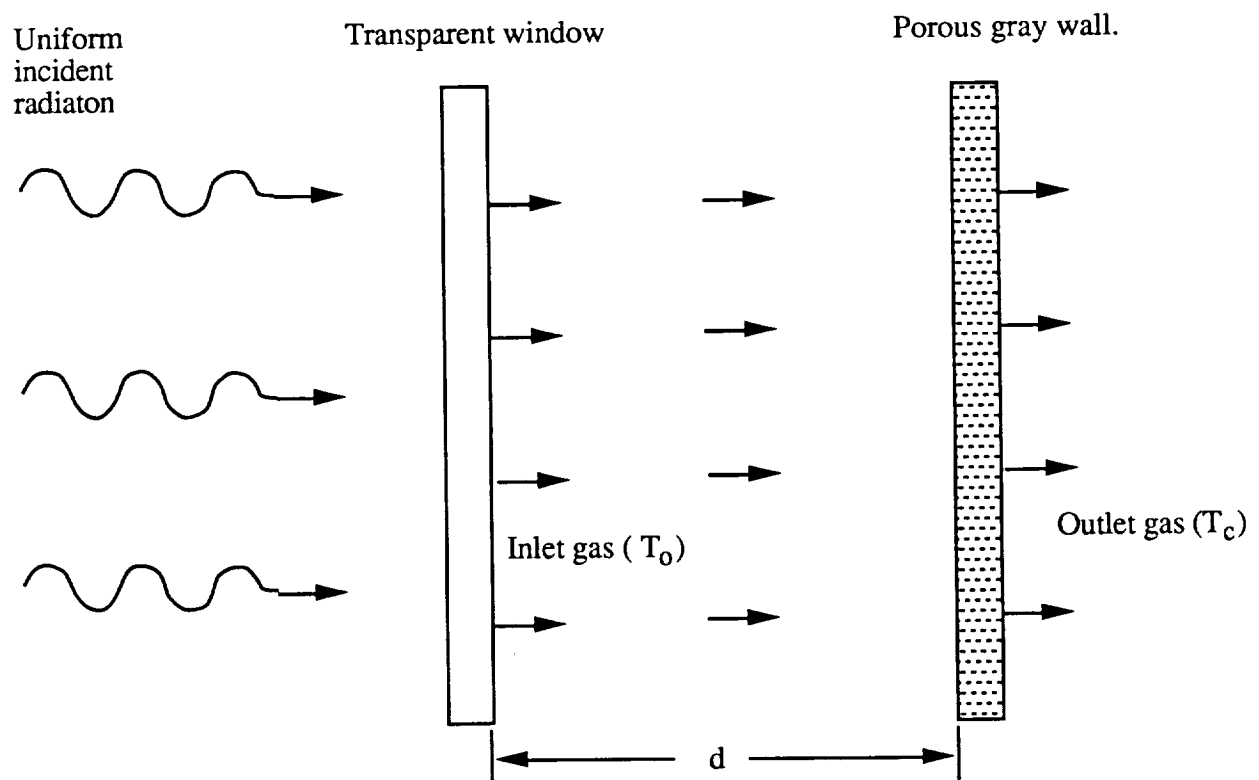


Figure II-3. Schematic of One-Dimensional Flowing Gas Radiation Heater Model.

$$G(\tau_v, \tau'_v) = -E_2(\tau'_v) - \text{sgn}(\tau_v - \tau'_v) E_2(|\tau_v - \tau'_v|)$$

$$\text{sgn}(x) = \text{sign of } x;$$

E_2 and E_3 are exponential integrals while C, F, G, and H are functions of frequency ν and position x . This equation was numerically integrated to obtain a temperature profile in the absorption chamber for a particular set of boundary conditions and propellant properties. A FORTRAN program written by K. McFall [5] was used to perform the calculations.

PROPELLANT SELECTION

The propellant for the SRA thrusters must satisfy two requirements. First, in order to maintain a high efficiency, the propellant must readily absorb solar radiation. Second, to provide a high specific impulse, the propellant must have a low molecular weight. A propellant consisting of two or more gases is necessary to meet both criteria. Alkali metal vapors can readily absorb the concentrated solar energy, however, their high molecular weights preclude their use as the primary propellant. Mixing the alkali metal vapor with a light gas such as hydrogen results in a propellant that has good absorption properties, as well as a low molecular weight.

Potassium was chosen for the alkali metal vapor because it absorbs a broad band of the solar spectrum (See Fig. II-4) and facilitates complete absorption of the incident radiation within a short distance. Potassium vapor has its strongest absorption mechanism in the 7,676 Å doublet transition of the potassium atom. Although the absorption over a broad part of the spectrum is weak at low temperatures, absorption improves with increasing temperature and pressure due to the effects of photoionization, inverse bremsstahlung, and K-photoionization [3]. Continuum absorption has also been observed but this was not considered due to a lack of reliable experimental data. At elevated

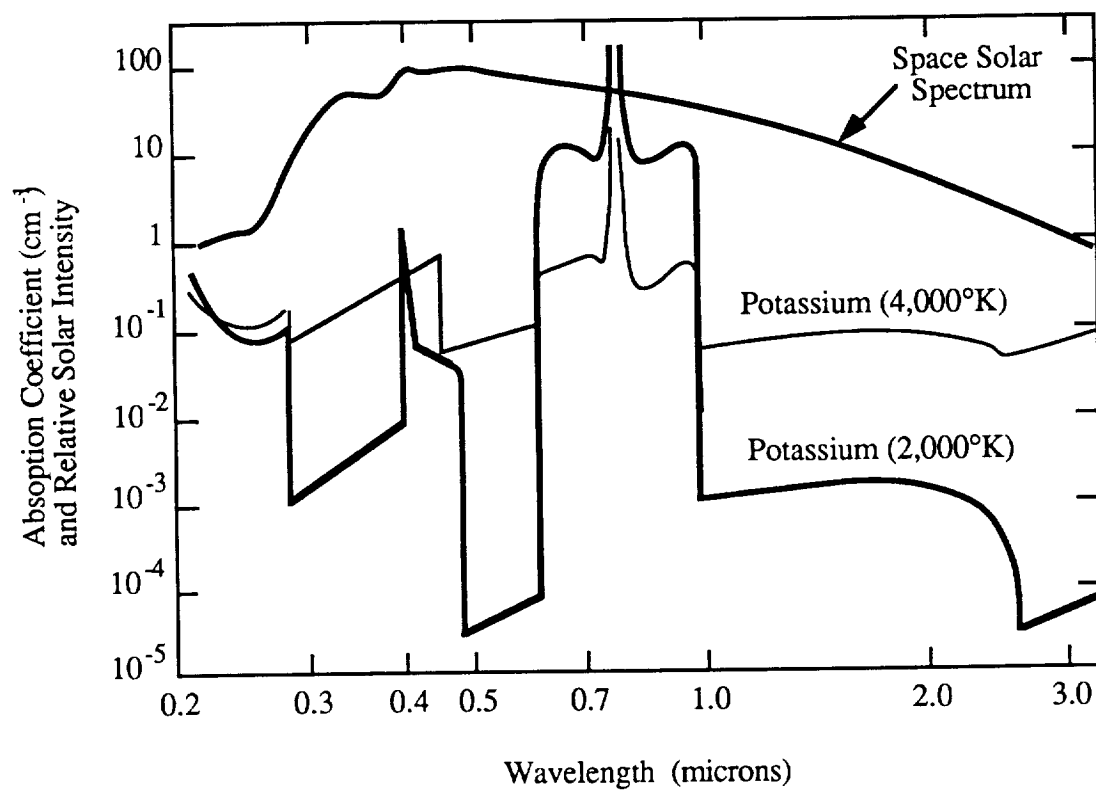


Figure II-4. Spectral Absorption Coefficient of Potassium Vapor [2].
(P = 1 atm)

temperatures, potassium absorbs especially well in the range of 0.6 to 1.0 microns, as shown in Fig. II-4. At elevated pressures, potassium also forms weakly bonded molecules, called dimers, which can absorb and store energy in internal rotational, vibrational, and electronic modes. The formation of dimers greatly enhances the absorption properties of the vapor. Internal energy is transferred to thermal energy in the carrier gas through a process called collisional quenching.

Hydrogen was selected as the carrier gas because it has the lowest molecular weight of any gas and it exists in diatomic form, which facilitates the energy transfer rate since diatomic molecules can store energy in their internal rotational and vibrational modes. A propellant consisting of a mixture of 90% hydrogen and 10% potassium vapor (by weight) provides good absorption of wavelengths between 0.4 and 1.0 micron of the sun's radiation [4] and has a molecular weight of 2.226 kg/kg-mole. Since the efficiency of the flowing gas volume absorber decreases above 3,500 K, in order to limit reradiation losses to no more than 10% the chamber temperature was not allowed to exceed 3,700 K. Another reason to limit the chamber temperature is to reduce the problem of losses due to dissociation. Of particular concern was the possibility of dissociating the potassium dimers which would lead to a loss of absorptivity. A chamber pressure of 10.13 MPa (100 atm) was selected to ensure that the potassium dimers and the hydrogen molecules do not dissociate at the high chamber temperatures. As can be seen in Fig. II-5, at a pressure of 100 atm, there is negligible dissociation of the hydrogen at a temperature of 3,680 K, thus the propellant has a ratio of specific heats, γ , of approximately 1.4. The axial temperature profile for this propellant mixture based on the mathematical model summarized earlier is shown in Fig. II-6. The temperature profile has a strong dependence on the initial flow rate. In the present case a maximum temperature of 3,680 K is achieved at a mass flow rate of 0.15 kg/s and a solar concentration ratio of 7,000.

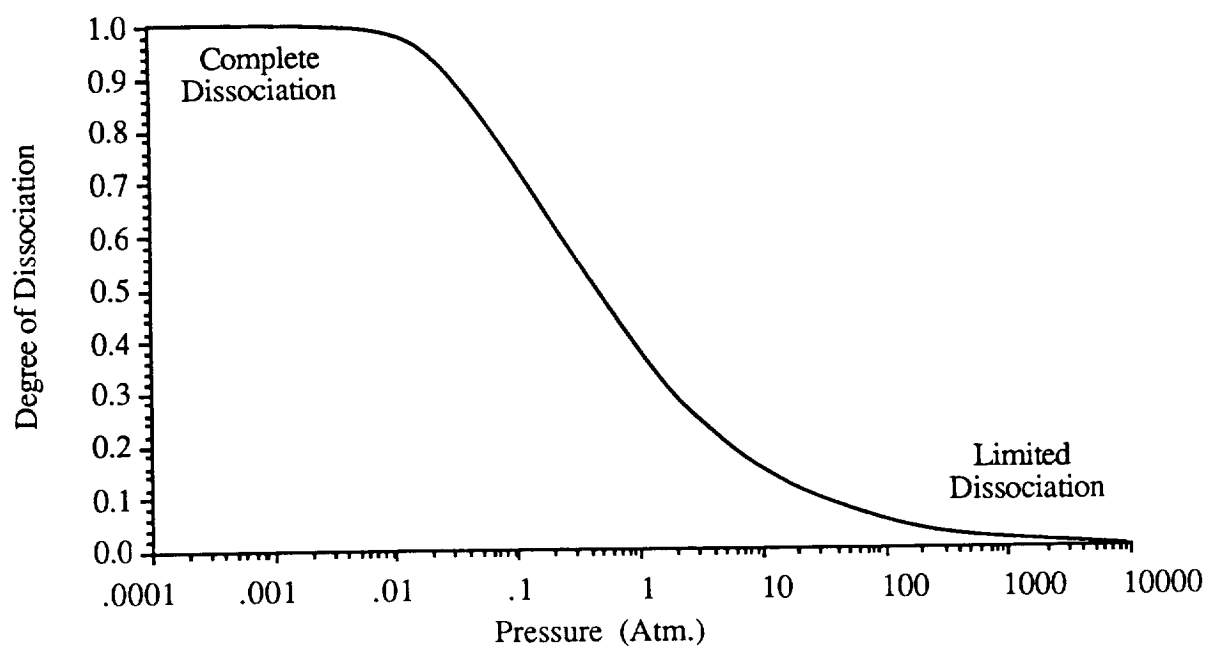


Figure II-5. Hydrogen Dissociation at 3,680 K.

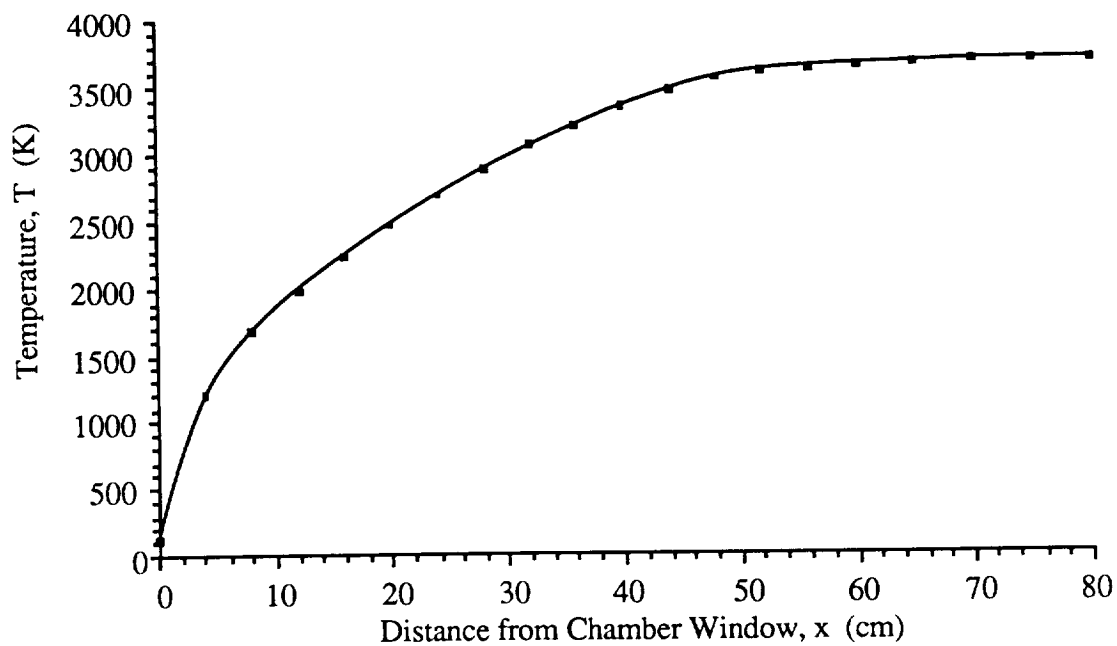


Figure II-6. Computed Absorption Chamber Temperature Profile

Performance

The thrust of a rocket , F is given by:

$$F = \dot{m}u_e + (P_e - P_a)A_e \quad (\text{II-2})$$

where \dot{m} is the mass flow of propellant ejected, u_e is the nozzle exit velocity, P_e is the propellant pressure at the nozzle exit, P_a is the ambient pressure, and A_e is the exit area of the nozzle. If it is assumed that the exhaust is ideally expanded then the equation reduces to:

$$F = \dot{m}u_e \quad (\text{II-3})$$

The exhaust velocity, u_e , for a given chamber temperature, T_c , is:

$$u_e = \sqrt{\left(\frac{2\gamma}{\gamma-1}\right) \frac{R_u}{M_w} T_c} \quad (\text{II-4})$$

where R_u is the universal gas constant, and γ and M_w are the ratio of specific heats and the molecular weight of the propellant, respectively. The specific impulse is defined as the thrust to propellant weight flow ratio. For an ideally expanded flow:

$$I_{sp} = \frac{u_e}{g_0} \quad (\text{II-5})$$

where g_0 is the gravitational acceleration at the surface of Earth.

The performance of the SRA thruster was calculated using the data from the numerical calculations and the propellant properties. The peak temperature of 3,680 K and

a mass flow of 0.15 kg/s were used for the performance calculations. Using Eq II-2 the exhaust velocity was calculated to be 9,809 m/s. The thrust is thus 1,470 N and the specific impulse is 1,000 sec. The performance of the SRA thruster is summarized in Table II-1.

Table II-1: SRA Thruster Propulsion Data

Chamber Temperature	3,680 K
Chamber Pressure	10.13 MPa
Propellant Mass Flow Rate	0.15 kg/s
Exit Velocity	9,809 m/s
Thrust	1,470 N
Specific Impulse	1,000 s

SOLAR OPTICS

Thai Tran

An optical system is required to concentrate and deliver solar energy into the rocket engine chamber to heat the alkali-seeded hydrogen gas. A solar concentration ratio sufficient to achieve a specific impulse of at least 1,000 s was specified. The system is designed to track the sun during periods of thrust.

CONCENTRATING SOLAR RAYS

The Concave Light Amplification Mirrors (CLAM) system is used to concentrate the 1.33 kW/m^2 solar intensity available in the vicinity of the earth to the 24 MW/m^2 intensity needed by the thermal rockets. Figure II-7 schematically shows two concentrators of the CLAM system focusing the solar radiation into two rocket engines. The concentrators are off-axis sections of a paraboloid of rotation created by rotating a parabolic curve (focal length 35 m) about its axis of symmetry, as shown in Fig. II-8a. As shown in Fig. II-8b, the frontal view of these sections are elliptical (with a major axis of 122 m and a minor axis of 86 m). This configuration is similar to the one discussed by Shoji [6]. The total power, P_R , delivered to each thruster by a CLAM section is calculated from

$$P_R = \eta_c I_s A_c \quad (\text{II-6})$$

where η_c is the reflective efficiency of the concentrator (taken to be 0.85 for the chosen reflecting surface. The details of the concentrators will be discussed later), I_s is the incoming solar intensity (1.33 KW/m^2) and A_c is the collector's frontal area. The total power delivered to the image by each concentrator is 10.1 MW.

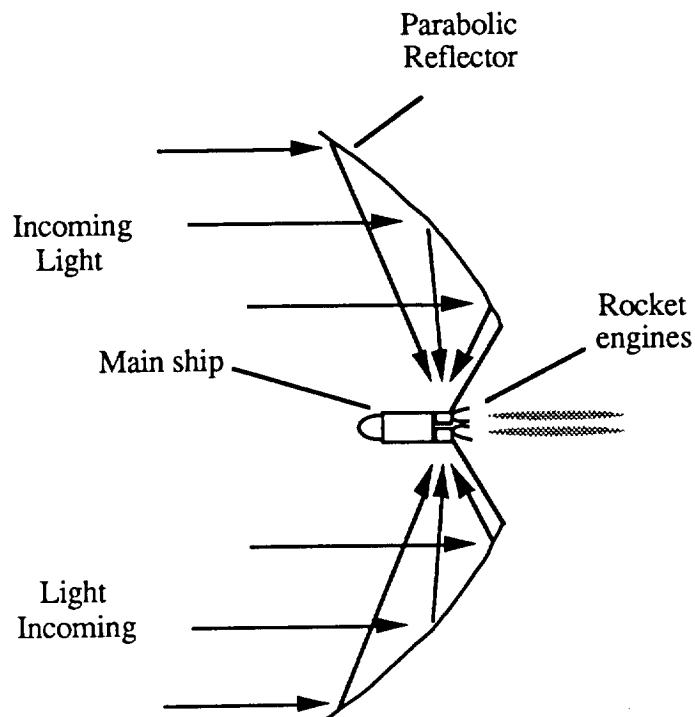


Figure II-7. Schematic of the Concave Light Amplification Mirror (CLAM) system.

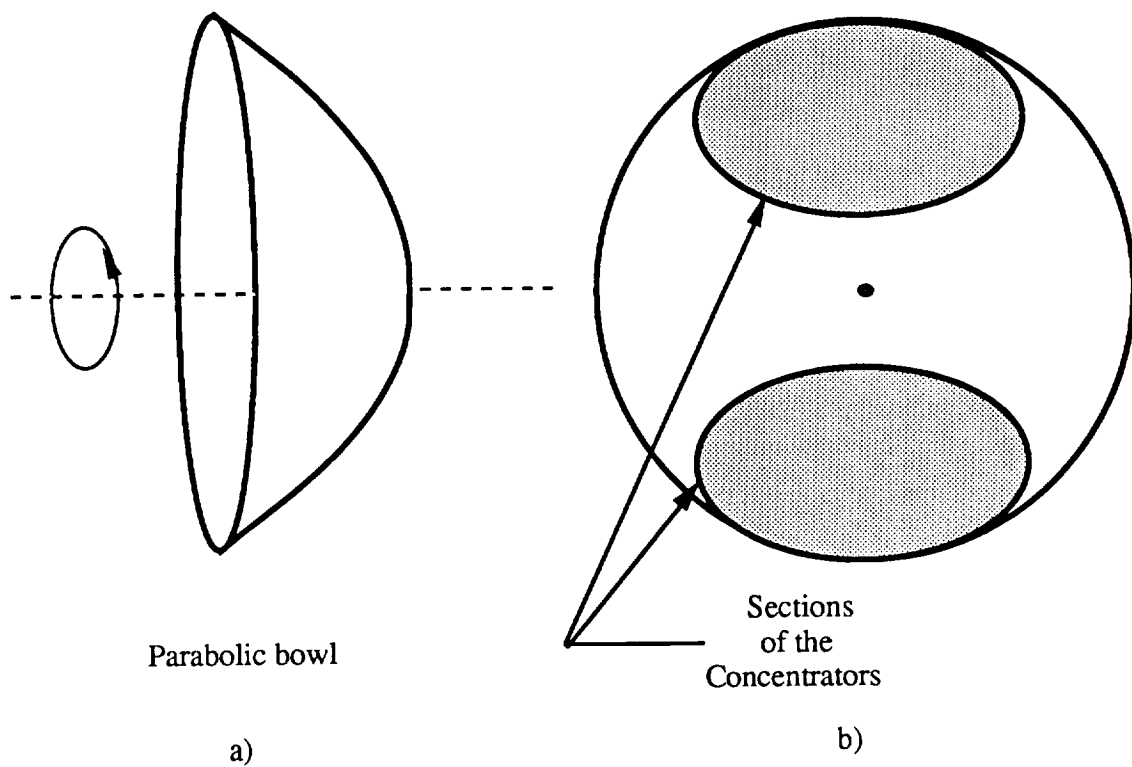


Figure II-8. Geometric Characteristics of the CLAM's Concentrators.

Image Analysis

As mentioned earlier, the CLAM system is similar to the concentrator system chosen by Shoji [6]. However, whereas Shoji used circular frontal projections (CFP), the CLAM has elliptical frontal projections. Given a specific frontal area, the CLAM can provide a greater concentration ratio than the circular projection. An area concentration ratio, CR, is defined as,

$$CR = \frac{\text{Collector area}}{\text{Image Area}} \quad (\text{II-7})$$

The CLAM system achieves higher CR than a CFP system by reducing the distance between the farthest tip of the concentrator to the focal point. Reducing this distance reduces the size of the image. The ray tracing analysis relating the image size and the distance between the concentrators' reflecting surfaces is as follows:

Consider a parabolic reflecting surface as shown in Fig. II-9. Sunlight which strikes the surface with a subtended angle, ϕ , of 0.5° (8.7×10^{-3} radians) will be reflected toward the focal point at a spreading angle of 0.5° . The image formed on the focal plane by a reflection from an element of surface will be an ellipse with a major axis length b_{im} calculated as follows:

$$b_{im} = \frac{S \phi}{\cos(\theta)} \quad (\text{II-8})$$

where S is the distance from the reflecting surface to the focal point and θ is the angle between S and the CLAM's rotating axis. The size of the final image is found by superimposing the images created by the reflecting surfaces from the rim of the concentrators.

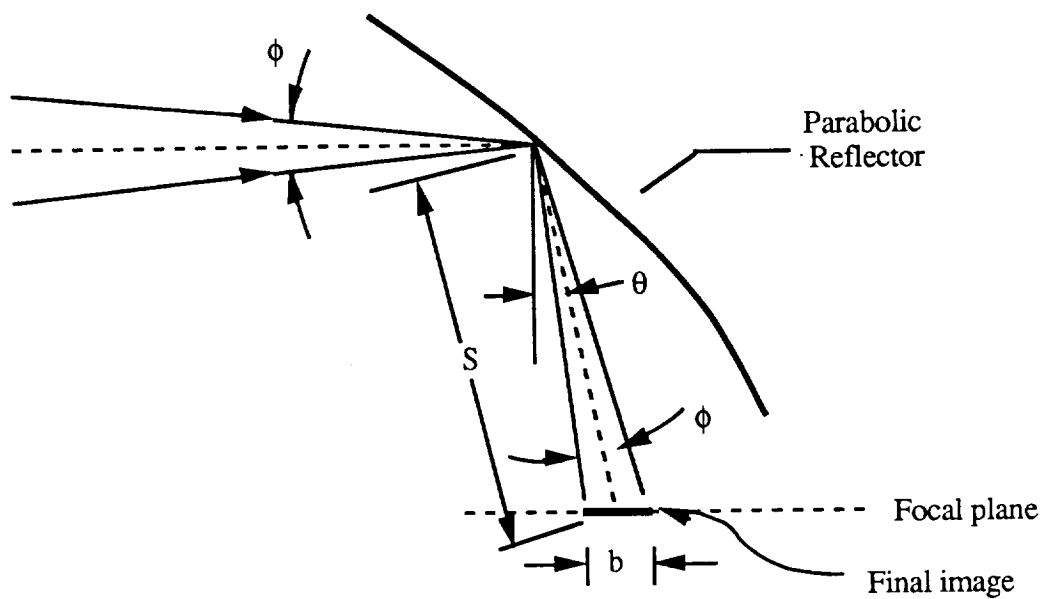


Figure II-9. Formation of the Final Image.

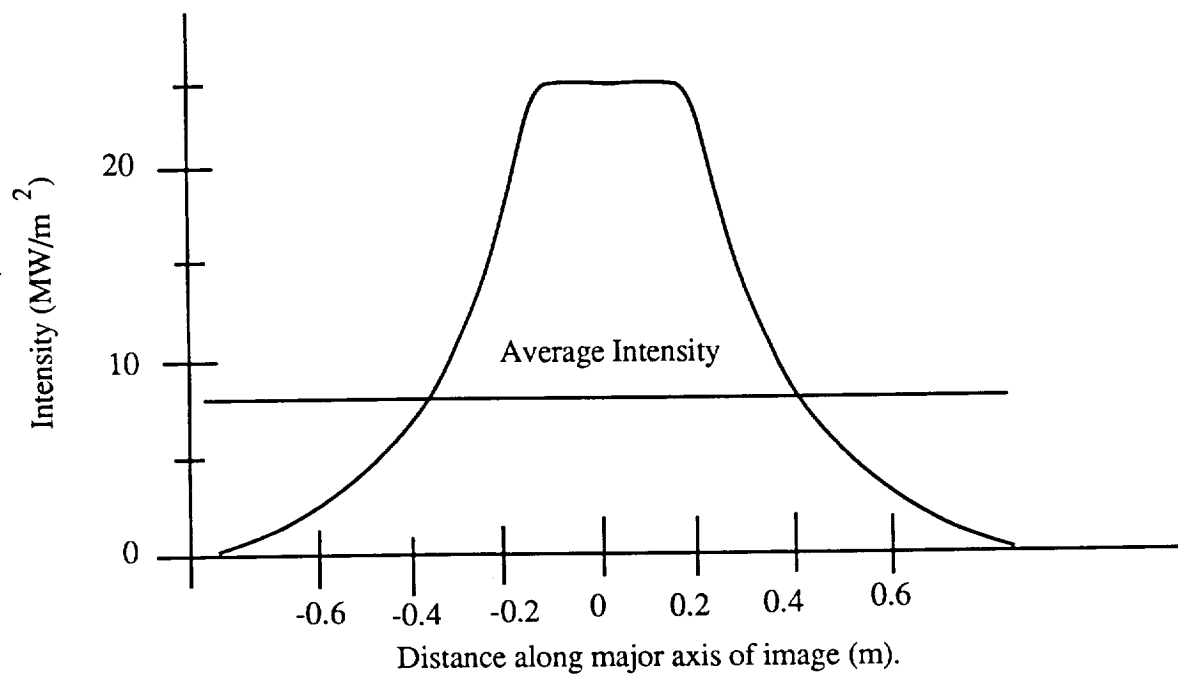


Figure II-10. Intensity Distribution Along the Final Image.

Using Eq. II-8, the image created by the concentrators of the CLAM was found to be elliptical with the major and minor axes to be 1.25 m and 1.23 m respectively (i.e. almost circular). A CFP system with the same frontal area will produce an elliptical image with the major and minor axis of 1.49 m and 1.32 m respectively. Thus, the CLAM system achieves 27% higher concentration ratio than the CFP system. The concentration ratio of the CLAM is 7,350.

Intensity distribution

Parabolic concentrators do not concentrate the solar energy uniformly across the projected image. Typically, the solar images have bell shaped intensity distributions. The analysis of this shape was completed using simple numerical procedures. Square elements located along the major axis of the elliptical image (calculated from above) were chosen. The intensity, I , at each element was calculated by summing the intensity contribution, I_n , from sections of the concentrator.

$$I = \sum I_n \quad (\text{II-9})$$

A typical concentrator section was chosen to have a frontal projection area, A_n of 100 m². The intensity contribution from each section is calculated from Eq. II-10.

$$I_n = I_s A_n / A_{n\text{Image}} \quad (\text{II-10})$$

where $A_{n\text{Image}}$, the area of the image created by each concentrator section, can be calculated from the image analysis procedure discussed earlier. If an element is outside the image area created by a concentrator section n , the intensity contribution from that section to the element is zero.

The resulting intensity distribution calculated using this analysis is shown in Fig. II-10. It can be seen that although the average intensity across the image is approximately 8.3 MW/m², local intensity at the center of the image can reach as high as

24 MW/m². The SRA thruster can achieve greater thermal efficiency by utilizing only the high intensity at the center of the image. This is discussed further in the engine design section.

SOLAR TRACKING

In order to concentrate the solar radiation properly, the primary concentrators must track the sun during periods of thrust. Figure II-11 shows a basic elliptical orbit of the ship and the regions where thrusting will occur. (The actual orbital mechanics will be discussed in a later section.) The reflectors must have two rotational degrees of freedom to satisfy the thrusting requirement (the second degree of freedom is required for out of plane orbits). The first degree of freedom is achieved by rotating the collector about the ship's lateral axis. The second degree of freedom is obtained by rotating the whole ship about its longitudinal axis using attitude control thrusters, and/or vectoring the thrust from the main engines.

Figure II-12 shows the rotations of the CLAM and the whole ship as the ship approaches and departs the region of perigee thrust. During the time of perigee thrust, the ship rotates clockwise as viewed from the front and the CLAM system rotates clockwise as viewed from the "top".

The reflectors are connected by trusses to a rotating platform on the ship. The details of the trusses will be discussed later. Electric motors mounted on the platforms rotate the reflectors about the vertical axis. The electric motors are powered by photovoltaic cells. The details of the rotation platforms, electric motors, solar panels and the support structure have yet to be designed.

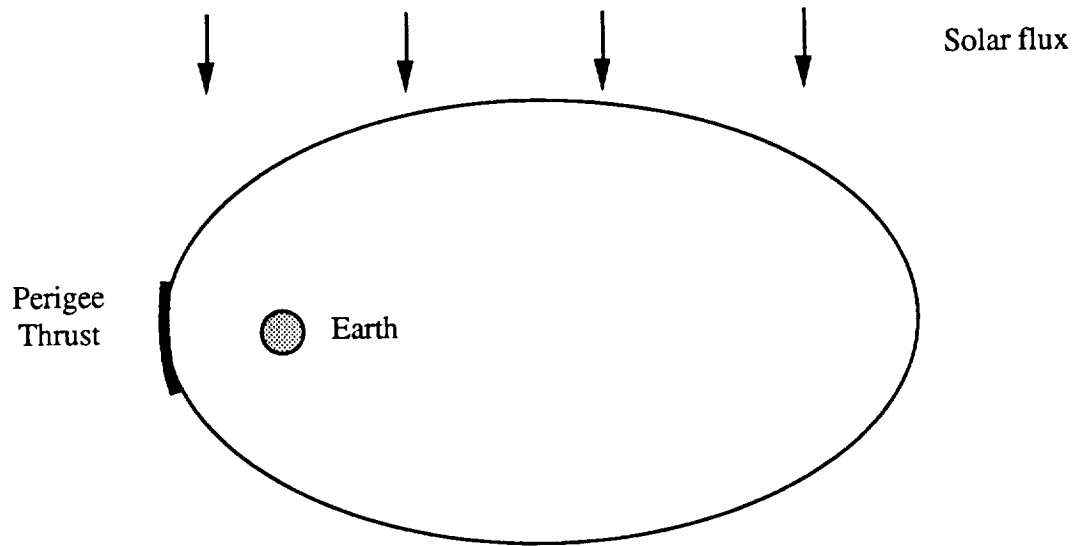


Figure II-11. Location of thrusting on elliptical orbit.

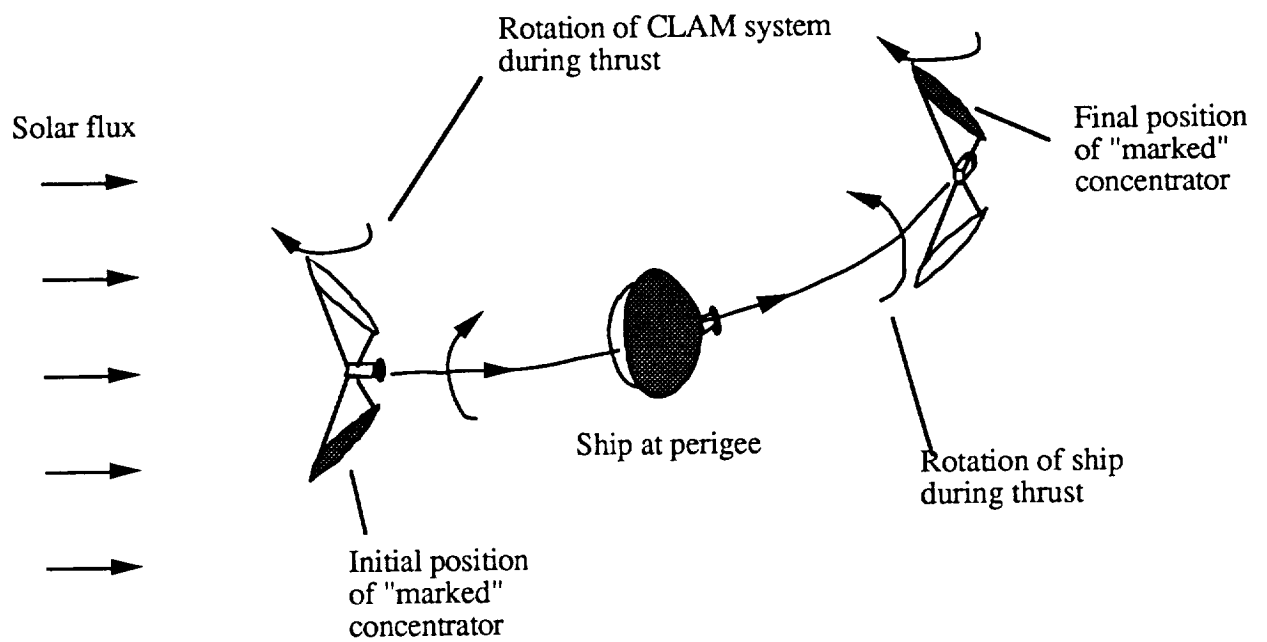


Figure II-12. Tracking of the Sun During Perigee Thrust.

DESIGN OF SPACECRAFT

Mark Beall
Ronald Teeter
Thai Tran

GENERAL

The SRA spacecraft consists of a main ship structure and two off-axis parabolic reflectors. The main ship houses the thrusters, propellant tanks, payload system, guidance and control systems, and photovoltaic power generators. The reflectors are attached to the main truss with four trusses as shown in Fig. II-13. These trusses connect to the main ship through a joint which allows the reflectors to be rotated relative to the main ship.

THRUSTER

The primary components of each SRA thruster are the absorption chamber, window, nozzle, potassium storage tank, helium pressurant tank, and the propellant preheater. Important features considered at this stage in the design were: power requirements, material requirements, heat transfer, and efficiency of such a design. The main engine configuration is shown to scale in Fig. II-14.

Absorption Chamber

Due to the low mass flow of the engine, a typical regeneratively cooled configuration is not possible. A configuration was devised as shown in Fig. II-15. The chamber consists of an inner, reflective liner possibly of tungsten or tantalum, surrounded by carbon-carbon composite insulation. Outside of this is a cooling jacket through which the hydrogen flows. On the outside of the structure is a jacket which provides the structural integrity of the chamber.

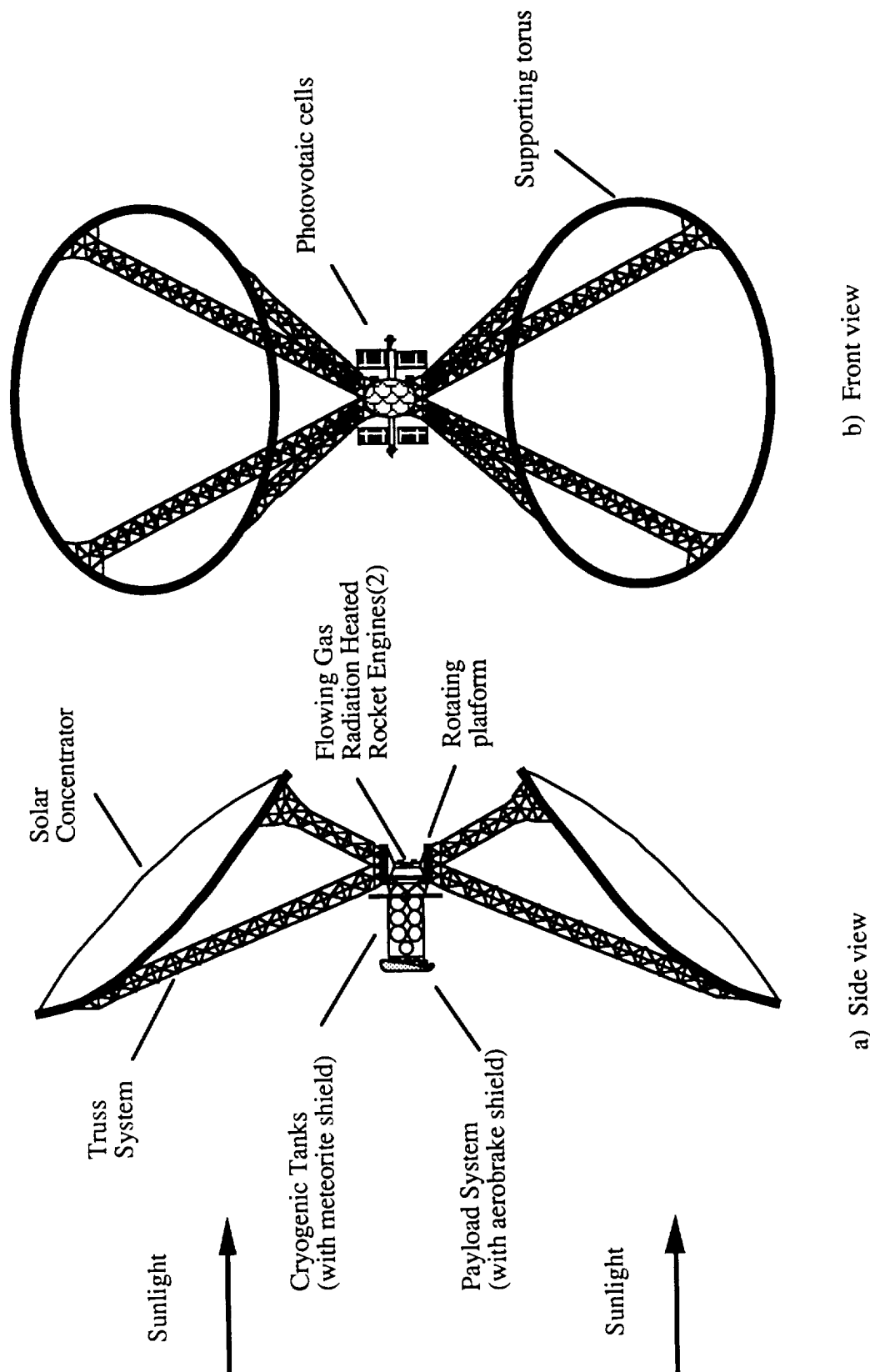


Figure II-13. General Configuration of the Spacecraft.

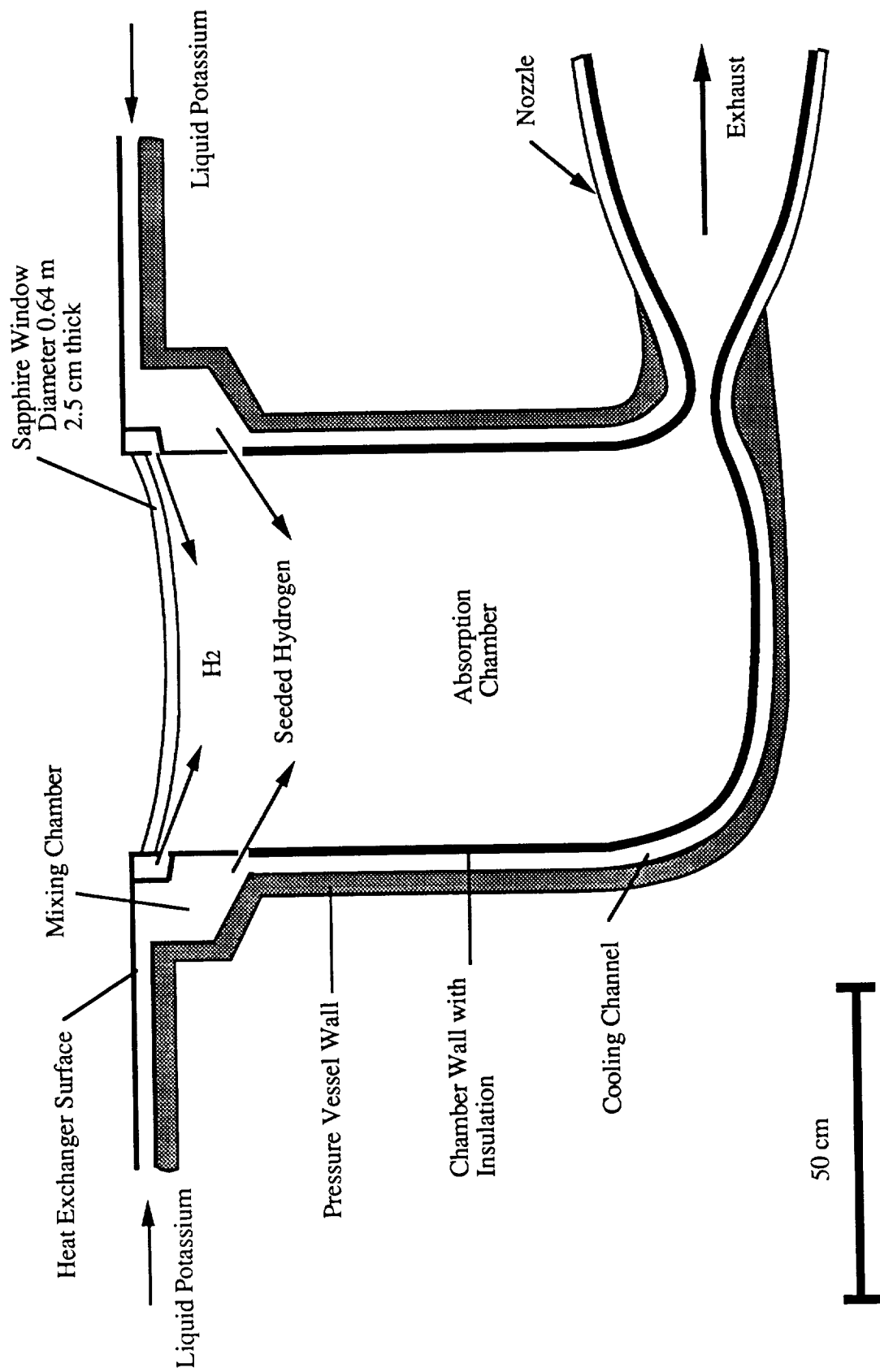


Figure II-14. Schematic of the Solar Radiation Absorption Rocket.
(Nozzle throat not shown to scale for clarity)

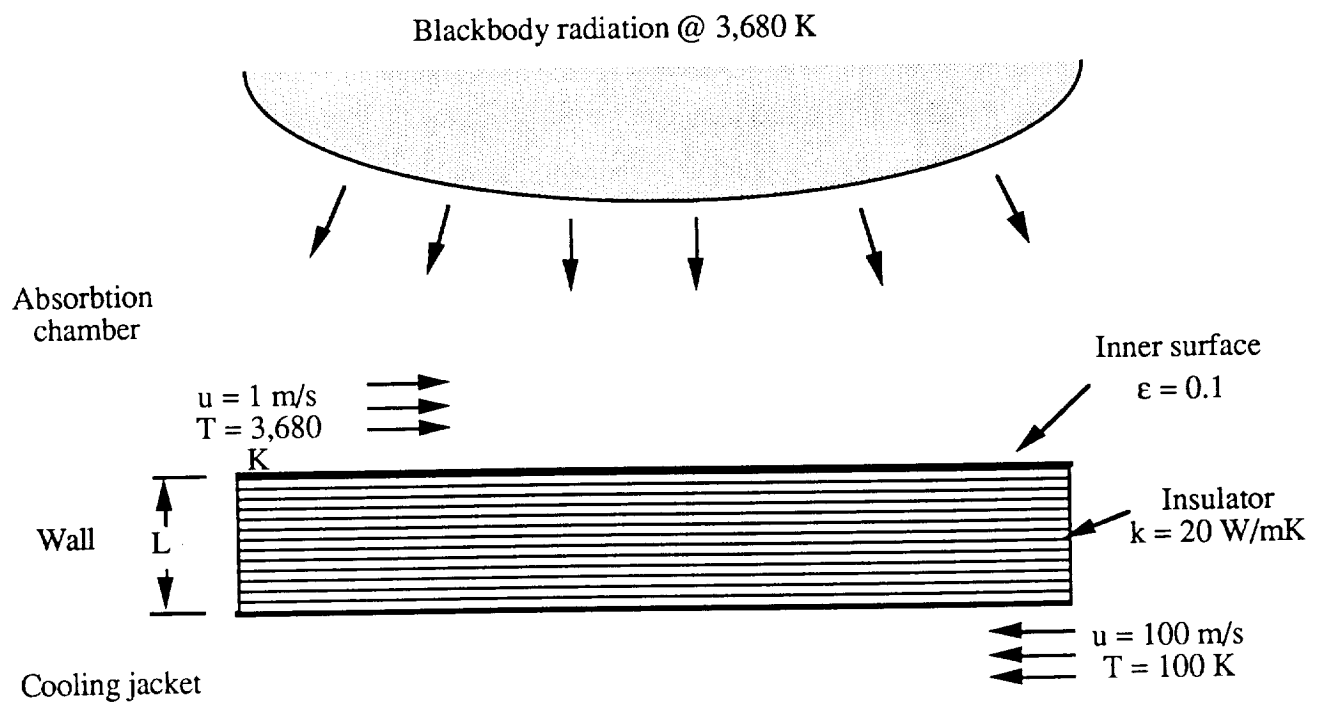


Figure II-15. Schematic of Heat Transfer Modeling.

An aluminum/silicon carbide metal matrix composite is used for the pressure vessel. The wall thickness is determined by the contained pressure, the radius of the vessel and the allowable stresses in the wall. The dominating stress is the hoop stress which is given by [7],

$$t = \frac{P_c r_c}{\sigma_N} \quad (\text{II-11})$$

where the yield stress of Al/SiC, σ_N , is 700 MPa at 600 K. This results in a pressure vessel wall 4.5 cm thick with a margin of safety of 22%. Although the steady-state operating temperature is well below 600 K, the outer chamber wall was designed to withstand stresses at the higher equilibrium temperature attained after engine shutdown. This higher equilibrium temperature is due to the conduction of heat from the inner engine through the wall when the regenerative cooling system is not operating.

Absorption Chamber Wall Heat Transfer Analysis

The model in Fig. II-15 was used for the preliminary heat transfer analysis of the chamber wall. This model is representative of a section of wall at the far end (near the nozzle) of the chamber. The gas temperature is 3,680 K and has a velocity of 1.0 m/s. The gas is assumed to radiate as a blackbody at the gas temperature ($T_g = 3,680$, $\epsilon_g = 1$). The wall is assumed to have an equal emissivity and absorptivity, ϵ_w , of 0.1.

The gas in the chamber is a mixture of potassium and hydrogen. The properties of this mixture are dependent on the mole-fraction rather than the mass-fraction of its constituents. The mole-fraction of potassium is 0.0057. Thus, the potassium in the gas has insignificant effects on the properties of the gas as a whole. For this reason the gas in the chamber was considered to be pure hydrogen.

Properties of hydrogen at the temperatures in the chamber were calculated by using the following relations and assumptions. The viscosity of a gas, μ , is independent of pressure and depends only on temperature [8]. The viscosity of a gas at a given temperature, T_1 , is related to the viscosity at a second temperature, T , by [8]:

$$\frac{\mu}{\mu_1} = \frac{T_1 + 120}{T + 120} \left(\frac{T}{T_1} \right)^{\frac{3}{2}} \quad (\text{II-12})$$

The thermal conductivity of a gas, k , is approximately equal to the product of the constant-pressure specific heat, C_p , and the viscosity. The specific heat of hydrogen in the range 300 - 3,500 K is given by [8]

$$C_p = 56.505 - 702.74\theta^{-0.75} + 1165.0\theta^{-1} - 560.70\theta^{-1.5} \quad (\text{II-13})$$

$$\text{where } \theta = \frac{T(\text{K})}{100}$$

The maximum allowable wall temperature was selected to be 3,300 K, since this is the upper limit for materials such as tungsten. For the purposes of convection heat transfer calculations the properties of the hydrogen were evaluated at the average film temperatures of both of the convective conditions.

The heat transferred per unit area, q'' , between two temperatures, T_1 and T_2 , can be determined by:

$$q'' = \frac{T_1 - T_2}{R''} \quad (\text{II-14})$$

where R'' is the thermal resistance of the area separating the two temperatures.

The thermal resistance of a convective boundary between a flowing gas and a surface is given by:

$$R'' = \frac{1}{h} \quad (\text{II-15})$$

where h is the film heat transfer coefficient. The film heat transfer coefficient may be found from [9]:

$$h = \frac{\text{Nu } k_f}{x} \quad (\text{II-16})$$

where Nu is a dimensionless parameter called the Nusselt number, k_f is the thermal conductivity of the gas and x is the distance from the edge of the plate. The thermal resistance of a solid surface of thickness, L , with thermal conductivity, k , is:

$$R'' = \frac{L}{k} \quad (\text{II-17})$$

When there are two or more thermal resistances in series through a given temperature difference, the thermal resistances may be added to obtain an overall thermal resistance.

The convective heat transfer coefficients, h , were evaluated for the hot and cold surface of the wall. The Reynolds number for the flow is given by:

$$\text{Re}_x = \frac{u_\infty x}{\nu} \quad (\text{II-18})$$

where u_∞ is the free stream velocity of the flow, x is the downstream distance from the beginning of the plate and ν is the kinematic viscosity of the fluid. For the hot surface $\text{Re}_x = 9,764$, thus laminar flow could be assumed.

For laminar flow over a flat plate the Nusselt number is given by [9]:

$$Nu_x = 0.332 Re_x^{1/2} Pr^{1/3} \quad (II-19)$$

where Pr is the Prandtl number of the gas. For the top plate $Nu_x = 29.32$. This gives a convection coefficient of $h = 40.0 \text{ W/m}^2 \text{ K}$.

The cold surface was evaluated to give $Re_x = 5.74 \times 10^5$. This is indicative of turbulent flow. Actually for this application on this surface turbulent flow is desirable since it give a higher heat transfer coefficient. Thus the coolant flow will be tripped to ensure turbulence. For turbulent flow over a flat plate the Nusselt number is given by [9]:

$$Nu_x = 0.0296 Re_x^{4/5} Pr^{1/3} \quad (II-20)$$

For the conditions on the cold surface $Nu_x = 1,064$. This gives a film heat transfer coefficient of $h = 713 \text{ W/m}^2 \text{ K}$.

The wall separating the two flows was selected to be a carbon-carbon composite, since this material has a great resistance to high temperatures and a low thermal conductivity. The thermal conductivity for carbon-carbon is relatively constant with temperature. For the purposes of this design it was taken to have a value of $k = 20 \text{ W/m}^2 \text{ K}$ [10].

A power balance at the wall gives the net radiative power exchange between the gas at temperature, T_g , and the wall at temperature, T_s , as:

$$q''_{\text{net}} = \sigma \epsilon_w (\epsilon_g T_g^4 - T_s^4) \quad (II-21)$$

At steady state operating conditions the inner surface of the wall must have a balance between the power entering due to convection and radiation from the gas in the

absorption chamber and the power leaving through the wall. Thus the resulting equation that must be solved for the wall temperature is:

$$\frac{T_g - T_w}{R_1} + \sigma \epsilon_w (\epsilon_g T_g^4 - T_s^4) = \frac{T_w - T_4}{R_2 + R_3} \quad (\text{II-22})$$

The solution for this equation with varying values of L , the thickness of the insulation, is shown in Fig. II-16. The corresponding heat transfer rates are shown in Fig. II-17. A maximum wall temperature of 3,300 K gives a desired thickness of insulation of 0.14 m with a corresponding heat transfer rate of 0.40 MW/m². Since the wall area of the chamber that is exposed to such conditions is approximately 2 m², and the remaining area is subjected to much lower heat transfer, the total power into the regenerative cooling system from the wall of the chamber was taken to be 1.0 MW.

Nozzle

The nozzle throat area, A^* , was calculated using standard isentropic flow relationships [11]. The throat diameter, D^* , is solely a function of chamber pressure, p_c , chamber temperature, T_c , ratio of specific heats, γ , molecular weight, M_w and mass flow rate, \dot{m} :

$$A^* = \dot{m} \left[\gamma \left(\frac{2}{\gamma + 1} \right)^{(\gamma + 1)/(\gamma - 1)} \frac{M_w}{R_u T_c} p_c^2 \right]^{-\frac{1}{2}} \quad (\text{II-23})$$

$$D^* = \sqrt{\frac{4 A^*}{\pi}} \quad (\text{II-24})$$

The nozzle throat diameter is calculated to be 1.4 cm. High heat transfer rates are expected in the nozzle due to the high temperature of the propellant and the small throat diameter. Regenerative cooling of the nozzle may be possible using the hydrogen propellant. However, the required mass flow of hydrogen to satisfactorily cool the throat

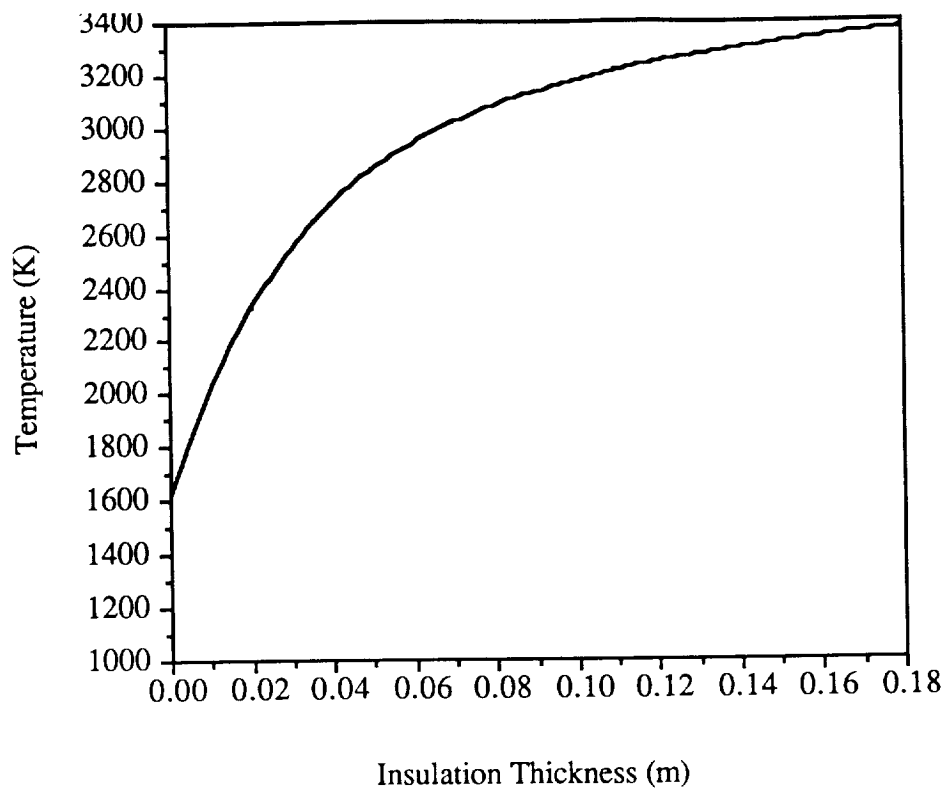


Figure II-16. Equilibrium Temperature at the Chamber Wall.

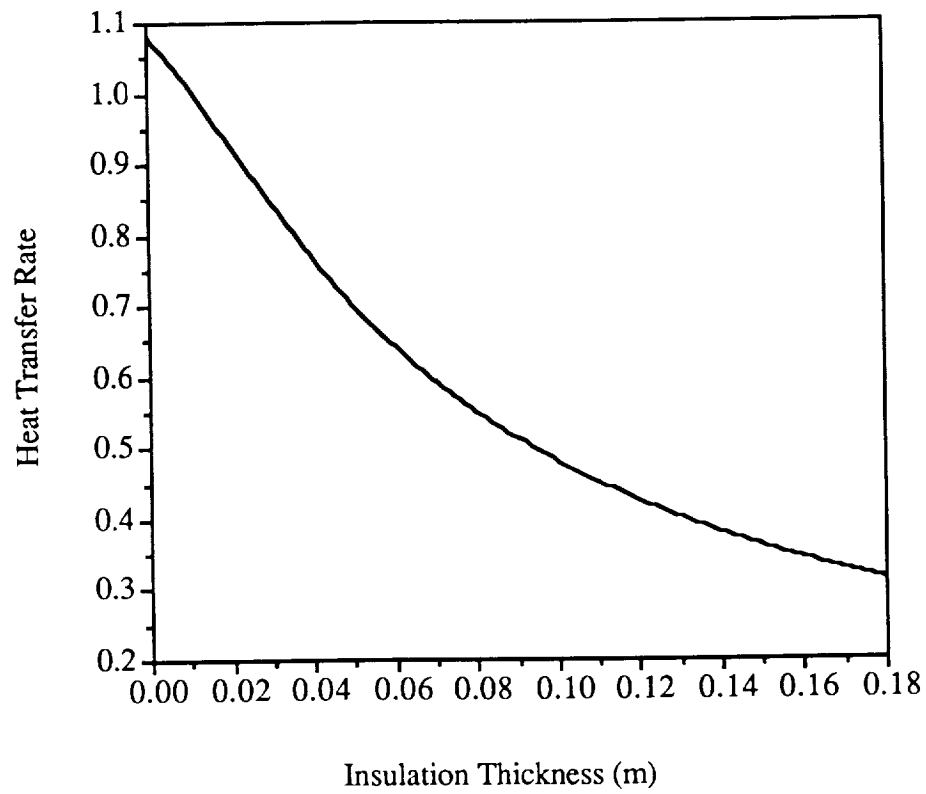


Figure II-17. Rate of Heat Transfer to the Wall.

may exceed the required mass flow for propulsion. In this case, film cooling, transpiration cooling, or a closed loop heat exchanger with radiators would be necessary.

The nozzle throat, which is constructed of the same material as the chamber, must be more heavily reinforced to prevent bending and buckling [12]. This may be accomplished by increasing the thickness of the nozzle material to form a cylindrical shell at the throat as shown in Fig. II-14.

Window

As shown in Fig. II-14 the window diameter is 0.64 m. This is the minimum aperture diameter necessary to deliver the required power to the absorption chamber. As shown previously in Fig. II-10 the intensity is not constant across the window it reaches a maximum of 24 MW/m^2 at the center of the window and drops off toward the edges. The window must be able to transmit the solar spectrum with a minimum amount of absorption. In addition, the window must withstand the stresses imposed by the high chamber pressure and minimize reflection losses due to the curved surface.

Sapphire (Al_2O_3) is a good transmitter of radiation from $0.25 \text{ } \mu\text{m}$ to $6.0 \text{ } \mu\text{m}$ and has an absorption coefficient of approximately 1%/cm. Sapphire also has the necessary compressive strength, as shown in Table II-2, to effectively support the pressure load. However, sapphire also reflects approximately 13% of the incident solar radiation from its two surfaces due to its high refractive index. To reduce this reflection loss a thin film dielectric anti-reflection coating is necessary. Using suitable refractory coatings the reflection loss per surface can be reduced to $< 1\%$ for angles of incidence up to 70° .

Table II-2: Properties of Linde Cz Sapphire [13]

Crystal Structure	Hexagonal
Compressive Strength @ 300 K	450 MPa - 670 MPa
Density	3,900 kg/m ³
Thermal Conductivity @ 300 K	c-axis: 44.2 W/m ² a-axis: 40.7 W/m ²

Since sapphire is very strong in compression but weak in tension the window is designed to be concave inward, that is, curving into the absorption chamber. The window thickness is calculated using membrane shell theory with a simply supported boundary condition along the edge. With this boundary condition the complex membrane stress equations reduce to a single simple sphere stress:[14]

$$t = \frac{PR}{2\sigma} \quad (\text{II-25})$$

This gives the window thickness in terms of the chamber pressure, P , radius of curvature, R , and the compressive yield strength, σ . A window with a radius of curvature of 2.2 m provides a balance between thickness, absorption, and reflection losses at the edges. The resulting thickness is only 2.5 cm, thus the window will absorb 2.5% and reflect less than 1% of the radiation. The total mass of each window is 115 kg.

A power balance done by equating the absorbed power at the window to that which is radiated from it gives an equilibrium temperature of approximately 1,900 K. This temperature is far in excess of that allowable. Therefore, some type of additional cooling must be provided.

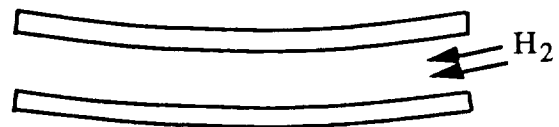
Several options have been considered for cooling the window and are illustrated in Fig. II-18. As yet none of these options have been fully evaluated. One option is to cool the window with a film of pure hydrogen that is flowed across the inner surface of the window. Indications are that the mass flow necessary to accomplish this is a significant fraction ($>50\%$) of the total mass flow of the propellant. Also the high velocities necessary to obtain an adequate convective film coefficient may induce vorticity that will draw the potassium vapor into the cool stream where it will condense. A second option is to use a "double pane" window configuration. In this configuration a second, thin, non-pressure bearing window is added inside of the 2.5 cm thick window. Cool hydrogen is flowed between the two surfaces to cool the first window. This configuration eliminates the potential for the cooling stream to entrain potassium vapor. However, the second window will cause additional reflection losses and the mass flow requirement is still a concern. The third option is to segment the window into many smaller parts with a supporting structure provided to connect the parts. Coolant hydrogen can be flowed through the supporting structure to provide a more direct means of removing the internal heat of the window. This configuration has a further advantage in that each segment of the window is smaller and thus can be thinner than the original 2.5 cm thick window. This reduces the absorption of the incoming radiation. This configuration could also be combined with the second configuration, the "double pane" window, to provide greater cooling.

Potassium Storage Tank

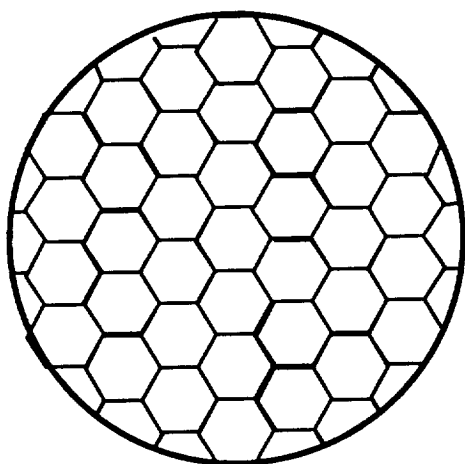
The potassium storage tank is separate from the rest of the engine. Since potassium melts at 337 K it was determined that very little power would be required to keep the potassium in a liquid state. A storage temperature of 422 K and pressure of 1 atm was chosen. At this temperature the density of potassium is 807.3 kg/m^3 . The required mass of potassium is 4,400 kg. The spherical storage tank for the potassium has a diameter of 2.18 m.



Film Cooling



Double pane



Segmented window

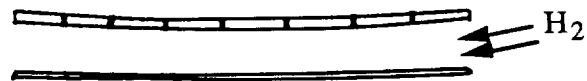


Figure II-18. Various Window Cooling Configurations.

Propellant Preheater

This subsystem is designed to vaporize the potassium and to mix the vapor with heated hydrogen prior to injection of the propellant into the absorption chamber. The potassium must be a dry vapor when it is injected into the absorption chamber. This requires that it be heated to a temperature of 1,200 K [4]. If the potassium entering the radiation receiver is not a dry vapor, then light scattering results from liquid droplets and the overall system efficiency drops. A liquid acquisition system using small capillary tubes is used to extract liquid potassium from the storage tank. The liquid potassium is then pumped to a black body heat exchanger to be vaporized. This blackbody heater surrounds the chamber window and collects the outer portion of the focal spot (Fig. II-14). The preheater is also responsible for heating the hydrogen to an inlet temperature of 1,200 K.

The actual design of the preheater has not yet been completed. It should be a relatively straight-forward design exercise. A flat, metal disk with machined coolant passages for the hydrogen and potassium should suffice for this application. An equilibrium temperature of approximately 1,400 K is desirable to obtain efficient heat transfer to the hydrogen and potassium. The front surface of the preheater should be anodized or otherwise coated to increase its absorptivity in the solar spectrum.

The hydrogen entering the preheater has already passed through either the regenerative cooling loop of the thrust chamber or through the cooling loop for the window. An additional 1.0 MW of power is added to the hydrogen in the preheater to raise its temperature to 1,200 K. The potassium enters the preheater at a temperature of 420 K. The mass flow of 0.015 kg/s of potassium requires 45.7 kW of heat to vaporize the potassium. The outlet temperature of the potassium is also 1,200 K. A schematic of the engine thermal power balance is shown in Fig. II-19.

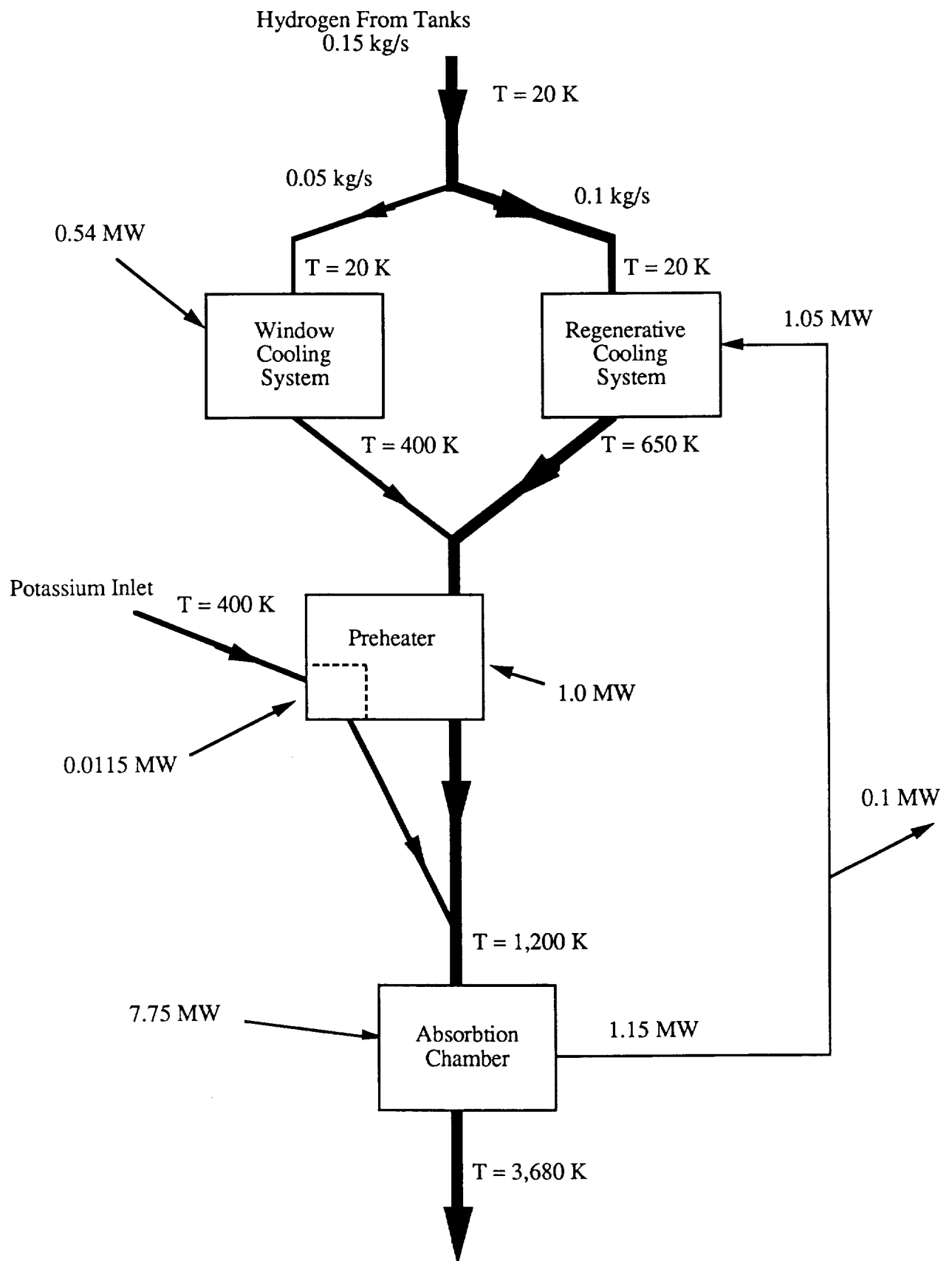


Figure II-19. Schematic of Engine Power Balance.

TRUSSES

The structure supporting each solar concentrator is made up of four triangular trusses. The trusses connect points on the concentrator's rim to the rotary joint on the main ship. The rotary joint allows the collector to rotate about the lateral axis to track the sun, as discussed earlier.

The design of the truss focused mainly on providing a high stiffness to keep the concentrator deflection within tolerance. A maximum deflection tolerance of 0.5 m was assumed for the truss structure. Analysis was carried out using a finite element program [15]. Pinned elements were assumed and the presence of joints to different material between the elements was ignored for simplicity. The pinned elements without a different material making up the joints gives a conservative estimate of the stiffness of the structure. Assuming that the truss is made of beam elements without joints in between each element overestimates the structure's stiffness because the joint material has a lower stiffness than the composite truss elements [16].

Individual Truss Members

The truss members are AS4-3502 graphite-epoxy [17] composite tubes with two titanium end fittings bonded to the tube with a cold-hardening adhesive system [18]. Each member is 5.08 cm in diameter, an unwritten NASA standard, making them easily handleable using gloves worn by astronauts. The graphite epoxy, titanium, and adhesive material are selected with very low, equal coefficients of thermal expansion (CTE's), meeting NASA's CTE limits ($\pm 5 \times 10^{-5}$ /deg F) [19]. All truss members are clad with aluminum in order to prevent erosion of the graphite-epoxy by atomic oxygen while in low earth orbit [20].

Graphite-epoxy tubes clad with aluminum show good mechanical properties, toughness, thermal/vacuum cycling stability, and tailorability of thermal-expansion coefficient. The excellent thermal conductivity of aluminum minimizes temperature

differentials around the circumference of the tube when one side is in the shadow and the other is sunlit, thus minimizing thermal stresses [20].

The composite layups for the tubular members are as follows (defining 0 deg as along the length of the tubular member): one layer of fibers oriented at 45° , the next at -45° , four layers at 0° , and six additional layers with the same orientations, making the ply symmetric. Using the INCAP Laminate Analysis Program [21], the modulus of elasticity in the principal direction of the member was computed to be $9.28 \times 10^8 \text{ N/m}^2$.

These primary structure members are connected by titanium node elements using a right-hand thread at one end and a left-hand thread at the other end of the tube (turnbuckle principle). This leads to very accurate regulation of the overall strut length, which enables the attainment of the stringent alignment requirements for the complete structure [20]. Figure II-20 shows a truss connection element.

The attachment of the end fittings to the tubular members incorporates bonding of the components in a way that leads to a continuous load transfer over the total length of the bonding area and reduces stress peaks at the ends of the overlapping length. In addition, the stiffness of the bonded components is balanced (the product of Young's modulus times material thickness is equal for both components at comparable locations), which leads to a symmetric stress distribution over the overlapping length. Increased adhesive layer thickness at the ends of the overlapping length leads to a further reduction of the stress peaks at these locations [18].

Truss Analysis

Loads causing failure were looked at with respect to the number of composite plies in a member. Using INCAP to determine the maximum tensile loads, with Eq. II-26 and

Eq. II-27 to determine maximum compressive loads, the number of plies to prevent failure in any member were determined.

$$P_{crit} = \pi^2 EI / l^2 \quad (II-26)$$

$$I = \pi (r_t)^2 t \quad (II-27)$$

where P_{crit} is the critical compressive load applied to cause member failure, E is the modulus of elasticity of the composite in the member's axis (9.28×10^8 N/m²), I is the tube's moment of inertia along its axis, r_t is the tube's radius, and t is the thickness of the member (based on one ply having a thickness of 1.524 mm) [16] An additional factor of safety of 1.5 was utilized. After considering several possible truss configurations, a design was found to meet the deflection tolerances. The configuration changes were limited to element wall thickness, truss depth, and number of elements. The diameter of the rotary joint was held constant. The mass of the final truss configuration is 3,890 kg for both collectors.

A dynamic analysis of the structure showed that the fundamental mode of the system is torsional. The natural frequency of the present configuration is 0.65 Hz. A desired frequency is approximately 1 Hz [22]. Stiffening of the individual elements or changing the truss cross section to increase the natural frequency will increase the mass of the trusses greatly, because it was found that the frequency is relatively insensitive to these changes. Increasing the diameter of the rotary joint and truss base would increase the polarmoment of inertia and should prove more effective in raising the natural frequency of the truss structure to the desired value. This will also reduce the deflection of the concentrators.

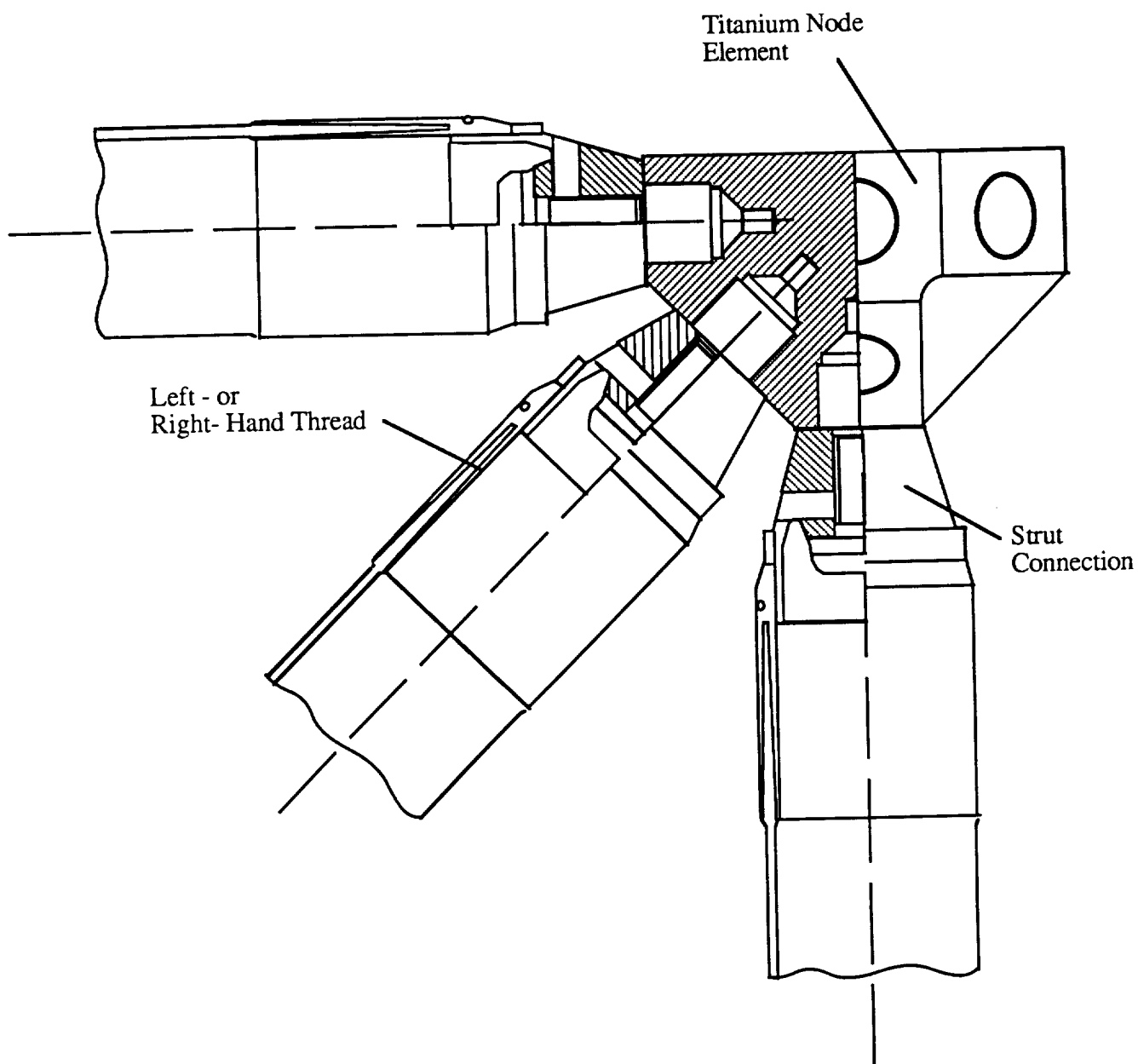


Figure II-20. Truss Connection Element [19].

ROTATIONAL JOINT

The preliminary analysis of the rotational joint for the collectors is based on an analysis of a similar joint being considered for the space station [23]. The joint consists of an annular ring with discrete roller assemblies (See Fig. II-21). In this analysis a diameter of 8.0 m is assumed for the ring. This is close to the minimum diameter which is allowable due to the requirement that the ring be outside the focal cone of the reflectors. As noted in the truss section a larger ring will probably increase the natural frequency of the truss structure, which is a desirable result. Further work is necessary to quantify the effects of the joint on the dynamic response of the truss assembly.

The initial preliminary model for the joint is a ring which is supported at 8 points equally spaced about the ring (45° intervals) shown in Fig. II-22. The truss was also assumed to have 8 rollers which attach to the ring. The maximum deflection of the ring is when the rollers are halfway between the support points, when the truss is rotated 22.5° with respect to the main ship. To further simplify the analysis, the loading was assumed to be eight equal loads applied at the roller locations. Due to the symmetry of the structure and of the loading condition only 1/8 of the ring need be considered in the analysis.

For the situation outlined above the deflection at the loading point, w , is given by [23]:

$$w = P R^3 \left(\frac{2.6 \times 10^{-3}}{E I} + \frac{4.1 \times 10^{-5}}{G J} \right) \quad (\text{II-28})$$

where P is the applied load, R is the radius of the ring, E and G are the elastic modulus and shear modulus of the ring material respectively, I is the bending moment of inertia of the ring, J is the torsional constant of the ring.

In order to evaluate the above expression, it was necessary to assume a cross section for the ring. A square box, 15.2 cm by 15.2 cm, with a variable wall thickness, t , was chosen. This cross section is not meant to be indicative of an actual ring design, but

was used to obtain real values for the deflection and mass of the ring. For such a cross section the expression below apply:

$$I = \frac{(0.152 + t)^4 - (0.152 - t)^4}{0.134} \quad (\text{II-29})$$

$$J = (0.152 - t)^3 t \quad (\text{II-30})$$

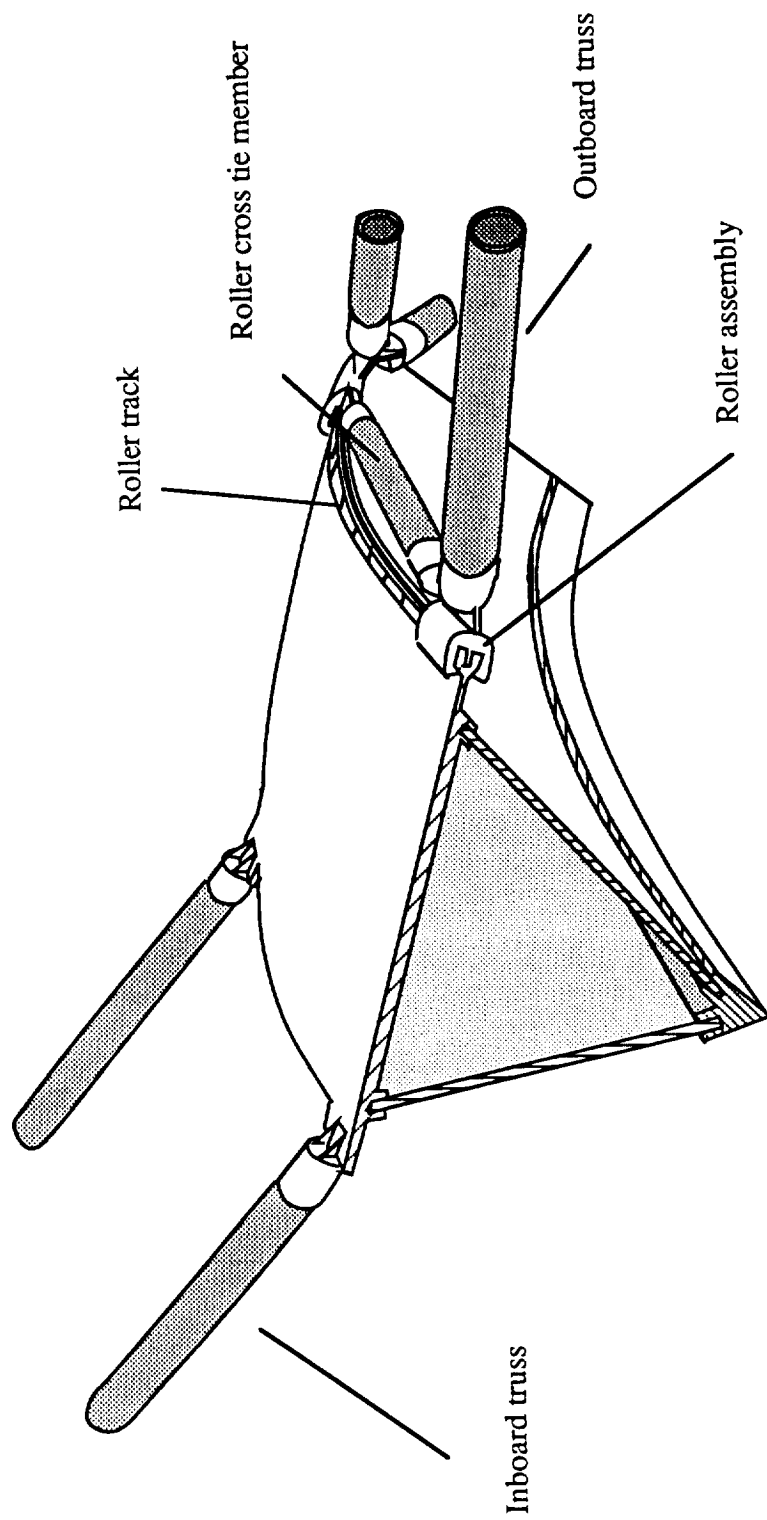
The material for the ring was assumed to be aluminum ($E = 70,000$ MPa, $\rho = 2,700$ kg/m³). The radius of the ring is 4.0 m.

The applied load was calculated by considering the maximum moment applied to the ring by the truss and reflector assembly. Each truss and reflector has a mass of approximately 2,500 kg. The maximum acceleration of the ship is 0.2 m/s². The center of mass of the reflector assembly was assumed to be 40 m from the ring. This gives a maximum applied moment of 20,000 N-m. If this moment is resisted by two equal forces acting at opposite sides of the ring, each of the forces has a magnitude of 2,500 N. This is much higher than the real loading condition in which the moment is supported by each of the supports, but was used to obtain a conservative estimate of the necessary ring thickness.

A maximum deflection of 1 mm was selected since such a displacement will cause a negligible displacement of the reflectors (< 1 cm). For the given conditions a ring thickness of 3 mm gives a maximum displacement of 0.85 mm. Such a ring, with the given cross section, has a mass of 123 kg.

Reflector Aiming Mechanism

Since the reflectors are located on the ends of a flexible support structure, it is recognized that some type of aiming mechanism will be necessary to correctly focus the reflectors on the engine chamber. The maximum deflection of the center of the reflector was specified to be 1 m. To correct for such a deflection it is necessary to rotate the



FigureII-21. Section of the Rotational Joint Assembly.

reflector 0.7° to move the focal spot back to the center of the engine inlet. Such a rotation could be accomplished by giving one edge of the reflector a vertical displacement of 1.5 m. A conceptual design for a mechanism capable of accomplishing this is shown in Fig. II-22.

The mechanism consists of three struts that extend from the top of each truss to a common point on the edge of the reflector. Each of these struts is connected to both the truss and the reflector through a ball and socket joint, thus allowing free rotation of the strut with respect to the truss and reflector. Each of the struts is capable of being varied in length through the use of a mechanism such as a screw actuator. The actual design of such an actuator was not considered at this time. By varying the length of the three struts a vertical displacement may be given to the reflector. Since each of the trusses is connected to the reflector through such an assembly the reflector may be rotated slightly by raising one side while lowering the opposite side.

REFLECTORS

The reflectors must be capable of concentrating the required amount of solar energy into the small aperture of the thrust chamber. The important considerations in the choice of the reflectors is their mass and their surface accuracy. A low mass is especially important since the reflectors are supported by a long truss structure, which creates a large moment about the base of the truss due to the acceleration of the ship. Surface accuracy is important to obtain the required light intensity at the thruster inlet without requiring the reflectors to be excessively large.

Three types of reflector systems were considered: adaptive, rigidized and inflatable optics. Adaptive optics consist of many small reflectors which are mounted on a truss structure. Each of these reflectors is independently controlled to focus the incoming radiation onto the focal spot. Rigidized optics consist of a single structure that is deployed, typically by inflation, in space. After deployment the structure is designed to have

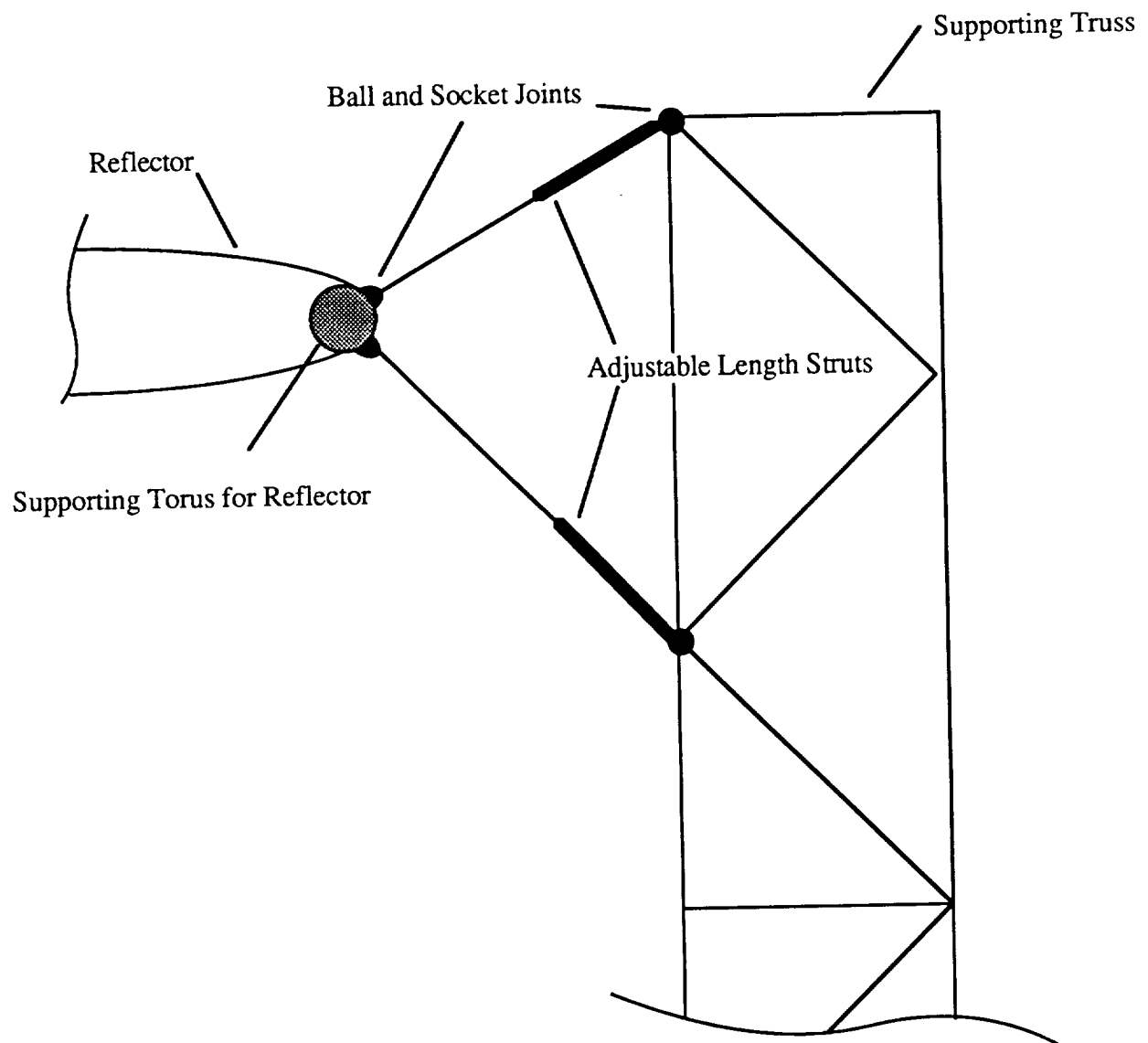


Figure II-22. Conceptual Design for Reflector Aiming Mechanism

sufficient rigidity to permit removal of the inflatable. This rigidity is obtained by making the structure out of a multi-layer film or a composite material that cures after deployment. Inflatable optics are also deployed in space using inflation. After deployment, the inflatable is used to maintain the shape of the surface rather than being removed. Each of these options is capable of satisfying the surface accuracy requirement for this system. The major difference between the three type of reflectors is in their specific mass as shown in Table II-3.

Table II-3: Specific Mass of Optical Systems [24]

Reflector Type	Specific Mass (kg/m ²)
Adaptive	20 - 100
Rigidized	1 - 2
Inflatable	0.02 - 1.0

The low end of the range of specific mass for inflatable reflectors is typical for reflectors of the size being considered for the SRA system. As can be seen, inflatable reflectors offer significant advantages in specific mass over the other optical systems. However, the use of inflatable space structures has been discounted in the past due to overconservative estimates of leakage rates due to meteoroid punctures. Although leakage rates for small inflated structures can be significant, for diameters of greater than 10 m the leakage rates are very small due to the low internal pressure required for the larger structures. Thus, inflatable reflectors were chosen for the present design.

Each reflector of the CLAM system has a surface area of 11,300 m². The inflatant mass loss from each reflector can be estimated from the following formula [25]:

$$\Delta m = 0.0264 \sqrt{M_w} P A t^2 \quad (\text{II-31})$$

where M_w is the molecular weight of the inflatant in grams, P is the optimum pressure (psi), A is the reflector projected area (cm²), and t is the time (years). Large reflectors are made by joining together a large number of individual pieces called gores. The optimum pressure (P) for such a reflector with a large number of gores is given by [25]:

$$P = \frac{2 W^2 E_G}{3 (1 - \mu) R D^2} \quad (\text{II-32})$$

where W is the maximum gore width, E_G is the product of film elastic modulus and thickness, ν is Poisson's ratio of the material, R is the radius of curvature, D is the diameter of the reflector. Depending on the material used, the optimum pressure for a reflector of this size is less than 10⁻⁵ psi. Using the above formulas, with hydrogen as the inflatant at a pressure of 10⁻⁵ psi, the loss of inflatant during one round trip (20 days) is less than 10⁻⁹ g. It was determined unnecessary to carry make-up inflatant during the trip since the leakage is negligible.

The material for the reflectors, for the purpose of mass and leakage calculations, is assumed to be 0.5 mil Tedlar (polyvinyl fluoride) with an aluminized back surface. Other possibilities for the film surface include polyester films such as Mylar. A further study of these materials is necessary to determine which material is best suited to the environment in which this vehicle operates.

The reflector is supported around its circumference by a rigidized or inflated torus. Typically, a rigidized torus is specified in the design of an inflatable reflector since an inflatable torus has a make-up inflatant requirement of approximately 300 kg/year for a 100

m diameter antenna. In this application the necessary make-up inflatant could easily be obtained from the thermodynamic venting system on the hydrogen tanks. Since the mass penalty of the rigidized torus is not large, it was decided to use a rigidized torus for the mass calculations of the reflectors. The mass of each reflector, including the reflector surface and the rigidized torus, was determined to be 450 kg.

CRYOGENIC STORAGE SYSTEM

The cryogenic storage system consists of tanks, insulation, and liquid acquisition devices. The cryogenic storage system is designed to store the necessary quantity of hydrogen for each mission while preventing boil-off due to heat entering through the insulation and structural supports.

The cryogenic storage system is designed to have the lowest possible mass in which to store a given quantity of liquid hydrogen. To accomplish this it was decided that the tanks would be launched from earth empty and filled in orbit. This allows the tanks to be optimized for the environment of the solar thermal rocket rather than the environment of the launch vehicle which brings them to LEO.

Thin tank walls can be effectively used to reduce the overall mass of the tank system. The tank wall thickness, t , as a function of pressure, P , tank radius, R and allowable wall stress, σ is obtained from:

$$t = \frac{P R}{\sigma} \quad (\text{II-33})$$

Since the mass of the tank increases linearly with the tank wall thickness, it can be seen that, for a given size tank, a low storage pressure allows the mass of the tank to be significantly reduced. It has been shown that the minimum practical storage pressure for liquid hydrogen in spacecraft is approximately 34 kPa [26]. This pressure provides the minimum net positive suction head at the boost pump inlet. At this pressure and a tank

radius of 2.2 m, the tank wall thickness approaches the minimum practical thickness that can be reliably manufactured. Therefore, reducing the pressure further does not significantly decrease the mass of the tanks. Table II-4 shows the properties of hydrogen at the selected storage conditions.

Table II-4: Hydrogen Storage Conditions

Temperature	20 K
Pressure	34 kPa
Density	70.8 kg/m ³

Due to the low density of liquid hydrogen a large volume is necessary to store a given mass. The maximum tank diameter was set by launch constraints. Currently the largest diameter payload bay available is the Shuttle or the planned Shuttle C. Both of these launch vehicles have a payload bay diameter of 4.57 m. Since various supports will be necessary around the tanks at launch a tank diameter of 4.40 m was selected.

Tank Walls

The tanks are made of 2090-T8E41 aluminum, which is an Al-Li alloy being developed by Alcoa [27]. The properties of this material are shown in Table II-5.

The nominal wall thickness of the tanks was determined to be 0.20 mm. The tanks are manufactured by a process of spin forming and chem-milling in two one-piece hemispheres. The chem-milling is done so that the tank is thicker than the nominal thickness at the joint between the two hemispheres and at the attachment points of the supporting struts. The joint between the two hemispheres is designed for simple construction in space so that the tanks can be launched in a compact stowed condition. The external struts that support the tank are connected to the tanks in this area. The mass of the

Table II-5: Properties of 2090-T8E41 Aluminum (@ 294 K)

Young's Modulus, E	75000 MPa
Tensile Ultimate Strength, F_{tu}	565 MPa
Density, ρ	2546 kg/m ³
Tensile Yield Strength, F_{ty} ¹	600 MPa
Fracture Toughness, K_{IC} ¹	51.6 MPa-m ^{1/2}

¹ Data at 77.6 K

tank wall is 50 kg per tank. A brief analysis of the stresses during launch showed that due to the low mass of the tanks very low stresses are encountered even at high g-loadings (9 g's).

Each of the tanks is proof tested after manufacturing to ensure that it will meet the life cycle requirements of the mission. A proof test is a pressurization of the tank to some level above the operating pressure. It is done to ensure that the largest flaws existing in the vessel are below the size that would grow to critical length during the operating lifetime and to induce residual compressive stresses at points of stress concentrations, thereby increasing fatigue life.

Proof testing can be done at temperatures other than the operating temperature by multiplying the proof test pressure ratio (the ratio of the proof test pressure to the operating pressure) by the ratio of K_{IC} at the test temperature to that at the operating temperature [26].

Tank Joint

The preliminary design of the tank joint is shown in Fig. II-23. To ensure a good seal between the two tank halves and to avoid stress concentrations in the joint, two interlocking continuous flanges were selected to make up the joint. On-orbit assembly of the tanks is accomplished by heating the outer flange, which causes the flange to expand.

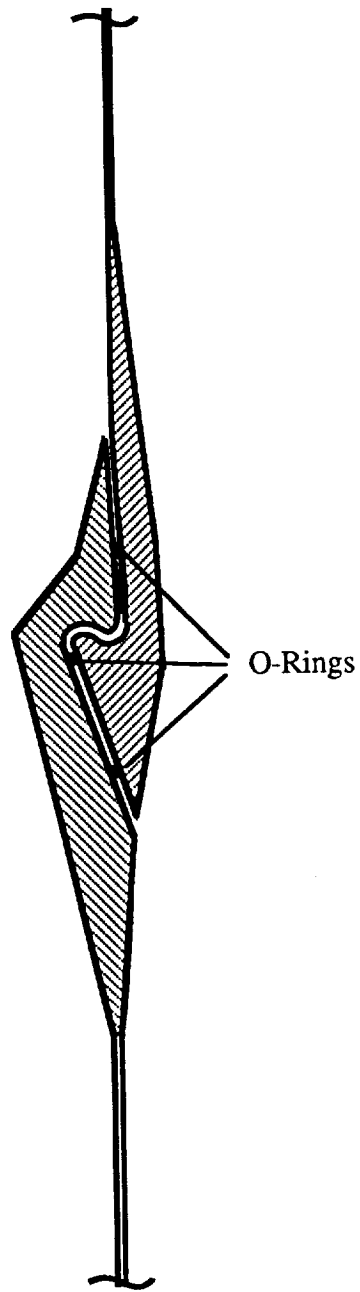


Figure II-23. Preliminary Tank Joint Configuration.

The heating is accomplished by using a strip heater which is placed in contact with the upper portion of the outer flange. An increase in radius of approximately 2 mm is necessary for the inner flange to pass through the outer flange. This requires a temperature differential of about 40° C between the two flanges. A total energy input of less than 10 kJ is necessary to achieve this temperature difference, thus heater power of less than 500 W should be sufficient. After the inner flange is in place, the outer flange is allowed to cool while the position of the inner flange is maintained. Several O-rings are used in the joint to provide the necessary sealing between the two parts. The location of the O-rings in Fig. II-23 is representative, their optimum location and material remains to be determined.

Insulation

A fully passive insulation system consisting of multi-layer insulation and a vapor cooled heat shield was chosen to minimize the mass of the system. Two routes exist for heat transfer to the tanks: conduction through the supporting struts and radiation transfer through the insulation. The struts supporting the tanks are of S-glass/epoxy composite construction which gives the best performance in terms of thermal conductivity and mass [28].

The multi-layer insulation system consists of a series of double aluminized Mylar radiation shields separated by Dacron net spacers. This type of insulation system has been used extensively in one form or another in space applications. A simplified model of the radiation shields shows the heat transfer to be given by [9]:

$$(q_{12})_N = \frac{1}{N + 1} (q_{12})_0 \quad (\text{II -34})$$

where $(q_{12})_0$ is the heat transfer with no shield, N is the number of shields and $(q_{12})_N$ is the heat transfer with N shields. As can be seen, increasing the number of shields greatly decreases the heat transfer. The thickness of the insulation was determined by trading off the mass of the hydrogen lost with the mass of the insulation.

A cross section of the tank wall is shown in Fig. II-24. The particular configuration chosen has a layer density of 24 reflectors per cm. Each of the tanks is covered with 1.5 cm of this insulation. The maximum hydrogen loss resulting from incident solar radiation was determined to be 0.16 kg/hr from each tank. Since the tanks are grouped together there is significant shielding of certain tanks by others. Therefore the actual average hydrogen loss per tank will be lower than 0.16 kg/hr.

The vapor cooled jacket intercepts the heat that is transmitted through the multi-layer insulation (MLI) and removes it from the system. A small amount of hydrogen is bled from the tank and passed through a Joule-Thompson valve (VCS) to lower its temperature and pressure [29]. This hydrogen is then passed between the MLI and the tank wall to absorb heat. The total mass of the MLI and VCS is 220 kg per tank.

Liquid Acquisition Device

The liquid acquisition device (LAD) chosen for this design is a total communication device, that is, a device that maintains contact with the liquid regardless of the position of the liquid in the tank. The LAD consists of a channel with a fine wire mesh screen that relays the liquid through surface tension.

This wire mesh is supported in two channels that are just inside the tank wall (Fig. II-25). It is recognized that a total communication device may not be the optimum configuration for a tank of this size since other configuration may give a lower mass. A trade study of other systems, such as a refillable trap, is needed to determine if such systems offer an advantage in mass over the present system.

Tank Support Structure

As noted above, the tank support struts are made of S-glass/epoxy to minimize heat transfer and mass. Each of the struts attaches to the tank along the joint between the two hemispheres. The tanks are thickest at this point to support the stresses applied by the supporting members. To avoid buckling of the tank wall the angle of the struts must be

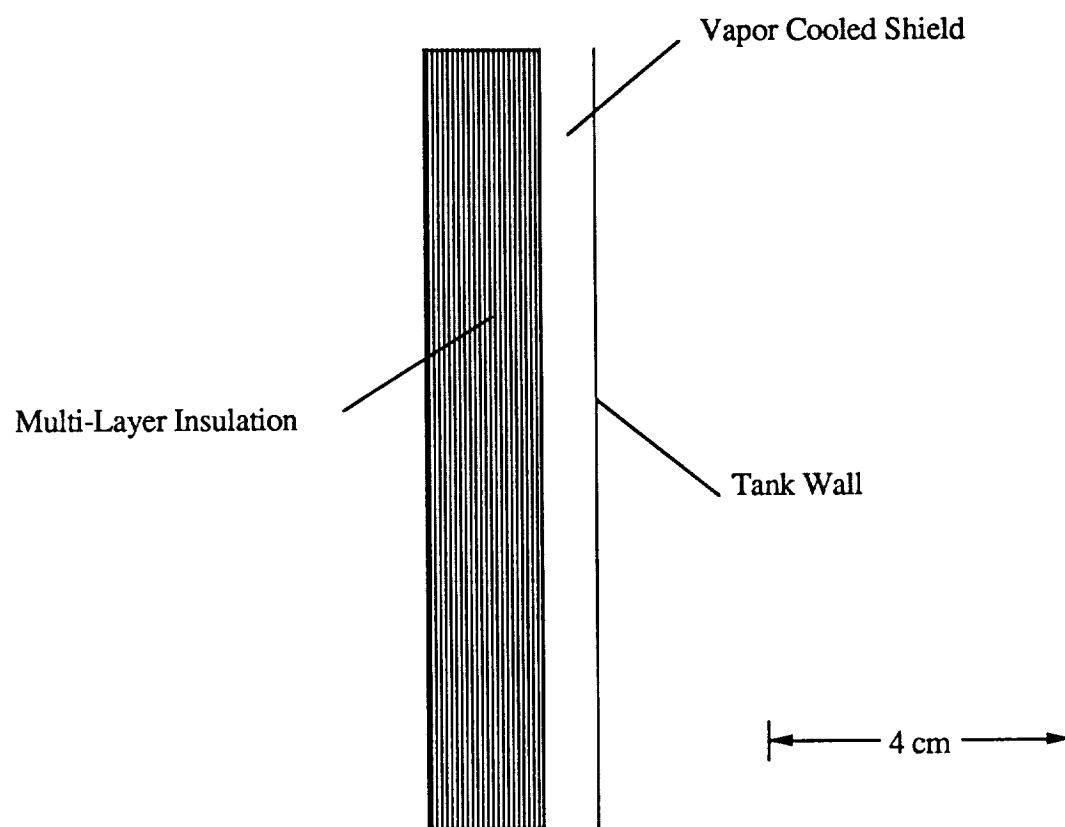


Figure II-24. Tank Wall Cross Section.

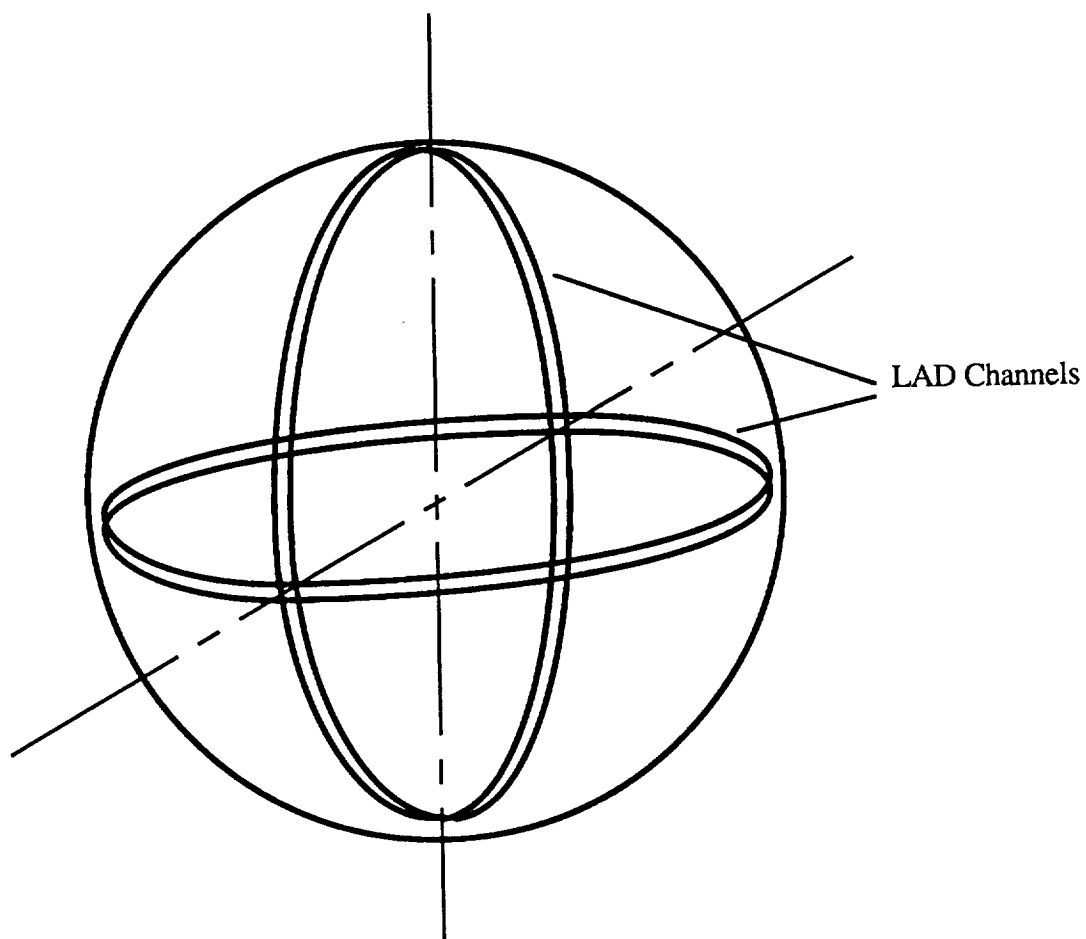


Figure II-25. Liquid Acquisition Device Configuration.

such that the tanks do not experience compressive forces. Fig. II-26 shows the strut arrangement.

The mass breakdown of each of the tanks is shown in Table II-6. Each tank is capable of storing 3,000 kg of LH₂ (95% filled). This gives a tank mass ratio, the ratio of the tankage mass to that of the stored liquid, of 5.7%.

Table II-6: Cryogenic Tank Mass Breakdown

Item	Mass (kg)
Tank Wall	50
TVS/VCS	23
MLI	54
LAD	43
Total	170

The overall configuration of the 14 tanks is shown in Fig. II-27. This truss network attaches to the payload system and to the support structure for the thrusters. The entire tank truss network is surrounded by several thin meteoroid shields (not shown) which are designed to protect the tanks from puncture.

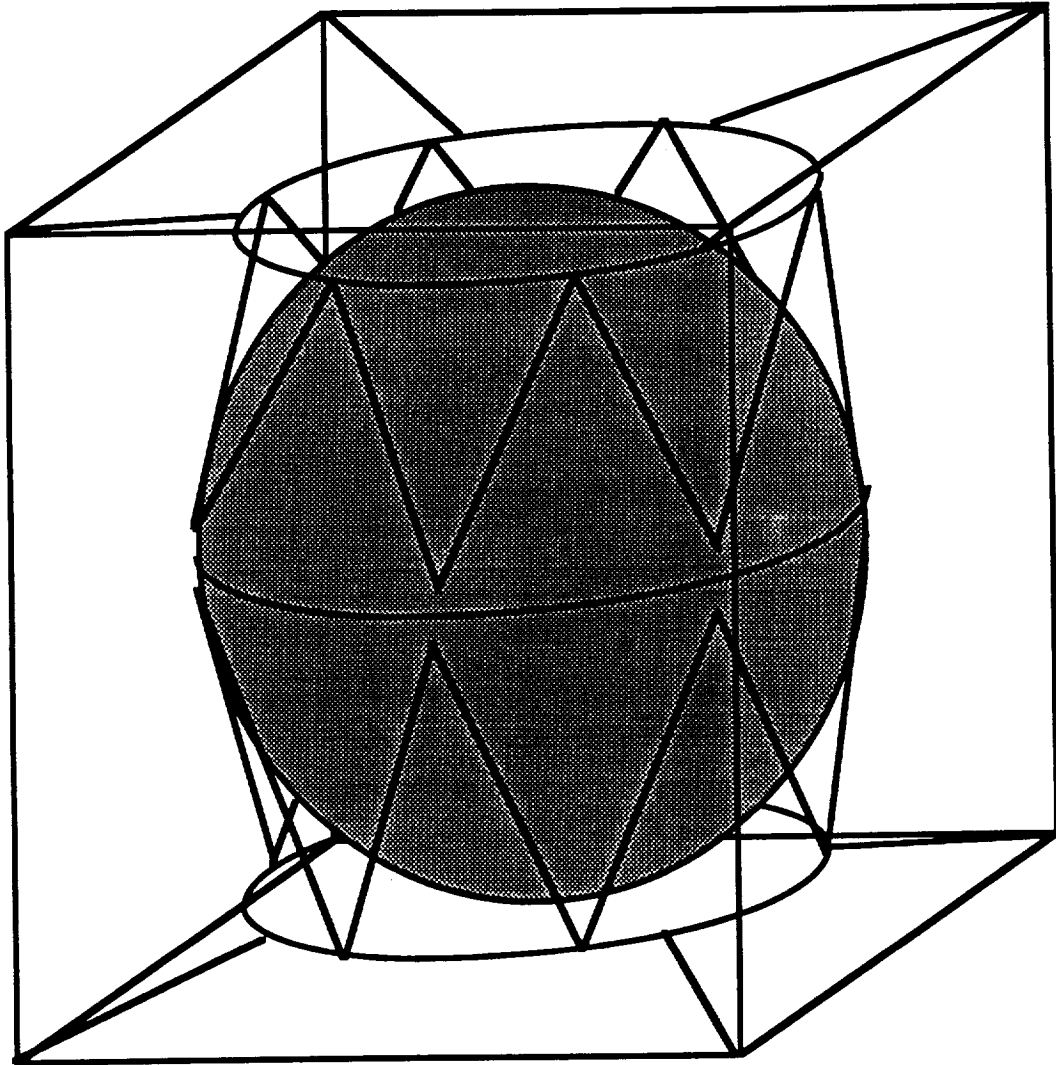


Figure II-26 Tank Strut Configuration.

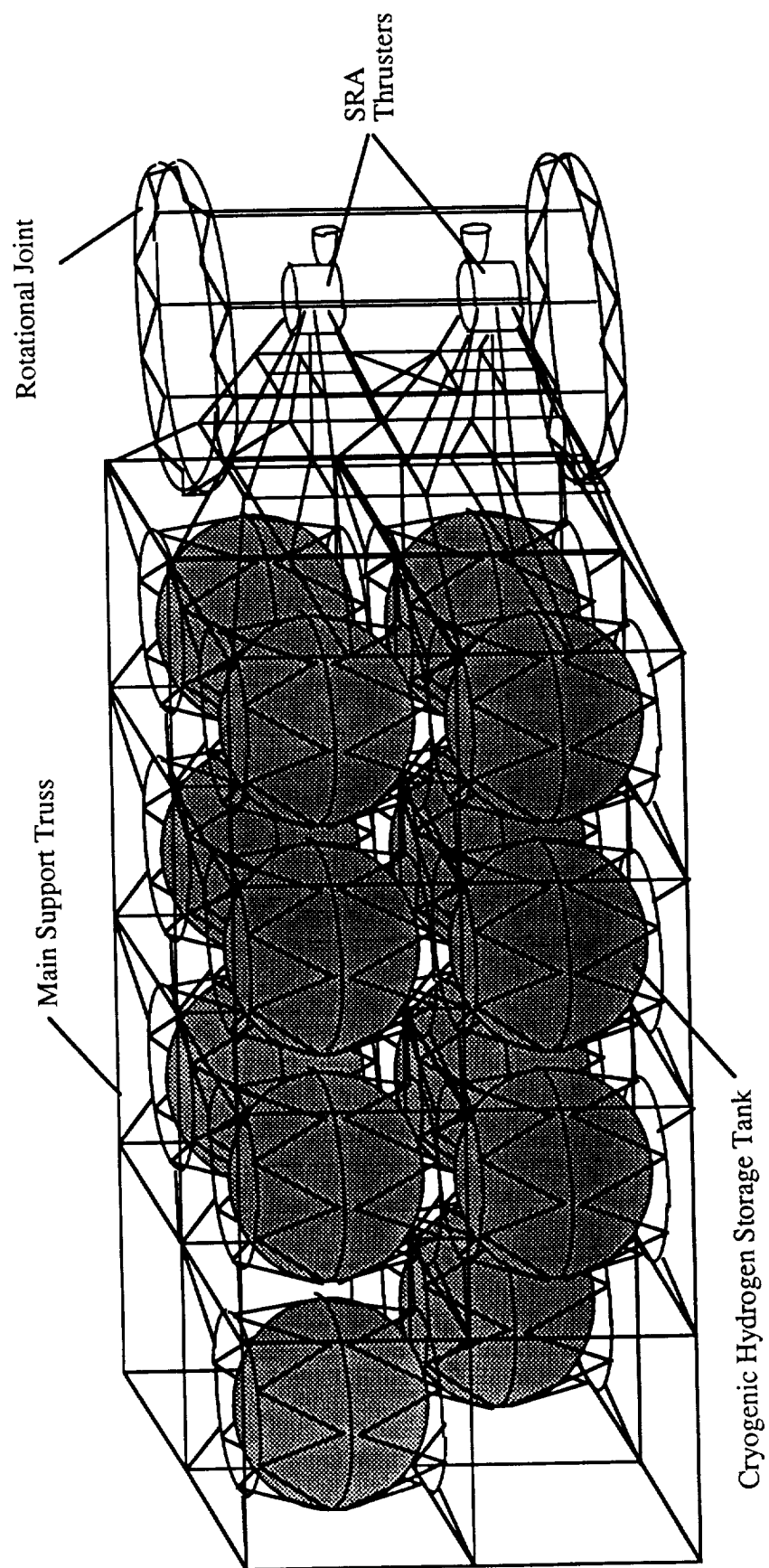


Figure II-27. Overall Configuration of Cryogenic Hydrogen Storage Tanks.

OVERALL MASS INVENTORY

The following table shows the mass breakdown of the spacecraft. As can be seen the actual spacecraft has a relatively low mass. This leads to a very high mass ratio (payload mass/initial mass) of approximately 37%. Further reduction in mass may be possible in several areas such as the support structure for the reflectors and the main ship structure.

Table II-7: Mass Breakdown

Collectors		5,150 kg
Inflatable Reflectors	900 kg	
Support Structure	4,000 kg	
Rotation Mechanism	250 kg	
Propulsion System		7,380 kg
Thrusters	4,000 kg	
Tanks	2,380 kg	
Pumps and Piping	1,000 kg	
Main Ship Structure		3,000 kg
Miscellaneous (Control Systems, Electrical Power Systems, Power Conditioning, Actuators, etc.)		2,570 kg
Total Dry Ship Mass		18,100 kg
Initial Fuel		43,400 kg
Hydrogen	38,160 kg	
Potassium	4,240 kg	
Hydrogen Lost (TVS)	1,000 kg	
Payload system		74,000 kg
Payload	50,000 kg	
Aerobrake System	12,600 kg	
Fuel for Injection	11,400 kg	
Total System Mass in LEO		135,500 kg

ORBITAL MECHANICS

Mark Beall

Spacecraft generally fall into one of two categories, low thrust or high thrust. Simple orbital mechanics is based on the approximation that thrusting can be considered to be impulsive and thus the effects of gravity during the periods of thrust can be considered negligible. This approximation is generally valid for high thrust spacecraft. For low thrust spacecraft the effects of thrusting and of gravity are of about the same order, thus such effects cannot be neglected. The SRA system falls in between these two categories. The accelerations of the ship are large enough that impulsive orbital mechanics can be used as a first approximation, but the effects of gravity must be considered for a complete analysis.

All space missions can be characterized by a velocity increment, ΔV . This ΔV is not necessarily the actual change in velocity of the ship, but is obtained from the following equation:

$$\frac{m_o}{m_i} = \exp\left(\frac{-\Delta V}{U_e}\right) \quad (\text{II-35})$$

For impulsive orbital mechanics the ΔV is the actual velocity change of the spacecraft. This is due to the neglect of the gravity terms in the equations of motion. For low thrust spacecraft the m_o/m_i term must be obtained by integration of the equations of motion, and from this an equivalent ΔV can be determined. The difference between the impulsive ΔV and that which is obtained from integration of the equations of motion is called the gravity loss. The equations of motion in polar coordinates are:

$$\ddot{\mathbf{r}} = \mathbf{F} \frac{\dot{\mathbf{r}}}{m\sqrt{\dot{r}^2 + r\dot{\phi}^2}} - g_0 \frac{\rho^2}{r^2} + r\dot{\phi}^2 \quad (\text{II-36})$$

$$\ddot{\phi} = F \frac{\dot{\phi}}{m \sqrt{\dot{r}^2 + r^2 \dot{\phi}^2}} - 2 \frac{\dot{r} \dot{\phi}}{r} \quad (\text{II-37})$$

where F is the thrust, m is the mass of the spacecraft, r is the radial position, \dot{r} , $\dot{\phi}$, \ddot{r} and $\ddot{\phi}$ are the radial and angular velocities and accelerations respectively, g_0 is the gravity at the Earth's surface, and ρ is the radius of the Earth.

Gravity losses arise from thrusting when the flight path angle is not at right angles to the gravity vector. The actual velocity increment that results from a thrust is the projection in the direction of the flight path of the vector sum of the thrust vector per unit mass and the gravity vector per unit mass as shown in Fig. II-28. When the flight path and the gravity vector are not at right angles to each other, the component of the velocity increment in the direction of the flight path is smaller than if they were at right angles. This decrease in the velocity increment is referred to as a gravity loss. In an elliptic orbit the flight path and the gravity vector are at right angles only at perigee and apogee. Typically, for a chemical propulsion system the thrust to mass ratio is relatively large, resulting in short burn times for a given velocity increment. If these short burns are done at perigee or apogee the misalignment of the flight path angle and the gravity vector is small and the resulting gravity losses are insignificant. As the thrust to mass ratio decreases, longer thrust times are required to acquire the same velocity increment. This requires thrusting when the angle between the flight path and the perpendicular to the gravity vector is significant, thus gravity losses must be accounted for when small thrust to mass ratios are used.

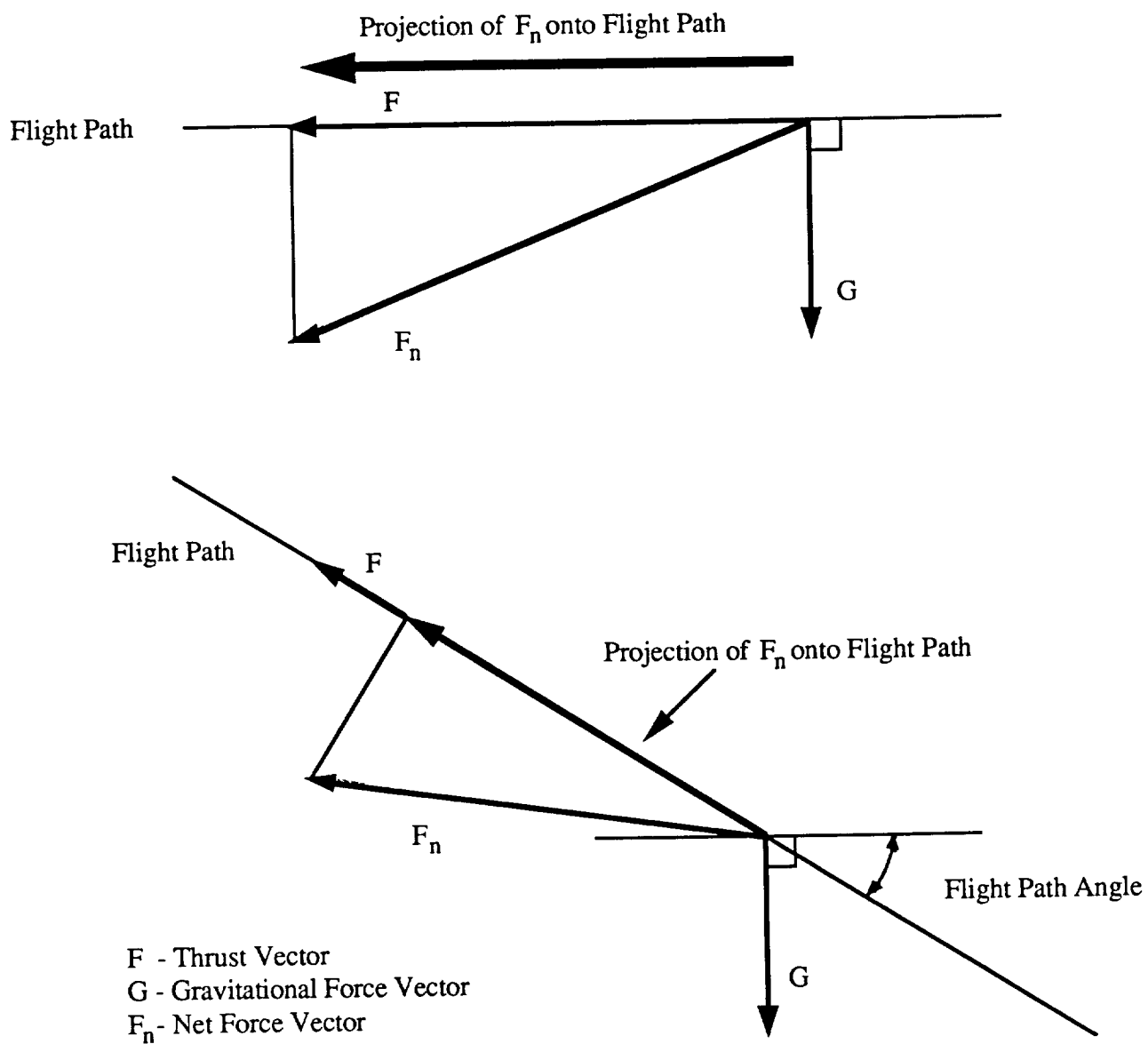


Figure II-28. Gravity Losses

For the initial approximation of the SRA orbital mechanics, impulsive orbital mechanics were used. The spacecraft was assumed to start in LEO with a radius $r_0 = 6,878$ km. In such an orbit the spacecraft has a velocity, V_{cs} , that is given by:

$$v_{cs} = \sqrt{\frac{\mu}{r_0}} \quad (\text{II-38})$$

where μ is the gravitational parameter of the body around which it is orbiting. In this case $\mu = 3.986 \times 10^5 \text{ km}^3/\text{s}^2$. This gives the circular velocity in the initial orbit to be $V_{cs} = 7.61 \text{ km/s}$. In order to enter a transfer orbit to another planet the spacecraft must acquire sufficient velocity to escape the earth's gravitational field with an excess velocity, V_∞ , which is determined by the transfer orbit to the other planet. The minimum energy transfer orbit to Mars requires $V_\infty = 2.98 \text{ km/s}$. From a given orbit the velocity necessary to leave earth with a specified excess velocity is:

$$v_1 = \sqrt{v_\infty^2 + \frac{2\mu}{r_0}} \quad (\text{II-39})$$

Thus at our specified initial orbit $V_1 = 11.17 \text{ km/s}$. Thus the necessary ΔV to enter into a Mars transfer orbit is 3.56 km/s . This ΔV can be obtained by using a series of small thrusts at one point in the orbit rather than one single large thrust. By doing a series of thrusts at the perigee the orbit is changed from the initial circular orbit to an elliptical one with its perigee at the altitude of the initial circular orbit (see Fig. II-29). This procedure is necessary due to the low accelerations of the SRA spacecraft. There is a limit, however, to the amount of the ΔV that can be obtained in this manner. If V_∞ is set to zero in Eq. II-40 the escape velocity from that altitude is obtained. Any velocity above this value will result in the spacecraft escaping earth orbit. For the initial orbit the escape velocity is $V_{esc} = 10.77 \text{ km/s}$. The importance of this figure is that there is a 0.40 km/s difference

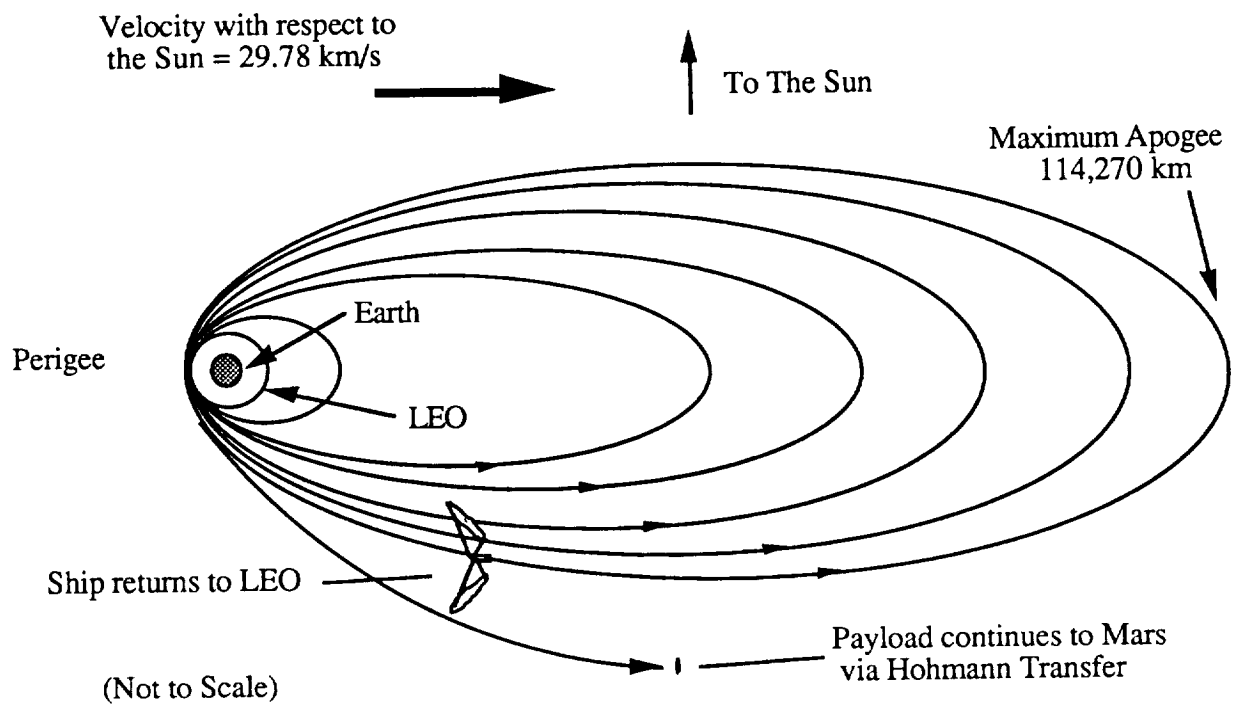


Figure II-29. Earth Orbits and Injection Trajectory to Hohmann Transfer.

between V_{esc} and V_1 . This difference is large enough that the SRA system cannot deliver it in a manner that approximates an impulsive thrust since the SRA acceleration at this point is on the order of 0.03 m/s.

At this point there are two options. First, the SRA can provide this final ΔV by using a continuous thrust, until the necessary velocity is reached. Second, the payload can be separated from the SRA propulsion unit and use a chemical rocket to impulsively gain the required velocity increment. The first option results in a larger effective ΔV since the burn time for the velocity increment is long. As the spacecraft thrusts it is getting farther from earth resulting in a reduction in velocity. Both this reduction and the initial ΔV must be gained before the required velocity is reached. The effective ΔV for this option is approximately 5.5 km/s. The second option retains the validity of the impulsive analysis and requires the chemical system to provide a ΔV of 0.7 km/s. The savings in mass due to the lower ΔV of the second option were determined to be greater than the mass penalty of the chemical rocket system and thus it was chosen for this particular mission.

Multiple perigee burns over a period of approximately 19 days are used to transfer from LEO to the separation point where the payload is released as shown in Fig. II-30. The separation occurs at perigee when the spacecraft has a velocity slightly less than that required to escape the Earth's sphere of influence. After separation, the payload system, which is discussed in detail in Appendix A, performs a short burn using a liquid chemical propellant rocket ($H_2 - O_2$) to achieve the additional small velocity increment needed for a heliocentric Hohmann transfer to Mars (Fig. II-30). The solar propelled spacecraft does not escape but returns to LEO for the next mission.

The actual propellant mass required was determined by estimating the initial vehicle mass using Eq. II-35 and then numerically integrating the full equations of motion for a spacecraft orbiting in a gravitational field to determine a revised propellant mass requirement. This revised propellant mass was then used recalculate the initial vehicle mass

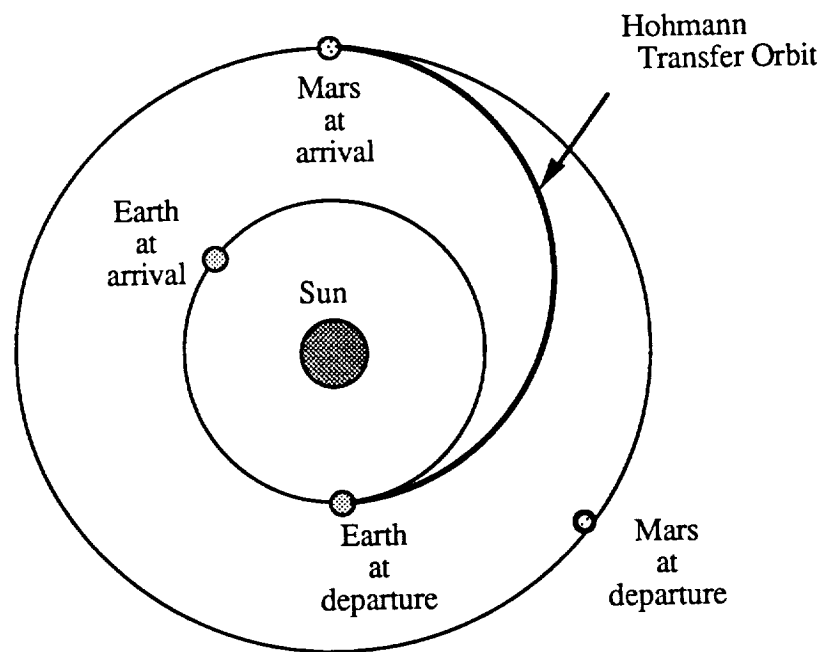


Figure II-30. Heliocentric Hohmann Transfer Orbit to Mars.

and the integration was repeated until a final propellant mass was determined. This iterative process resulted in a propellant mass of 42,400 kg.

The numerical integration of the equations of motion showed that the optimum burn pattern was one that started with relatively small burn angles (the angle relative to perigee) which increase as the orbit becomes more eccentric. The thrust of the ship must be vectored slightly inward (toward the Earth) during thrusting to avoid raising the perigee of the orbit. The actual optimum angle is a function of position in the orbit. The program that was used to determine the orbits did not allow the thrust angle to be varied with position in the orbit. This resulted in the perigee increasing slightly with each revolution. A small increase in perigee was determined to be necessary to avoid continuous passes through the congested area of LEO, so this constraint did not pose a major problem. The numerical investigation of the orbital mechanics showed that the gravity losses are quite small, on the order of 0.2 km/s. Also, the amount of propellant consumed and the time required to enter the injection orbit are not very sensitive to the duration of the burns around what was determined to be the optimum burn profile. The resulting orbit is shown in Table II-8.

A chemical rocket is used to achieve the final velocity increment to escape from Earth as discussed earlier. This chemical rocket gives the payload a ΔV of 0.7 km/s: 0.3 km/s to achieve escape velocity and 0.4 km/s to send the payload on the Hohmann transfer. This approach offers three advantages:

- (1) The time to escape Earth is reduced. The relatively large thrust to mass ratio of chemical rocket allows a nearly impulsive final velocity change. Without the chemical rocket it would be necessary to travel through numerous elliptical orbits with periods of more than 2 days, thereby greatly increasing the time to escape Earth.

- (2) The total required velocity change is lowered since the gravity loss is small.
- (3) The velocity change to bring the main ship back to LEO for re-use is kept low since the spacecraft does not escape from Earth's gravitational field.

Table II-8: Orbit Summary

Orbit number	Time (days)	Perigee radius (km)	Apogee radius (km)	Perigee velocity (km/s)	Apogee velocity (km/s)	Mass (kg)
1	0.000	6,871	6,975	7.66	7.53	135,120
2	0.068	6,876	7,075	7.68	7.45	134,740
3	0.135	6,880	7,176	7.70	7.37	134,370
4	0.203	6,885	7,280	7.73	7.29	133,990
5	0.272	6,889	7,388	7.75	7.21	133,600
10	0.630	6,910	7,965	7.87	6.82	131,680
15	1.012	6,931	8,625	8.00	6.41	129,730
20	1.421	6,959	9,390	8.13	6.01	127,730
25	1.863	6,977	10,281	8.27	5.60	125,700
30	2.346	7,004	11,334	8.40	5.18	123,630
35	2.877	7,035	12,590	8.54	4.76	121,530
40	3.469	7,051	14,105	8.70	4.34	119,410
45	4.137	7,086	15,985	8.85	3.91	117,250
50	4.904	7,118	18,365	9.00	3.48	115,060
55	5.806	7,134	21,480	9.18	3.04	112,830
60	6.898	7,178	25,728	9.34	2.59	110,570
65	8.278	7,201	31,900	9.53	2.14	108,250
70	10.132	7,237	41,609	9.71	1.68	105,890
75	12.885	7,285	58,965	9.89	1.21	103,500
80	17.793	7,299	99,172	10.11	0.74	101,060
81	19.367	7,297	114,270	10.16	0.64	100,580

The mission start time for the 258 day Hohmann transfer from Earth to Mars is given in Ref. 30. When a 19.3 day Earth escape time is used, the mission start time occurs 134.0 days prior to heliocentric opposition between Earth and Mars. Possible launch dates are shown in Table II-9. These dates were calculated from the heliocentric opposition dates for 1989 [31] and the synodic period of Mars. The conditions for a Hohmann transfer to Mars only occur about once every two years and the flight time for the main ship is less than three weeks. The option also exists for a Venus fly-by trajectory to deliver the payload to Mars. This trajectory is less energetic than a Hohmann transfer to Mars but takes almost three times as long. Since the flight time of the main ship is very short and the opportunity for payload delivery to Mars occurs only once every two years, the ship could also be used for other missions to avoid a long waiting period between missions. Other missions could include: near-Earth orbital transfers, moon missions, and missions to other planets than Mars.

Table II-9: Launch Dates for Hohmann Transfers to Mars.

February	23,	2001
April	10,	2003
May	26,	2005
July	11,	2007
August	30,	2009
October	15,	2011
December	3,	2013
January	21,	2016
March	8,	2018
April	25,	2020
June	11,	2022
July	26,	2024

CONCLUSION

Ronald Teeter

The SRA propulsion system is designed to deliver a 50,000 kg payload from LEO to low Mars orbit in under a year. It concentrates 16.3 MW of solar energy to heat hydrogen gas seeded with a small amount of potassium vapor and develops 2,940 N of thrust at a specific impulse of 1,000 s. The spacecraft uses multiple perigee burns to accelerate to near the velocity necessary to escape the Earth's sphere of influence. The payload system is released and uses a chemical rocket to obtain the small necessary velocity increment for a Hohmann transfer to Mars. At Mars the payload system uses aerobraking to assist in entering low Mars orbit.

The solar thermal propelled spacecraft is a viable concept, assuming the infrastructure is in place to construct large space vehicles and that several challenging technical problems can be solved. These include construction and cooling of the thruster window, cooling the nozzle throat, controlling vibration in the large truss structures, and developing high temperature, high strength materials. Further design should be able to reduce the mass and increase the efficiency of the system. Future work should concentrate on improving the optical system, solving the thruster window cooling problem, advancing the mathematical model to simulate the actual thruster behavior, detailing the heat and mass transport characteristics of the thruster, and further defining the other subsystems. In addition, further experimental work should be done to verify the performance of the flowing gas volume absorber at the pressure and temperature needed in the SRA thruster. It is assumed that the infrastructure will be in place and that the technical problems will be solved by the year 2010, thus the SRA propulsion system could be operational by the period 2010-2020.

NOMENCLATURE

A	area
b_{im}	image diameter
C_p	specific heat
CR	concentration ratio
D	reflector diameter
E	modulus of elasticity
f	focal length
F	thrust
g_0	surface gravity of earth
G	shear modulus
h	film heat transfer coefficient
I	moment of inertia
I_s	solar intensity
I_{sp}	specific impulse
J	torsional constant
k	thermal conductivity
K_{IC}	fracture toughness
m	mass
\dot{m}	mass flow
M_w	molecular weight
Nu	Nusselt number
P	pressure
P_c	chamber pressure
Pr	Prandtl number
P_R	power

P_{Re}	exhaust power
q	heat transfer rate
\dot{r}	radial velocity
\ddot{r}	radial acceleration
r_c	chamber radius
r_t	truss member radius
R	gas constant
R	radius of curvature
R	thermal resistance
Re	Reynolds number
S	distance
t	thickness
T_c	chamber temperature
u_e	exhaust velocity
V	rocket velocity
w	displacement
α	absorptivity
ϵ	emissivity
Δ	discrete change in the quantity
ϕ	sun's subtended angle
$\dot{\phi}$	angular velocity
$\ddot{\phi}$	angular acceleration
γ	ratio of specific heats
η_c	cavity efficiency
η_M	reflector efficiency
μ	gravitational parameter

μ	viscosity
ν	kinematic viscosity
ν	Poisson's ratio
θ	reflector focal cone angle
ρ	reflectivity
σ	Stephan-Boltzman constant
σ_N	normal stress

Superscripts

*	throat conditions
"	per unit area

Subscripts

c	chamber
e	exit
i	incoming
M	reflector
N	normal
o	sea level
w	wall
g	gas
s	surface

A dot above a variable ($\dot{}$) indicates a time derivative. Successive dots indicate successive time derivatives.

All values are in MKS units.

REFERENCES

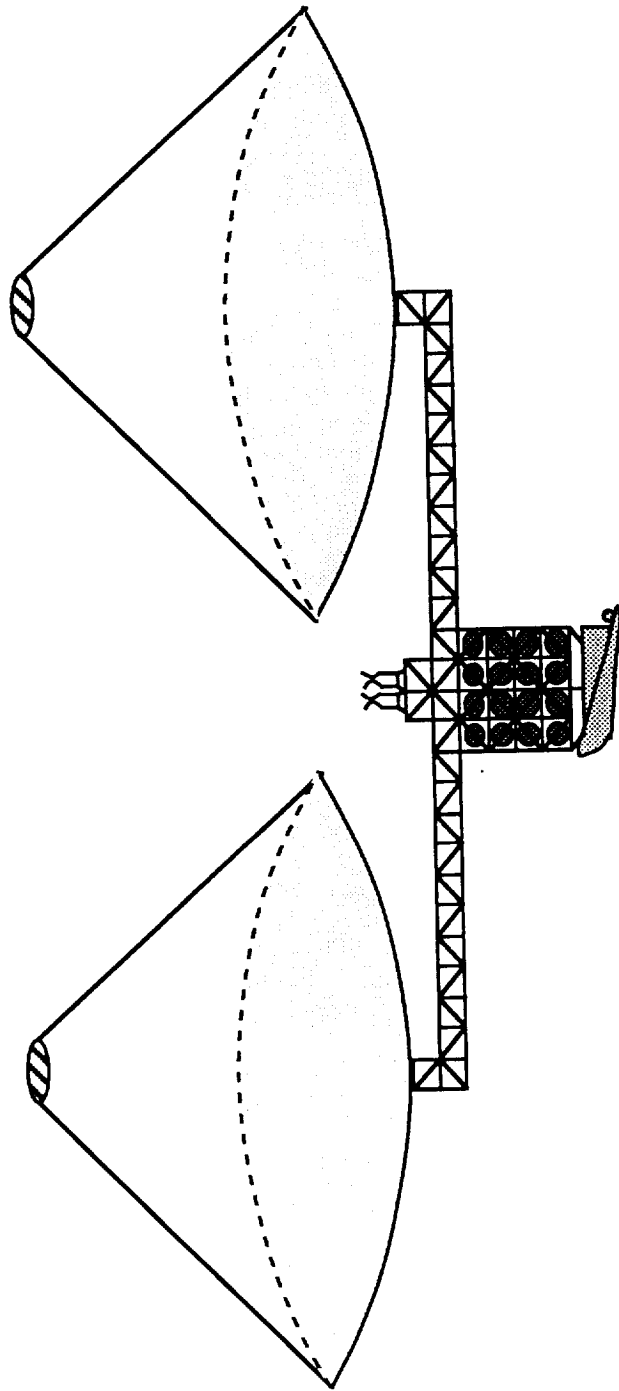
1. Mattick, Arthur T., "Coaxial Radiative and Convective Heat Transfer in Gray and Nongray Gases", J. Quant. Spectrosc. Radiat. Transfer, Vol. 24, pp. 323-334, 1980.
2. Mattick A. T., Hertzberg, A., Decher, R., and Lau, C.V., "High Temperature Solar Photon Engines", Journal of Energy, Vol. 3, pp. 30 -39, 1979.
3. Rault, D.F.G., "Radiation Energy Receiver for High Performance Energy Conversion Cycles", Doctoral Thesis, University of Washington, 1983.
4. Rault, D.F.G. and Hertzberg, A., "Radiation Energy Receiver for Laser and Solar Propulsion Systems", AIAA Paper No. 83-1207, June, 1983.
5. McFall, K., Predoctoral Research Associate, Department of Aeronautics and Astronautics, University of Washington, private communication, March, 1989.
6. Shoji, J. M., "Performance Potential of Advanced Solar Thermal Propulsion", AIAA Paper No. 83-1307, June, 1983.
7. Popov, Edgar Paul, Mechanics of Materials, Second Edition. Prentice-Hall, Inc., Englewood Cliffs, N.J., p. 291, 1978.
8. Van Wylen, G.J. and Sonntag, R.E., Fundamentals of Classical Thermodynamics, 3rd Edition, John Wiley and Sons, Inc, 1985.

9. Incropera, F.P. and De Witt, D.P., Fundamentals of Heat and Mass Transfer, 2nd Edition, John Wiley and Sons, Inc, 1985.
10. Goetzel, C.G., "High-Temperature Properties of Some Carbon-Carbon Composites", High Temperatures-High Pressures, Vol 12, p. 11-22, 1980.
11. Kuethe, Arnold M. and Chow, C.Y., Foundations of Aerodynamics, John Wiley and Sons, Inc, New York, 1986.
12. NASA, "Liquid Rocket Engine Fluid Cooled Combustion Chambers", NASA SP-8087, 1972.
13. "Optical Properties and Applications of Linde Cz Sapphire", Union Carbide Technical Bulletin, 1972.
14. Young, W.C., Roark's Formulas for Stress and Strain, 6th Edition, McGraw-Hill, 1989.
15. Modifications of Finite Element Analysis Program (FEAP), Holsapple, K. A., Department of Aeronautic and Astronautics, University of Washington.
16. Bush, H. G., and Mikulas, M. M., "Advances in Structural Concepts", NASA CP-2269 Part 1, May, 1983.
17. Swanson G., Gurdal, Z., and Stannes, J.H., Jr., "Structural Efficiency Study of Graphite-Epoxy Aircraft Rib Structures," AIAA Paper No. 88-2218, April, 1988.

18. Franz, J. and Laube, J., "Design and Manufacturing Aspect of Tubular Carbon Fiber Composite/Titanium Bonded Joints", Composite Structures: Elsevier Applied Science Publishers Ltd., England, 1986.
19. Space Station Program Office, "Space Station Truss Structures and Construction Considerations," Structures and Mechanics White Paper: NASA Johnson Space Center, July ,1984.
20. Leger, L.J., Visentire, J.T., and Schliesing, J.A., "A Consideration of Atomic Oxygen Interactions with Space Station," AIAA Paper No. 85-0476, Jan., 1985.
21. INCAP Laminate Analysis Program, The Boeing Company, Seattle WA, Feb., 1989.
22. Mikulas M., NASA Langley Research Center, private communication, March 1989.
23. Lake, M.S. and Bush, H.G., "An Analytical Investigation of a Conceptual Design for the Space Station Transverse Boom Rotary Joint Structure", NASA Langley Research Center TM-87665, Jan., 1986.
24. Frisbee, R.H., Horvath, J.C., and Sercel, J.C., "Space-Based Laser Propulsion for Orbit Transfer", JPL D-1919, Jet Propulsion Laboratory, Pasadena, CA, 1984.
25. Thomas, M. and Friese, G.J., "Pressurized Antennas for Space Radars", AIAA Paper No. 80-1928, 1980.

26. Terre, C.N., "Low Pressure/ Lightweight Cryogenic Propellant Tank for the Space-Based Orbital Transfer Vehicle", General Dynamics Space Systems Division, A86-38826.
27. Glazer, J., et al., "Cryogenic Mechanical Properties of Al-Cu-Li-Zr Alloy 2090", Lawrence Livermore National Laboratory, University of California, Livermore, CA, 1985 Cryogenic Engineering/International Cryogenic Materials Conference, Cambridge, MA, Aug., 1985.
28. Eberhardt, R.N. and Fester, D.A., "Shuttle Compatible Cryogenic Liquid Storage and Supply Systems," AIAA Paper No. 81-1509, July 1981.
29. Aydelott, J.C., Carney, M.J., and Hochstein, J.I., NASA Lewis Research Center Low-Gravity Fluid Management Technology Program, NASA TM 87145, NASA Lewis Research Center, Cleveland, OH, Nov., 1985.
30. Bate, R.R., Mueller, D.D., and White, J.E., Fundamentals of Astrodynamics, Dover Publications, Inc., New York, 1971.
31. Stuhlinger, E., "The Flight Path of an Electrically Propelled Space Ship", Jet Propulsion, Vol. 27, pp. 410-414, April 1957.
32. Astronomical Almanac for the Year 1989, U.S. Government Printing Office, 1988.

III. SOLAR PUMPED LASER PROPELLED SPACECRAFT



INTRODUCTION

Anna Cinniger
Melanie Miller

The search for more efficient and effective propulsion techniques for interplanetary transport has stimulated research into the feasibility of using laser propulsion. In 1972, laser propulsion was first proposed by Kantrowitz [1]. During the past decade, research has been supported by NASA, DARPA, and the Air Force [2,3,4]. Research has been concentrated primarily in the propulsion and laser areas.

The principle behind laser propulsion is the use of a remotely stationed laser as an energy source to propel a spacecraft as illustrated in Fig. III-1. The primary advantage of laser propulsion over other advanced propulsion methods is that the energy source is not onboard the spacecraft, and thus, it does not add to the mass of the ship. As a result, a high thrust to mass ratio is attainable. Another advantage of laser propulsion is that it provides a higher specific impulse than chemical propulsion and a higher thrust than electric propulsion.

Two types of lasers are suitable for laser propulsion: Continuous Wave (CW) and Repetitively Pulsed (RP). In the CW laser thruster, a continuous laser beam is directed into an absorption chamber, where a propellant is heated and then expanded through a nozzle [1]. In the Repetitively Pulsed (RP) laser thruster, detonation waves from a solid propellant are initiated by bombarding the propellant with a train of pulsed laser energy. The propellant flow from the RP laser thruster is therefore very unsteady and predicting the flow characteristics requires detailed experimental data. Because of the inherent complexities of the Repetitively Pulsed laser thruster [5], the Continuous Wave laser thruster was chosen for the proposed.

The proposed preliminary design of a laser propelled spacecraft system includes a solar pumped CO₂ laser platform, residing in LEO, that beams energy to a receiver on board a spacecraft. Once the craft receives the laser energy, it is converted into thermal energy and finally into thrust. The laser propulsion system includes two subsystems, the spacecraft thrusters and the laser/optical system.

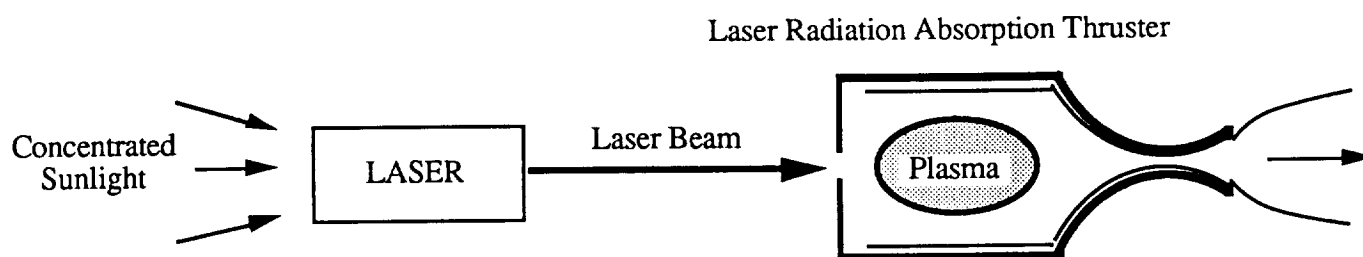


Figure III-1. Solar Pumped Laser Thruster System.

PROPULSION SYSTEM

Melanie Miller

Conceptually, the Continuous Wave (CW) laser thruster is a fairly straightforward design (See Fig. III-2); however, the engineering details concerning the components of the CW thruster are quite complicated. A window in the thruster allows the laser beam to pass into the absorption chamber, where it is absorbed by a plasma discharge in the propellant gas. This plasma transfers energy to the surrounding propellant flow by radiation and convection. The heated propellant is expanded through a nozzle to produce thrust.

THRUSTER THEORY

Given the incident laser power, P , at the thruster, the jet power, P_j , is obtained from

$$P_j = P - P_{\text{loss}} \quad (\text{III-1})$$

where P_{loss} represents the power losses in the thruster system. These include the radiative losses from the thruster, the nozzle efficiency losses, and the power absorbed by the thruster window.

In order to calculate the available thrust, the exit velocity of the propellant is needed. The effective propellant exit velocity, u_e , is calculated from

$$u_e^2 = 2(h_c - h_e) \quad (\text{III-2})$$

where h_c is the enthalpy of the propellant within the chamber and h_e is the enthalpy of the exiting propellant. For the selected propellant, typically hydrogen, h_c can be found from standard tables given the chamber temperature and pressure. Assuming the gas is perfectly expanded through the nozzle, h_e is the energy lost to dissociation of the propellant gas.

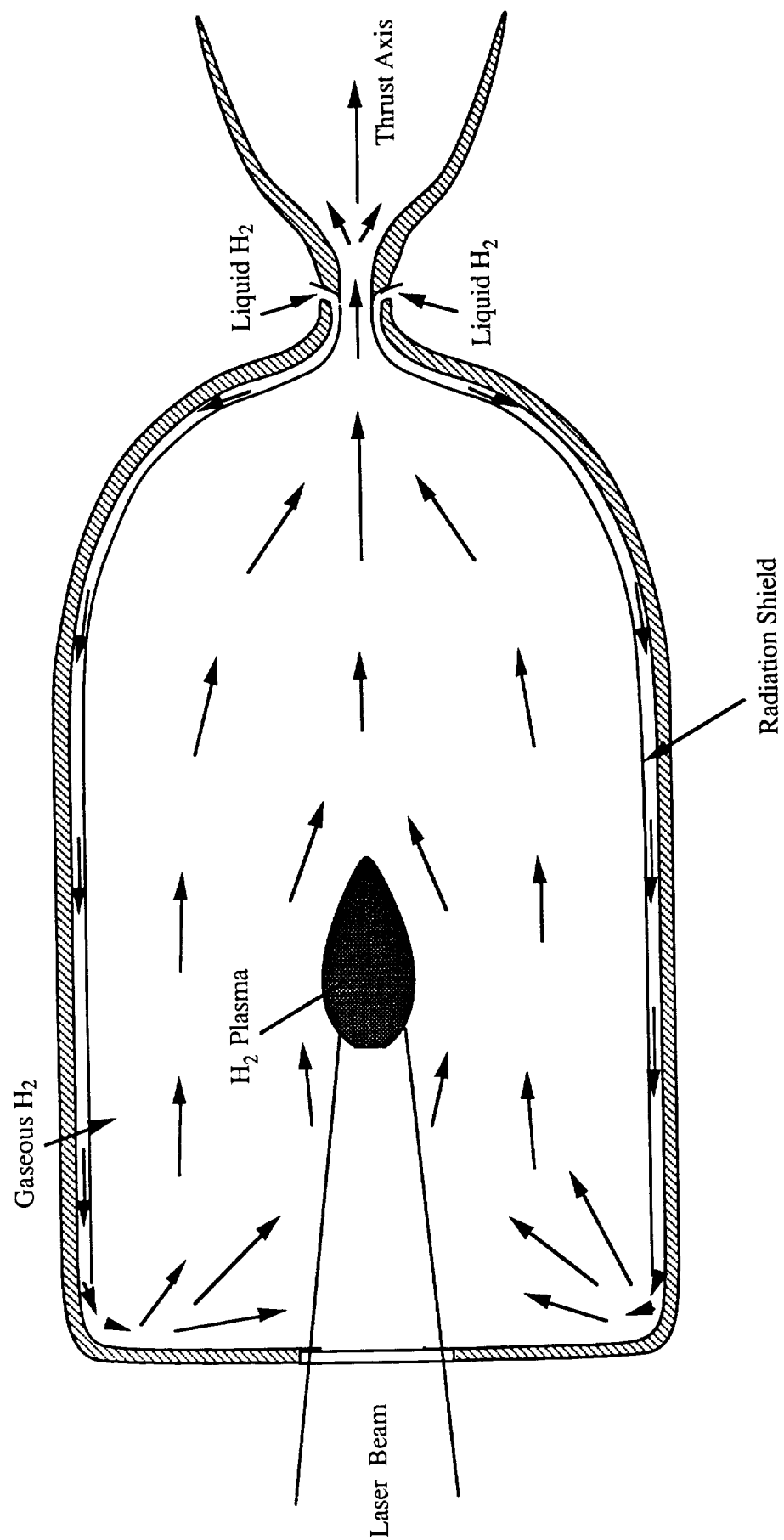


Figure III-2. Schematic of Laser Thruster.

$$h_e = \alpha_1 \epsilon_d N_o \quad (\text{III-3})$$

where α_1 is the percent dissociation, ϵ_d is the energy of dissociation for the given propellant, and N_o is the number of molecules per unit mass of the undissociated propellant. The thrust, F , is calculated from the jet power, P_j , and the propellant exit velocity, u_e , by

$$F = 2 \frac{P_j}{u_e} \quad (\text{III-4})$$

The mass flow rate, \dot{m} , is calculated from

$$\dot{m} = \frac{F}{u_e} \quad (\text{III-5})$$

The specific impulse, I_{sp} , is calculated from the exit velocity

$$I_{sp} = \frac{u_e}{g_o} \quad (\text{III-6})$$

where g_o is the reference acceleration of gravity of the Earth, 9.81 m/s^2 .

The rocket nozzle area at the choking point is calculated from

$$A = \dot{m} \sqrt{T_o} / \left[p_o \left(\left(\frac{\gamma}{R} \right) \left(\frac{2}{(\gamma+1)} \right)^{(\gamma+1)/(\gamma-1)} \right)^{1/2} \right] \quad (\text{III-7})$$

where p_o is the chamber pressure, T_o is the chamber pressure, R is the gas constant for the propellant, and γ is the ratio of specific heats.

CONCEPTUAL DESIGN OF LASER THRUSTER

Due to the high temperature of the propellant within the absorption chamber, the thruster design centered around the use of regenerative cooling concepts (See Fig. III-2). The nozzle is regeneratively cooled by the incoming liquid hydrogen. A radiation shield surrounds the absorption chamber which is also actively cooled by the incoming hydrogen. During the process of cooling the chamber, the hydrogen is preheated. As a result, the efficiency of the entire thruster system is maximized.

Optimizing Propellants

Hydrogen is the optimal propellant for the laser propulsion system. Since hydrogen has the lowest molecular weight, as a propellant, it will give the highest possible specific impulse. A disadvantage of using hydrogen as a propellant is that, as a result of its low density, hydrogen requires more storage volume than other propellants. Considering these performance trade-offs, the advantages of using hydrogen propellant outweigh the disadvantages. Eskridge, et al., confirm these findings in their calculations [6].

Thruster Performance

Due to constraints of the feasibility of high powered lasers, the laser system is assumed to produce 6 MW of laser energy of which 5.4 MW is received by the spacecraft (See section: Laser and Associated Optical System). The radiative losses from the thruster are calculated to be 0.1 MW, given that the temperature of the gas adjacent to the chamber wall is 4,000 K. This temperature was determined from the 2-D model discussed in Appendix B. The nozzle efficiency was assumed to be 95% which led to a power loss of 0.26 MW. The thruster window absorbed 14.8 kW of the incoming laser energy (See subsection: Absorption Chamber Window). The resulting jet power is approximately 5 MW. The efficiency is calculated from the ratio of the exhaust power, P_j , to the incoming laser power, P , and is approximately 93%.

Downstream of the plasma, the fluid mixing results in an estimated average temperature, T_o , of 4,300 K at the entrance to the nozzle [5]. The thermodynamic properties of the hydrogen at this temperature are taken as the chamber conditions used to calculate the engine performance. The chamber pressure, p_o , is optimized to be 10 atm (See subsection: Optimizing Chamber Pressure).

For hydrogen at the given chamber temperature and pressure, the % dissociation was found to be 40%, which results in an exit velocity of 12,600 m/s ($I_{sp} = 1285$ s). The corresponding mass flow rate is 0.036 kg/s, resulting in a thrust of 600 N.

DETAILED THRUSTER COMPONENT DESIGN

Absorption Chamber Design

The design of the absorption chamber begins with an estimation of the inside diameter of the chamber. This diameter needs to be large enough so that the temperatures of the flow adjacent to the wall will be sufficiently moderate to avoid damage of the chamber wall. From the available data on material properties [7], the maximum permissible temperature for an actively cooled radiation shield (See Fig. III-3) is assumed to be 4,000 K. The radius at which the 4,000 K isotherm is a tangent to the thruster radiation shield was determined by calculations made from the 2-D mathematical model (See Appendix B). The resulting absorption chamber inner diameter is 26 cm. The active cooling duct requires approximately a 1 cm spacing between the radiation shield and the outer chamber wall (See Fig. III-4). Therefore the outer chamber wall has an inside diameter of approximately 28 cm.

The proposed thruster system is composed primarily of Molybdenum [7]. Molybdenum is currently used in the design of rocket chambers and heat exchangers which require the ability to endure large thermal stresses. The use of a single material was chosen due to the extensive thermal cycling the thruster may have to endure.

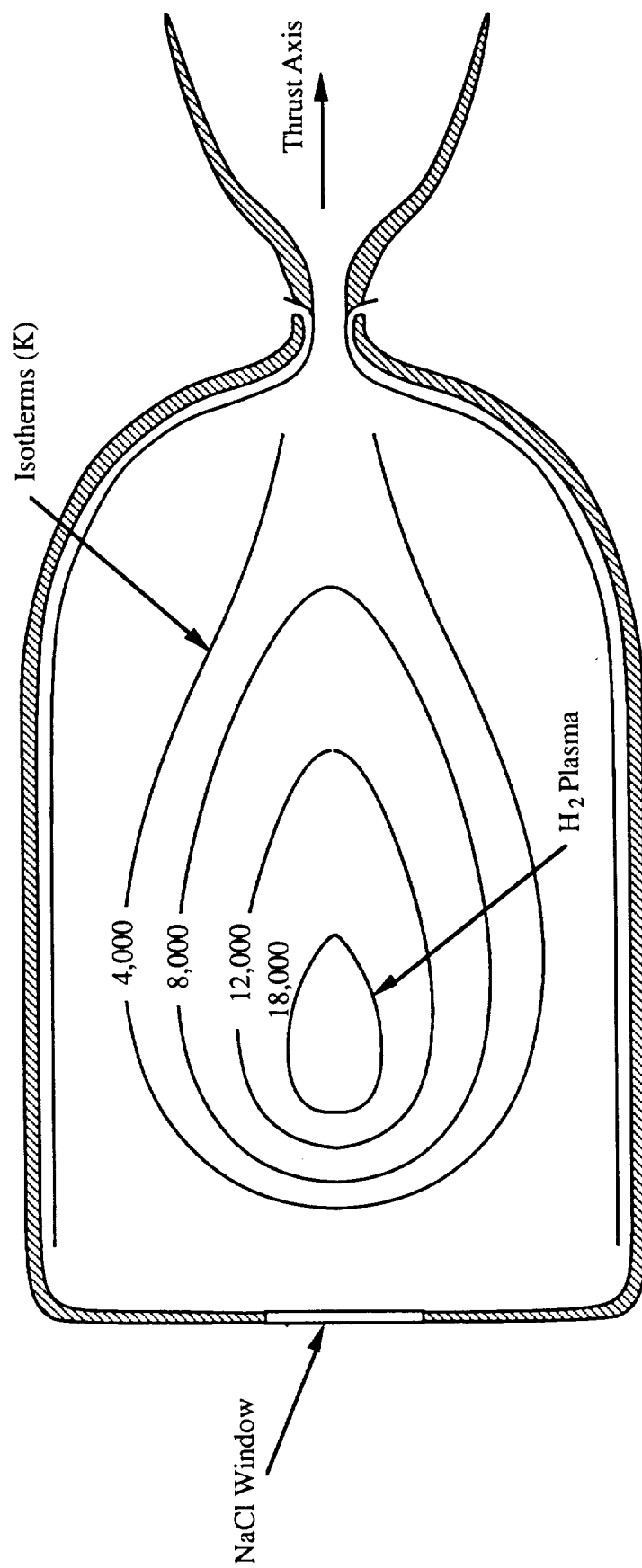


Figure III-3. Steady State Thermal Characteristics of Thruster.

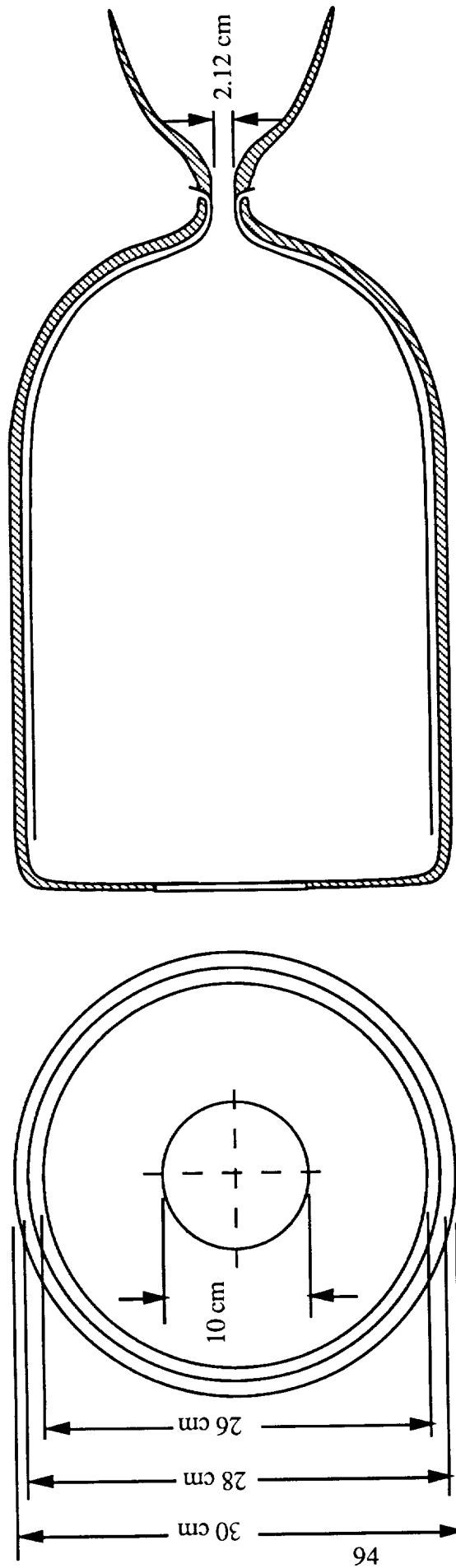


Figure III-4. Thruster Design.

For stress calculations, the outer chamber wall was modeled as a cylindrical, thin-walled pressure vessel. The hoop stress, σ , of this outer wall is calculated from

$$\sigma = \frac{pr_v}{t_w} \quad (\text{III-8})$$

where p is the pressure differential, r_v is the radius to the wall, and t_w is the wall thickness.

Since the external chamber wall is actively cooled, it is estimated to reach a maximum temperature of 1,500 K. Given the internal pressure of 10 atm, a maximum allowable stress of 241 MPa for Molybdenum at 1,500 K, and an internal radius of 14 cm from the thruster design, the required outer chamber wall thickness is 2.5 mm. Although the calculated wall thickness will withstand the pressure stresses, additional stresses are generated by the thermal gradients through the material. With a factor of safety of four, the thickness of the outer chamber wall is 1 cm.

Optimization of Chamber Pressure

A major engine design consideration is to minimize any damage that might occur to the thruster during the ignition of a plasma. For approximately 300 nanoseconds before plasma formation, the nozzle area could be exposed to a large fraction of the laser radiation directed into the absorption chamber. The solution to this problem is to direct the laser beam in such a manner that during ignition the beam exits the nozzle throat area without impinging on the thruster structural material (See Fig. III-5). By decreasing the chamber pressure, and therefore increasing the nozzle throat area for the choked condition, a nozzle throat area was found which is large enough to allow the beam to exit the nozzle in the manner described. Because the materials used for the chamber walls have definite stress limitations, an iterative process of calculating the optimum chamber pressure, wall thickness, and position of the focal point of the incoming laser beam was also conducted. In this manner, the chamber pressure is determined to be 10 atm, resulting in a nozzle throat area of 3.53 cm².

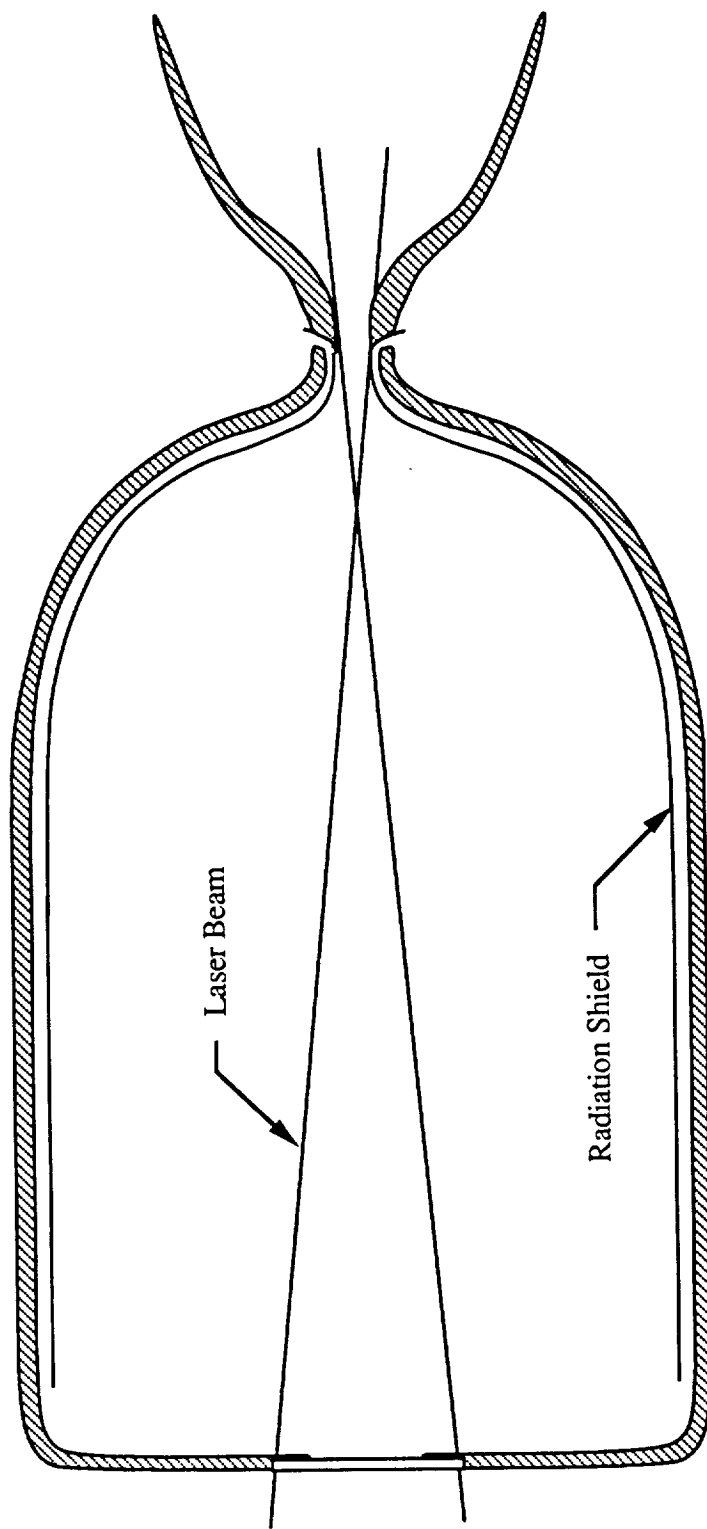


Figure III-5. Laser in Chamber Prior to Plasma Ignition.

Temperature Distribution within the Thruster Chamber

The temperature gradients in the absorption chamber during steady state operation are relatively large. The plasma core has the highest temperature, and the temperature decreases in the upstream, downstream, and radial directions. The high kinetic energy of the molecules, ions and free electrons within the plasma raises the thermal energy of the hydrogen gas that flows around the core (See Fig. III-2). From a 2-D mathematical model of the thermal characteristics within the chamber [8], the plasma core temperature was found to be 18,000 K while the hydrogen gas temperature range at the radiation shield walls is 1,500 to 4,000 K (See Fig. III-3). The isotherms within the engine were calculated from the thermal flux through the hydrogen [8]. By varying the chamber pressure, mass flow rate, and laser intensity, it was possible to optimize the temperature profile within the absorption chamber and the temperature of the plasma. At plasma temperatures greater than 19,000 K, a significant fraction of the flow within the chamber is dissociated, thus decreasing the efficiency of the thruster. At lower plasma temperatures, there is less absorption of the laser energy. To optimize the energy efficiency of the system, it is desirable to design the thruster such that the temperature of the plasma core is approximately 18,000 K.

Absorption Chamber Window

A major problem concerning the design of a laser thruster is finding a transparent medium that allows a 5 MW laser beam to enter the absorption chamber. The chamber window must absorb as little of the incident laser energy as possible to minimize the heating of the window surface, while also having the capability to structurally withstand the energy that it does absorb. The optimal transparent substance appears to be Polytran NaCl window manufactured by the Harshaw Chemical Company [9]. This window was chosen due to its extremely low absorption coefficient at the wavelength of 10.6 μm , generated by the CO_2 laser used in the proposed system.

Assuming the window is circular and clamped uniformly at the edges, the ratio of the optimum thickness, t , to the diameter, D , of the window is determined from

$$\frac{t}{D} = \left[S.F. \cdot \left(\frac{K}{4} \right) \right] \sqrt{\frac{p}{Y}} \quad (\text{III-9})$$

where S.F. is the factor of safety, K is an empirically derived constant, p is the pressure differential on the window, and Y is the yield strength of the window material. The factor of safety which is suggested by the manufacturer is 4. Research into decreasing the allowable factor of safety in calculating the window thickness might lead to a more efficient design. K is dependent upon the window mounting; for the proposed engine design, $K = 0.75$ [10]. Since the thruster is operating in a vacuum, p is the chamber pressure. For the Polytran NaCl window, $Y = 1.48 \times 10^7$ Pa [10].

Because the absorption coefficient and the strength of the window are functions of the its diameter and thickness, the window size is optimized. A minimum window diameter is taken to be 10 cm due to the focusing limitations of the laser beam, to provide some capacity to manipulate the focal point placement within the chamber, and to be able to dissipate the heat absorbed by the window. An increase in pressure leads to a greater window thickness (See Fig. III-6). From the window diameter, the specified 10 atm chamber pressure, and Eq. III-9, the necessary window thickness is 1.93 cm.

The amount of radiation that passes through the window is [10]

$$I_t = I_e e^{-\alpha t} \quad (\text{III-10})$$

where I_t is the transmitted radiation intensity through thickness, t , I_0 is the intensity of the incident radiation, and α is the absorption coefficient of the Polytran window [10]. The absorption coefficient at 10.6 μm wavelength is 0.0014 cm^{-1} [9]. Minimization of the thickness decreases the amount of energy absorbed which results in an increase in the efficiency of the thruster system.

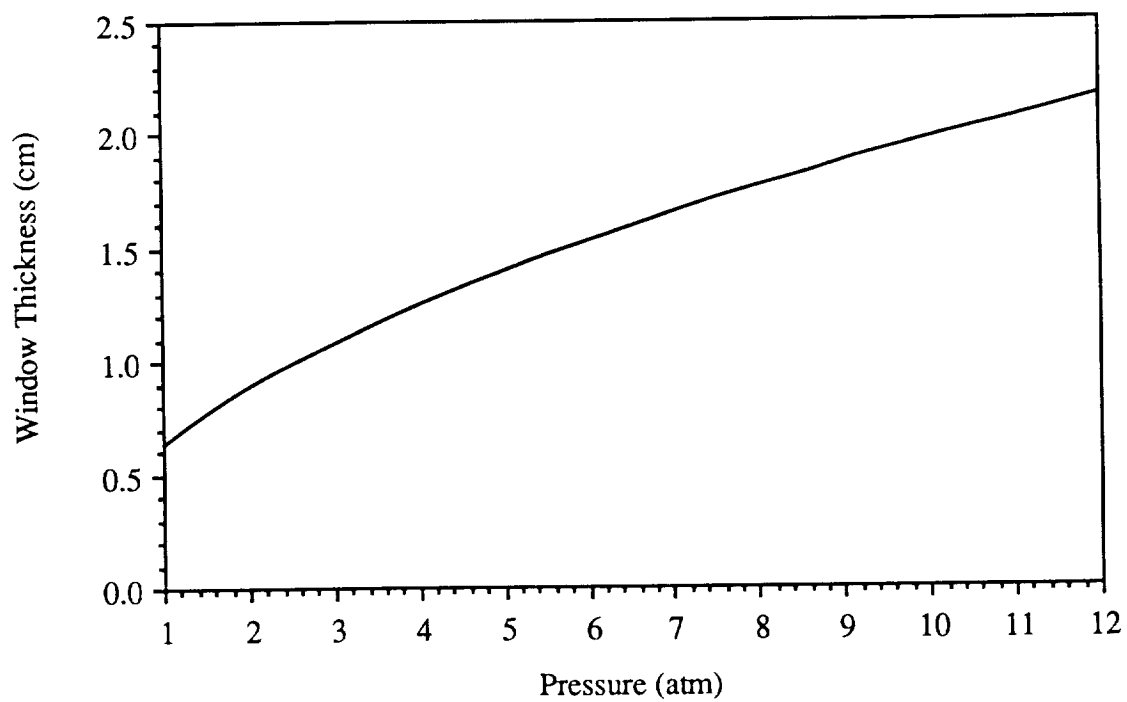


Figure III-6. Window Thickness as a Function of Chamber Pressure and Incident Radiation of 5 MW.

The amount of energy absorbed by the window, I_{ab} , is the difference between the intensity of the incident radiation, I_0 , and the transmitted radiation:

$$I_{ab} = I_0(1 - e^{-\alpha t}) \quad (\text{III-11})$$

The amount of energy absorbed as a function of chamber pressure is plotted in Fig. III-7 for laser power levels of 4, 5, and 6 MW. The power absorbed increases with chamber pressure due to the concomitant increase in the window thickness. For the chosen chamber pressure of 10 atm and $I_0 = 5.4$ MW, 14.8 kW of power is absorbed by the window. The energy that is not radiated from the window needs to be dissipated by active cooling. It is suggested by Eskridge, et al. [6] that film cooling of the window is an appropriate method of heat dissipation.

THEORETICAL LASER ENERGY ABSORPTION

Hydrogen Plasma Formation

The initial plasma formation was a major concern of early researchers on the subject of laser propulsion [5]. This concern is attributed to the low absorptivity of hydrogen at low temperatures. To ignite the hydrogen plasma in the absorption chamber, a source of free electrons must be present to absorb the laser light and heat the hydrogen to plasma temperatures. Once the hydrogen forms a plasma, nearly 100% of the incoming laser energy is absorbed in the plasma.

There are three methods of obtaining a source of free electrons for laser energy absorption. These methods include ignition of the hydrogen plasma by laser bombardment of seedants, by the use of electrical discharges, and by pulsing an additional laser.

Using seedants is the most complex of the ignition systems and contains more performance penalties than the pulsed laser concept. A seedant is most likely to be added to the hydrogen flow for only a short period of time. The seedant thus needs its own storage and mixing systems, which requires further research. Many of the seedants such as H_2O

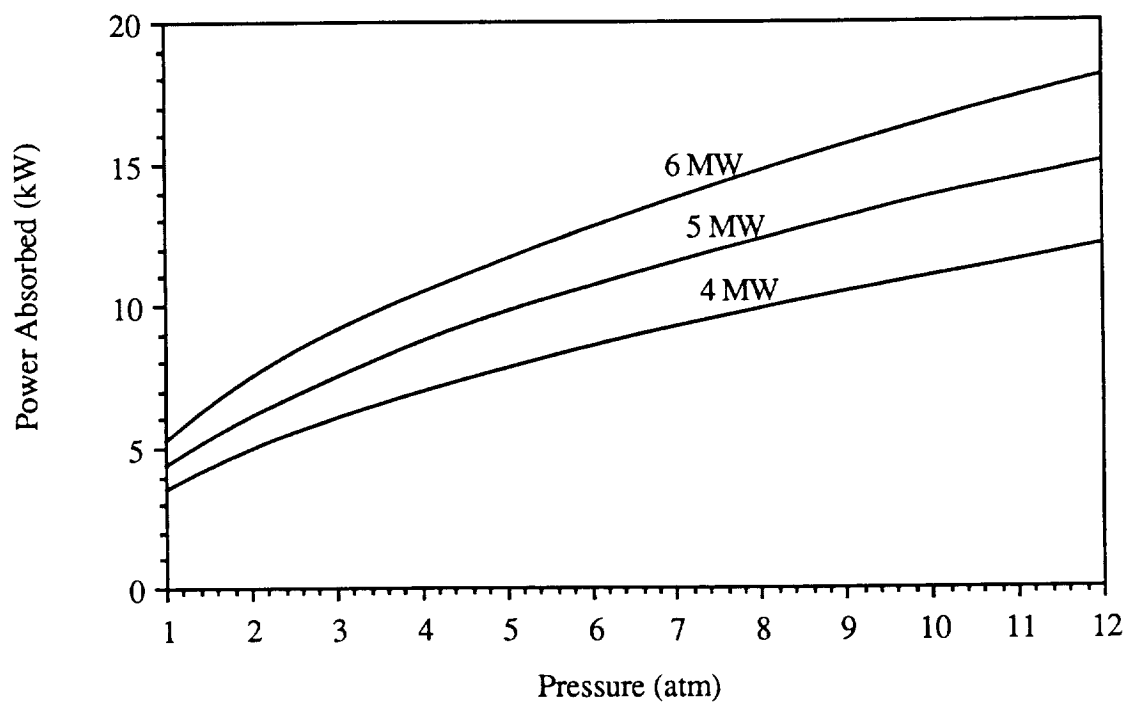


Figure III-7. Power Absorbed by Window as a Function of Chamber Pressure for Various Incident Radiation Levels.

or Al_2O_3 contain oxygen [11]. As a result, using seedants causes oxidation which erodes the inner chamber walls and nozzle. Besides the engineering complications that seedants incur, seedants in the exhaust interfere with the incoming transmitted laser beam. For the aforementioned reasons, it is not proposed to employ seedants to ignite the plasma.

Electrical discharge methods, although more favorable than the use of seedants, are also quite complex. These methods require the addition of a cathode/anode electrode pair in the absorption chamber. The survival for reuse of such a setup is questionable and requires further investigation.

The preferred method for the ignition of the hydrogen plasma is to produce gas breakdown by a pulsed laser in addition to the continuous laser. Since the laser pulse is obtained by Q-switching the laser, the complexity of the onboard system is kept to a minimum. The pulsed laser is also the "cleanest, least intrusive, and most reliable of the available options." [6] Furthermore, there are no additional thruster performance penalties associated with this method.

In the pulsed laser ignition system, the pulse of laser energy produces a gas breakdown within the propellant. When this occurs, a small region of high electron density (i.e. a plasma core) is formed. A detailed explanation of the exact method of pulsed plasma ignition is discussed by Eskridge, et al., [6] and Moody [12]. The results of their experimental work show that the pulsing of a 30 kW laser for 150 nanoseconds is enough to spark a plasma at the focal point in hydrogen gas. The laser used for their experiments was a CO_2 laser of the same wavelength as in the proposed laser system.

Since the proposed system is to operate with hydrogen at 10 atm, a pressure higher than what has been tested, it is necessary to discuss the effects of this higher pressure on the breakdown intensity, i.e., ease of plasma ignition. In general, absorptivity increases linearly with increasing pressure. Thus the breakdown intensity, which is inversely proportional to absorptivity, decreases as the pressure increases [13]. In support of this theoretical relationship, experimental data confirms that the breakdown intensity of

hydrogen gas decreases with increasing pressure (See Fig. III-8). The assumption is therefore made that the breakdown intensity of hydrogen is lower for a pressure of 10 atm than that of 5 atm in the studies conducted by Eskridge, et. al. [6].

Steady State Hydrogen Plasma

In the steady-state case, a sustained hydrogen plasma resides in the absorption chamber and absorbs nearly 100% of the incoming laser energy [6]. Experimental data from Eskridge, et al. [6] shows that, as the intensity of the laser increases, the radiation which is not absorbed by the plasma decreases rapidly (See Fig. III-9).

Experimental results for steady-state hydrogen plasmas are limited, but gases similar to hydrogen, such as argon, prove to be successful in forming sustained plasmas. Experimental data for the plasmas tested confirms the mathematical modeling of the temperature and pressure gradients [6].

The absorption of the energy within the plasma region is attributed mainly to inverse Bremsstrahlung absorption. This type of absorption is explained as follows:

Absorption occurs when a photon is absorbed by a free electron during a collision with either a neutral atom or an ion. The excited electron eventually transfers its energy to the surrounding gas through collisions, raising the bulk temperature of the gas [5].

Because of the high temperatures within the plasma, the hydrogen becomes sufficiently ionized to produce an abundance of free electrons. This source of electrons is responsible for the successful absorption of laser energy by the inverse Bremsstrahlung process.

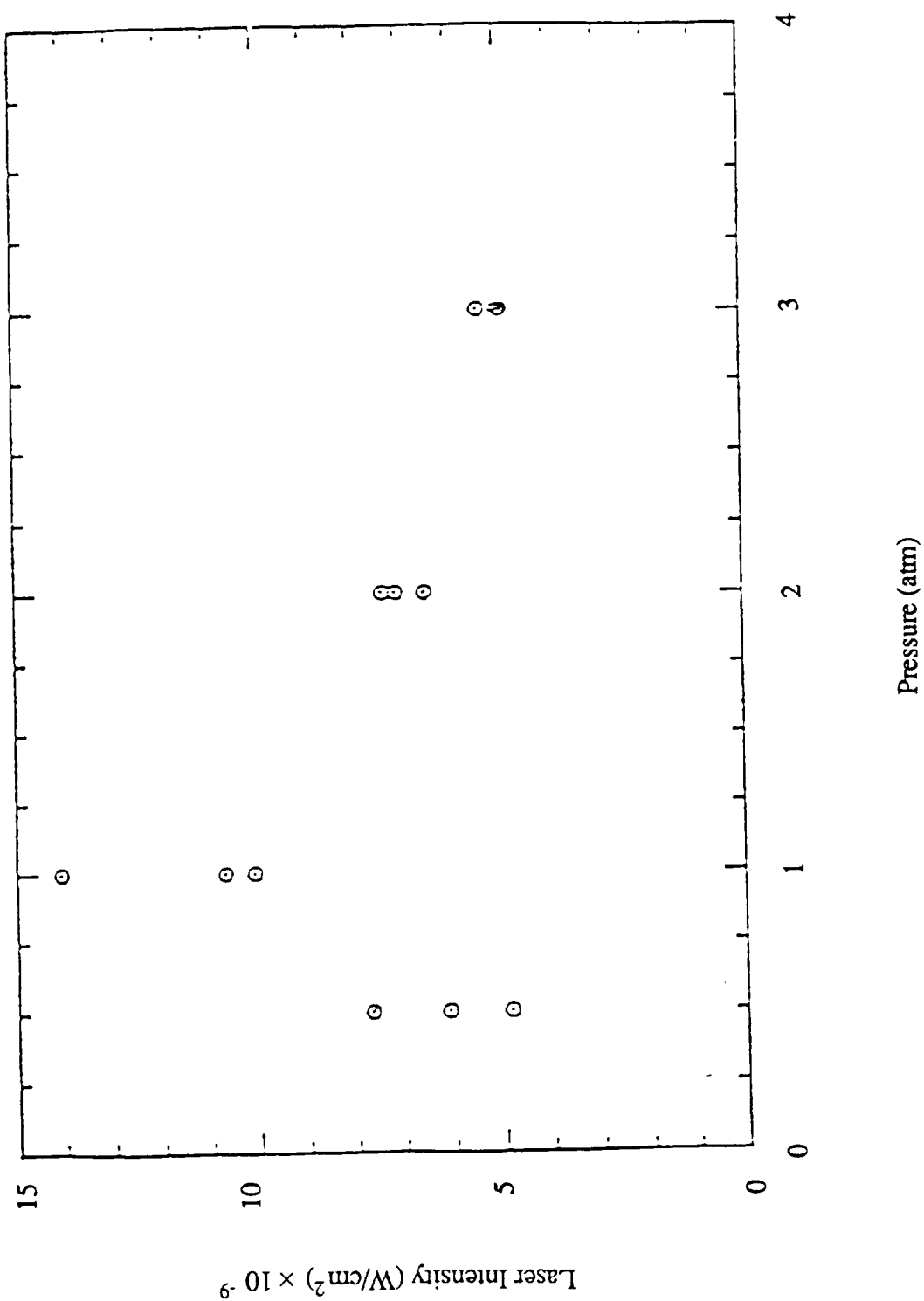


Figure III-8. Measured Gas Breakdown Intensity of Pure Hydrogen for Varying Pressure [6].

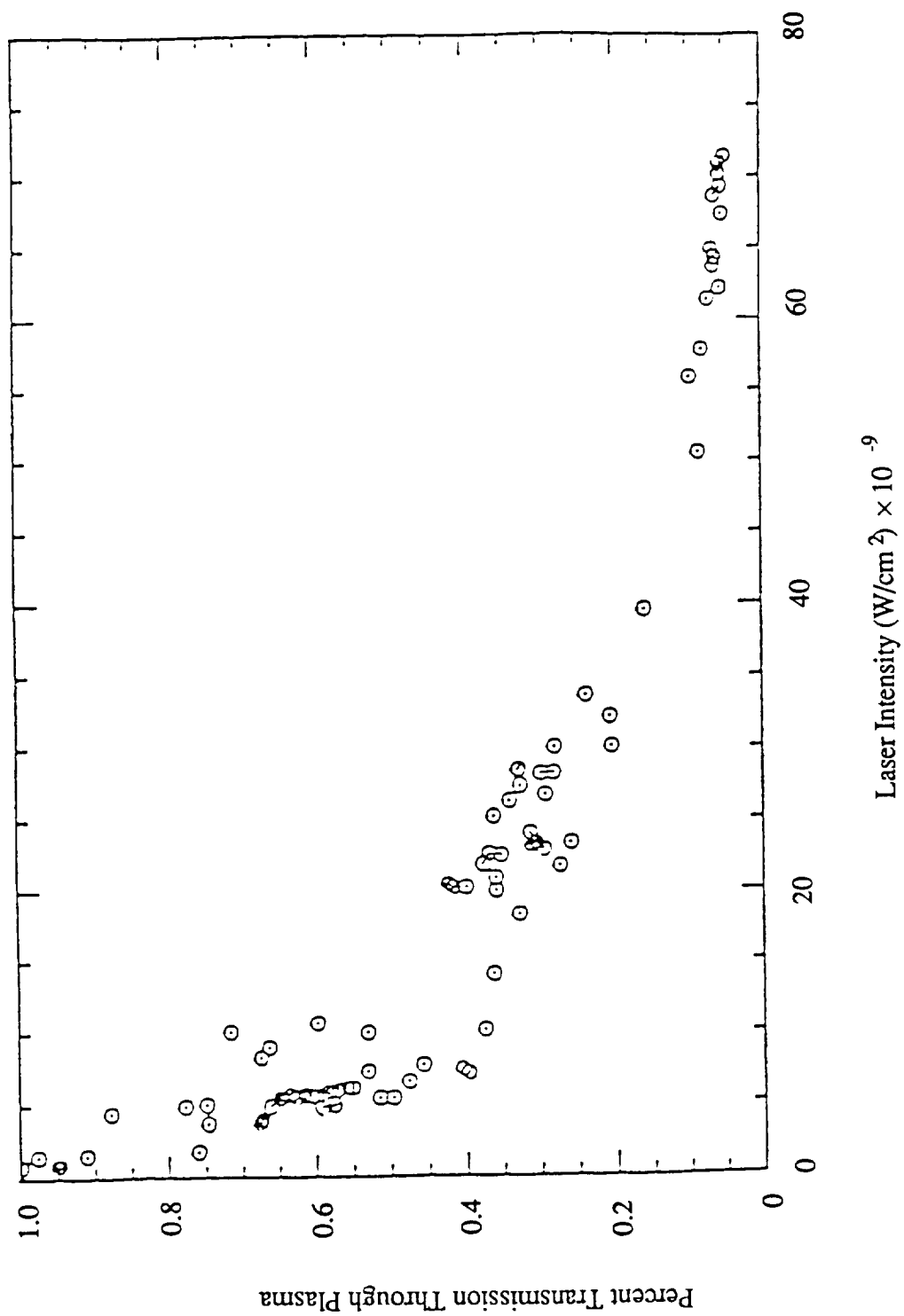


Figure III-9. Escaped Energy in Pure Hydrogen Plasma as a Function of Input Intensity [6].

Plasma Stability

The plasma is initially formed at the focal point of the incoming laser beam. In the steady state, the plasma tends to propagate up the laser beam until the intensity of the beam becomes too small to sustain the plasma. At this point, the plasma extinguishes; however, there are methods that force the plasma to translate back to the focal point. One method of controlling the plasma propagation is manipulation of the propellant characteristics in the absorption chamber. The velocity of the propellant counterflow in the chamber can be increased to "hold" the plasma downstream of the incoming beam (See Fig. III-2). The pressure in the absorption chamber may also be manipulated to "hold" the plasma in a smaller region around the focal point of the laser beam. Further experimental research of hydrogen plasmas must be performed to determine whether the proposed flow parameters result in an inherently stable plasma.

LASER AND ASSOCIATED OPTICAL SYSTEM

Anna Cinniger
Amy Prochko
Jeff Slostad
Terri Schmitt

The spacecraft thrusters receive energy from two solar pumped lasers in sun-synchronous orbit around the earth (See Fig. III-10). Solar pumping is achieved by concentrating solar energy into blackbody cavities which serve to excite the lasing medium in tubes lining the blackbody cavity [14]. The output beam of each laser is transmitted and directed by a system of mirrors and laser relay units to one of two inflatable receivers on the spacecraft. Optical trains direct the beamed energy from each receiver to its respective thruster window.

SOLAR COLLECTOR

A 15% efficiency is projected for solar to laser power conversion [14]. Given a solar flux of 1.3 kW/m^2 at Low Earth Orbit, a solar collector area of $5,155 \text{ m}^2$ is required for each megawatt of laser output. In the proposed design, each laser has six solar collectors. Figure III-11 illustrates the circular arrangement of the collectors, which are positioned opposite the sun from the six blackbody cavities of the laser. The collectors concentrate the solar flux directly into the blackbody cavities. Frontal and side views of the solar concentration system are also shown in Fig. III-11. The reflective surface of the collectors is fabricated of aluminized Kapton to provide high reflectivity over a broad band of wavelengths. The total mass of the collectors for each laser is estimated to be 31,000 kg [15,4].

LASER

To meet the propulsion requirement of 5.4 MW at each thruster window, each laser must generate approximately 6 MW to compensate for the losses at the reflecting surfaces and the losses due to diffraction. Losses at each of the reflective surfaces are on the order

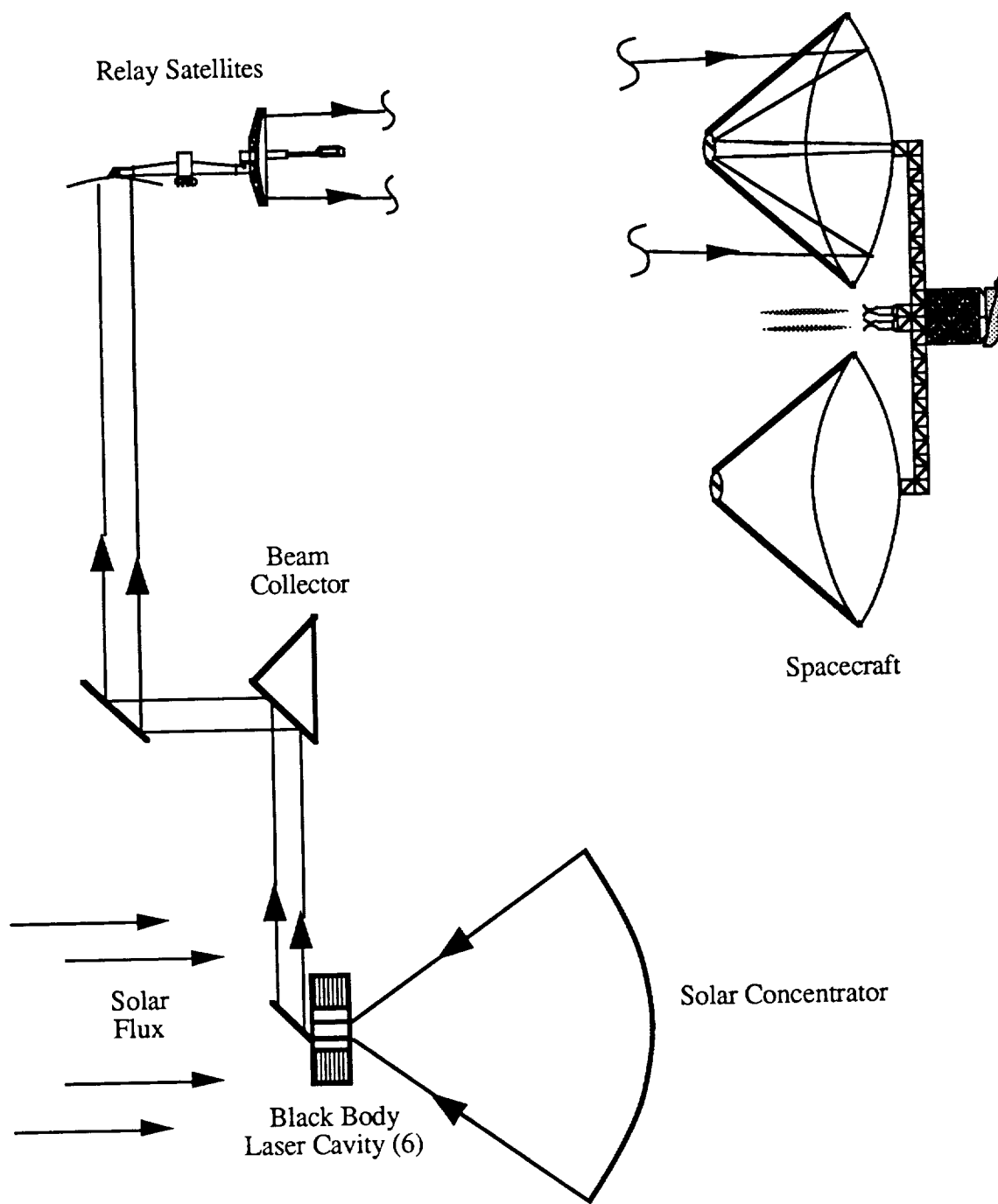
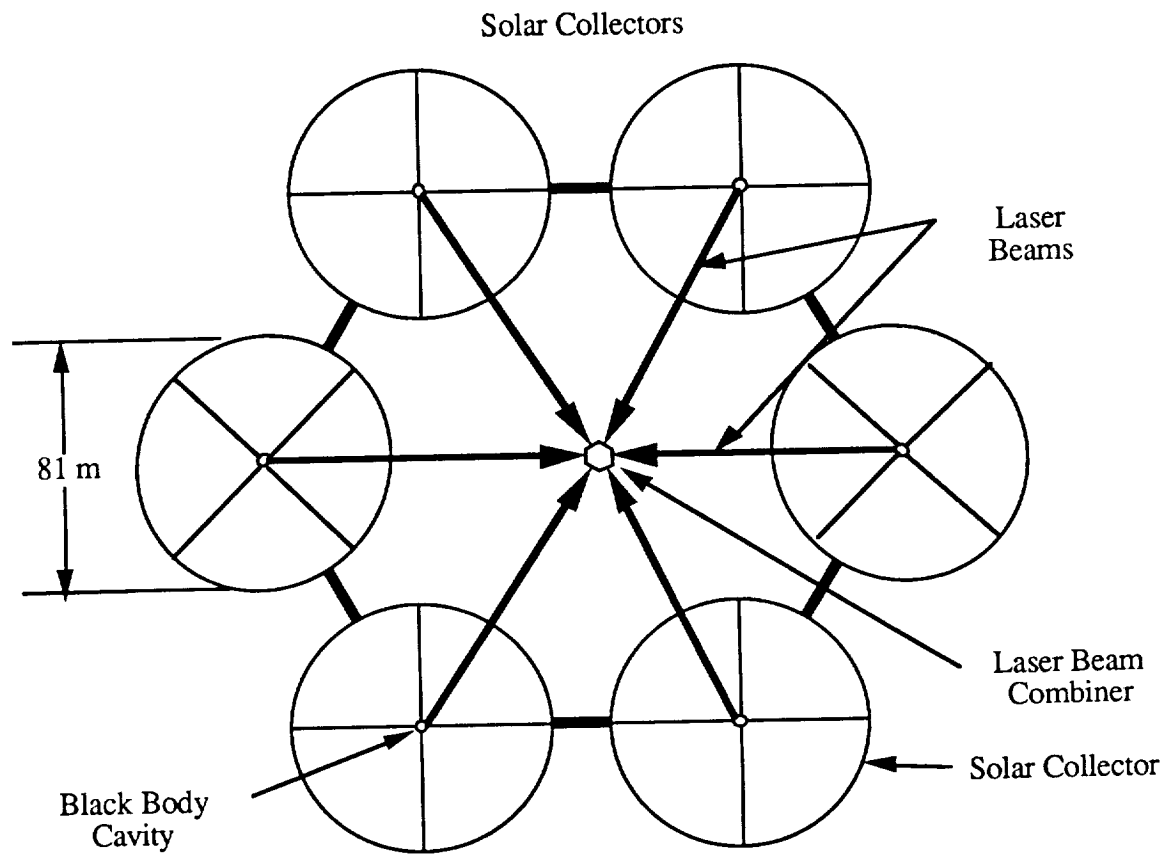
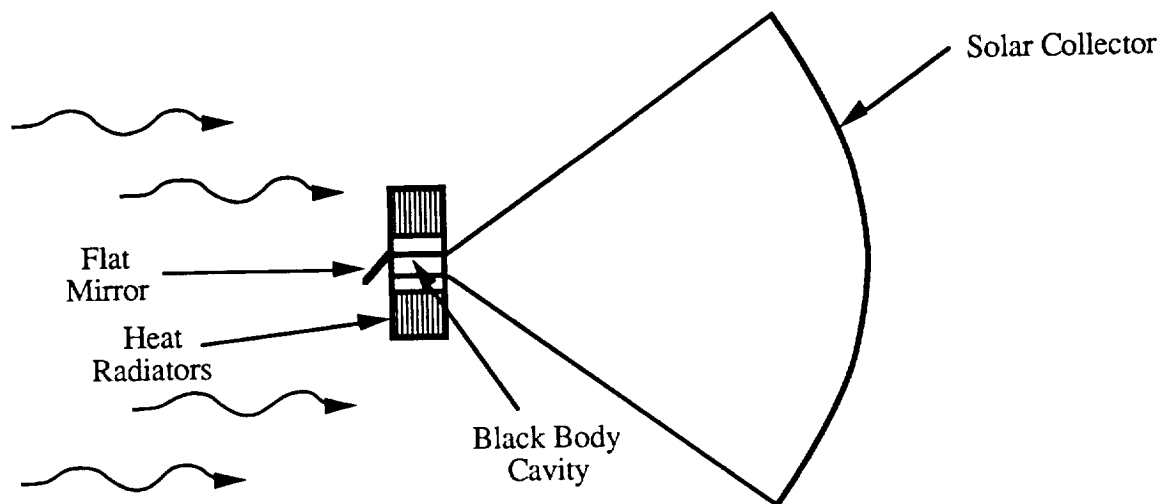


Figure III-10. Schematic of Solar Pumped Laser Propulsion System.



Solar Concentrators As Viewed From Sun



Side View of Solar Concentrator

Figure III-11. Schematics of Solar Collector Configuration.

of 0.5% of the incident energy. The total number of reflections of the laser beam is 16. The resulting loss due to less than ideal reflection is 0.45 MW.

Current research indicates that multi-megawatt CO₂ lasers are technologically feasible [14]. Using the indirect solar pumping method, a CO₂ laser offers an efficiency of 15%, which is significantly higher than that obtainable from direct solar pumping [14]. Indirect solar pumping is also more efficient than converting solar flux to electricity to power a conventional laser.

The proposed 6 MW laser design consists of six insulated blackbody cavities, each lined with 123 laser tubes. Figure III-12 shows the geometry of the blackbody cavities. Each blackbody cavity is cylindrical, with a 2.78 m inside diameter. Each laser tube has a length of 1 m and a diameter of 6 cm. The blackbody cavity material is carbon in order to withstand the 2,000 K equilibrium temperature. This temperature is an effective in terms of cavity efficiency and total laser mass [14]. Approximately 25 cm of carbon felt surrounding the blackbody cavity serve to insulate the cavity and limit the heat losses which would otherwise reduce the efficiency of the laser [14]. Although cesium iodide, CsI, is a good candidate for the laser tube material because it is highly transparent to the radiation in the blackbody cavity, other, stronger materials, such as ZnSe, may have to be used even though they may only be moderately transparent [14].

The lasant must be kept around 300 K to reach threshold in a blackbody cavity at 2,000 K [14]. Accordingly, inside each of the laser tubes is a coolant tube which serves to keep the lasant temperature low enough to lase well. The cooling tubes have a diameter of 2 cm and circulate a coolant through the laser, to a radiator, and back to the laser. The lasant also circulates slowly through the tubes to a radiator to further assist in keeping the CO₂ gas cool. Further analysis into the exact cooling requirements and methods is required.

Since the coolant must be kept below the temperature of the lasant, less than approximately 300 K, a large radiator is required. An advanced concept radiator, such as

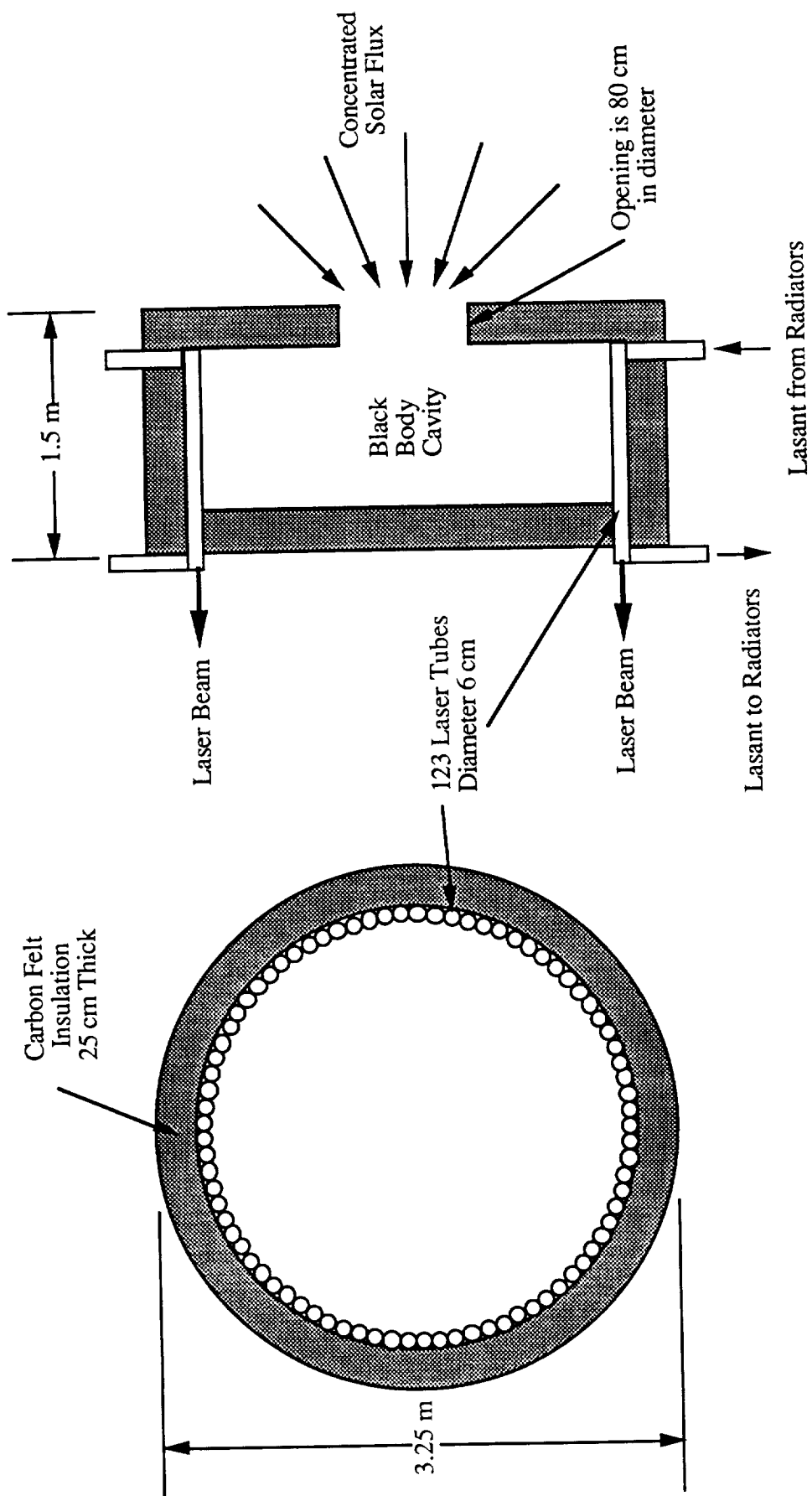


Figure III-12. Black Body Solar Pumped Lasers.

the liquid droplet radiator, could be used to minimize the mass of the system [16]. The liquid droplet radiator is estimated to have a specific radiative power of 1 kW/kg and would weigh 34,000 kg for each of the proposed 6 MW lasers [16].

TRANSMITTER SYSTEM

Combining multi-megawatt laser beams presents a difficult problem. The beams must be combined such that they constructively interfere (i.e., they must all be in phase). If they are out of phase, the combined beam will diffract at the same angle as the individual beams, resulting in excessive diffraction losses. Looking at the combination of the output from all of the laser tubes as the total laser beam yields a near field intensity distribution of six 2.74 m diameter annuli which make up a single 5.73 m annulus. As shown in Fig. III-13, the beams are converged to a concave reflector by an annular reflector. The combined laser beams are directed to laser relay units which redirect the beam to the spacecraft. The beam pattern in the far field remains as a topic for future research.

Laser relay units (LRUs) are necessary components to direct a beam of proper diameter to the spacecraft. By using a Cassegrainian system, the LRUs first diverge the beam and then refocus it to the desired transmittance width. The beam is then directed to the spacecraft.

Each of the reflecting surfaces in the transmitter system is made up of a substrate with a dielectric coating [17]. In the proposed transmitter system, the small reflectors receive a high power flux and require active cooling. The best substrate material is copper because of its high conductivity. Active cooling is performed by running coolant tubes through the substrate. Gold coating the copper increases the reflectivity to 99%. By enhancing the gold with a dielectric coating the reflectivity is as high as 99.4%. Adding the dielectric coating reduces the cooling requirement by 24 kW and subsequently decreases the mass of the liquid droplet type radiator by 24 kg for each of the smaller reflectors in the receiver and transmitter system. If such a mass savings is considered cost effective, the

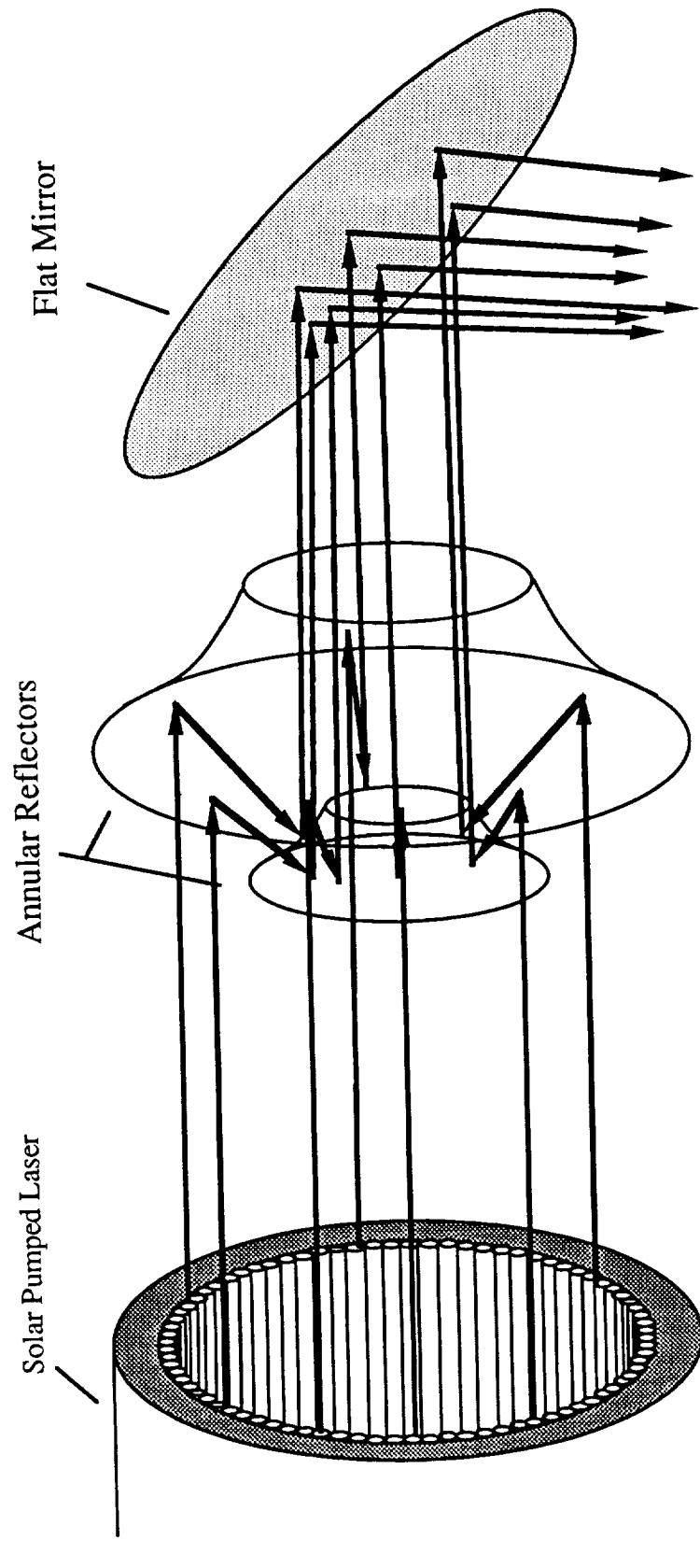


Figure III-13. Annular Reflectors Laser Beam Combiner.

best dielectric coatings for the 10.6 μm wavelength are ThF_4 and ZnSe . These materials are currently used for high power laser systems [17].

BEAM TRANSMISSION

A system of optical relays is needed for transmission of the laser energy in space. A series of laser relay units (LRUs) in orbit around the Earth continuously direct the laser beam to the spacecraft during the thrusting phase of the mission.

The relay system consists of six separate units in a circular, equatorial orbit. The number of LRUs depends on the desired altitude, h_n , and the minimum beam approach altitude to the Earth, Y_n (See Fig. III-14) [18]. Quantitatively, these can be represented as

$$h_n = R_e \left(\frac{\tan 60^\circ}{\tan 60^\circ \cos \theta_n - \sin \theta_n} - 1 \right) \quad (\text{III-12})$$

$$Y_n = R_e (\cos \theta_n - 1) + h_n \cos \theta_n \quad (\text{III-13})$$

where $\theta_n = 360(2n)^{-1}$ is the half-angle between the relays, n is the number of relays in the orbit, and R_e is the radius of the Earth. Although Eq. III-12 is applicable to a space-based laser system, it was derived for a ground-based system and therefore does take into account that transmission of the laser energy through the atmosphere is limited to 60° from the vertical because of atmospheric attenuation.

A minimum beam approach altitude, Y_n , of 250 km must be maintained to prevent excessive atmospheric absorption of the laser energy. Equation III-12 can be solved for the minimum altitude, h_n , the relay units must orbit. However, the simultaneous solution of Eq. III-12 and Eq. III-13 will give orbital radii for various relay systems, each with a different number of relay units [18].

For a system with only one space-based laser system, four relay units at an altitude of 3,000 km, where θ_n is 45° , are sufficient for continuous transmission of the laser

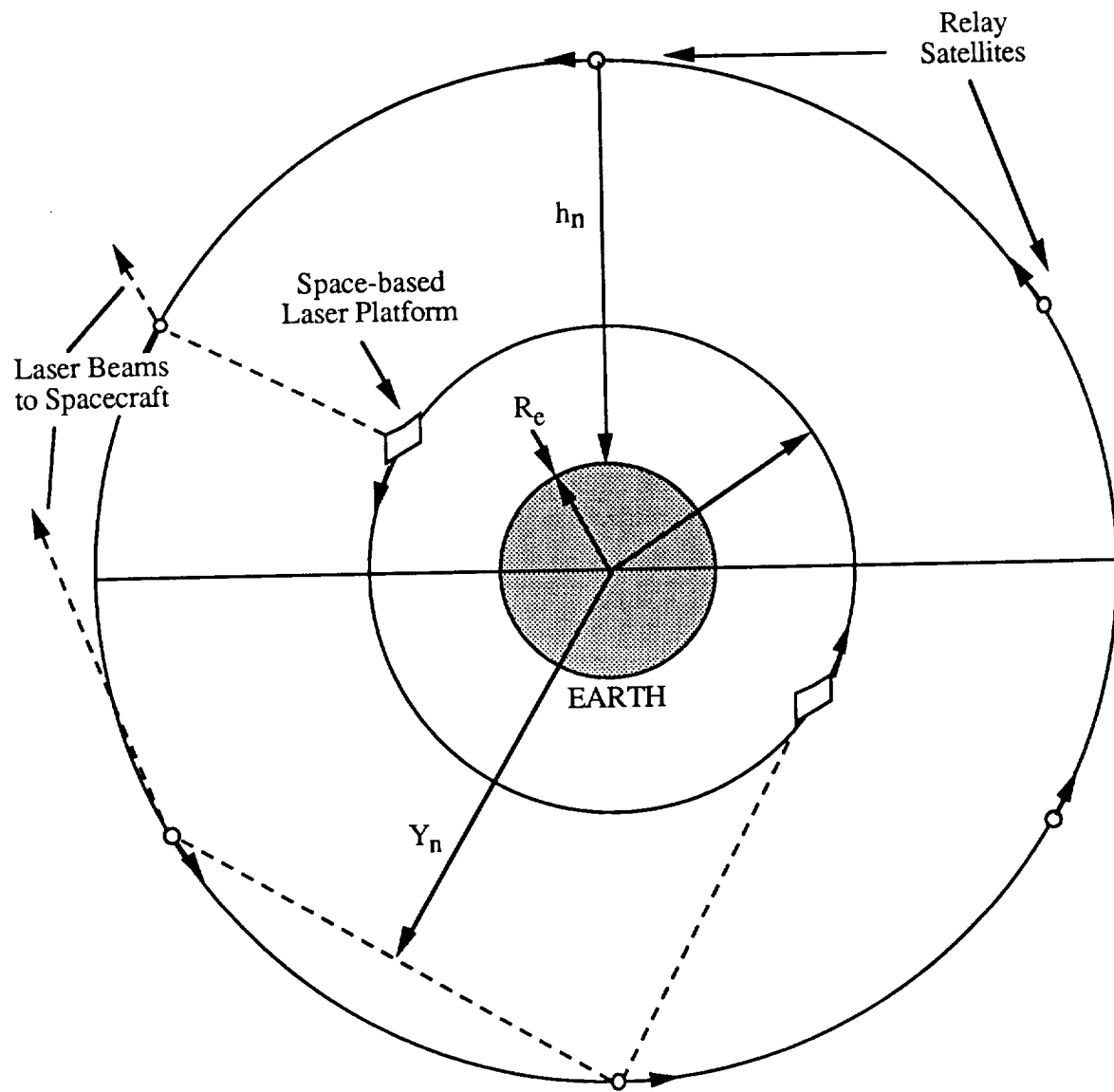


Figure III-14. Space Based Laser Relay System. [18]

energy. However, the proposed laser propulsion technique requires two laser platforms in a 500 km, sun-synchronous, polar orbit. At the 3,000 km altitude, two additional relay units are needed for both of the laser beams to be directed at the spacecraft at all times.

As seen in Fig. III-15, the laser relay unit optics consist of a Cassegrainian system that redirects the beam to the spacecraft. The primary receiver rotates on two axes. The receiver arm can rotate 360° while the receiver itself has a 180° rotation capability on a perpendicular axis. The primary transmitter is capable of similar rotation, although the orientation is different. The unit's structure also contains the electronics and power supply needed in orbit [19]. Studies by Lockheed advocate the use of segmented mirrors for the receiver and transmitter [20]. Inflatable optics should be investigated as a method of reducing the mass of the LRUs.

To minimize the masses of the receivers and transmitters the laser beam is focused such that its beam waist diameter at maximum distance matches the diameter of the receiver. If the diameter of the laser beam exceeds that of the receiver, the collected power drops off rapidly. Figures III-16 and III-17 show that for a given maximum distance, there is a minimum transmitter radius and corresponding receiver radius. The necessary transmitter radius ρ is calculated from

$$\rho^2 = \rho_o^2 \left[1 + \frac{\lambda_1 z}{(2\pi\rho_o^2)^2} \right] \quad (\text{III-14})$$

where ρ_o is the radius of the receiver, λ_1 is the wavelength of the laser, and z is the distance between the transmitter and receiver. For the present design the burnout distance between the LRUs and the spacecraft is 1.5 million km, and therefore, the spacecraft receiver diameter is 101 m, corresponding to an optimum LRU transmitter diameter of 142.3 m.

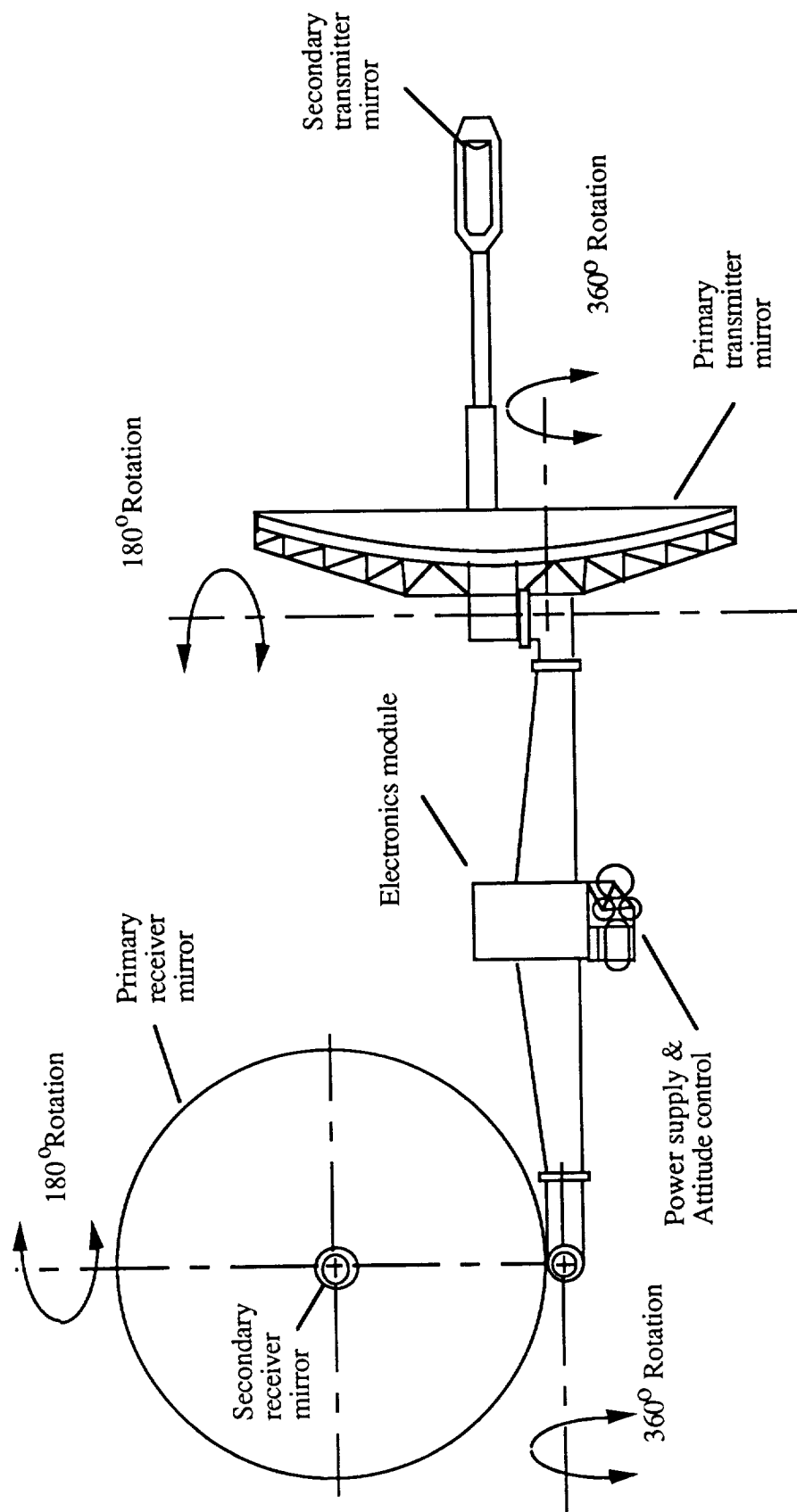


Figure II-15. Laser Relay Unit. [19]

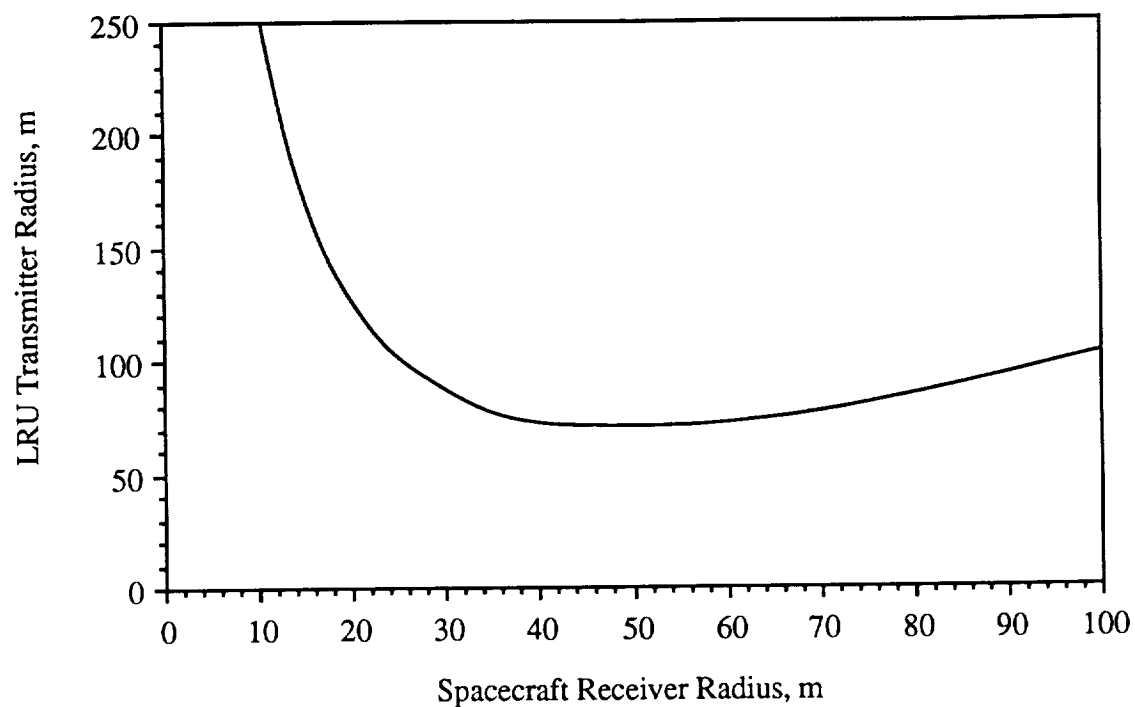


Figure III-16. Optimum Transmitter and Receiver Radii at 1,500,000 km.

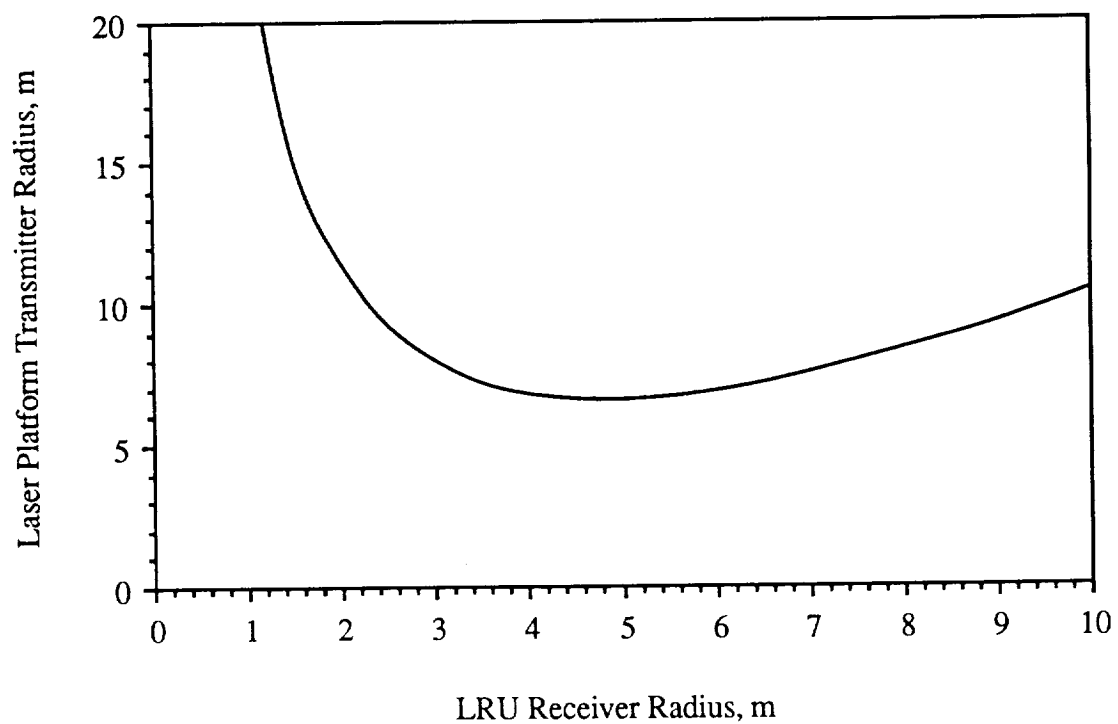


Figure III-17. Optimum Transmitter and Receiver Radii at 13,230 km.

The maximum distance between the laser platform and a LRU is 13,200 km. Figure III-16 shows that the best combination of laser platform transmitter and LRU receiver diameters is 13.3 m and 9 m, respectively.

TRACKING AND POINTING

The ability of the tracking and aiming system to hit its target is a major concern of any beamed energy system. Most research in this area is done by the Department of Defense for application towards the Strategic Defense Initiative. Consequently, most information regarding even peaceful uses of tracking and aiming systems, such as a laser powered spacecraft, is classified and unavailable for use in this report.

The tracking problem includes knowledge of the exact location of the spacecraft, the laser platform, and the laser relay units. The location of the laser platform and laser relay units can be determined through a variety of methods. The TOPEX program, for example, utilizes laser ranging using cube corner reflectors and various Doppler ranging techniques. The most accurate Doppler ranging technique uses the NAVSTAR satellites. For space systems using the NAVSTAR system, location accuracies up to 2 - 3 cm can be achieved [21].

Accurate aiming of the laser necessitates knowledge of the real time locations, in other words, the instantaneous positions, of the laser platform, laser relay units, and the spacecraft. Unfortunately, the accuracy of the laser and Doppler ranging techniques is greatly reduced for systems demanding real time information instead of the Doppler history. Even with onboard data analysis, which avoids the time delay incurred by ground processing, the best accuracy that can be attained instantaneously is approximately 15 m.

Using Doppler ranging from earth to locate the spacecraft would not be feasible due to the feedback time of the system. The signal travel time to the ship, and then back to the laser platform would take several seconds.

The location of the spacecraft could most easily and accurately be determined using a star scanner. A star scanner system uses an onboard computer to compare the location of the sun and stars from video inputs to an internal star catalogue stored in the computer. The error of the incoming beams could then be transmitted to the laser platform, and beam adjustments could then be made for aiming the laser.

The aiming or pointing of the laser is a control problem, relying on powerful computers located on each component in the laser system. Advancements in system modeling and computerized artificial intelligence will determine whether a closed or open loop control system is used. Several inherent difficulties however, are associated with aiming the laser beam.

One major difficulty of the laser propulsion system is the mechanical aiming of the beam over the large distances required. An initial aiming error of five microradians results in a beam displacement of approximately 10 m at a distance of 2 million km. The most accurate aiming that could be hoped for in the near future is on the order of 500 nanoradians [22]. An analysis of this substantial error when compared to the unavoidable beam spreading by diffraction shows the beam spreading to be 5 times smaller than the aiming error.

Errors in an orbiting system are further increased by outside influences on the laser system, including thermal shocks due to day-night cycling, aerodynamic drag force, which is greatly influenced by sun-spot activity, and gravity gradients induced by variations of the Earth's surface height.

These smaller disturbances can be eliminated by placing the system at a libration point, where the Earth's and the Moon's gravity fields will cancel. Placing the laser system in operation at a libration point however, is more expensive than placing the system in a low Earth orbit. Serviceability of the system also becomes increasingly more difficult and expensive when considering anything but a low Earth orbit.

Considering all of these factors leads to the conclusion that, without substantial advances in tracking technology, this system will not be possible within the foreseeable future. At this time, only by greatly decreasing the burnout distance of the ship by adding more thrusters, or using a more powerful laser beam, could the problems of tracking and aiming be overcome. However, as stated previously, the DOD is sponsoring a considerable amount of research in this area, and many answers may already exist.

SPACECRAFT RECEIVER SYSTEM

Anna Cinniger
Amy Prochko

One of the primary constraints on the choice of a receiver onboard the spacecraft is its mass. Three generic types of receivers are considered for this mission. Table III-1 shows the estimated masses for adaptive, rigidized, and inflatable optics; inflatable optics are the most attractive choice. The adaptive optics have the highest possible concentration ratio, but the lower concentration ratios attainable with rigidized and inflatable optics are sufficient to supply the engine with the required laser power [15]. Although the estimated mass of rigidized optics is not completely unreasonable, inflatable optics are the better choice because they are less massive and have been shown to retain a more ideal surface shape [15]. The inflatable optics also allows a micro-meteoroid to pass through the balloon with little damage to the optical performance.

The inflatable optics consist of a balloon supported by a rigidized torus and aluminum wires inset in the reflecting material. The inflation gas, reflecting surface, and the balloon must be lightweight and non-absorbing to infrared radiation. Furthermore, the balloon material must be flexible and resistant to separation. The back surface of the balloon is aluminized for reflection. Upon inflation, the wires that support the collector become stressed beyond their yield point and maintain the desired surface shape even when the collector is deflated. An internal gas pressure of 10^{-5} atm is sufficient to generate the required parabolic shape [15]. With the addition of piping and refill gas, the total mass of each receiver is approximately 8,100 kg.

Table III-1. Specific Mass of Optical Systems

Reflector Type	Specific Mass (kg/m ²)
Adaptive	20 - 100
Rigidized	1 - 2
Inflatable	0.02 - 1.0

The balloon material must be both lightweight and flexible, which suggests a polymeric shell. Unless the shell is very thin, organic materials are generally unsuitable since they will absorb a significant amount of the CO₂ laser energy. The thin shells are also highly susceptible to damage due to micro-meteoroid flux, which ultimately leads to a higher leakage rate of the inflatant. In addition, the carbon-hydrogen covalent bonds, which are relatively weak, tend to decompose when exposed to ultra-violet radiation. However, polyphosphazenes are lightweight polymers that do not experience undesirable tendencies of typical organic materials and should be tested for feasibility [23]. Poly(dichlorophosphazene), which is unusually flexible and elastic, is the most suitable polymer for the proposed inflatable design.

Several gases were considered for the inflation agent, including all noble gases as well as hydrogen. Although Helium is lightweight, leakage and cryogenics problems eliminate it as a viable option. Hydrogen was also eliminated because of leakage problems. Because of the relatively large size of the Argon atom, leakage through the intact balloon material is negligible. Thus, Argon was chosen to inflate the receiver because it has minimal absorption at 10.6 μm ; and, as a noble gas, it does not react with the shell materials. Leakage area due to micrometeorite punctures has been estimated to be 0.001% over 10 years [15]. Neglecting leakage, assuming an internal gas temperature of 200 K,

and assuming a spherical balloon with a 50.5 m radius, approximately 14 kg of Argon is needed to inflate the balloon.

The reflective coating suggested for the reflective side of the balloon is dielectric coated aluminum [15]. The maximum flux at the receiver is less than 0.5 kW/m^2 , which is small enough that active cooling of the receiver is unnecessary.

OPTICAL TRAIN TO THRUSTER WINDOW

The function of the optical train is to direct the beam from the receiver to the thruster window. Figure III-18 illustrates how the Cassegrainian receiver passes the laser beam to the optical train within the receiver support structure. The receiver is able to rotate 360° around the support structure. The mirrors of the optical train are driven by motors to adjust to every movement made by the receiver and continuously deliver the beam to the thruster window. The directing mirror, at the top of the structure, moves with the receiver in order to keep the beam directed down through the center of the structure. At the bottom, the second directing mirror rotates with the engine as it moves around the support structure. This mirror also focuses the beam into the thruster chamber to the necessary spot size to sustain a plasma breakdown within the hydrogen propellant.

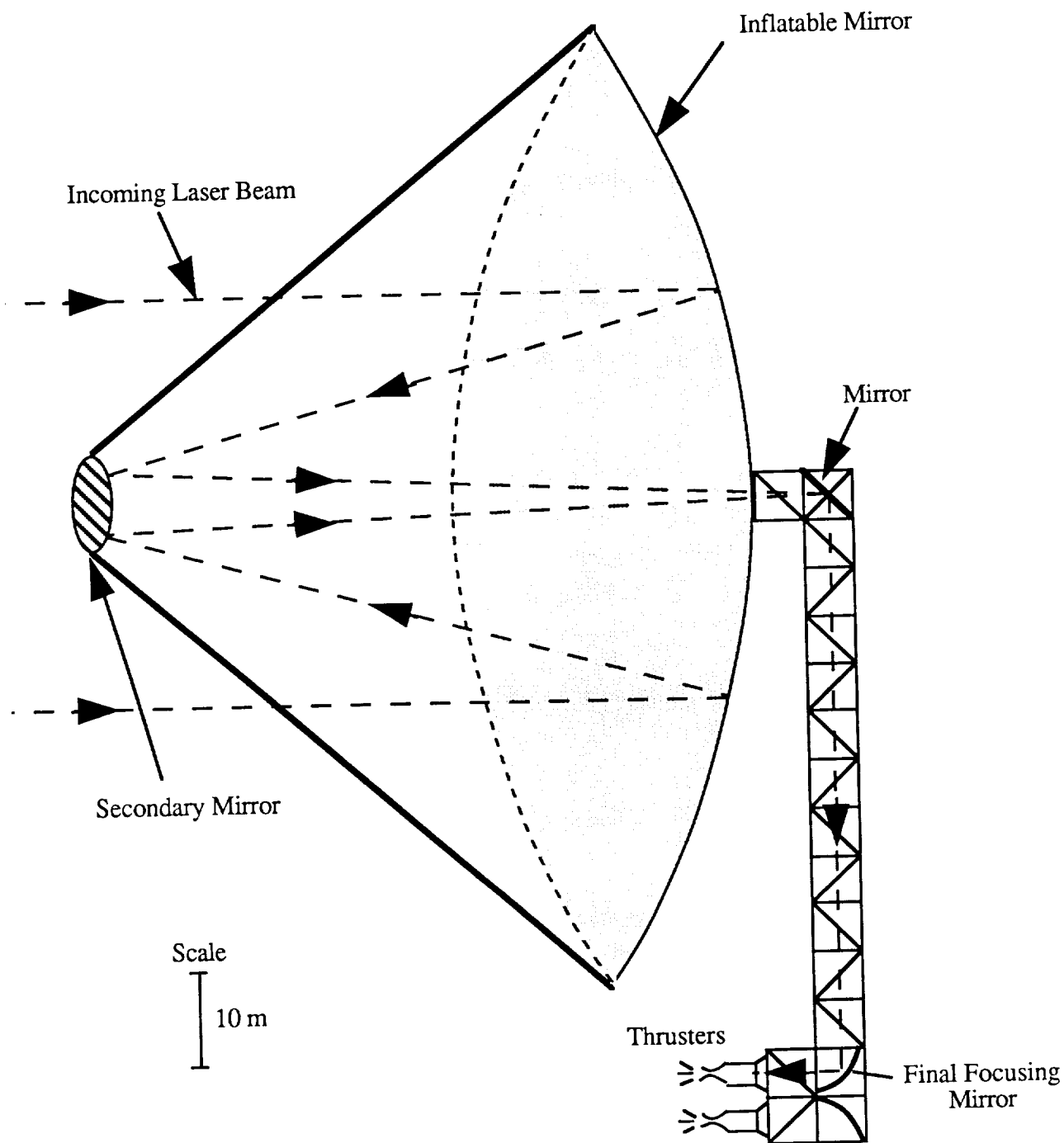


Figure III-18. Optical Train Of The Solar Pumped Laser Spacecraft.

SPACECRAFT DESIGN

Joseph Burianek

When considering the design of the structure for the spacecraft there are many parameters to consider. As with all space structures, it is important to keep both the mass and the cost as low as possible. This spacecraft also has the added design problem that it has to be stiff enough that the laser radiation that is received by the collectors proceeds to the thruster without deviation or loss of optical quality. The structures of the spacecraft also need to be protected from both the atmosphere and any thermal radiation from the sun.

In order to obtain a workable design for the spacecraft all of these considerations were taken into account. As seen in Fig. III-19 the spacecraft consists of four main parts: the payload and aerobrake, the propellant tanks and its surrounding structures, the thruster, with the collectors and their surrounding structure.

The payload and aerobrake are placed on the front of the spacecraft for easy jettisoning. The propellant tanks are clustered in a 20x20x25 m box (made up of individual 5 m boxes) that can accommodate up to 64 tanks (192,000 kg of propellant). Each tank is 4.2 m in diameter and will be carried to LEO on the space shuttle as half shells. The shells will be assembled in space and placed inside individual 5 m boxes. This spacecraft will use 39 tanks, or 117,000 kg of propellant. The propulsion units are placed in such a way that thrust is provided through the center of mass of the spacecraft. Finally, each collector is located at the end of a 100 m truss, which is able to rotate.

TRUSS ELEMENTS

The main truss elements of the proposed design are 5 m hollow rod elements that have an outer diameter of 4.11 cm, and a wall thickness of 2.2 mm. Each element is fabricated of graphite/epoxy (Gr/Ep) with a coating of anodized Aluminum on the inner and

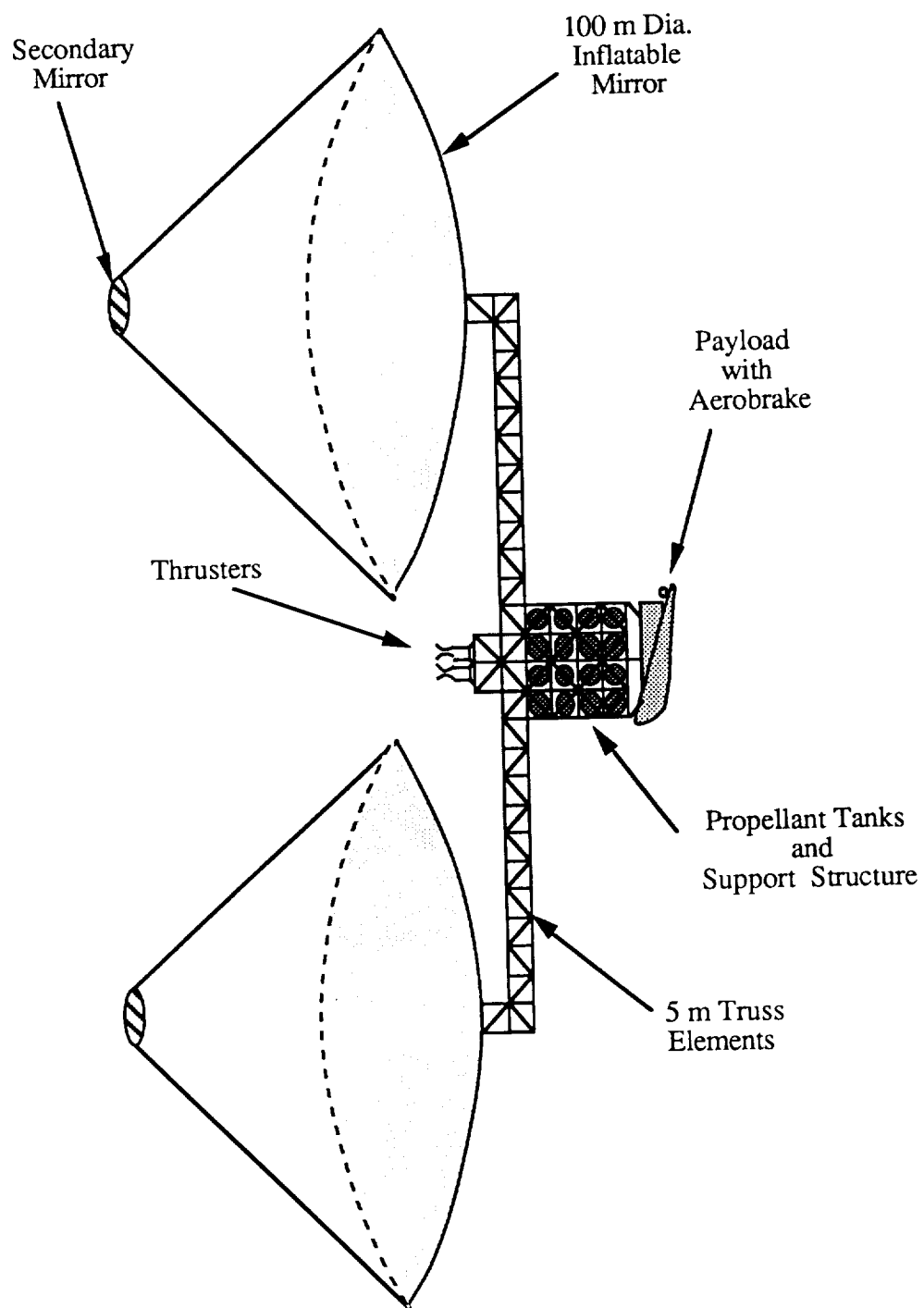


Figure III-19. Solar Pumped Laser Propelled Spacecraft.

outer surfaces. These dimensions and materials were chosen for several reasons: 1) Similarity to the elements that will be used in the space station, 2) compatibility with space shuttle payloads, 3) lower mass than conventional metals, 4) higher stiffness than conventional metals, 5) lower cost through fewer parts than a truss structure with smaller elements, and 6) compatibility to grow in three dimensions when needed.

Since the space station will be built primarily of 5 m elements, the truss elements should be readily available. In fact, a smaller, ten-bay truss structure has already been constructed in space during Mission 61B of the Space Shuttle Atlantis (Nov./Dec. 1985). The experiments were designed to study space construction by astronauts in extravehicular activity (EVA). According to Heard [24], the program's principal director, the experiment was a success and confirmed the feasibility of EVA space assembly. At that time, there were plans to test the feasibility of the full 5 m truss structure, but that has not yet happened.

An additional advantage of using this size element is the advantageous relationship between the largest space shuttle cargo and the element length. The diameter of the space shuttle cargo bay is 4.6 m. Therefore, any payloads transported in the Space Shuttle can fit into the truss bays of this structure (e.g. the propellant tanks).

Furthermore, whenever space flight is considered, the mass of the spacecraft is critical. Mikulas and Bush [25] show that when constructing a similar size structure with struts of equal thickness, structures with longer truss elements have a lower overall mass. They show that for structures of equal length, using elements with the same bar thickness, 3 m elements would have an approximately 20% greater mass than 5 m elements. However, there is an upper limit of strut length which is determined by ease of construction in space and ease of transportation to LEO. For the proposed design that upper limit has been chosen to be 5 m in an effort to make the truss compatible with the space shuttle cargo bay, and have the same size that NASA has baselined for use on the space station truss structure.

It should be noted that pre-packaged deployable structures were considered when deciding which type of structures to use. Deployable structures have a smaller assembly time in space. However, due to the extra space required to store the subsystems used in deploying the structures, the individual elements must be shorter. The reduced assembly time was not deemed to make up for the disadvantages of smaller elements.

The proposed spacecraft design has some needs similar to that of the space station, which further illustrates the advantage of using similar truss elements. Due to the optical integrity needed to keep the laser beam pointed in the correct direction, the structure must provide a stable (i.e. stiff) structure. Mikulas and Bush found that for a 3 m truss to have similar stiffness characteristics, it would have to weigh two to three times as much as the 5 m truss [25]. Thus, using smaller elements would cause a substantial weight penalty or compromise needed stiffness, which cannot be tolerated.

Since similar truss elements to that of the space station are proposed, it is practical to use similar node attachments. This requires the use of nodes that include the possibility of 26 strut attachments (a picture of these struts appears in the referenced paper by Mickulas and Bush). It is possible to attach struts in each of the three principal directions (6 nodes), each of the 45° angle possibilities (12 nodes) and 8 other nodal locations. This allows for growth in many possible directions. Each node has been designed to be able to attach to its corresponding strut quickly and easily. The main reason to use these quick attachment joints is to minimize EVA time. In fact, when possible, these could be bolted in place before leaving earth, to further minimize EVA time. It should be noted that such nodes have been used for many years in the construction of ground structures and there is a large database of information relative to use in space.

Materials

Materials used for space structures need to be very light weight, have low mass-to-strength and mass-to-stiffness ratios, and be resistant to radiation. Several materials which offer these advantageous characteristics have been considered. The materials include the

broad categories of graphite/epoxy composites (Gr/Ep), metal matrix composites, and carbon-carbon composites.

Of these materials, metal matrix and carbon-carbon composites demonstrate the best combined stiffness and thermal resistance. However, these also have numerous disadvantages. First of all, the metal matrix composites have a poor response to thermal cycling and experience large hysteresis and residual dimension changes during this cycling. There is work being done to eliminate this through postfabrication of the metal matrix, but this is still under development [26]. Another drawback to these two types of composites is cost. Both the metal matrix and carbon-carbon composites are expensive and the large added cost to use them may not be worth the advantages gained. Finally, the fact that metal matrix and carbon-carbon composites are relatively new makes them less common, less available and less reliable. For simplicity it is better to stick with a reliable, well known material.

Graphite/epoxy (Gr/Ep) also exhibits low mass-to-stiffness characteristics (although not as good as some metal matrix and carbon-carbon composites). Also, the Gr/Ep material exhibits better thermal cycling properties [27]. Because the Gr/Ep has favorable characteristics, is relatively inexpensive, and has a history of frequent application, it is the material chosen for the majority of the structure. In areas where extremely high temperatures may be encountered, the metal matrix or carbon-carbon material should be considered for use, due to their lower thermal conductivity.

Tube Coatings

Due to the fact that the spacecraft may spend much of its time in LEO and that it requires high stiffness and stability with little or no degradation, many environmental aspects must be considered. The main problems to be considered are atomic oxygen exposure, thermal cycling, charged particle radiation, ultraviolet radiation, micrometeorites, and space debris. Many of these problems may cause a degradation in the unprotected graphite/epoxy composite. Therefore a protective coating or wrap must be employed to

resist this degradation. The requirements of this coating include resistance to the above problems, adhesion to graphite/epoxy, abrasion resistance, and coating uniformity.

In a study conducted by Dursch and Hendricks [28], four types of coatings were considered: anodized Al foil, sputtered $\text{SiO}_2/\text{Al}/\text{Al}$ foil, bare Al foil and electroplated Ni with and without a SiO_x coating. Coatings were applied to 2 in diameter tubes made of P75S/934 Gr/Ep with a longitudinal tensile modulus of 45 Msi. The targeted optical values of the coatings were set at a solar absorbance of 0.2 to 0.35 and a thermal emittance of 0.15 to 0.25. This low absorbance reduces the maximum temperature reached by the tube when exposed to direct radiation and the low emittance reduces the temperature extremes experienced in deep space. The overall effect is to reduce the thermal cycling temperatures to which the composite tubes are exposed, thereby increasing stability of the structure. The Al foil used during testing was .005 cm thick 114-H19, which is the lightest weight foil which can be consistently wrapped onto the 2 in dia. tubes without tearing or forming pinholes from handling.

Dursch and Hendricks looked at four major areas: thermal cycling, atomic oxygen exposure, adhesion, and abrasion resistance. Originally, 50 thermal cycles of 350 K to 355 K were conducted, but with no changes in any of the coated tubes, 500 cycles of 322 K to 339 K were applied. After examination, no microcracking or other adverse effects were found on any of the tubes that were coated. After exposure to atomic oxygen, the electroplated Ni exhibited total adhesion loss to the Gr/Ep composite. Also, any non-protected material experienced deterioration. Because the Al is inert to the atomic oxygen, the foils experienced no deterioration and there was no evidence of adverse affects on the protected composite. Furthermore, when a pinhole was made in the Al foil, the diameter of the hole remained constant and therefore significantly reduced the total amount of atomic flux which the composite received.

When testing adhesion, it was found that unanodized Al foil could be peeled off rather easily, yet the peel strength for anodized Al foil was greater than the foil's tensile

strength. Also, there was no effect on the peel strengths due to thermal cycling. Finally, in testing abrasion resistance, which will be encountered when transporting and handling the tubes, there was no change in the Al foiled tubes, but the tubes covered with $\text{SiO}_2/\text{Al}/\text{Al}$ became darkened along the line of contact. In the end, it was decided that a chromic acid anodized Al foil would be the optimum type of protection for the composite.

The proposed spacecraft design will use 0.1 mm anodized Al foil to protect the graphite epoxy truss elements. In summary, the reasons this coating was determined to be the optimum include: its environmental durability in LEO, including retention of foil-to-graphite/epoxy bond strength, retention of optical properties during LEO exposure, excellent adhesion to graphite/epoxy, ease of manufacture, low cost, and its excellent handling properties.

Thermal Protection

The structure (or other parts of the spacecraft) may be exposed to high thermal fluxes from the excess thermal energy radiated by the thruster. In order to protect the structure from these fluxes, a multilayer insulation is applied to all necessary members. This insulation generally consists of very thin (approximately 3 μm) polymeric film with a metallic, low emissivity coating. Insulating separators are used to space each layer. The mass density for one layer is approximately 13 g/m^2 . Therefore, the total mass, M_i , of the multilayer insulation is

$$M_i = 0.26 I \frac{\epsilon}{q} \quad (\text{III-15})$$

where q is the heat flux allowed at the composite surface, I is the intensity of the incident radiation, ϵ the emissivity and the number of layers is assumed large. If gold is used as the metallic coating, an emissivity of .03 can be achieved.

By knowing the allowable flux at any surface, the number of insulation layers, n_i can be determined:

$$n_i = 2 I \frac{\epsilon}{q} - 1 \quad (\text{III-16})$$

Thus, the appropriate amount of insulation on any surface is found by simply setting a maximum allowable heat flux on that surface. The insulation layers are reduced by the fact that the struts are coated with Al foil which helps maintain the temperature range on the Gr/Ep.

MASS INVENTORY

A breakdown of the masses of the main components or subsystems of the spacecraft is shown in Table III-2. The overall mass of the spacecraft is 204,900 kg. Thus with the payload mass being 50,000 kg, the payload mass fraction is 24%.

Table III-2: Mass Inventory

Component	Mass (kg)
Propellant Mass for the following maneuvers:	
Transfer to Mars	99,000
Spacecraft Return to Earth	18,000
Propellant Tanks (39 @ 200 kg)	7,800
Receivers & Receiver Truss Arms (2 @ 8,100 kg)	16,200
Additional Truss Structure	1,200
Aerobrake Structure	62,600
Thruster Systems (2 @ 35 kg)	70
Total Mass of Spacecraft	204,870

ORBITAL MECHANICS

Terri Schmitt

In the analysis of the orbital mechanics, all phases of the flight to Mars were examined. The flight was segmented into (1) the spiral out of Low Earth Orbit; (2) the transfer to Mars; (3) payload jettison; and (4) the return spiral into Low Earth Orbit.

SIMPLIFYING ASSUMPTIONS

The orbital planes of Mars and Earth lie at approximately 1.8 degrees to each other, and the eccentricities are 0.017 and 0.093, respectively [29]. This eliminates the need to consider out of plane orbit changes, and the complexity of elliptical planetary orbits. Second, the rotational period of the Earth is assumed to be constant, so that the planet returns to the same location every year. The problem of recapture then becomes much simpler. Even though these assumptions appear significant, they actually introduce little error into the calculations.

ESCAPE FROM LOW EARTH ORBIT

Due to the low acceleration inherent in the continuous wave laser propulsion method, the process of escaping Low Earth Orbit (LEO) requires the use of a constant thrust spiral. For this mission, LEO is defined to be 500 km above the surface of the Earth. In this maneuver, enlargement of the spiral radius increases the potential energy of the spacecraft. Although the spacecraft is thrusting continuously, the velocity decreases as the orbit radius increases. The rate at which the potential energy increases exceeds the reduction rate of the kinetic energy, thus resulting in a net increase in the energy of the system.

To ease the difficulties associated with orbital mechanics, only the two-body problem is considered. The two-body problem consists of one central mass (i.e. a planet

or the Sun) and an orbiting spaceship. Thus, gravitational attraction exists only between the two bodies and all other external forces are ignored.

Only the gravitational force and the thrust provided to the spacecraft influence the equations of motion [30,31]. These are

$$\ddot{r} = \frac{F \dot{r}}{\left(M_t \left(\dot{r}^2 + r^2 \dot{\phi}^2\right)^{0.5}\right)} - \frac{g_0 R_e^2}{r^2} + r \dot{\phi}^2 \quad (\text{III-17})$$

$$\ddot{\phi} = \frac{F \dot{\phi}}{\left(M_t \left(\dot{r}^2 + r^2 \dot{\phi}^2\right)^{0.5}\right)} - \frac{2 \dot{r} \dot{\phi}}{r} \quad (\text{III-18})$$

where r is the spiral radius, R_e is the radius of the Earth, g_0 is the gravitational acceleration at planet surface ϕ is the angle from an arbitrary reference line (in radians), M_t is the mass of the spacecraft at time t , and F is the thrust. The equations must satisfy four basic assumptions [30]:

- (1) The mass of the ship is not constant, but decreases linearly with time due to propellant consumption.
- (2) Only one central gravity field is considered at any one time (the two-body problem).
- (3) All orbital maneuvers are coplanar.
- (4) No other external forces besides gravity and thrust are present.

Direct integration of the equations of motion yields a spiral trajectory with increasing radius (See Fig. III-20). These equations are subjected to the following initial conditions:

$$r(0) = r_0 \quad (III-19)$$

$$\dot{r}(0) = 0$$

$$M(0) = M_0$$

$$\phi(0) = 0$$

$$\dot{\phi}(0) = \sqrt{(\mu_e/r_0^3)}$$

where r_0 is the initial altitude, M_0 is the initial mass of the ship, and μ_e is the gravitational parameter of the Earth ($3.9806 \times 10^5 \text{ km}^3/\text{s}^2$)

A fourth order Runge-Kutta integration program (See Appendix D) was employed to integrate these equations to determine the spiral needed to escape the Earth's gravitational field. By use of this program, the propellant mass is optimized by iteration. The required spiral time as well as the propellant mass depends upon the transfer orbit needed to complete the mission.

TRANSFER TO MARS

Once the required velocity is attained, the spacecraft enters a heliocentric transfer orbit to Mars. The mission can be accomplished with many different transfer orbits. The limiting factor is the ability to obtain the needed velocity increment (ΔV) for such missions. Larger increments require greater propellant consumption, which increases the spacecraft's mass. Several transfer orbits were considered: Hohmann transfer, a two-year time of flight fly-by orbit, quasi-impulsive method of jettisoning the payload into the transfer orbit, and gravitational assist fly-bys of Venus.

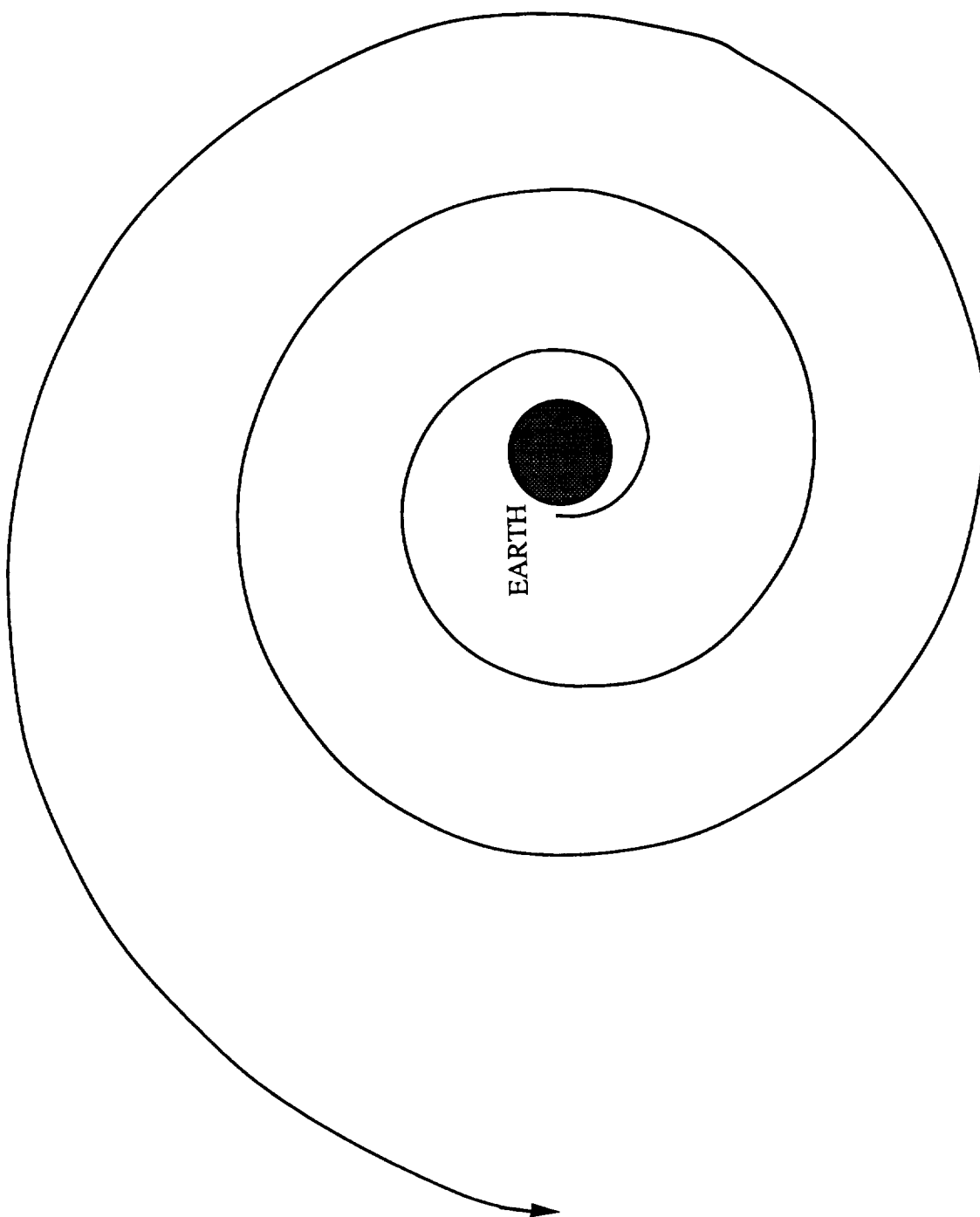


Figure III-20. Spiral Trajectory to Escape from Earth's Sphere of Influence.

Hohmann Transfer

As the lowest energy transfer, the Hohmann transfer is the easiest to achieve from a power perspective. After the spacecraft attains Earth escape velocity, an additional 259 days are required to reach Mars, at which time, the spacecraft passes Mars at the aphelion of the orbit (See Fig. III-21). Recovery of the spacecraft at the Earth is a problem of intercepting two orbital arcs in both space and time. In order to avoid this situation, a waiting period in a Mars parking orbit is necessary. However, it is not possible to power the spacecraft at Mars from the laser system in LEO. Consequently, for the spacecraft to be recaptured at the Earth for future reuse, the Hohmann transfer is not a viable option.

Two-Year Elliptical Transfer Orbit

In order to simplify the recapture procedure, an elliptical orbit extending beyond the orbit of Mars (See Fig. III-22) was considered. Due to the rotation period of the Earth, an ellipse with an integer-year ($n > 1$) round-trip time of flight (TOF) will result in a successful recapture maneuver. The most reasonable transfer orbit requires two years to complete. For this orbit, the aphelion extends 325 million km from the sun and is characterized by an eccentricity of 0.37.

In order to enter this orbit, a ΔV of 5.08 km/s must be obtained. The spacecraft spirals from LEO and enters the transfer orbit at a radius of 1.74 million km in 15.6 days. Although this radius is greater than the limits of the earth's sphere of influence (approximately 10^6 km), the equations of motion (Eq. III-16 and Eq. III-17) are not modified to account for the sun's influence on the spacecraft. It is assumed that the earth is the only gravitational influence on the spacecraft until it enters into the transfer orbit.

The spacecraft travels along this transfer orbit and passes Mars on the outbound leg of the journey 143 days after launch. At this point, the payload is jettisoned in order to avoid the mother-craft entering into Mars' sphere of influence. Entering the sphere of

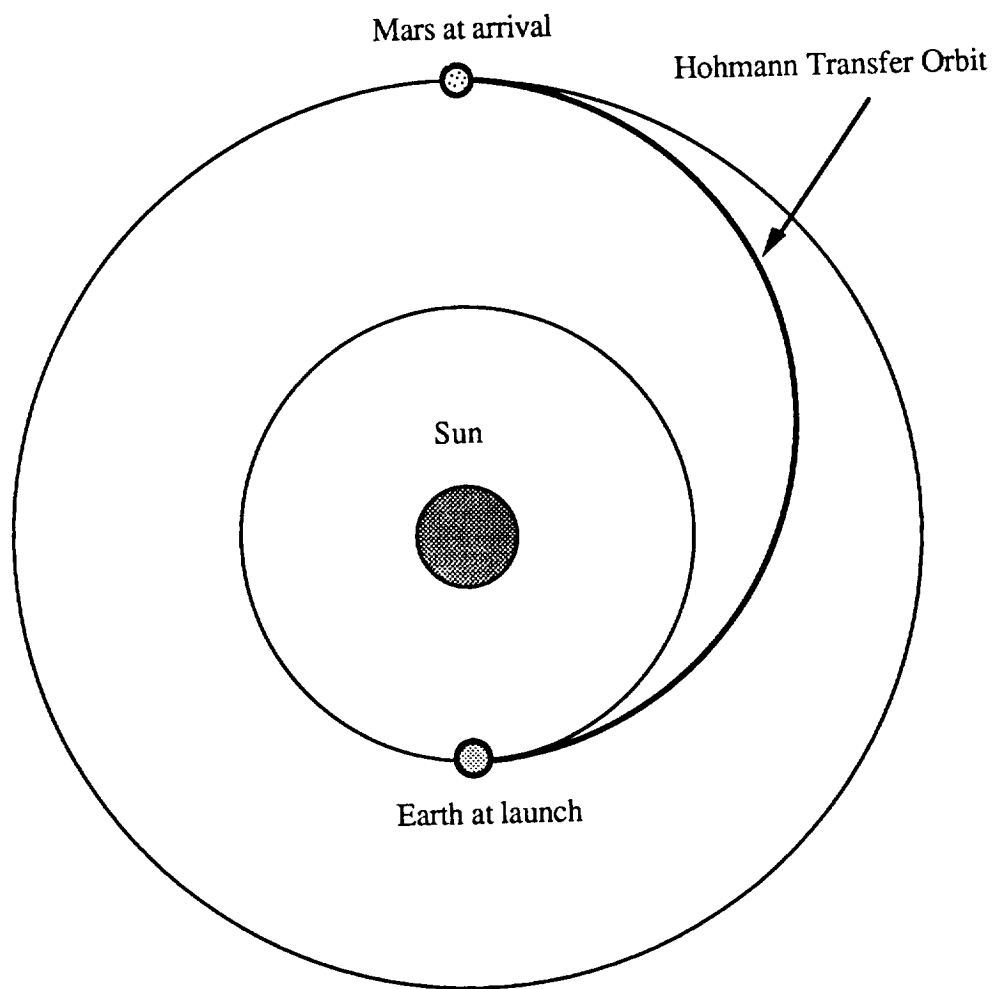


Figure III-21. Hohmann Transfer Orbit to Mars.

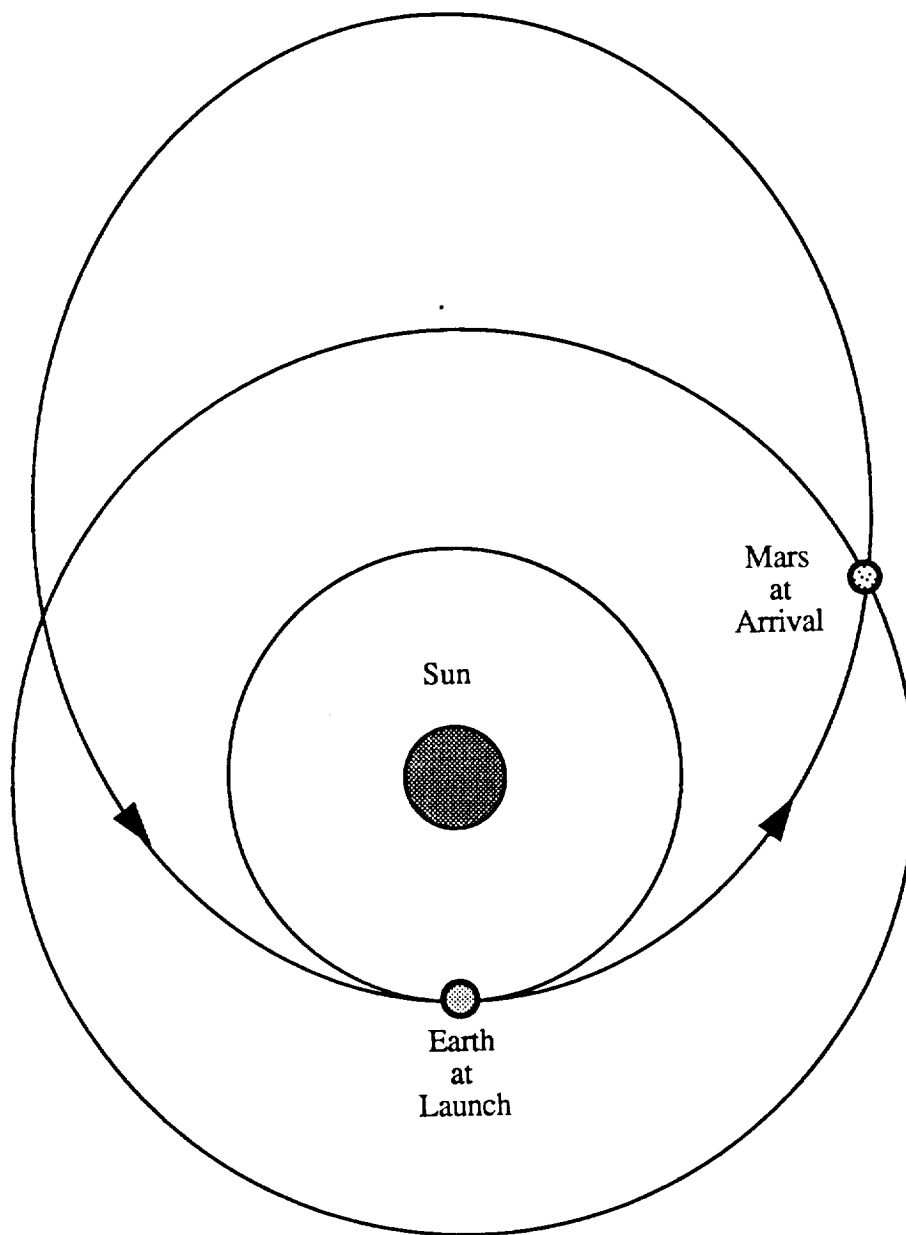


Figure III-22. Elliptical Transfer Orbit To Mars.

influence would require a powered maneuver, which is not possible for the laser system. The mother-craft returns to the earth on the elliptical trajectory. As the spacecraft nears Earth, the thrusters onboard the craft are re-enabled for the spiral back into LEO, where the spacecraft will reside until it is reused.

Quasi-Impulsive Method

A third option was considered in which the payload is jettisoned into the transfer orbit without the mother-craft leaving the earth's gravitational field. This quasi-impulsive method requires the spacecraft to thrust for a short duration at the perigee of a series of elliptical orbits. Detailed analysis of this maneuver is presented in Section II of this report.

The short thrusting cycles require less propellant to complete the mission, which contributes to the lower initial spacecraft mass of approximately 88,000 kg. An actual design of the spacecraft could not be completed in time, so the dry mass of the craft was estimated as 10,000 kg. Since the spacecraft attains a velocity 0.75 km/s below the required velocity for a Hohmann transfer, chemical propellants are needed to jettison the payload assembly into the transfer orbit to Mars. After the payload is jettisoned, the spacecraft returns to LEO to await reuse.

The maximum perigee radius for this orbit, which is attained in approximately 60.5 days, does not exceed 8,500 km. This burn distance determines the size of the laser system's optical components. The transmitter at the laser platform retains its 13.3 m diameter. Similarly, the 9 m diameter of the LRU receiver remains constant. The LRU transmitter and the spacecraft's receiver are 10.7 m and 7.6 m, respectively.

Detailed analysis of this quasi-impulsive method has yet to be completed. Further investigation is necessary in many areas, such as degradation to the thrusters and changes in the laser system, before this method is implemented. However, this method offers versatility by using the spacecraft as an orbital transfer vehicle (OTV).

Planetary Fly-bys

Gravitational assists from neighboring planets are commonly used in unmanned, interplanetary exploration missions. However, this method requires powered maneuvers far from the earth. The laser system stationed in LEO does not have the capability of transmitting the laser energy to the required distances. For this reason, planetary fly-bys are not possible for the laser propelled spacecraft.

Launch Windows

Interplanetary travel is determined by the launch windows. The alignment of the Earth and the target planet occurs at regular intervals. In the Earth-Mars system, the synodic period is 2.13 years [29]. This is the time for any given angle between the two planets to repeat itself, and thus missions to Mars may only occur at intervals of this period.

PAYLOAD JETTISON

Only the two-year elliptical transfer is suitable for the laser spacecraft. As the spacecraft passes Mars on the outbound leg of the transfer orbit, the cargo is jettisoned while the spacecraft is outside Mars' sphere of influence. The payload performs a chemical burn to bring it into Mars' atmosphere, where it performs an aerobraking maneuver to enter into a Mars parking orbit. Details of the aerobraking scheme are presented in Appendix A. The aerobraking system and the payload have a combined mass of 62,660 kg, which includes the needed propulsion mechanism to place the payload into a Mars parking orbit.

RECAPTURE AND RETURN SPIRAL INTO LEO

Recapture and reuse of the spacecraft are major mission considerations which determine the choice of the transfer orbit. As the returning spacecraft approaches the earth, the continuous wave laser thrusters are re-activated for the inbound spiral maneuver to enter into LEO. This spiral is very similar to the outbound spiral used to enter the transfer orbit.

The inbound spiral requires only 2.61 days to complete because the mass of the returning spacecraft is significantly less than when outbound. Once the spacecraft is back in LEO, it is refueled and refitted with new cargo. The use of a two-year elliptical transfer allows the spacecraft to begin its mission with a minimal amount of waiting. A total flight time of 748.2 days, which includes the outbound and inbound spiral time, is necessary to complete the mission.

CONCLUSION

Melanie Miller
Terri Schmitt

The Solar Pumped Laser (SPL) propelled spacecraft indirectly uses solar flux as its primary energy source. The incident flux is converted into two 6 MW CO₂ laser beams by means of indirect solar pumping. Through a transmission system, including six orbiting laser relay units and two laser platforms, the laser beams are directed to inflatable receivers onboard the spacecraft. The beams are then redirected, via an optical train, into two continuous wave (CW) laser thrusters. Within the absorption chamber of each thruster, the incident laser energy is absorbed by a hydrogen plasma which then transfers heat to the surrounding hydrogen propellant flow. Each CW thruster is capable of producing 600 N of thrust with a specific impulse of 1,260 s.

The initial spacecraft mass of 204,900 kg includes the 117,000 kg of hydrogen propellant needed to complete the orbital maneuvers necessary for the spacecraft's mission to Mars. Since the spacecraft is designed to transport 50,000 kg of payload, the payload mass fraction of the SPL powered spacecraft is 24%.

The SPL system has many difficulties inherent in the design. For example, the current design assumes that by the time it would be implemented, the combination of six 1 MW beams in phase to produce the desired 6 MW laser would be feasible. Transmission of the high powered beam over great distances also poses a significant obstacle. With current technology, it is possible to accurately track the beam for only one-seventh of the required burnout distance. Without accurate tracking, there will be a risk that the spacecraft may not receive the laser energy. The CW thruster design is mainly in the theoretical stages and actual testing of the design using hydrogen propellant has not yet been performed. Because of the high temperatures associated with laser energy absorption, current material limitations are also an important issue.

The current research indicates that the system may not be practical. This study has assumed that the necessary laser platforms and relay units will be placed in orbit and available for use. The cost associated with the engineering, manufacturing, launching to orbit, and assembling of such a laser systems has not been estimated; however, it is likely that the cost will be so high as to render the system impractical in the foreseeable future.

Preliminary research has indicated that the SPL propelled spacecraft may be redesigned as an orbital transfer vehicle (OTV). One of the salient difficulties, tracking the spacecraft over long distances for transmission of the laser beam, would be minimized if the vehicle were only required to transport payload within the Earth's sphere of influence. An OTV requires a lower propellant mass, and thus, results in an increased payload mass fraction. Further research into the application of laser propulsion for orbital transfer vehicles may increase the feasibility of the concept of a laser powered spacecraft.

NOMENCLATURE

A	nozzle throat area
C_p	specific heat at constant pressure
CW	Continuous Wave
D	diameter
EVA	extravehicular activity
F	thrust
g_0	gravitational acceleration
Gr/Ep	Graphite/Epoxy
h	enthalpy
h_n	altitude of LRUs
I	intensity of incident radiation
I_{ab}	energy absorbed
I_{sp}	specific impulse
I_t	transmitted radiation intensity
I_o	incident laser radiation intensity
K	empirically derived constant
LEO	Low Earth Orbit
LRU	Laser Relay Unit
\dot{m}	mass flow rate
M_i	total mass of insulation
M_o	initial mass of the spacecraft
M_t	mass at time t
n	number of LRUs
n_i	number of insulation layers
p	pressure differential

P_o	chamber pressure
P	incident laser power
P_j	jet power
P_{loss}	power losses
q	heat flux allowed at composite surface
r	spiral radius
r_o	initial altitude
r_v	radius of chamber
R	gas constant
R_e	radius of the Earth
RP	Repetitively Pulsed
S.F.	factor of safety
t	window thickness
T_o	chamber temperature
TOF	time of flight
tw	chamber wall thickness
u	velocity
Y	yield strength
Y_n	minimum beam approach altitude
z	distance between transmitter and receiver
α	absorption coefficient
α_1	percent dissociation
ϵ	emissivity
ϕ	angle from reference line (rad)
γ	ratio of specific heats
λ	wavelength of the laser

μ	gravitational parameter of the Earth
η	efficiency
θ_n	half-angle between LRUs
ρ	transmitter radius
ρ_o	receiver radius
σ	hoop stress

Subscripts

c	chamber
e	exhaust

A dot above a variable ($\dot{}$) indicates a time derivative. Successive dots indicate successive time derivatives.

All values are in MKS units.

REFERENCES

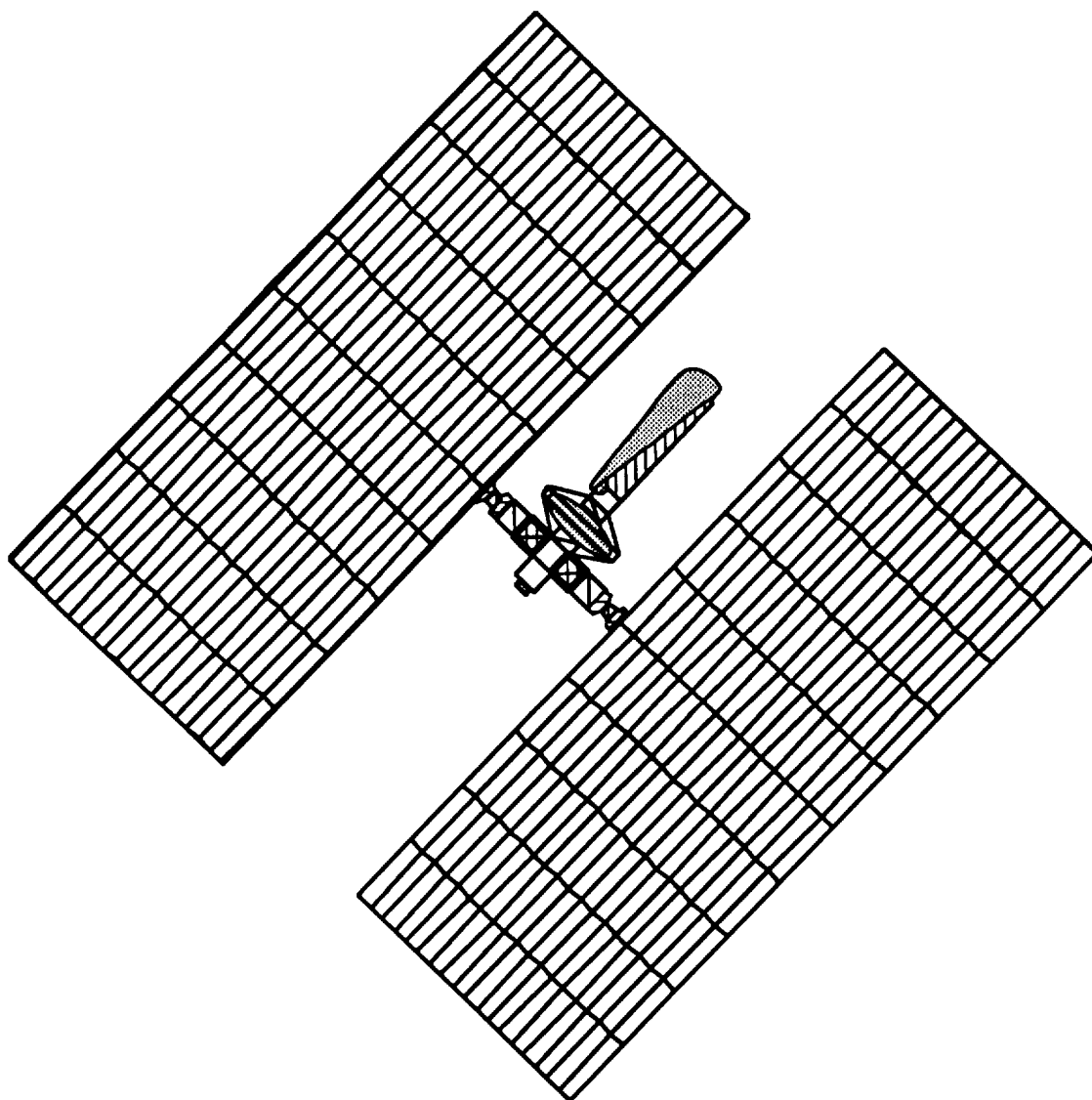
1. Kantrowitz, A., "Propulsion to Orbit By Ground-Based Lasers", Astronautics and Aeronautics, Vol. 10, pp. 74-76, May, 1972.
2. Jones, L. W. and D. R. Keefer, "NASA's Laser-Propulsion Project", Astronautics and Aeronautics, Vol. 20, pp. 66-73, 1982.
3. SDIO/DARPA, Volume 1--Executive Summary, Workshop on Laser Propulsion Proceedings, Lawrence Livermore National Laboratory, July, 1986.
4. Huberman, M. et al., "Investigation of Beamed Energy Concepts for Propulsion", Vol. I and II, AFRPL-TR-76-66, Oct., 1976.
5. Glumb, R. J. and H. Krier, "Concepts and Status of Laser-Supported Rocket Propulsion", Astronautics and Aeronautics, Vol. 21, pp. 70-79, Aug., 1983.
6. Eskridge, R. H. et al., "An Experimental Study of Laser Supported Plasmas for Laser Propulsion", NASA TM-86583, Marshall Space Flight Center, Jan., 1987.
7. Deak, A., Rocket Research, Redmond, WA., Private Communication, May, 1989.
8. Keefer, D. R. and H. Crowder, "A Two-Dimensional Model of the Hydrogen Plasma for a Laser Powered Rocket", AIAA Paper No. 82-0404, Jan., 1982.
9. The Harshaw Chemical Company, "High Power Laser Optics", TP-120478, 1989.

10. Nestor, O. H. et al., "Large Diameter Polytran NaCl Windows for CO₂ Lasers", The Harshaw Chemical Company, Solon, Ohio, TP-0403772M, 1989.
11. Conrad, R. W. et al., "Laser-supported Combustion Wave Ignition in Hydrogen", Army Missile Command, TR-RH-80-1, 1980.
12. Moody, D. C., "Maintenance of a Gas Breakdown in Argon Using 10.6 Radiation", Journal of Applied Physics, Vol. 46, No. 6, June, 1975.
13. Brooks, R., University of Washington, Aerospace and Energetics Research Laboratory, Private Communication, March, 1989.
14. Taussig, R., et al, "Solar-Pumped Lasers for Space Power Transmission", AIAA Paper No. 79-1015, June, 1979.
15. Frisbee, R. H., J. C. Horvath, and J. C. Sercel, "Space-Based Laser Propulsion for Orbital Transfer", JPL D-1919, Jet Propulsion Laboratory, Pasadena, CA, 1984.
16. Mattick, A. T. and A. Hertzberg, "Liquid Droplet Radiator Technology Issues", In Space Nuclear Power Systems 1984, Orbit Book Company, Malabar, FL, 1985.
17. Soales, R., CVI, San Diego, CA, Private Communication, March, 1989.
18. Taussig, R., E. Klosterman, and H. Willenberg, "Space Laser Power Transmission, Task IV Final Report", Contract No. NAS 3-22477, Mathematical Sciences Northwest, Inc, July, 1981.

19. Hertzberg, A., K. Sun, and W. Jones, "Laser Aircraft", Astronautics and Aeronautics, Vol. 17, pp. 41-49, March, 1979.
20. "Laser Rocket System Analysis", Lockheed Missiles and Space Co., NASA CR-159521, Sept., 1978.
21. Cleven, C., Jet Propulsion Laboratory, Private Communication, May, 1989.
22. Kopf, T., Jet Propulsion Laboratory, Private Communication, May, 1989.
23. Allcock, Harry R., "Polyphosphazenes: New Polymers with Inorganic Backbone Atoms", Science, Vol. 193, Sept., 1976.
24. Heard, W. L., and J. J. Watson, "Results of the ACCESS Space Construction Shuttle Flight Experiment", AIAA Paper No. 86-1186-CD, June, 1986.
25. Mikulas, M. M. and H. G. Bush, "Design, Construction, and Utilization of a Space Station assembled from 5-meter Erectable Struts", NASA TM-89043, Oct., 1986.
26. Tompkins, S. S., "High Strength Al Alloys for Graphite Reinforced Metal Matrix Composites", NASA TM-89037, 1986.
27. Hedgepath, J. M., "Support Structures for Large Infrared Telescopes", NASA-CR-3800, July, 1984

28. Dursch, H. W. and C. L. Hendricks, "Protective Coatings For Composite Tubes In Space Applications", NASA-CR-178116, 1986.
29. Bate, R. R., D. D. Mueller, and J. E. White, Fundamentals of Astrodynamics, Dover Publications, New York, N.Y., 1971.
30. Stuhlinger, E., "The Flight Path of an Electrically Propelled Space Ship", Jet Propulsion, Vol. 27, pp. 410-414, 1957.
31. Stuhlinger, E., Ion Propulsion for Space Flight, McGraw-Hill, New York, 1964.

IV. MAGNETOPLASMDYNAMIC PROPELLED SPACECRAFT



INTRODUCTION

Jacqueline Auzias de Turenne

Magnetoplasmadynamic (MPD) propulsion was discovered by Adriano Ducati in 1964 [1,2]. Ducati had been experimenting with a conventional electrothermal arcjet when he lowered the propellant mass flow, along with the chamber pressure, thus developing a 3,000 A current across the anode and the cathode and giving rise to a self-induced magnetic field. He also observed exhaust velocities in the range of 10^6 m/s and a greatly reduced erosion rate at each electrode.

For the first time, researchers had a practical, steady, electromagnetic thruster. Earlier efforts had resulted in operational thrusters with large, bulky electromagnets, which made these thrusters hardly suitable for space flight. Without the additional burden of external magnets, the promising new MPD thrusters were considerably more compact devices. Due to the inherent limitation of the new propulsion units to produce thrusts only on the order of tens to hundreds of newtons, however, MPD propulsion is suitable only for exoatmospheric missions, for which it has become a viable alternative to ion propulsion.

Experimental MPD thrusters have produced thrust levels as high as 2,000 N [2]. Higher thrust levels, though, also correspond to increased power requirements. Consequently, the thrust performance of MPD propulsion in space is limited by the amount of power practically available. Exhaust velocities up to 50,000 m/s [2], indicating correspondingly high specific impulses, however, suggest MPD propulsion as a promising option for extended, deep space missions.

This section of the report presents the design of an MPD propelled cargo spacecraft for Mars missions. The spacecraft uses MPD thrusters producing 100 N of thrust at Earth, diminishing to 40 N of thrust at Mars, with a constant specific impulse of 2,490 s. The four main design aspects of the MPD propelled spacecraft include the MPD propulsion system, the solar power supply, the structural analysis, and the orbital mechanics. This preliminary design analysis illustrates the feasibility of a solar-powered MPD propelled spacecraft for Mars missions.

THE MPD THRUSTER

R. Jay Wornath
John Thorpe

The steady state magnetoplasdynamic arc thruster, depicted in Fig. IV-1, is a propulsion device capable of high specific impulses [2]. The MPD device produces thrust using electrical power in the form of a high current arc to ionize the incoming propellant and accelerate the resulting plasma to high exhaust velocities. The high exhaust velocities lead to specific impulses which enable an MPD propelled spacecraft to deliver a high payload mass with a relatively low propellant mass. This section will examine several areas: 1) the theory of the MPD thruster, 2) the thruster design and configuration for specific mission requirements, 3) the propellant type and propellant acquisition device, 4) the thermal protection of the propellant tank, and finally, 5) the component masses.

THRUSTER THEORY

Understanding the basic principles of the MPD thruster is necessary in order to design a thruster and a thruster configuration for a specific mission. As mentioned above, the thrust is a result of a high current arc between the anode and cathode of the MPD thruster. This azimuthally symmetric diffuse arc current, shown in Fig. IV-1, creates an azimuthal magnetic field, B_θ , which interacts with the current flow to produce a Lorentz body force on the propellant gas. Two components of this magnetogasdynamic interaction provide the accelerating force on the plasma. The first, f_z , is referred to as electromagnetic "blowing." This component is the axial accelerating force produced by the interaction of the radial component of arc current, j_r , with the self-generated azimuthal magnetic field. The blowing force provides the majority of the thrust for the engine. The second component of magnetic interaction is known as electromagnetic "pumping," f_r . It is produced by the interaction of the axial arc current, j_z , with the azimuthal magnetic field.

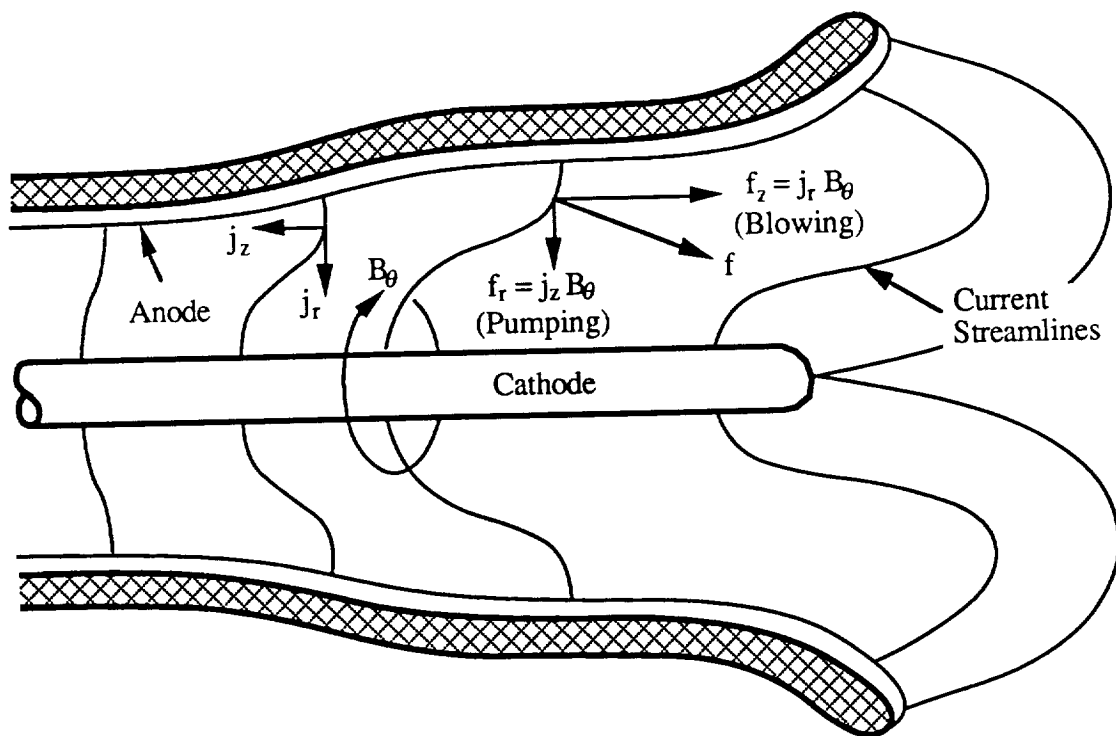


Figure IV-1. Force Components of the MPD Thruster.

The pumping force establishes a radial gradient in the gas dynamic pressure which results in a reaction force on the cathode. The high dynamic gas temperatures, typically on the order of 10^4 K or higher [3], also contribute to an acceleration of the plasma through the "magnetic nozzle" formed by the self-field. The result of these two processes accelerates the plasma to speeds up to 50,000 m/s.

The performance of the MPD thruster can be analyzed using the relationships presented in the following four equations. Theoretically, the thrust, F , is predicted to be proportional to the square of the arc current, J [3]:

$$F = bJ^2 \quad (\text{IV-1})$$

where the constant of proportionality, b , is a function of geometry:

$$b = \left(\frac{\mu_0}{4\pi} \right) \left[\ln \left(\frac{r_a}{r_c} \right) + 0.75 \right] \quad (\text{IV-2})$$

where r_a and r_c correspond to the radius of the anode and cathode respectively, and μ_0 is the permeability of free space ($\mu_0 = 4\pi \times 10^{-7}$ henry/m). The empirical relationship in Eq. IV-2 indicates that the total electromagnetic thrust is not dependent on the shape of the arc, but only on the ratio of the anode and cathode radii.

As with any propulsion system an MPD thruster has inherent limitations. The performance of the MPD has been found to be limited by a critical value of J^2/m [5], known as "onset." Onset is typically associated with voltage oscillations, rapid erosion of the cathode, and other instabilities. The critical value of J^2/m is solely a function of thruster geometry and propellant properties, and can be approximated by the following equation [5]:

$$\left(\frac{J^2}{m} \right)_{cr} = \sqrt{\frac{2eN_0}{b}} \left(\frac{\epsilon_i}{M} \right) \quad (\text{IV-3})$$

where e is the electron charge, equal to 1.6×10^{-19} coulomb, N_0 is Avogadro's number, equal to 6.02×10^{23} /gm-mole, and ϵ_i and M are the ionization potential and the molecular weight of the propellant, respectively.

The overall efficiency, η , defined as the ratio of the exhaust jet power to the input electrical power, can be approximated as follows [4]:

$$\eta = \frac{F^2}{2\dot{m}JV} \quad (\text{IV-4})$$

where \dot{m} is the mass flow rate, and V is the voltage drop across the thruster.

Several factors work to decrease the efficiency of the MPD thruster. The two most significant losses are heat transfer losses and "frozen flow" losses. The heat transfer losses are in the form of radiation from the cathode tip, radiation from the exhaust jet, and heating of the anode. The "frozen flow" losses are due to unrecovered internal energy of the gas in the exhaust jet. These "frozen flow" losses result from the ionized gas re-combining after exiting the thruster.

THRUSTER DESIGN

The MPD arc thruster for this Mars mission is a relatively compact device, as shown in Fig. IV-2. The characteristics of this thruster were determined by adapting the MPD thruster to the specific requirements for a solar powered Mars mission. It has been determined, as will be explained later in this section, that optimal performance will be achieved if each thruster produces 20 N of thrust. Knowing the values for thrust, efficiency, and onset, Eq. IV-1 through Eq. IV-4 can be manipulated to determine the mass flow rate of propellant, the power requirement, and the current and voltage requirements. Power conversion efficiencies as high as 40% have been achieved in experimental tests of the MPD thruster [6]. It has also been shown that the critical value of onset, J^2/\dot{m} , occurs at values on the order of $80 \text{ kA}^2/\text{g/s}$ [7]. Assuming a typical value of 10 for the ratio r_a/r_c

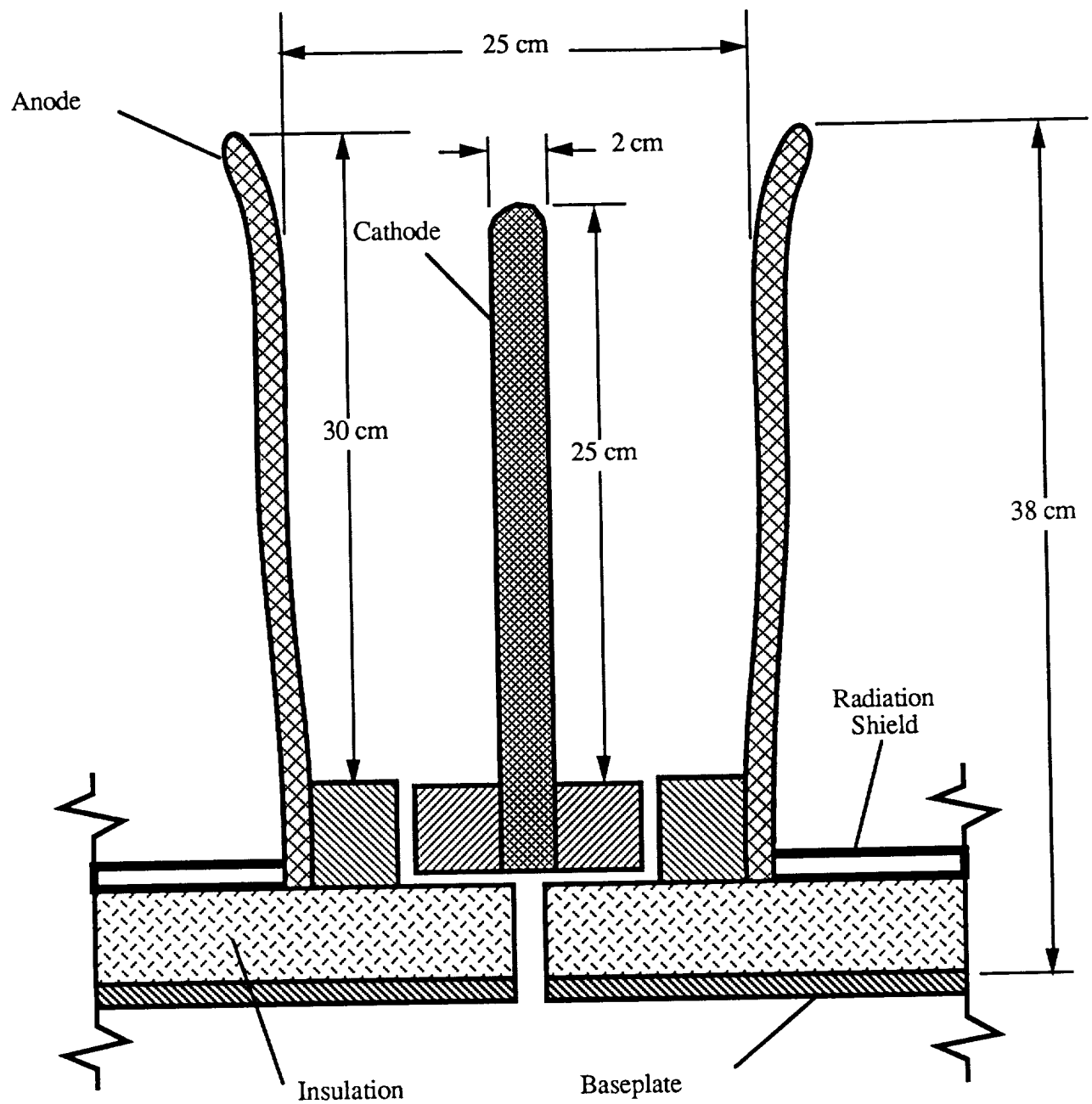


Figure IV-2. Dimensions of MPD Thruster.

fixes the constant of proportionality, b , in Eq. IV-1. The result is an anode, which forms the nozzle of the device, with an inner diameter of 20 cm, an exit diameter of 25 cm, and a length of approximately 30 cm from the baseplate to the nozzle exit. The cathode has a diameter of 2.0 cm and a length of 25 cm, also measured from the baseplate. Each thruster requires 0.61 MW of power at a current of 8.1 kA and a potential difference of 75 V. This current and geometry requires a mass flow rate of 0.82 g/s and produces an exhaust velocity of 24,400 m/s, corresponding to a specific impulse of 2,490 s. The anode and cathode of the thruster must withstand high temperatures so both are constructed of tungsten. The baseplate is also made of tungsten and a boron nitride insulator separates the anode and cathode.

THRUSTER THERMAL MANAGEMENT

Any high powered propulsion device has a significant heat rejection problem in space. For the MPD thruster, 2% of the electrical energy heats the cathode while 15% of the electrical energy heats the anode [6]. For the 0.61 MW thruster module the heating of the cathode does not pose a problem; for the anode, however, heating results in 92 kW of thermal energy that must be radiated. If an emissivity of 0.5 is assumed for the tungsten anode, which is achievable if the tungsten surface is slightly roughened, and radiation is considered to occur from the exterior as well as the interior of the thruster module, an equilibrium anode temperature of approximately 2,000 K will result. This value is well under the melting temperature of tungsten.

THRUSTER CONFIGURATION

Many of the design problems of the solar powered MPD thruster stem from its low thrust to power ratio. The thrust to power ratio of the MPD thruster is currently on the order of 30 N/MW. When the power is supplied by photovoltaic cells this results in a very large solar array. At the low thrust levels of a single thruster, 20 N, a spacecraft would

require hundreds of days to follow a spiral maneuver out of Earth orbit and the overall trip time to Mars would be excessive. Lengthy trip times would require unrealistic reliability and lifetime requirements and would generally be impractical for a transport vehicle. A thrust of 100 N in LEO enables the spacecraft to spiral out of Earth orbit and complete the trip to Mars in 2.39 years.

A problem related to the low thrust and long mission duration of the solar MPD powered spacecraft is the length of thruster burn time. This mission requires the thrusters to be fired for a total of approximately 664 days. The MPD thruster, however, has a limited lifetime of about 2000 hours, roughly 83 days [8]. To provide a constant thrust for 664 days, additional thrusters are required to replace those which burn out.

The power decrease as the spacecraft travels away from the Sun presents another design difficulty. The MPD thruster has a constant geometry which gives maximum performance at a specific current. As the power generated by the solar arrays decreases, reducing the power to the thruster would significantly lessen the thruster efficiency. One thruster cannot be designed to efficiently provide 100 N in LEO and retain its efficiency at distances farther from the Sun.

To circumvent these problems a multiple thruster configuration is proposed. The thruster configuration for the LEO to Mars transport vehicle is designed to house 43 thrusters in four concentric circles of 6 thrusters each, with the 43rd thruster located in the center as shown in Fig. IV-3. The thrusters are located at 60° intervals in each ring.

This multiple thruster arrangement has the capability to fire any number of thrusters in any combination. This capability serves several functions; the first is to overcome the short thruster lifetime. The thrusters are required to burn a total of 664 days throughout the mission. Burning five thrusters at a time provides the 100 N of thrust necessary to spiral out of a LEO in the shortest amount of time. Consequently a minimum of 40 thrusters are required to successfully complete the mission. The use of 43 thrusters, however, allows redundant thrusters in case of component failures or for a mission variation. The second

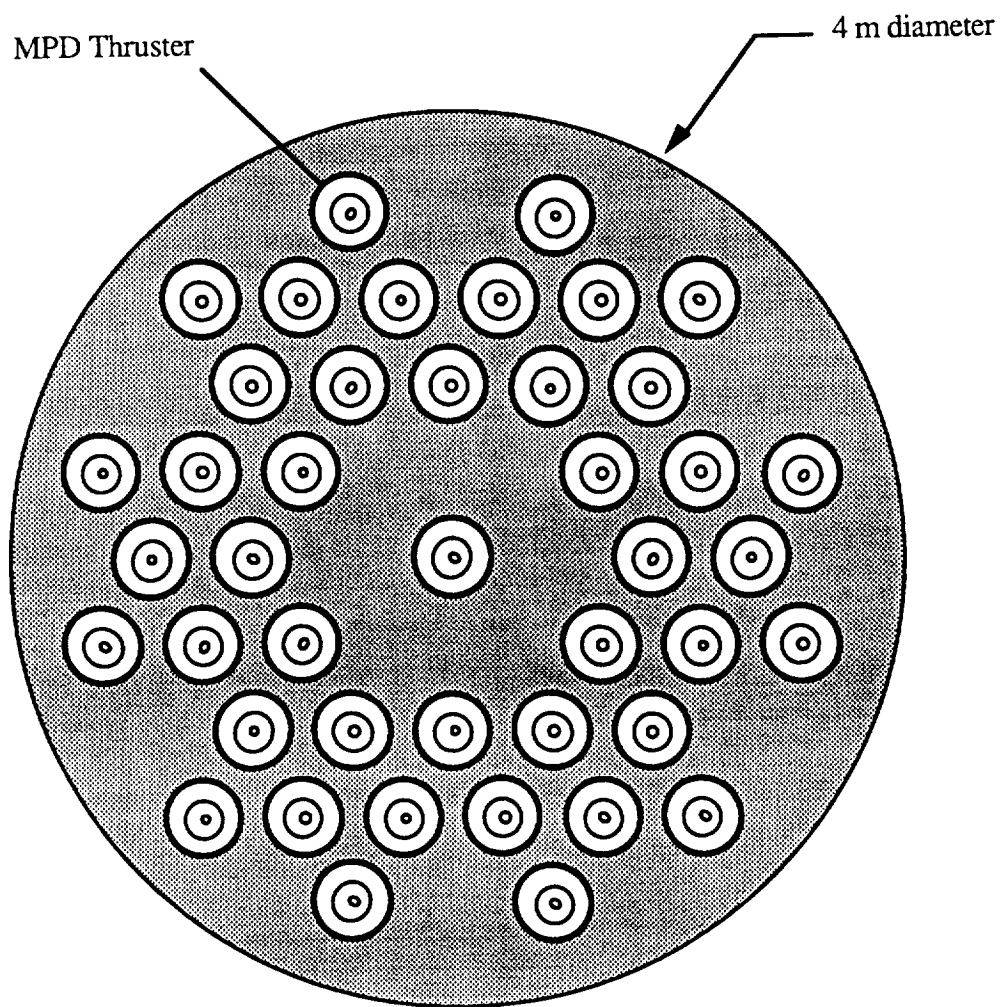


Figure IV-3. Schematic of MPD Thruster Configuration.

function of the multiple thruster arrangement is to allow a variety of thruster burn combinations that do not produce a moment about the spacecraft center of mass. The third function of the multiple thruster configuration is to make efficient use of the available solar power. Multiple thrusters allow better utilization of the available solar power as the spacecraft travels farther from the Sun. In low Earth orbit 3.05 MW of power are available to the thrusters, as shown in Fig. IV-4. This system is designed to use all 3.05 MW to fire five thrusters at a time and deliver 100 N. At Mars 1.3 MW are available, so that two thrusters can be fired to provide 40 N of thrust. The number of thrusters available at increasing distances from the Sun are shown in Fig. IV-4. Table IV-1 shows the thrust developed, the power requirements, and the mass flow rate of propellant to fire thrusters at Earth and Mars.

Table IV-1: Thruster Characteristics

	Earth (5 Thrusters)	Mars (2 Thrusters)
Thrust (N)	100	40
Power (MW)	3.05	1.22
Mass flow (g/s)	4.1	1.64

The final advantage of the multiple thruster arrangement is that it gives the solar-powered MPD transport vehicle the capacity to perform alternate missions. The ability to fire any number of thrusters in any combination and to carry redundant thrusters makes this an inherent benefit.

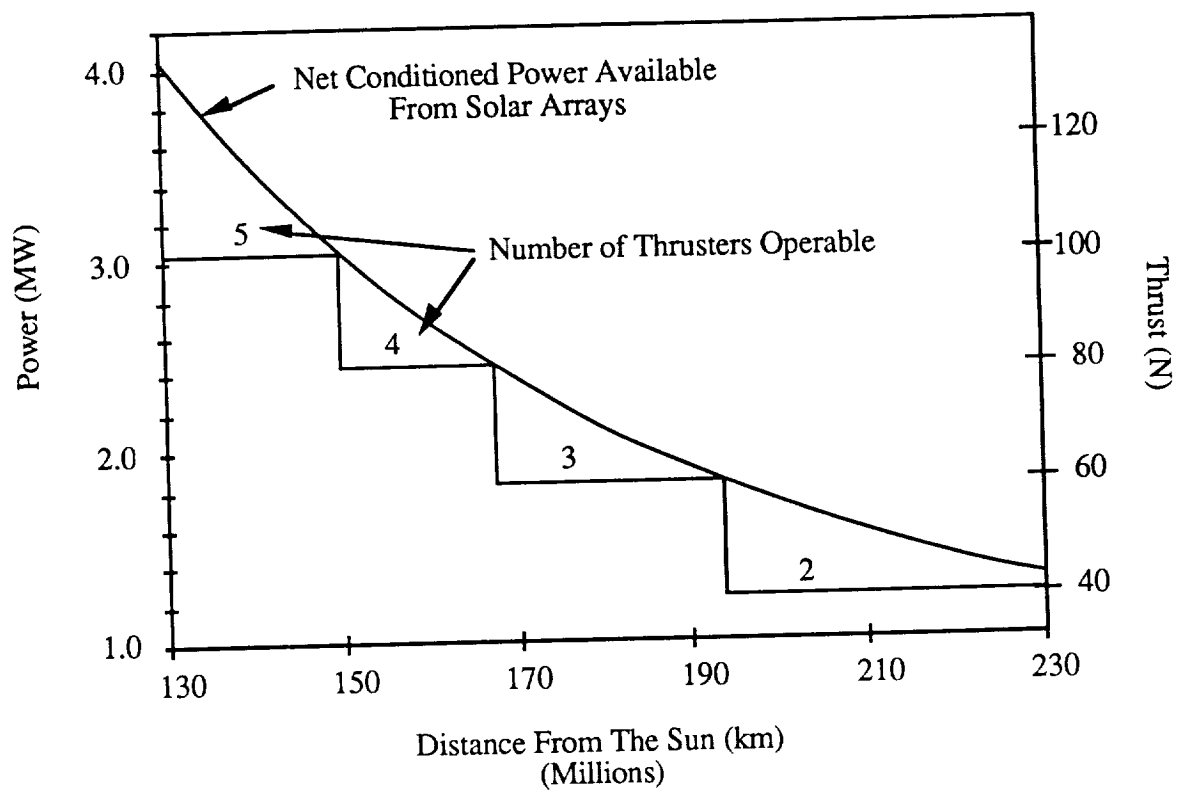


Figure IV-4. Power and Thrust as Functions of Distance from Sun.

CHOICE OF PROPELLANT

Various propellants such as argon (Ar), ammonia (NH₃), nitrogen (N₂), and hydrogen (H₂), have been successfully used in experimental tests of MPD thrusters [2,3]. The type of propellant appropriate for this mission is determined by considering the liquid density, the energy required for vaporization, and the energy required for long term cryogenic storage of each propellant. The energy required for refrigeration depends on the heat flux from the exterior of the tank to the liquid propellant. This heat flux, \dot{Q} , for conductive heat transfer through the tank wall is proportional to the difference between the exterior surface temperature, T_{ext} , and the liquid storage temperature, T_{liq} [9];

$$\dot{Q} = \frac{kA}{d}(T_{ext} - T_{liq}) \quad (IV-5)$$

where k is the thermal conductivity of the tank wall, A is the surface area of the tank, and d is the wall thickness. The liquid density plays an important role in sizing the propellant tank. A higher propellant density signifies a smaller storage volume, resulting in a smaller propellant tank with a lower mass. Since the liquid propellant must be vaporized prior to reaching the thrusters, a low vaporization energy is preferred since the heater requires less electrical energy. A high boiling point allows the use of refrigerators that are more efficient, less expensive, and less massive than propellants with a low boiling temperature.

Table IV-2 compares the energy required for vaporization, the exterior/liquid temperature difference, and the density of the cryogenic liquid [10]. The exterior surface temperature of the propellant tank resulting from solar radiation in the vicinity of Earth is 327 K. This surface temperature was determined by performing an energy balance on the propellant tank [11]:

$$\alpha I_s = \epsilon \sigma T^4 \quad (IV-6)$$

where α is the absorptivity of the multilayered insulation, I_s is the intensity of the sun at a particular radius from the sun, ϵ is the emissivity of the exterior surface, and σ is the Stefan-Boltzmann constant, equal to $5.67 \times 10^{-8} \text{ W/m}^2\text{-K}^4$.

Table IV-2: Propellant Characteristics

Propellant	T_{liq} (K)	$T_{\text{ext}} - T_{\text{liq}}$ (K)	ρ_{liq} (g/cm ³)	ΔE_{vap} (j/g)
NH ₃	239.8	87.2	0.608	1368.6
Ar	87.2	239.8	1.423	157.3
H ₂	20.6	306.4	0.070	451.9
N ₂	77.6	249.4	0.810	199.2

Table IV-2 indicates that Ar is an attractive propellant. In addition it is non-toxic, readily available, and relatively inexpensive. For these reasons Ar was chosen as the propellant for the MPD thruster system.

PROPELLANT TANK

The propellant tank must serve two functions: 1) shield the cryogenic Ar from solar radiation and 2) allow easy acquisition of vapor for the thrusters. The propellant tank has two parts. The outer tank, a vapor cooled shield, is constructed of thin lightweight aluminum and contains the inner tank, or pressure vessel, which is fabricated of 0.5 cm thick aluminum as indicated in Fig. IV-5.

A stable liquid-vapor interface is necessary for successful acquisition of propellant vapor for the thrusters. To create a stable liquid-vapor interface in zero gravity an ellipsoid of revolution was selected as the tank shape. Such a tank shape allows a vapor bubble with diameter equal to the minor axis of the ellipse to be formed. Once this vapor bubble is formed, surface tension forces it into the largest cross-section of the tank, which is located

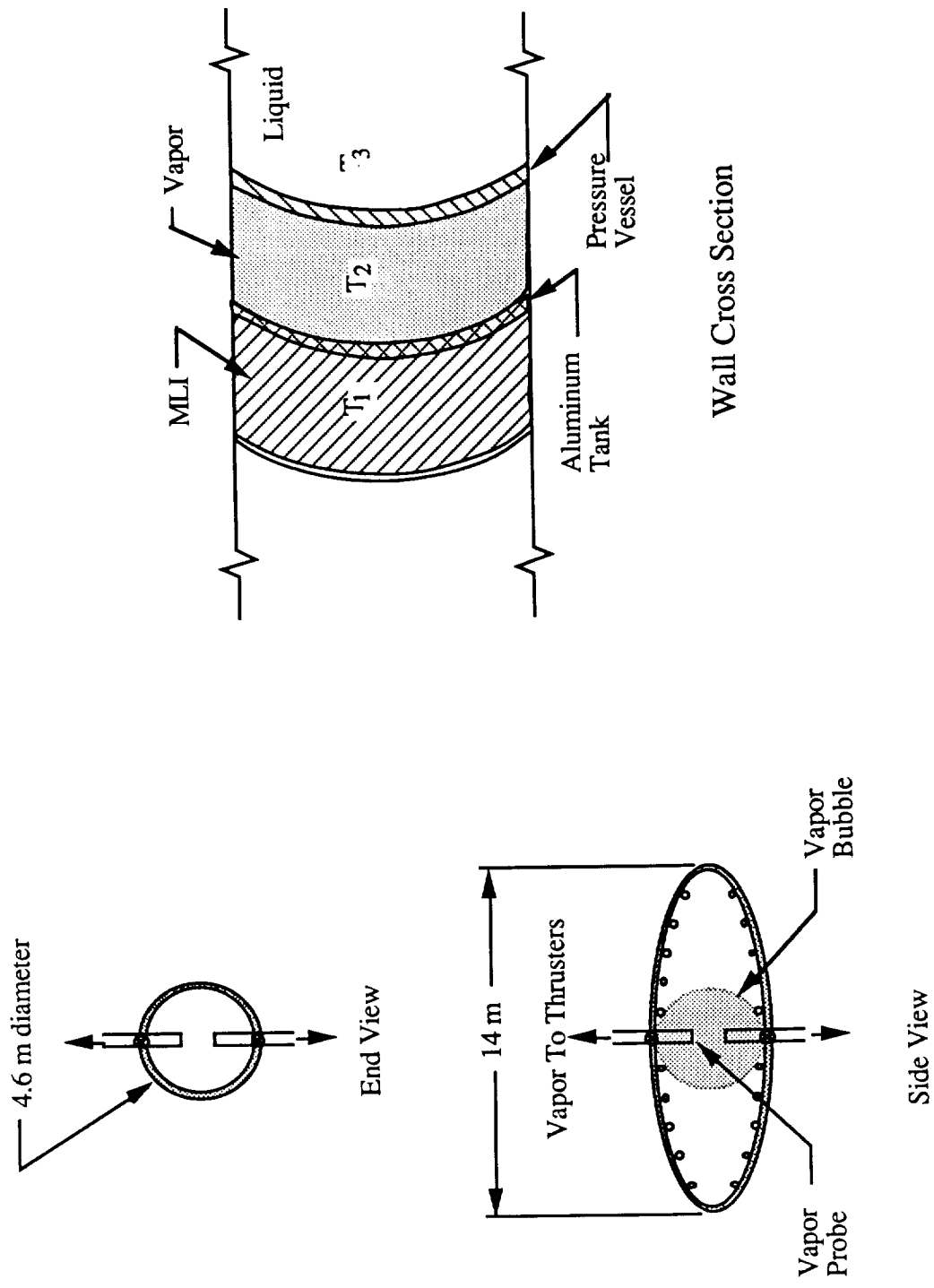


Figure IV-5. Propellant Tank.

at the center, as shown in Fig. IV-5 [12]. The vapor bubble may be formed in the propellant tank by rotating the tank about the minor axis. This is considered as part of the fueling procedure. The dimensions of the propellant tank were chosen to hold 170,000 kg, corresponding to 120 m³ of liquid Ar, to contain a vapor bubble of sufficient size, and to fit inside the cargo bay of the space shuttle. Consequently the tank is 14 m long with a 4.6 m diameter.

PROPELLANT ACQUISITION

In order to fulfill the requirement of the mass flow of propellant to the thruster and prevent the passage of liquid Ar into the vapor cooled shield surrounding the tank, a vapor acquisition system is necessary. Since the location of the vapor bubble is known, the propellant vapor can be extracted directly from the bubble using vapor probes as shown in Fig. IV-5. These probes, or tubes, are constructed of a ceramic composite material which demonstrates low thermal conductivity and high strength. The vapor withdrawn from the pressure vessel passes through a valve where it is either directed through the surrounding vapor shield or to the thrusters. During thrust conditions, the valve is closed to the vapor cooled shield and opened to the thrusters providing the proper mass flow of propellant to the thrusters. When the thrusters are not in operation, the valve is closed to the thrusters and opened to the vapor cooled shield permitting vapor to cool the pressure vessel, as will be explained later.

The valve used in the vapor acquisition device may be represented by the Joule-Thompson throttling effect if the process is assumed to occur adiabatically with negligible change in kinetic energy. The assumption of an adiabatic process is valid if the flow through the valve occurs at a high velocity so that there is neither sufficient time nor area for heat transfer. Therefore, the total enthalpy of the flow remains constant across the valve, resulting in a drop in the vapor temperature.

PROPELLANT HEATER

In order to supply the thrusters with the required mass flow of vapor during their operational phase, the boil off rate in the pressure vessel must equal the mass flow rate of propellant to the thrusters. To fulfill the mass flow requirements, a series of small electric heating coils are placed circumferentially on the inside of the pressure vessel walls. Since the location of the vapor bubble is known, the point where the tank wall, liquid, and vapor intersect is also known. The heating coils corresponding to these thin fluid film locations can be activated sequentially to generate bubbles which will merge with the larger vapor bubble due to their proximity and the surface tension of the liquid. In LEO, when 5 thrusters are fired, the mass flow rate required is 4.1 g/s. This corresponds to 650 W of electrical power needed to heat the coils and vaporize the necessary amount of liquid. As the distance of the spacecraft from the sun increases and fewer thrusters are used, the mass flow rate of argon and the electrical power necessary to vaporize the argon are reduced.

PROPELLANT TANK INSULATION

In order to minimize the heat flux into the cryogenic pressure vessel, a combination of multilayered insulation and a vapor cooled shielding are used. Multilayer insulation, MLI, consists of layers of highly reflective metallized polymeric film separated by low conductivity materials such as dacron or nylon. MLI has an effective conductivity of 0.000017 W/K-m. As shown earlier, the surface temperature for the propellant tank near LEO is 327 K. Since the surface temperature is known, the heat flux, \dot{Q}_1 , through the MLI to the outer tank wall can be determined from Eq. IV-7 below:

$$\dot{Q}_1 = \frac{kA}{d}(T_1 - T_2) \quad (IV-7)$$

where T_1 and T_2 are the external surface temperature and the vapor temperature in the vapor cooled shield, respectively, as shown in Fig. IV-5, and k is the effective thermal

conductivity of MLI. The effects of the thin aluminum walls of the vapor cooled shield were neglected in this approximation.

The Ar gas from the vapor acquisition probes circulates through channels outside the pressure vessel, absorbing heat from the tank exterior that has penetrated the insulation. Since there is a drop in the vapor temperature across the valve, the vapor in the vapor cooled heat shield also serves to cool the liquid in the pressure vessel [13]. The Ar gas is then reliquefied and returned to the pressure vessel. For a given mass flow the amount of heat, \dot{Q}_2 , that can be absorbed by the Ar can be found from:

$$\dot{Q}_2 = \dot{m}C_p(T_2 - T_3) \quad (\text{IV-8})$$

where C_p is the specific heat of the Ar vapor, and T_2 and T_3 are the temperatures of the exiting Ar vapor and the Ar liquid, respectively.

In LEO where the intensity of the Sun is greatest, 4.8 W of thermal energy penetrate the MLI and reach the propellant tank. When the thrusters are not in operation, the 4.8 W of heat is removed using a Stirling refrigerator in a process of reliquefaction. The Stirling refrigerators developed for use in space incorporate magnetic bearings to suspend a reciprocating compressor and expander. For a power input of 220 W, a maximum cooling rate of 5 W is achieved [10].

COMPONENT MASSES

A major advantage of the MPD thruster system lies in its low component masses. Low component masses make it possible to include redundant components at very little penalty. The masses of the components are shown in Table IV-3. Each thruster (anode, cathode, and base) has a mass of only 35 kg. To operate each thruster, an assortment of valves and propellant lines are required. Each thruster requires one valve, estimated to have a mass of 5 kg, and approximately 5 kg of propellant lines. In addition, engine

sensors and controls will be needed; this total mass is estimated at 50 kg. The mass of the propellant tank, including the pressure vessel and the vapor cooled thermal shield was based on the density of aluminum and the tank size. The mass of the insulation around the tank was determined by the insulation thickness and tank surface area. The overall mass of the entire thruster system, including the propellant tanks is just under 5,500 kg.

Table IV-3: Component Masses

Component	Mass (kg)
Thrusters (43)	1,500
Propellant Tank	2,900
Insulation and Thermal Shields	540
Engine Sensors and Controls	50
Valves	215
Fuel Lines	215
Total	5,420

POWER SUPPLY

Eric Haberman

MPD thrusters require a combination of low voltage and high current, thus a high power level, for efficient operation. The power must be delivered to the thrusters at a constant 75 V DC. For this specific mission, a thrust level of 100 N requiring 3.05 MW of power was determined optimum. The necessary power is generated by a photovoltaic array and conditioned to the levels acceptable for the MPD thrusters and auxiliary power units such as batteries, stationkeeping, and engine start-up. The design of the photovoltaic array must take into account the degradation of the photovoltaic cells caused by radiation encountered in the Van Allen radiation belts [14] and the normal space environment.

PHOTOVOLTAIC SOLAR ARRAYS

Advanced photovoltaic arrays capable of achieving power densities of 300 W/m² and 300 W/kg are expected to be available within the next 20 years [15]. The specific power of 300 W/m² applies to a near-earth orbit where the solar flux is approximately 1,380 W/m². The solar flux decreases to 565 W/m² at Mars, thus reducing the power density of the cells. Presently, the best array in use produces only 130 W/m² at Low Earth Orbit [16].

Currently, there are two main types of photovoltaic cells included in the projections. These are indium phosphide (InP) and gallium arsenide (GaAs) cells. Gallium arsenide cells have obtained efficiencies of 21%, while presently the best InP cells are 13.6% efficient. However, with continuing research and development, InP cells are expected to eventually be able to achieve efficiencies in the vicinity of 21% [17,18]. The characteristics of the two cells are projected to be similar, thus allowing the assumption that a photovoltaic array constructed from either InP or GaAs cells will be similar in size, mass, and power output at Beginning Of Life (BOL). Several other types of cells, such as silicon, are under

research, yet are not as promising as GaAs or InP; therefore, they are not considered in this analysis. A comparison of the three primary cells is shown in Table IV-4 [17].

Table IV-4: Photovoltaic Cell Comparison

Solar Cell Type	Advantages	Disadvantages
Silicon	Abundant 18% efficient	Degradation
Gallium Arsenide	Abundant 21% efficient	Degradation
Indium Phosphide	Self-annealing 21% efficient (projected)	Limited supply 14% efficient (presently)

RADIATION EFFECTS

A primary problem associated with current photovoltaic cells is degradation induced by exposure to electron and proton radiation. The greatest exposure experienced by the photovoltaic cells to these kinds of radiation is encountered within the Van Allen radiation belts [14]. The Van Allen belts consist of electrons and protons that are trapped by the magnetic field around the Earth. The Van Allen belts contain particles from both cosmic radiation and solar radiation. The amount of cosmic radiation remains relatively constant, while the amount of particle radiation from the sun varies greatly with time. The solar radiation is caused by solar flares. The difference from the maximum to the minimum radiation levels, corresponding to the activity of the solar flares, is several orders of magnitude. It is therefore, desirable to perform the spiral maneuvers from LEO during periods of low solar flare activity, if possible.

For the Mars mission, the spacecraft spends approximately 60 days in the Van Allen Radiation belts. The amount of radiation that the ship encounters in the belts depends on several factors. These include the amount of time spent in the various regions of the radiation belts and the activity of the solar flares. For degradation estimates, it was assumed that radiation levels were at average intensities throughout the belts.

Indium phosphide and gallium arsenide cells have very different reactions to radiation exposure, each with definite advantages and disadvantages. With the state of present technology, GaAs cells would provide the best choice. Of the presently abundant cells, GaAs has the highest efficiency and is most resistant to radiation. The major disadvantage of GaAs cells is the amount of degradation that they will experience during the mission. After traveling through the Van Allen Radiation belts, they will produce approximately 20% less power than at BOL. Throughout the rest of the mission, these cells will lose approximately another 3% of their power output due to natural radiation aging [14,17,19]. In order to contend with the degradation in power output, the size and mass of the entire photovoltaic array would need to be increased, thus lengthening the duration of the mission. The mission to Mars would in fact be possible with GaAs cells, but operation at Mars would be limited by the decreasing efficiency of the cells. A large cost in refurbishing the spacecraft with new photovoltaic cells, creating a virtually new spacecraft, would be incurred.

Indium phosphide cells are a promising alternative to GaAs cells. Although research on InP cells during the past few years has been limited, a recent interest has developed. InP cells have one important feature, the ability to regenerate after radiation damage, through a process known as self-annealing. In an environment where an adequate amount of thermal energy is available, thermal annealing is accomplished by tailoring the emissivity of the array in order to maintain the cells at a temperature of 115⁰ C. For this specific Mars mission, the required level of solar intensity is never encountered by the spacecraft. Therefore, an alternative method of annealing is employed for the mission by

passing a current through the degraded cells under forward bias conditions. Through the process of self-annealing, no degradation of InP photovoltaic cells in a space environment will occur [17].

The projected power performance of InP cells is comparable to the present level of GaAs cells [17]. Although, the BOL specific mass of InP cells is slightly greater than the BOL specific mass of GaAs cells, InP is superior to any other cell presently under research when radiation damage is considered. Currently, the largest InP cell available is on the order of 10^{-5} m^2 and is available only on a very limited basis. Through increased interest and research on InP cells, a corresponding increase in development and availability should occur in the next 20 years [17]. Therefore, InP cells have been selected for this solar-powered MPD mission.

ARRAY CONFIGURATION

The photovoltaic cells necessary for this mission are configured in two large arrays placed on either side of the main spacecraft. To provide 3.21 MW of power at LEO, each photovoltaic array has a surface area of $5,540 \text{ m}^2$ providing 1.6 MW of power at BOL. Table IV-5 shows the variation of array area and system mass with supplied power.

Table IV-5: Array Sizing

Supplied power (MW)	Array Area (m^2)	System Mass (kg)
1.6	5,540	8,730
3.2	11,080	19,370
4.8	16,620	31,913
6.4	22,160	46,320
8.0	27,700	58,020
9.6	33,240	79,681

Each 1.6 MW array contains 290 photovoltaic cell "blankets", each measuring 11.67 m x 1.6 m, as shown in Fig. IV-6. These blankets are arranged in 29 rows and 10 columns. Each array measures 116.7 m x 46.4 m, as shown in Fig. IV-7 [16]. Blankets can simply be added or subtracted from each row as power requirements for the mission change.

For the configuration of the current carrying wires, each array is subdivided in five separate "power" blocks. Each block consists of two columns of blankets that are wired in parallel to a single current carrying wire. To provide the 3.21 MW required for the mission, each block provides 1,640 A at 200 V, the five blocks provide a total of 8,200 A at 200 V. This configuration is also shown in Fig. IV-7. It is required that 200 V not be exceeded in the main line power feed due to the possibility of arcing [20].

Each blanket assembly is comprised of 36 panels of photovoltaic cells as seen in Fig. IV-6. The construction consists of a carbon loaded Kapton polyimide film as the substrate material. This material has a sufficiently low resistivity to permit grounding of the blanket substrate, thus preventing electrostatic charge buildup caused by the natural radiation environment. The resistivity is sufficiently high to prevent shorting of the photovoltaic cell strings.

The individual InP photovoltaic cell is a composite referred to as a "stack" as shown in Fig. IV-8. The outer layer is a cerium oxide doped borosilicate coverglass that is coated with an ultraviolet reflective coating. The outer layer is secured with an adhesive to an InP cell. The cell is attached to the carbon loaded Kapton substrate with an adhesive. All cells on the blanket are attached to the substrate. Cells are electrically connected to each other with shallow, in-plane soldered interconnectors. Two of these interconnectors are required for each intercell connection. The density of the stack is approximately 0.5 kg/m² which corresponds to 40 mg/cell [20]. The cell density on the panels is 1,234 cells/m².

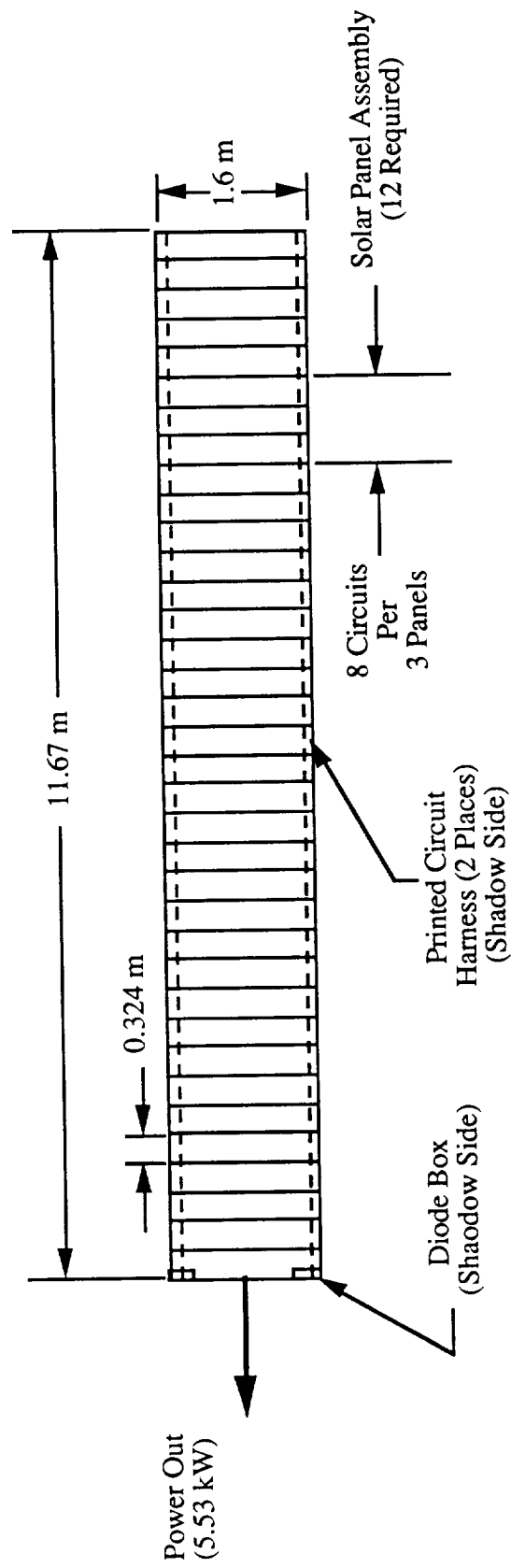


Figure IV-6. 5.53 kW (BOL) Solar Blanket.

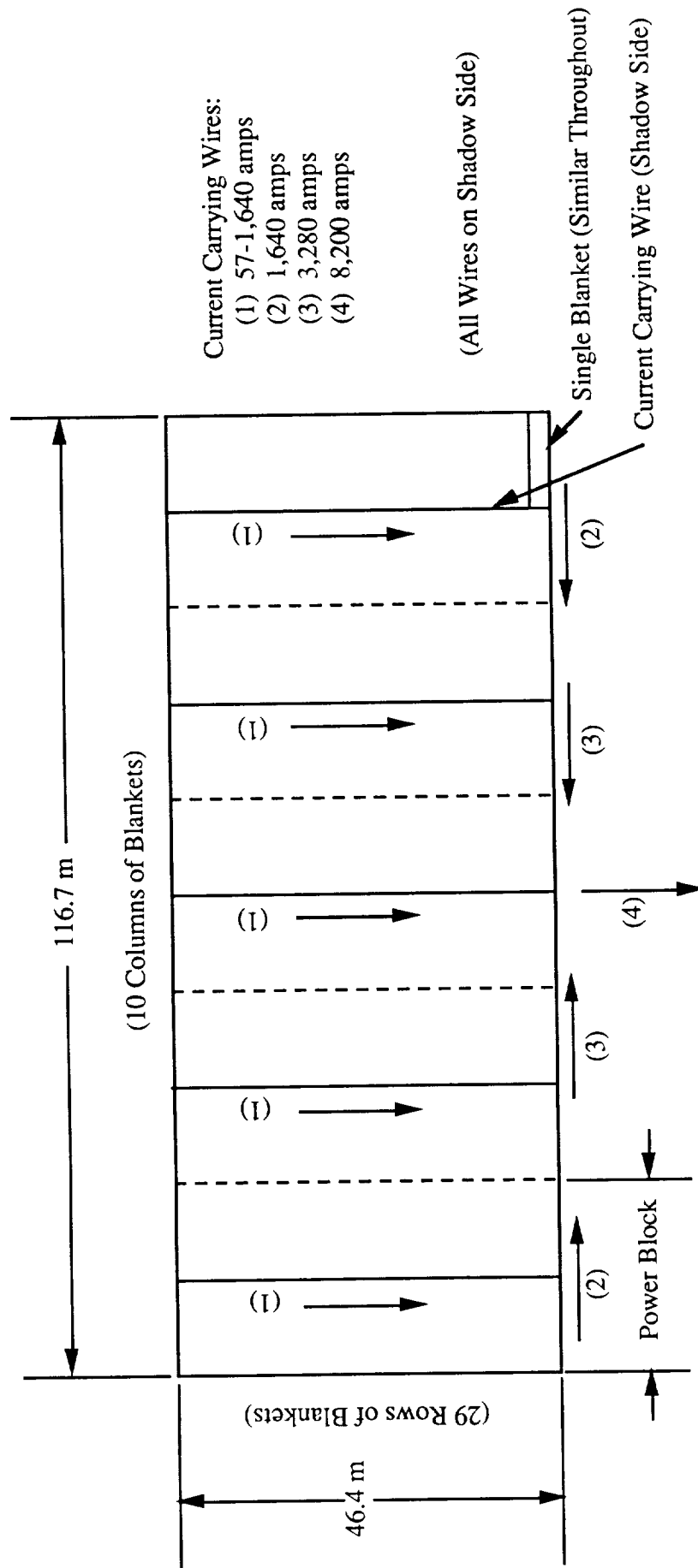


Figure IV-7. 1.6 MW Array Containing 290 Solar Blankets.
(2 Required for 3.21 MW System)

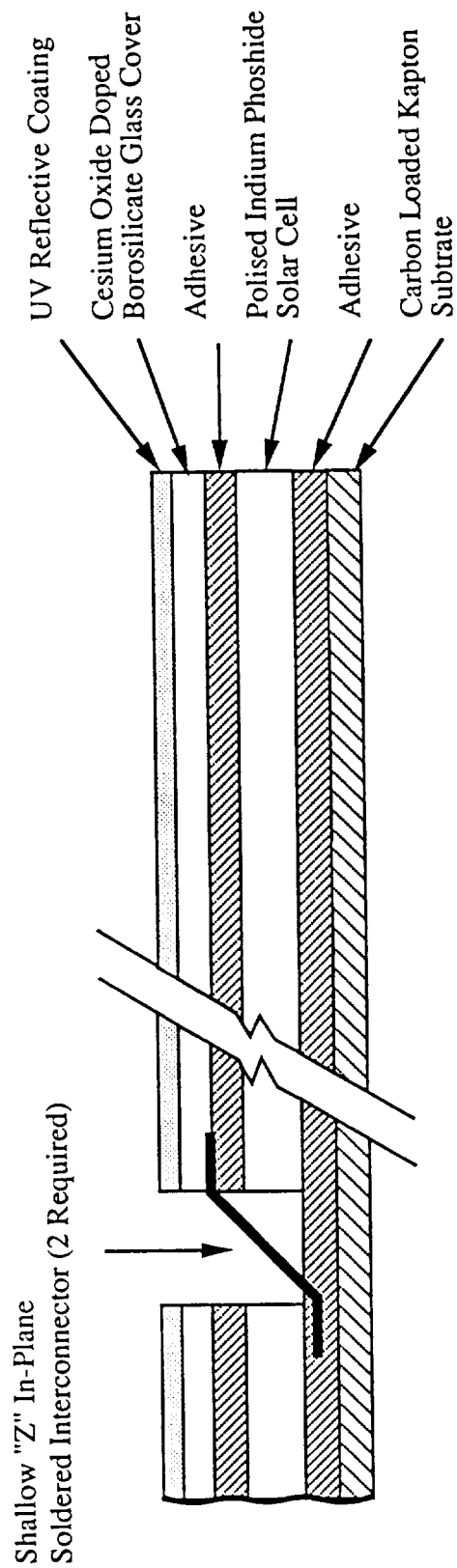


Figure IV-8. Indium Phosphide Solar Cell Stack.

The cell rows are arranged in a serpentine manner to create electrical circuit modules. Each module consists of 240 cells wired in series, producing 0.3 A at 200 V BOL. All positive and negative terminators for each circuit occur along the shaded side of the blanket adjacent to a printed circuit harness. The harness is bonded to the basic blanket substrate as seen in Fig. IV-8. Should the blanket become damaged and unable to produce current at 200 V, a diode box is placed in-line between the printed circuit harness and the main power line to prevent reverse current flow. These electrical components account for about 1/3 of each blanket's mass, or 4.6 kg. The circuit harness and diode box are both located on the shadow side of the blanket to allow cooling by self radiation.

POWER CONDITIONING

Each MPD thruster requires constant power delivered at 75 V DC with a current of 8.1 kA. Photovoltaic cells provide the necessary power, however, this power must be conditioned to the form required by the MPD thrusters. The power conditioning process is shown in Fig. IV-9. DC output from the photovoltaic arrays is passed via a high current bus through a DC to AC converter. The high frequency, 2,300 Hz, single phase AC current from the inverter is fed through a constant-voltage transformer (CVT) and rectifier [21]. High frequency current is used because it allows for a lighter and more efficient transformer. This series of electrical components conditions the power to the appropriate current and voltage levels required by the MPD thrusters.

The DC to AC converter is assumed to have a 97% efficiency and the transformer is assumed to have a 99% efficiency [21]. A 1% power dissipation from the rectifier is expected [6]. The power dissipated from the electrical components is removed by a heat pipe system. It is desirable to keep all wires as cool as possible to maintain an optimum level of electrical efficiency. Therefore, the wires are placed on the shadow side of the photovoltaic arrays wherever possible. Aluminum wires are used since they have a lower mass and have a larger surface area than copper wires. The added surface area allows

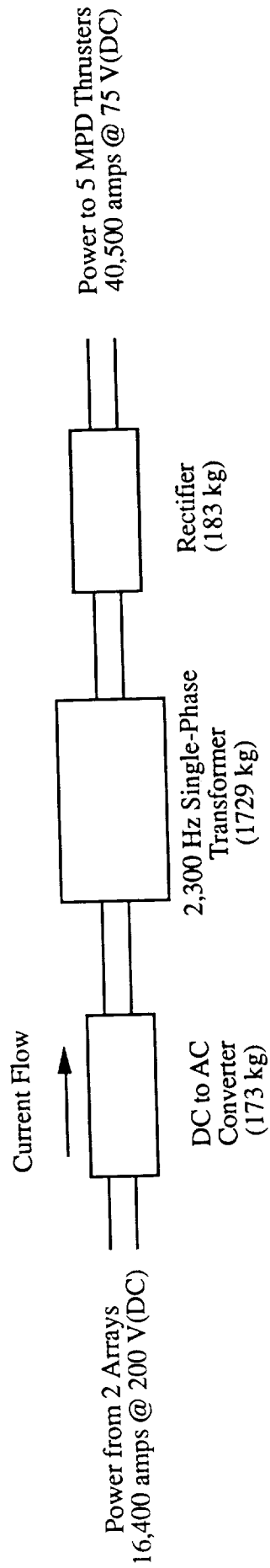


Figure IV-9. Power Conversion Components for the 3.21 MW System.

the wires to radiate excess heat at a lower temperature than copper wires, thus, increasing their efficiency. Power losses through the wires are assumed negligible [6].

AUXILIARY POWER SYSTEMS

The photovoltaic arrays also provide power to the housekeeping equipment, stationkeeping equipment, and thruster start-up controls. Housekeeping includes navigation, guidance computers, and thruster management systems. Stationkeeping is concerned primarily with keeping the arrays properly aligned, through the use of solar alpha joints and attitude control jets mounted on the array support structure. Thruster start-up requires a 500 V pulse supplied by a small capacitor bank to be placed across the anode and cathode. The array is slightly oversized to provide power for housekeeping, stationkeeping and to compensate for losses in the conversion system.

In the earth's shadow the solar cells are ineffective. Therefore, batteries are required. As a result of their high mass, however, batteries are only used for housekeeping purposes and *not* to power the thrusters. Nickel Hydrogen (NiH_2) batteries are used to provide 100 WH/kg [22]. These batteries are pre-charged when installed at the beginning of the mission and are recharged as needed by extra power from the arrays. It is expected that the power necessary for stationkeeping and housekeeping will be small, therefore, the batteries should add no significant mass to the spacecraft.

SPACECRAFT CONFIGURATION AND STRUCTURE

Tad A. Unger

The three main structural components of the MPD propelled vehicle are the solar array platform, the main body, and the cargo containers. The array platform structure must rigidly support the array while remaining lightweight. The main body, attached to the array platforms' main masts, serves to hold the thrusters, propellant tanks, guidance systems, power conditioning equipment and the payload assembly.

The preliminary analysis uses beam theory to approximate the characteristics of the trusses as beams so that stress components and, ultimately, truss element dimensions can be determined. The natural frequency of the structure is estimated by Rayleigh's method. More accurate and detailed analyses could be carried out using a finite element approach; however, the objective of this analysis is to give a general idea of the masses involved. Generation of a structural model for every proposed configuration would have been too time consuming. Accordingly, there is much optimization left for future studies.

CONFIGURATION OF THE SOLAR ARRAY

The solar cell array structure consists of two platforms, each extending to either side of the vehicle's main body. A series of tetrahedral trusses are attached to a box-truss main mast to form a square platform, as shown in Fig. IV-10. The tetrahedral truss arrangement of the platform is chosen since it uses fewer elements per cell, as compared to a box truss system, while supporting the same area. The term "cell" refers to the smallest section of a truss which has a square base on which to rest the solar cells, i.e. two tetrahedrons or one box.

The box truss is chosen for the main mast since a square has a greater stiffness than a triangle for the same depth. The box truss also provides a flat side to which the roots of the tetrahedral trusses can be attached.

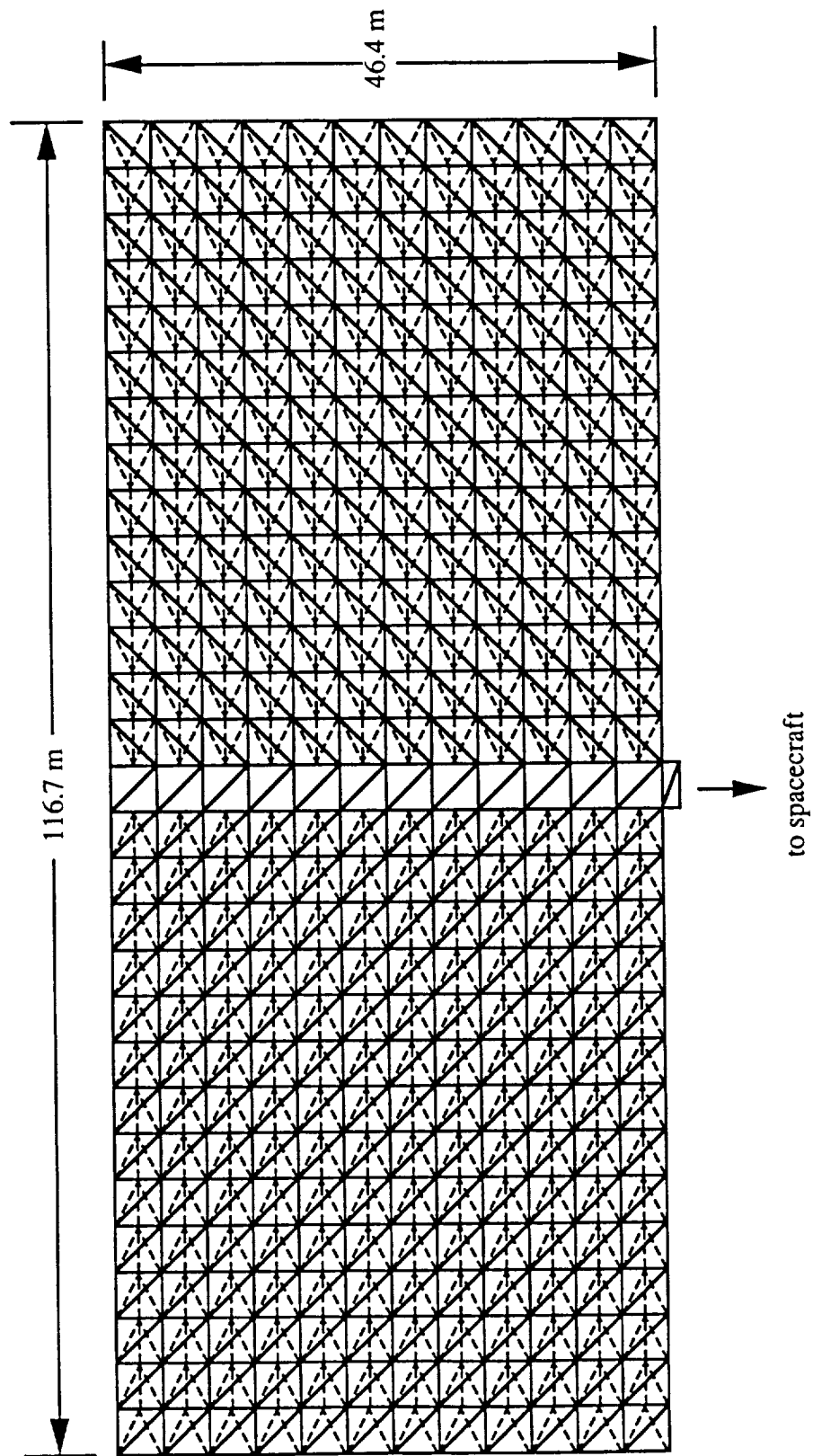


Figure IV-10. One Array Platform.

The solar arrays must be able to turn about one axis so they can be oriented towards the sun. The joint used for this must be able to support the solar arrays and maintain strength and stiffness. The joint must also be able to transmit electrical power from the solar arrays to the main body. The solar alpha joint, designed for the Space Station, could be used for this purpose [23]. This joint rotates about one axis and has the capability of transmitting electrical power. A schematic of the solar alpha joint is shown in Fig. IV-11.

Materials for the structure are the next major consideration. After comparing several types of composite materials on the basis of their mechanical and thermal properties, a graphite/epoxy composite was chosen. Graphite/epoxy has a high longitudinal ultimate tensile strength and stiffness and is lightweight. Typical values for graphite/epoxy composites are shown in Table IV-6.

Table IV-6: Mechanical Properties of the Materials Used in the Structure [24]

Material	Density (kg/m ³)	Axial Tensile Strength (N/m ²)	Young's Modulus (N/m ²)
Graphite/Epoxy, $V_f=55\%$	1490	1.34×10^9	1.5×10^{11}
Ti6AL-4V	4430	1.10×10^9	1.1×10^{11}

Graphite/epoxy also has a very low coefficient of thermal expansion (CTE), which minimizes thermal stresses. Titanium is used for the nodal joints.

The truss elements are hollow cylindrical tubes that are designed to provide sufficient stiffness with minimum mass. A titanium fitting is bonded to each end of the elements to allow attachment to titanium nodes, shown in Fig. IV-12. The manufacturing process for these tubes and successful applications are outlined by Franz

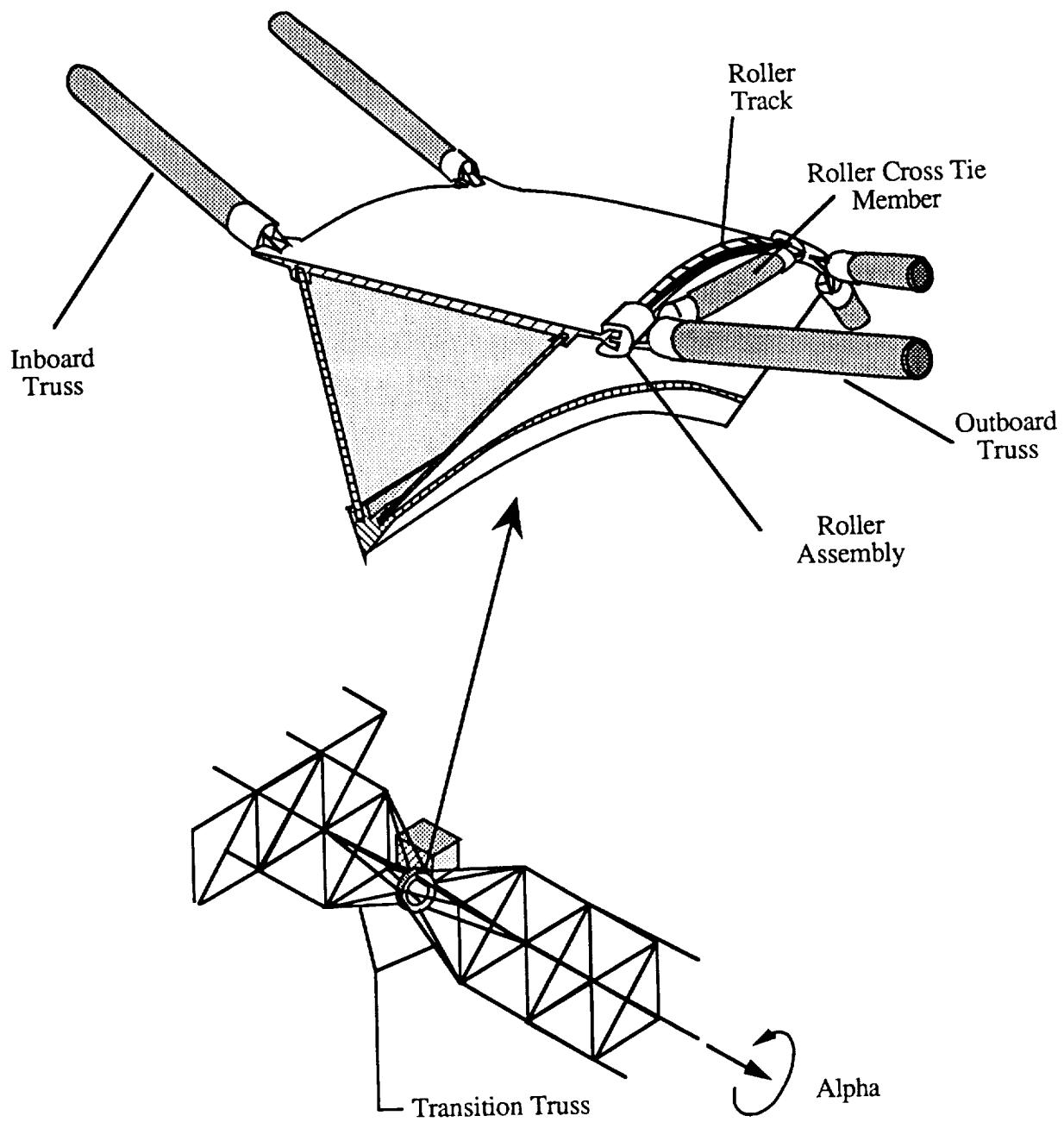


Figure IV-11. Section of the Solar Alpha Joint Assembly.

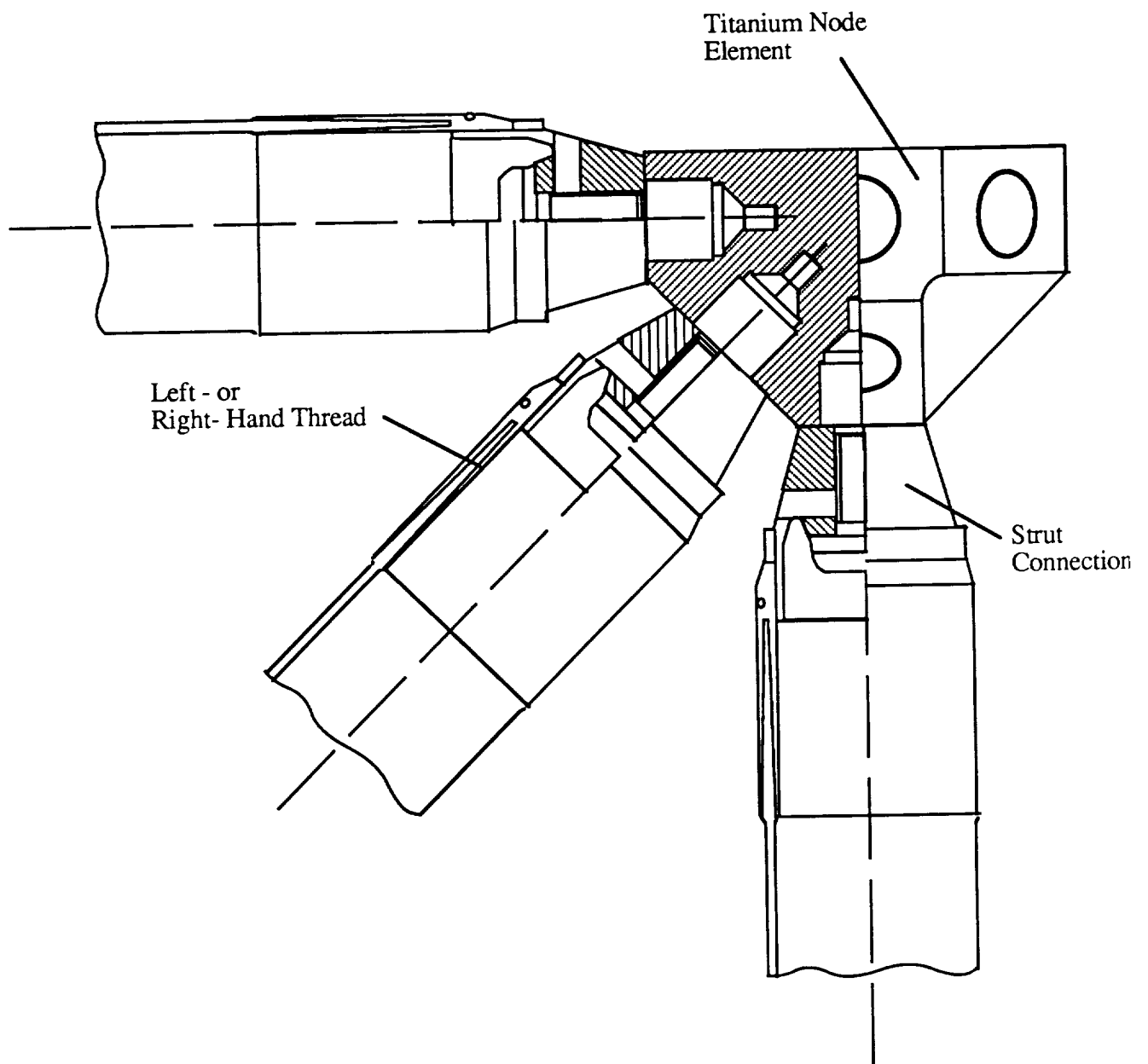


Figure IV-12. Truss Connection Element [19].

and Laube [25]. Both the end fitting and the node are threaded to allow the element to "turnbuckle" into place (Figure IV-12), providing a simple way to achieve good alignment and easy assembly.

STATIC AND DYNAMIC ANALYSIS OF THE ARRAY STRUCTURE

The mast and the platform are made up of truss beams. Beam theory is used to determine displacements and stresses in the longitudinal elements where the stresses are greatest. Beam theory provides the simplest way to estimate element dimensions such as cell size, element diameter, and wall thickness. The maximum stress of the root elements determines the minimum tube size.

The loads on the solar array structure come primarily from inertia and drag. The inertial loads are created by accelerating the structure supporting the solar arrays, the wires for power transfer, and the solar cells themselves.

Drag is a function of density, frontal area, velocity, and a characteristic coefficient of drag associated with a particular design shape. Since the largest density that the spacecraft will encounter occurs in Low Earth Orbit, the drag in this orbit needs to be examined. The atmospheric density in LEO (equivalent altitude of 500 km) is approximately 10^{-13} kg/m³. The velocity of the ship at this altitude is roughly 7.6 km/s. The drag coefficient for a flat plate, in the worst case when the arrays are perpendicular to the direction of travel, is 4 from free molecular flow theory [26]. Table IV-7 shows the drag on the vehicle for a variety of array areas.

Table IV-7: Drag of the Solar Arrays in LEO

Thrust (N)	Total Array Area (m ²)	Total Drag (N)
50	5,540	0.06
100	11,080	0.13
150	16,620	0.19
200	22,160	0.26
250	27,700	0.32
300	33,240	0.38

Another source of loads comes from attitude control jets at the tips of the arrays. These were omitted in this preliminary analysis, but still need to be addressed. Loads from the attitude control jets will probably be instantaneously higher than the inertial or drag loadings.

The strength criteria for the truss elements are determined by the critical compressive buckling stress, which is less than the ultimate tensile strength of the material. Calculations using Euler's formulas for beam columns determine the critical buckling stress in the longitudinal elements at the root of the mast, near the vehicle centerline. Each element is assumed to have pinned ends. The applied moment, from the distributed loads, produces axial stresses along the longitudinal members. The axial stresses must be smaller than the critical buckling stresses to prevent the elements from buckling.

The fact that the elements are interspersed with titanium joints is ignored for simplicity. These joints must be accounted for in later stages of the design since they tend to reduce the stiffness of the structure [27]. Because the beam theory calculations did not include the diagonal elements, the stresses borne by the longitudinal elements are overestimated. The stress results from beam theory are therefore conservative.

The natural frequency of the array structure is another important design consideration. The stiffness of the structure depends on the required natural frequency.

The minimum allowable frequency is roughly 1 Hz, a value comparable with the natural frequency of the space station structure [28]. Below this frequency, maintaining control of the structure becomes difficult.

The structure's natural frequency must not coincide with the frequency of any varying applied loads such as a pulsed thruster or the cyclic thermal expansion and contraction of the structure. Since the MPD thrusters for this mission are steady-state, they do not create an oscillatory force. Also, since the array does not rotate with respect to the sun, cycles of thermal expansion and contraction arise only from entering and leaving the Earth's shadow. This frequency is too low to couple with the natural frequency of the structure.

The most important part of the array structure, dynamically speaking, is the bending of the mast. The natural frequency depends inversely on $L^{3/2}$, where L is the distance from the spacecraft centerline to the tip of one of the arrays. The mast's lowest natural frequency is estimated using Rayleigh's method as outlined in Appendix C. The frequencies for each of the thrust conditions are presented in Table IV-8.

The dimensions of the tube elements for the structure specified by the natural frequency requirement result in such a high critical compressive buckling load for the elements that it becomes unnecessary to worry about any strength criteria. Essentially, the tube size, and therefore the structure mass, is set by the dynamics. The truss element tubes vary in diameter from 5 cm for the smaller arrays to 30 cm for the largest array. The tube wall thickness also varies according to where it is used, the thicker tubes in the mast and thinner tubes in the platform. For the 100 N thrust condition the mast tubes are 5 cm in diameter and have a wall thickness of 6 mm. The mast cells are cubes 9.3 m on a side. The tubes used in the platform are also 5 cm in diameter and have a wall thickness of 2 mm. The platform cells are 8.14 m long and 9.3 m deep.

**Table IV-8: Characteristics of the Array Structure
for Five Thrust Conditions**

Thrust (N)	ω_n (Hz)	Total Array Structure Mass (kg)	m_{sp} (kg/m ²)
50	1.0	3,539	2.2
100	0.9	8,710	2.5
150	1.0	36,810	4.1
200	0.9	72,665	5.4
250	0.9	123,731	6.6
300	0.9	389,445	14.1

The deflection of the array platform under a load, which could reduce the power output from the solar cells, is not a problem. This is due to the high stiffness needed to meet the natural frequency requirement. Under the worst case loading of acceleration and maximum drag, the slope change at the tip for all thrust conditions is negligible.

MASS ESTIMATION AND OPTIMIZATION OF THE ARRAY STRUCTURE

Once the analysis of the structure is performed to verify that the stress and natural frequency requirements are met, the mass of the structure can be determined. The total mass of the tube elements is found by summing the lengths of all elements and multiplying by their mass per unit length as outlined in Appendix C. The structure is assumed to have one uniform tube size for the platform trusses and another for the mast. The uniform tube size assumption is useful for simplified initial configuration studies. In Table IV-8, the masses for five different thrust conditions are presented. This mass includes the elements and the nodal joints.

The total mass of the titanium joints is found by counting the number of nodes and multiplying by the mass per joint. To estimate the mass per joint, a sphere is assumed.

For element attachment, 14 holes, equally spaced over the surface, are bored. The mass of one of these joints is then just the volume times the density.

The specific mass (m_{sp}) of the array structure shown in Table IV-8 is the amount of mass supported by the array structure per unit area, which includes the mass of the structure, solar cells, and wires. The specific mass for current solar array structures is about 1.7 to 2 kg/m² [28]. The specific masses presented in Table IV-8 are much higher than this for the larger structures. This is due mostly to the arcing between solar cells on the array, which makes larger and more wires necessary. For the 100 N thrust condition the wire mass is 43% of the total array. As the power level increases, this figure rises. Further optimization can reduce the structure mass by more efficient utilization of trusses, such as reducing the element mass per unit length as stresses are reduced along the length.

Figure IV-13 indicates that the total mass of the structure, for constant element diameter and thickness, decreases with an increase in element length, or cell size. However, the critical buckling stress decreases with the square of the element length. It was found that stiffening the element by increasing the wall thickness, rather than shrinking the cell size, is more effective per unit mass of the structure as a whole.

With larger cell sizes, it is possible that the solar cells may not be able to support themselves under a load, such as drag. If this is the case, the truss cell size can be reduced. Since cell size has an extreme effect on the overall mass, it may prove beneficial to attach the solar cells to a stiffening mesh backing strong enough to support the loading, then attach the mesh to the truss.

MAIN BODY STRUCTURE

Figure IV-14 shows the main body configuration. The components of the main body include the primary container, two secondary containers, and the structure to hold the propellant tank. The main body is made up of box trusses.

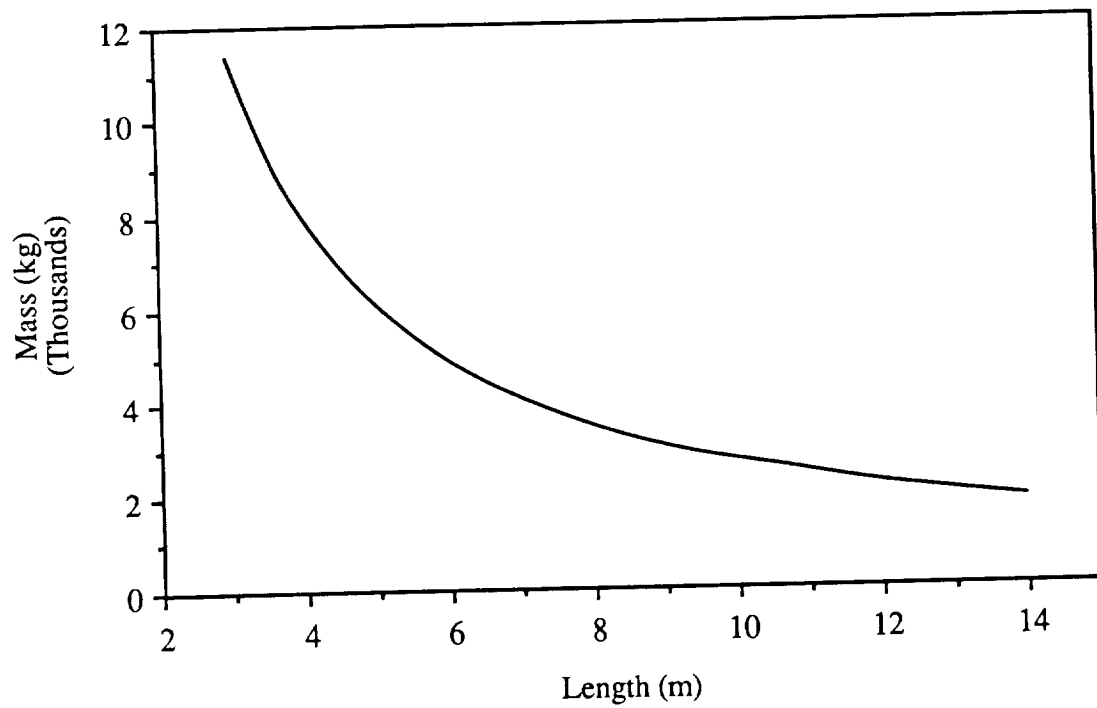


Figure IV-13. Array Structure Mass vs. Element Length for Constant Tube Size.
($d=5$ cm, $t=1$ mm)

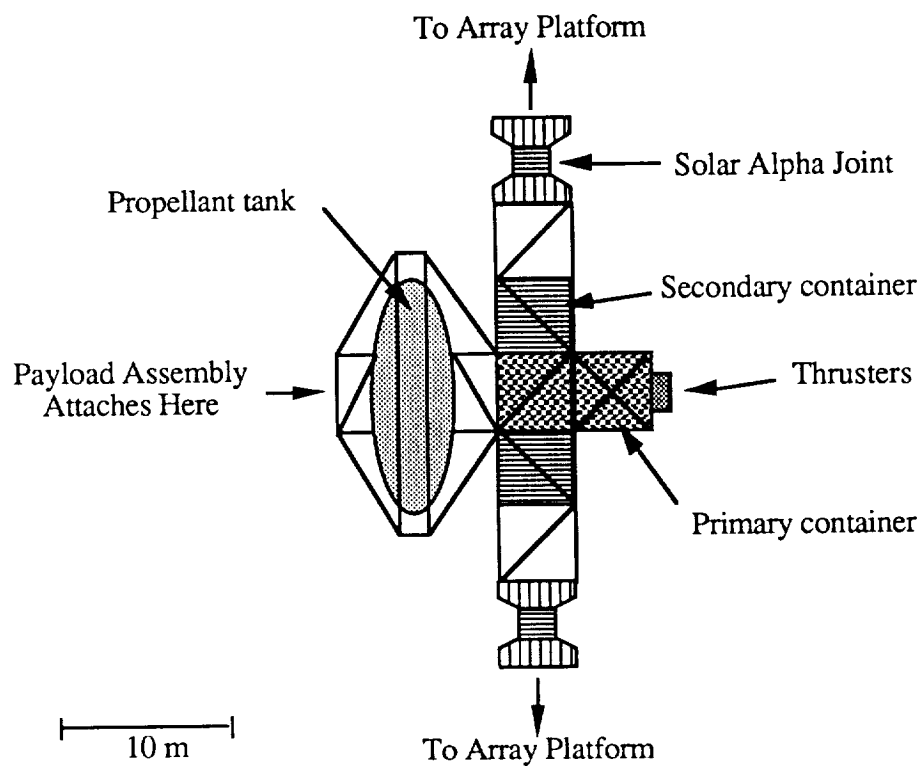


Figure IV-14. Main Body Structure Arrangement.

The primary container holds the thrusters, pumps, cooling systems, power conditioning equipment, and navigational equipment. The primary container, made from graphite/epoxy, is cylindrical in shape. This cylinder is 8 m long and 2 mm thick with a radius of 2 m, allowing it to fit inside the main body truss system. The two secondary containers house the electronics for communications equipment and control equipment needed to operate the attitude control jets (propellant, pumps, electronics, etc.). The secondary containers are also made of graphite/epoxy and are cylindrical in shape. The dimensions of the support containers are 4 m in length, 2 mm thick with a radius of 2 m. The structure needed to support the propellant tank uses 64 truss elements and 16 titanium joints. The mass of the main body structure is given in Table IV-9.

Table IV-9: Main Body Structure

Component	Mass (kg)
Primary Container	337
Secondary Containers (2)	375
Propellant Tank	2,250
Structure	46
Total	3,008

Cargo Containers

The cargo containers, two in all, are cylinders 18 m long and 4.3 m in diameter. These dimensions allow the containers to be carried up on the space shuttle. Each container will hold 25,000 kg of payload.

A stress analysis was carried out on the containers to determine their mass. The maximum loading of the containers will occur during the aerobraking maneuver where an acceleration of about 1.5 g's will be felt. Details of the aerobrake structure are discussed in Appendix A. As a first approximation the cargo is assumed to be uniformly distributed

along the cylinder. This load may then be treated as dead weight. The stress in the cylinder away from the ends is given by shell theory for cylinders. Close to the ends of the cylinder this theory does not apply. However, because of the end plates, the ends of the container should be stronger than the middle. The stress results from this procedure lead to a wall thickness of 2 mm giving a container mass of 1,000 kg. Additional material near the ends of the cylinder, to resist any significant bending moments induced, should not change this result by very much.

MASS INVENTORY OF SPACECRAFT

The mass of each component of the spacecraft is presented in Table IV-10.

Table IV-10: Spacecraft Mass Inventory

Component	Mass (kg)
Main Body and Array Structure	11,700
Power Supply (cells, wires, transformers, etc.)	19,370
Thruster Assembly	5,420
Payload Assembly	62,660
Total Dry Mass	99,150
Propellant Mass	170,000
Total Initial Mass	269,150

ORBITAL MECHANICS

Jacqueline Auzias de Turenne
Barbrina Dunmire

The solar-powered MPD propelled spacecraft begins its mission from an initial low Earth orbit (LEO), 500 km above the surface of the Earth and aligned with the ecliptic plane. As opposed to the SRA powered spacecraft and the SPL powered spacecraft, however, the MPD powered spacecraft does not return to the Earth. Instead, the spacecraft remains in a high Mars orbit providing an orbiting control center for the subsequent manned Mars missions. The one-way transfer of the MPD propelled spacecraft from LEO to Mars can be separated into three phases:

- (1) Earth Escape
- (2) Earth-to-Mars Transfer
- (3) Mars Encounter

Due to the low thrust nature of the MPD propelled spacecraft, impulsive orbital maneuvers such as a Hohmann transfer, or similar elliptical transfers which intersect the orbit of Mars and require a minimum hyperbolic excess speed at Earth orbit of 3 km/sec, which cannot be performed. The patched conic technique was used to approximate an orbital trajectory from the Earth to Mars. The patched conic approximation defines distinct spheres of influence about each gravitational body, allowing the sequential solution of the two body problem [28]. The interplanetary trajectory of the MPD propelled spacecraft is depicted in Fig. IV-15.

It should also be noted that throughout this orbital analysis, the following assumptions were made:

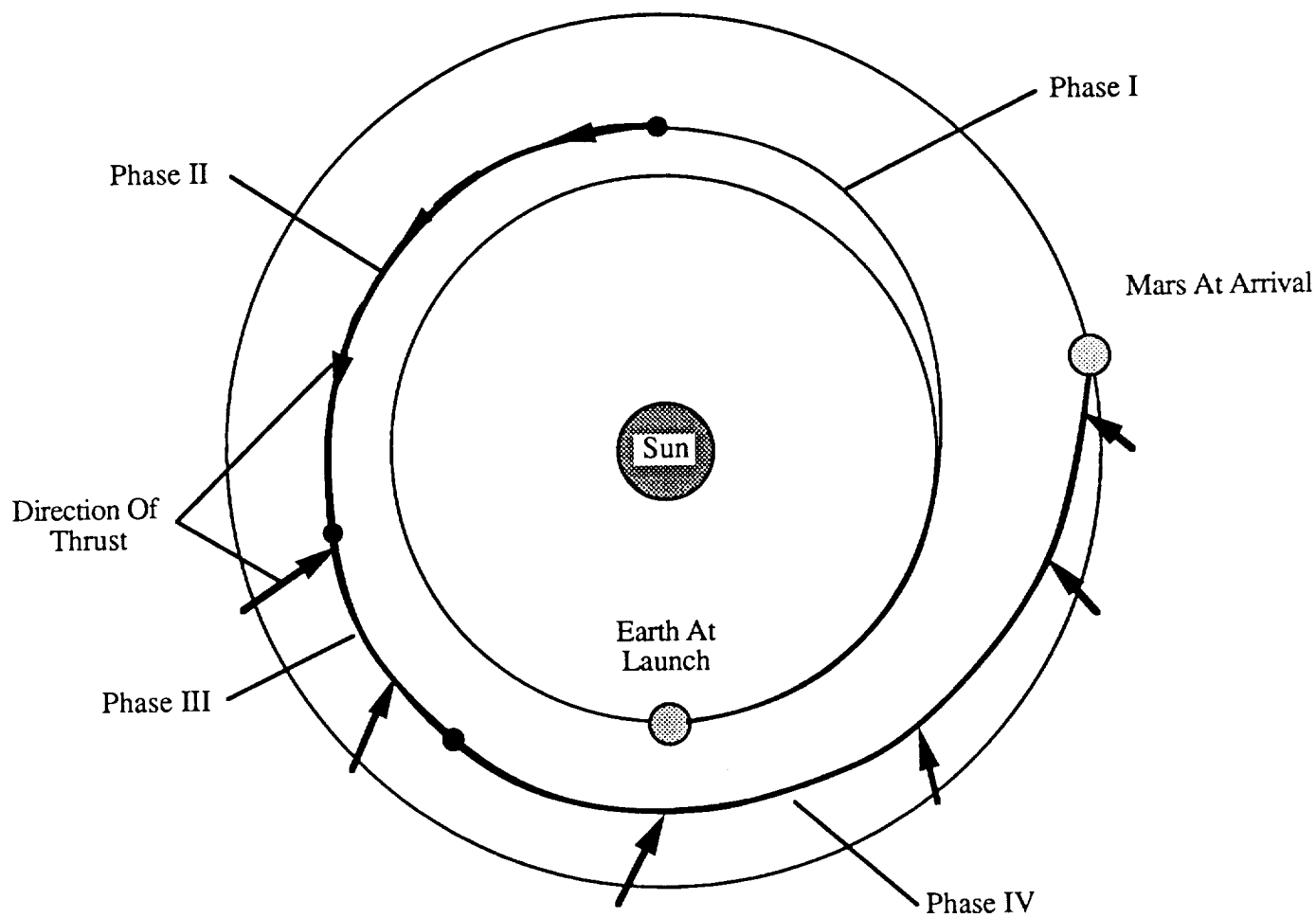


Figure IV-15. Heliocentric Interplanetary Trajectory.

- (1) At any time during the transfer, the spacecraft is under the influence of only one gravitational body.
- (2) The spacecraft operates in the absence of aerodynamic drag. The drag effects felt by the spacecraft near the Earth are negligible, as determined earlier.
- (3) The orbits of both the Earth and Mars are circular and coplanar.

The following analysis is a preliminary examination of the orbital mechanics for this solar-powered MPD propelled vehicle. It should be noted that the patched conic analysis presented here indicates *one* possible orbital trajectory of an MPD propelled spacecraft designed for Mars missions. The basic elements of this interplanetary transfer to Mars are described. Further research will be required to determine a more optimum interplanetary transfer.

EARTH ESCAPE

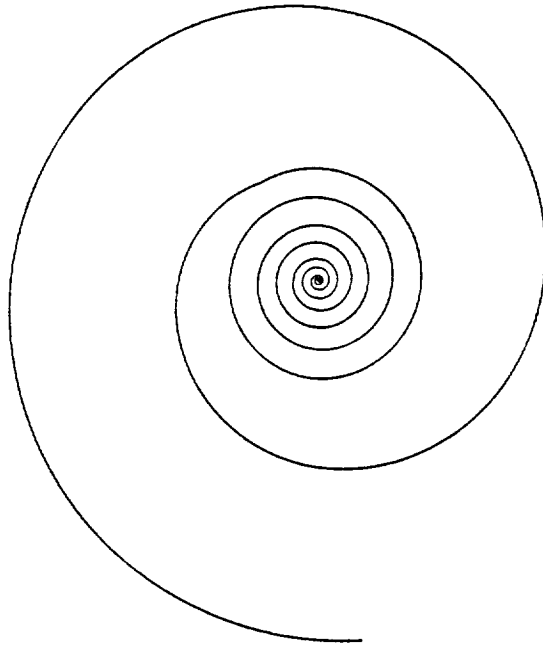
The MPD propelled spacecraft uses a spiral transfer orbit to escape the Earth's gravitational field, as shown in Fig. IV-16. Spiral maneuvers allow for slower energy gains, which can be supplied by the low thrust MPD thrusters. The equations governing the motion of the spacecraft [29] are shown below:

$$\ddot{r} = \frac{F \cos \theta \dot{r}}{m_t v} - g_0 \left(\frac{r_e}{r} \right)^2 + r \dot{\phi}^2 + \frac{F \sin \theta}{m_t} \quad (\text{IV-9})$$

$$\ddot{\phi} = \frac{F \cos \theta \dot{\phi}}{m_t v} - \frac{2 \dot{r} \dot{\phi}}{r} \quad (\text{IV-10})$$

where

$$v = \left(\dot{r}^2 + (r \dot{\phi})^2 \right)^{0.5} \quad (\text{IV-11})$$



Altitude of Initial Orbit: 500 km

Thrust: 100 N

Radius at Escape: 734,744 km

Time of Escape: 196 days

Radius of Sphere of Influence: 1×10^6 km

Time to Reach Sphere of Influence: 201 days

All spiral transfers are representative cases. Not all revolutions are shown.

Figure IV-16. Earth Escape

The equations of motion define the radial position, r , of the spacecraft measured from the center of the Earth and the angular position, ϕ , of the spacecraft measured from its initial position. The thrust from the MPD thrusters and the instantaneous mass of the vehicle are represented by F and M_t , respectively, while the gravitational acceleration at the surface of the Earth is indicated by g_0 and the radius of the Earth is indicated by r_e .

A fourth-order Runge-Kutta integration of the equations of motion was used to determine the characteristics of the spiral trajectory [30]. The integration was carried out over arbitrary intervals of 500 seconds, or 8.33 minutes. Smaller time intervals resulted in increased computational time without any significant increase in accuracy.

The MPD propelled spacecraft begins the spiral transfer solely under the gravitational influence of the Earth. The spacecraft uses constant, tangential thrust throughout the maneuver. Upon achieving the local escape velocity, the spacecraft ceases its spiral trajectory and enters a parabolic orbit. The local escape speed, v_{esc} , is determined from the equation below:

$$v_{esc} = \sqrt{\left(\frac{2\mu}{r}\right)} \quad (IV-12)$$

The escape speed is defined in the reference frame of the Earth and depends on the gravitational parameter of the Earth, μ_e , and the radial distance from the center of the Earth to the spacecraft, r .

The computer program used to perform the Runge-Kutta integration, designated SPIRAL, appears in Appendix D. Using SPIRAL, the time required to reach the point of departure and the altitude at the point of departure were determined for various thrust levels of the MPD thrusters and the corresponding spacecraft configurations. Since the MPD propulsion system operates only when solar energy is available, SPIRAL accounts for a coast phase during each revolution about the Earth as the spacecraft travels through the Earth's shadow.

The time results from SPIRAL are shown in Fig. IV-17. Since the spiral maneuver is a constant thrust maneuver, the time duration of the spiral transfer also indicates the corresponding thruster burn time. Vehicles operating at higher thrust levels are able to complete spiral maneuvers faster and have lower thruster burn times than vehicles operating at lower thrust levels. At thrust levels above approximately 100 N, however, the increasing total mass of the spacecraft becomes the dominant factor and increases in thrust can no longer accommodate the corresponding increases in total vehicle mass. Consequently a minimum thruster burn time required to reach escape speed occurs at the 100 N level. The minimum thruster burn time eliminates the need to carry and configure an excess of thrusters as well as the associated solar array and structural components. The radius at escape for a spacecraft providing 100 N of thrust is approximately 7.3×10^5 km.

The characteristic velocity change, Δv , for the spiral transfer is determined from the equation below:

$$\Delta v = u_e \ln \left(\frac{m_o}{m_f} \right) \quad (IV-13)$$

The Δv of a mission is a measure of the energy input to the spacecraft and depends on the exhaust velocity of the thrusters, u_e , and the initial and final masses of the spacecraft, m_o and m_f , respectively. Low thrust missions in the near vicinity of a gravitational body experience large gravity losses. Consequently, more energy is needed to perform orbital maneuvers, and the characteristic Δv for the transfer is increased. The Δv value required to reach escape speed at the 100 N thrust level was 7.3 km/sec.

EARTH-TO-MARS TRANSFER

When the spacecraft attains the escape velocity, it has not yet departed the Earth's sphere of influence. At the 100 N thrust level, the radius at escape is 7.3×10^5 km, as stated earlier, while the sphere of influence of the Earth is approximately 10^6 km.

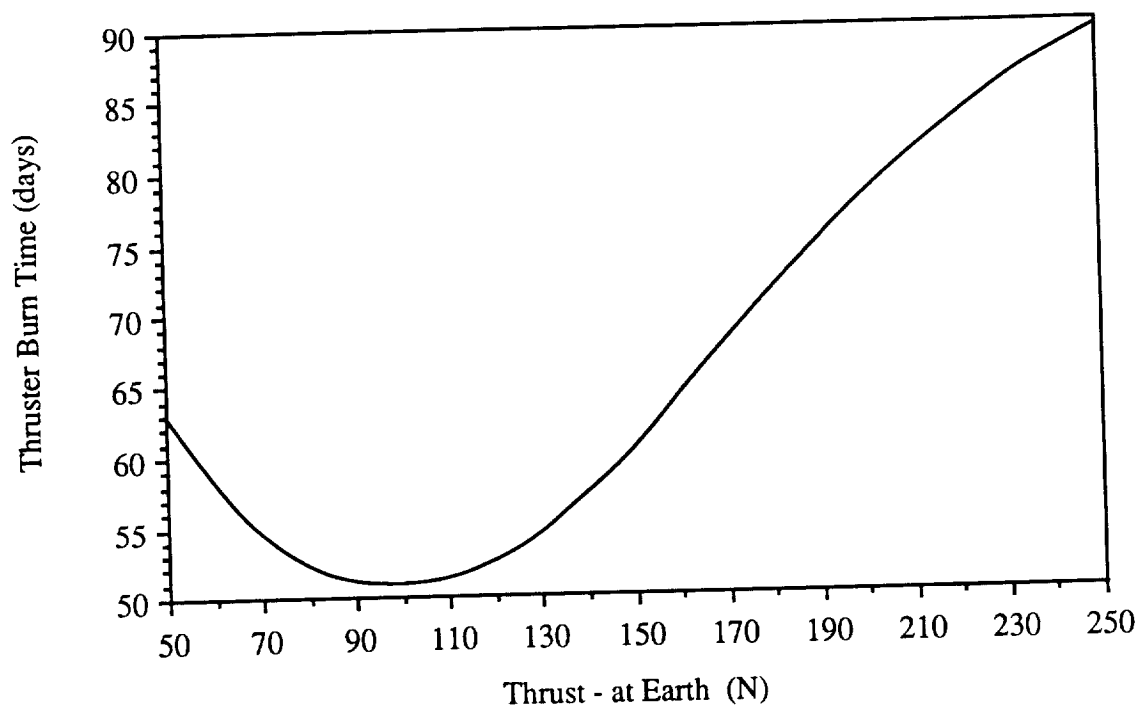


Figure IV-17. Thruster Burn Time Dependency on Thrust.

Therefore, the spacecraft remains under the effect of the Earth's gravitational influence. Maintaining a constant tangential thrust of 100 N, the spacecraft achieves a velocity of approximately 30.8 km/sec, with respect to the sun, at the edge of the sphere of influence, as determined through SPIRAL.

Upon escape from the Earth's sphere of influence, the MPD propelled spacecraft begins to experience the gravitational effects of the sun. All geocentric coordinates are converted to a heliocentric coordinate system [31]. The spacecraft coasts, accelerates, and then decelerates as it travels en route to Mars [33,34]. Throughout the heliocentric transfer, the MPD propelled spacecraft accounts for the diminishing thrust available as the distance from the sun increases, as shown in Fig. IV-4. All orbital calculations during the heliocentric transfer were performed through a computer program, HELIOCENTRIC, which also uses a Runge-Kutta integration to numerically solve the equations of motion of the spacecraft about the sun. HELIOCENTRIC appears in Appendix D.

The desired Earth-to-Mars transfer orbit requires a minimum radial velocity approaching Mars in order to reduce the amount thrust required to enter a Mars parking orbit. The heliocentric interplanetary transfer is shown in Figure IV-15. The radius and thrust angle, along with the thrust at each radius, the time spent at each radial stage of the heliocentric transfer, and a nominal phase reference, are listed in Table IV-11.

During Phase I of the heliocentric transfer, the spacecraft coasts in order to decrease the velocity of the spacecraft through a reduction of the radial velocity component. Without further application of thrust, however, the spacecraft would return to the Earth's Orbit along an elliptical path after reaching a radius of 1.8×10^8 km. Therefore, during Phase II, a tangential thrust of 60 N is applied in order to maintain the outbound trajectory toward the Martian Orbit. Although 80 N of thrust is available during Phase II, only a 60 N tangential thrust is required to produce a sufficient velocity increase.

In Phase III, 80 N of thrust is applied at a thrust angle of -110° to again begin decreasing the radial component of velocity. Finally, during Phase IV of the heliocentric

Table IV-11: Characteristics of the Heliocentric Transfer Orbit

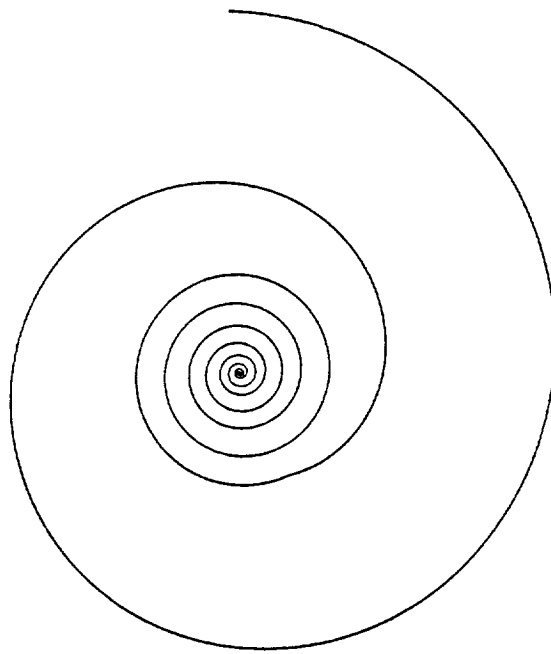
Phase	Radius Range $\times 10^8$ (km)	Thrust (N)	Thrust Angle (deg)	Time (days)	Radial Velocity (km/s)	Tangential Velocity (km/s)
I	1.50 to 1.83	0	0	209	0.166	25.61
II	1.83 to 1.85	60	0	140	3.031	29.30
III	1.85 to 2.00	80	-110	56	2.52	26.14
IV	2.00 to 2.4	60	-65	235	1.881	26.48

transfer orbit, 60 N of thrust is applied at a thrust angle of -65° to further decrease the radial component of velocity, and to reduce the tangential velocity, on the spacecraft's final approach to the Martian orbit. The final velocity upon approach to the orbit of Mars is approximately 26.5 km/sec and corresponds to an angle of 3° between the orbit of Mars and the flightpath of the spacecraft. The approach velocity relative to Mars is approximately 2.41 km/sec. The total time of the Earth-to-Mars transfer, excluding any time spent performing spiral maneuvers at either the Earth or Mars, is approximately 640 days, or 1.75 years.

MARS ENCOUNTER

The Mars encounter consists of maneuvers by the MPD propelled spacecraft to deliver its payload into a low Mars parking orbit, while the mother spacecraft enters into a high Mars parking orbit and becomes an orbiting control station for ensuing manned Mars missions. The payload's aerobrake maneuver is discussed in detail in Appendix A. The altitude of the low Mars parking orbit was selected arbitrarily through a density analysis of the Martian atmosphere to be 300 km above the planet's surface [32]. At an altitude of 300 km, the density of the Martian atmosphere is equal the density of the Earth's atmosphere at an altitude of 500 km, thereby determining the equivalent to LEO at Mars. The altitude of the high Mars parking orbit is designated, also arbitrarily, to be 4600 km.

After releasing the payload assembly, the mother spacecraft proceeds to follow a spiral descent into the high Mars parking orbit, as shown in Fig. IV-18. At Mars, a maximum thrust of 40 N is applied tangentially throughout the spiral maneuver. The characteristics of the Martian spiral descent were determined through a modified version of SPIRAL, MSPIRAL, specific to Mars. MSPIRAL appears in Appendix D. The spacecraft required 33 days to perform this maneuver. The total flight time from LEO to the high Mars orbit is 873 days or 2.39 years.



Altitude of Parking Orbit: 4600 km

Thrust: 40 N

Time of Spiral: 33 days

Figure IV-18. Mars Encounter.

CONCLUSION

Jacqueline Auzias de Turenne

This section of the report has presented a feasibility study of an MPD propelled spacecraft for use as a cargo ferry to deliver a 50,000 kg payload to Mars. The MPD propulsion system ionizes the incoming gaseous argon propellant and uses electromagnetic forces to accelerate the resulting plasma to a high exhaust velocity. The thrusters are low thrust devices (20 N each) with a 2000 hour lifetime per cluster. A multiple thruster configuration, consisting of 43 thrusters, allows a cluster of five units at a time to be fired for the lifetime of the thruster set before an alternative set of thrusters is fired. Argon appears to be a promising propellant as a result of its high density, high liquefaction temperature, and low vaporization energy. The argon is stored in an ellipsoidal fuel tank, with a volume of 78 m³.

The power to operate the thrusters comes from two indium phosphide solar arrays. Indium phosphide solar cells are expected to achieve efficiencies of 21%, along with an increased production rate, within the next 20 years. The degradation incurred from the Van Allen radiation belts is eliminated through the process of self-annealing. Self-annealing passes current from operational solar cells through forward biased diodes within degraded cells to maintain a maximum efficiency for the duration of the mission. The power from the solar arrays is conditioned through a constant voltage transformer and an inverter prior to use in the MPD thrusters.

The support structure for the MPD propelled spacecraft is composed of graphite/epoxy truss elements interconnected with titanium joints. Graphite/epoxy minimizes structural mass while providing maximum rigidity for the spacecraft. A key structural element is the solar alpha joint, which allows the solar arrays to rotate about one axis while transmitting electrical power from the solar arrays to the power conditioning components within the main body of the spacecraft.

The orbital mechanics of the MPD propelled spacecraft was determined through patched conic approximations. The spacecraft follows a spiral trajectory to escape the gravitational influence of the Earth, and enters a heliocentric transfer to Mars, which consists of a coast phase, an acceleration phase, and a deceleration phase. As the spacecraft approaches Mars, the payload assembly is jettisoned to follow an aerobrake maneuver into a low Mars parking orbit. The mother spacecraft uses a spiral maneuver to enter a high Mars parking orbit, where it remains as an orbiting control station. The total flight time required for the spacecraft to reach Mars is approximately 873 days, or 2.39 years while the total vehicle mass is 269,150 kg, indicating a payload mass ratio of 19%.

Refinements in the orbital transfer of the spacecraft are expected to reduce the required thruster burn time, and thus propellant consumption, consequently increasing the payload capacity (mass ratio). Nevertheless, an MPD propelled spacecraft is a viable option for deep space travel.

NOMENCLATURE

A	surface area
b	constant of proportionality
BOL	beginning of life
B_{θ}	azimuthal magnetic field
C_p	specific heat
CTE	coefficient of thermal expansion
d	thickness
e	electron charge
E_{vap}	vaporization energy
F	thrust
f_r	electromagnetic pumping force
f_z	electromagnetic blowing force
g_0	gravitational acceleration at the earth's surface
I_s	intensity of the sun
j_r	radial arc current
j_z	axial arc current
J	diffuse arc current
k	conductivity of heat coefficient
L	distance
LEO	low Earth orbit
m	mass
\dot{m}	mass flow rate
M	molecular mass
MLI	multilayer insulation
MPD	magnetoplasmdynamic

N_o	Avogadro's Number
\dot{Q}	heat flux
\dot{Q}_1	heat flux through the MLI to the outer propellant tank wall
\dot{Q}_2	heat absorbed by the propellant
r	radius
T	temperature
T_{liq}	liquid storage temperature
T_{ext}	external storage temperature
T_1	external surface temperature of the vapor cooled shield
T_2	temperature of propellant vapor in the vapor cooled shield
T_3	temperature of the exiting propellant liquid
u_e	exit velocity
v	velocity of the ship
V	potential difference
α	absorptivity
Δ	change in
ϵ	emissivity
ϵ_i	ionization potential
η	overall efficiency of the thruster
μ	gravitational parameter
μ_o	permeability of free space
θ	thrust angle
ρ	density
σ	Stephan-Boltzman constant
φ	angular position
ω_n	natural frequency

Subscripts

a	anode
c	cathode
cr	critical value
e	Earth
esc	escape
f	final state
liq	liquid
o	initial state
sp	specific
t	instantaneous value

A dot above a variable ($\dot{}$) indicates a time derivative. Successive dots indicate successive time derivatives.

All values are in MKS units.

REFERENCES

1. Cassady, R. J., "An MPD Thruster Driven Cargo Ferry for Support of the Manned Mars Mission", AIAA/ASME/SAE/ASEE 24th Joint Propulsion Conference, AIAA Paper No. 88-2896, July, 1988.
2. Jahn, R. G., Physics of Electric Propulsion, McGraw-Hill Book Co., New York, 1968.
3. Rudolph, L. K. and Pawlick, E. V., "The MPD thruster Development Program", AIAA Paper No. 79-2050, Oct., 1979.
4. Tahara, H., "A Quasi-Steady MPD Arc Jet for Space Propulsion", 17th International Electric Propulsion Conference, Tokyo, Japan, May 28-31, 1984.
5. Malliaris, A. C., et al., "Performance of Quasi-Steady MPD Thrusters at High Powers", AIAA Journal, Vol. 10, 1972.
6. King, D. Q. and Sercel, J. C., "A Review of the Multimegawatt MPD Thruster and Current Mission Applications", AIAA Paper No. 86-1437, June, 1986.
7. King, D. Q., et al., "Effect of Thrust Chamber Configuration on MPD Arcjet Performance", AIAA Paper No. 79-2051, Oct., 1979.
8. Coomes, E. P., et al., "The Pegasus Drive - A Multimegawatt Nuclear Electric Propulsion System", in Space Nuclear Power Systems, Orbit Book Company, Malabar, FL, pp. 365-373, 1987.

9. Kit, B. and Everud, D., Rocket Propellant Handbook, The Macmillan Co., NY, 1960.
10. Brown, N. S., "Advanced Longterm Cryogenic Storage Systems", Lewis Research Center Microgravity Fluid Management Symposium, Cleveland, OH, April, 1987.
11. Holman, J. P., Heat Transfer, McGraw-Hill Book Co., New York, 1986.
12. Carney, M. J., "Liquid-Vapor Interface Locations in a Spheroid Container Under Low Gravity", NASA N86-23854, April, 1986.
13. Eberhardt, R. N., Feste, D. A., and Aydelott, J. C., "Shuttle Compatible Cryogenic Liquid Storage and Supply Systems", AIAA Paper No. 81-1509, July, 1981.
14. Hess, W. N., The Radiation Belt and Magnetosphere, Blaisdell Publishing Co., New York, 1968.
15. Scott-Monck, J. and Stella, P., "Advanced Photovoltaic Solar Array Design Assessment", N87-26429, Jet Propulsion Laboratory, Pasadena, CA., May, 1987.
16. Kurland, R. and Stella, P., "Status of Advanced Photovoltaic Solar Array Program", TRW Space and Technology Group, Redondo Beach, CA. / Jet Propulsion Laboratory, Pasadena, CA., 1988.

17. Brinker, D.J. and Weinberg, I., "Indium Phosphide Solar Cells - Status and Prospects for Use in Space", NASA TM-87315, NASA Lewis Research Center, Cleveland, OH., 1986.
18. Curtis, H.B., and Hart, R.E., Jr., "Performance of AlGaAs, GaAs, and InGaAs Cells After 1 MeV of Electron Irradiation", NASA Lewis Research Center, Cleveland, OH., 1987.
19. Weinberg, I., NASA Lewis Research Center, Cleveland, OH., Private Communication, Feb., 1989.
20. Stella, P., Jet Propulsion Laboratory, Pasadena, CA., Private Communication, Feb., 1989.
21. Calloway, T. M., Leeman, J. E., and Key, T. S., "Comparison of Designs for Photovoltaic Power Conditioners", Sand 86-0184, Sandia National Laboratories, Albuquerque, NM., 1986.
22. Faymon, K. A., "Space Power Technology to Meet Civil Mission Requirements", AA420 Guest Lecturer, University of Washington, Jan. 31, 1989.
23. Mikulas, M. and Bush, H., "Design, Construction, and Utilization of a Space Station Assembled From a 5 Meter Erectable Truss", NASA TM-89043, NASA Langley Research Center, Oct., 1986.
24. Chetty, Satellite Technology and its Applications, Tab Book, Inc., 1988.

25. Franz, J. and Laube, H., "Design and Manufacture of Tubular Carbon Fiber Composite/Titanium Bonded Joints", *Composite Structures*, Vol. 6, No. 1-3, pp. 183-196, 1986.
26. Eberhardt, S., Department of Aeronautics and Astronautics, University of Washington, Private Communication, Feb., 1989.
27. Bush, H. G. and Mikulas, M. M., "Advances in Structural Concepts", NASA CP-2269 Part 1, NASA Langley Research Center, May 1983.
28. Mikulas, M., NASA Langley Research Center, Private Communication, March 6, 1989.
29. Bate, R. R., Mueller, D. D., and White, J. E., Fundamentals of Astrodynamics, Dover Publications, Inc., New York, 1971.
30. Stuhlinger, E., "The Flight Path of an Electrically Propelled Space Ship", *Jet Propulsion*, Vol. 27, pp. 410-414, 1957.
31. Paris, S. W., Flight Mechanics Specialist, Boeing Aerospace Co., Seattle, WA, private communication, March, 1989.
32. Stuhlinger, E., Ion Propulsion for Space Flight, McGraw-Hill Book Company, New York, 1964.
33. Bruckner, A. P., Research Professor, Department of Aeronautics & Astronautics, University of Washington, Seattle, WA, private communication, March, 1989.

V. CONCLUSION

CONCLUSION

Amy Prochko

Each propulsion system collects and exploits solar energy in very different ways. The spacecraft designs are unique according to the individual requirements of the propulsion system. The Solar Radiation Absorber (SRA) system directly concentrates the solar radiation into two chambers where it is absorbed by alkali metal vapor which transfers the energy to the primary component of the propellant, hydrogen. The Solar-Pumped Laser (SPL) system uses concentrated solar energy to pump two 6 MW CO₂ lasers located on two platforms in sun-synchronous orbit around the Earth. The resultant laser beams are directed and transmitted to receivers on the spacecraft, which relay them to two thruster chambers, where the laser beams generate a hydrogen plasma. The Magneto-plasmdynamic (MPD) system converts solar energy to electricity which is used to ionize argon and accelerate the resultant plasma by electromagnetic body forces. Specific impulses vary from 1,000 s for the solar radiation rocket to 2,490 s for the magneto-plasmdynamic thruster.

The SRA system offers the largest payload mass fraction (37%) and the lowest initial mass (135,500 kg). The latter is an important parameter because all of the components, materials and propellant necessary for the Mars cargo mission must originally be brought up from Earth to LEO. Thus, even with anticipated reductions in the cost of lifting payloads to LEO, there is a great premium on minimizing the initial mass of the interplanetary spacecraft. The superior performance of the SRA spacecraft is a direct result of the ability of its thruster to deliver both a high specific impulse (1000 sec) and a relatively high thrust (30 times higher than the MPD system). This dual capability reflects back in a considerable savings in the required amount of propellant, resulting in a low initial mass and a high payload fraction. The total trip time to Mars (281 days) is relatively short. Furthermore, the SRA spacecraft can be used in a novel "slingshot" orbital

maneuver which sends only the payload system to Mars and returns the mother craft to LEO only 23 days after launch, whereupon it can be reused for other missions. Clearly, such favorable performance invites more comprehensive investigation of this propulsion concept.

The SRA system presents a number of important technological problems, however. Although experimental proof of concept has been demonstrated, much work remains to be done on the physics of the interaction of solar energy with the alkali seeded hydrogen, on the handling of the high temperature, corrosive potassium, on the design of a suitable window, and on the problems of heat transfer and erosion in the thrust chamber. Research in these areas is currently under way at the University of Washington.

The SPL system has an initial mass of nearly 205,000 kg and a payload mass fraction of 24%, which render it less desirable than the SRA system. However, the most serious shortcoming of the SPL system is that it requires a complex infrastructure of space-based lasers and relay satellites, as well as extremely stringent tracking capabilities. The latter could be ameliorated by using an orbital mechanics scenario similar to that of the SRA system. Many additional problems also need to be resolved before the laser propulsion concept can be implemented. The required CW laser power levels have not yet been attained on Earth. Additional research is needed in the areas of plasma stability, reradiation losses, and cooling requirements. Even for an optimal orbital transfer scenario, the complexity and cost of the entire system is likely to make it impractical.

The MPD propulsion system appears to be the most technologically feasible at this time; however, its implementation is predicated on the availability of indium phosphide photovoltaic cells of 21% efficiency. Even so, its payload mass fraction (19%) appears to be only marginally better than that which might be achieved using a Shuttle-derived chemical propulsion system, and its initial mass, nearly 270,000 kg, is the highest of the three spacecraft presented here. In addition, the MPD spacecraft requires the longest trip time, 2.39 years, and must remain in Mars orbit, preventing its reuse for subsequent cargo

missions. Clearly, considerable work remains to be done to enhance the payload mass fraction and reduce the initial mass of the solar-MPD system, to decrease its trip time, and to permit recovery of the spacecraft for reuse in future missions.

The propulsion concepts presented here use the most abundant source of energy available in space: the sun. However, much further research is required if this resource is to be effectively exploited to transport large payloads to Mars and other planets within the solar system.

VI. APPENDICES

APPENDIX A

Aerobraking at Mars

Shawn McCracken
Mike Rhodes

Since cargo missions to Mars require vehicles of considerable size, containing large amounts of propellant, missions become very expensive. Therefore, this report has presented alternative high performance propulsion methods which use solar energy. The three vehicle concepts in this report release the payload outside the sphere of Mars. Large amounts of propellant would also be required to impulsively decelerate the payload with chemical thrusting into low Mars orbit (LMO). Because of this, efforts have been made to consider an alternative orbital maneuvering approach. Recent advances in technology have made it possible to design an aeroassisted transfer vehicle (ATV) which uses the atmosphere of Mars to decelerate the vehicle through its drag and lift, in order to maneuver into an elliptical orbit with the apogee extending beyond the atmosphere. A small burn is then required to circularize into the desired parking orbit. The ATV thus reduces the amount of propellant required for the mission and increases the payload capacity of the spacecraft by eliminating the propellant necessary for a retro-burn to decelerate the vehicle from a hyperbolic orbit. Only propellant to circularize from an elliptical orbit is thus required. Accounting for the thermal shield mass, aerobraking results in a lower overall system mass, and thus, more efficiently decelerates the vehicle than thrusting for impulsive maneuvers [1,2]. As a result, aerobraking was chosen for capture into LMO for all three designs in this report. Discussions on the vehicle design, flight path, stability and control, flow impingement, heat transfer, shielding materials, and component masses follow.

Aerobrake Vehicle Design

Many vehicle designs have been studied for Mars missions. The ATV with a raked-off sphere cone aeroshell, shown in Fig. A-1, is the best design for aerocapture missions where landing the vehicle is not required [3]. This aeroshell design consists of a spherical nose with a radius of 4m and a circular cone after-body raked-off 62° from the cone axis. The aeroshell shields the cargo while it provides lift and drag to decelerate and maneuver the ATV into the desired orbit. With this design, the overall dimensions of the vehicle are 25 m for the frustum diameter (major axis) and 16.5 m for the minor axis diameter.

In the raked-off sphere cone configuration, the cargo is located behind the shield with its center of mass on the line of force that represents the lift and drag of the vehicle. Around the cargo, propellant containers for circularizing the orbit and for trajectory adjustments outside of the atmosphere are located symmetrically around this line of force. Two tanks for liquid oxygen are located in front and behind the payload, and two liquid hydrogen tanks are located on each side of the payload. The propellant acquisition uses surface tension to draw out the liquid. This acquisition system is the same as the ones used in the solar thermal and laser propulsion designs discussed in the main report. Multilayer insulation and a vapor shield venting system, both of which will be discussed further in the component masses section, are used for thermal protection.

Two rockets are positioned forward of the cargo and are used to circularize the orbit at the apogee. At the apogee, hatch doors in the shield similar to the landing gear doors used on the Space Shuttle will open in the shield, allowing the telescopic rocket nozzles to extend out and provide thrust [4]. In the event of a rocket failure, a small amount of oxygen may be shifted so this rocket configuration does not produce a moment on the vehicle during the circularizing burn.

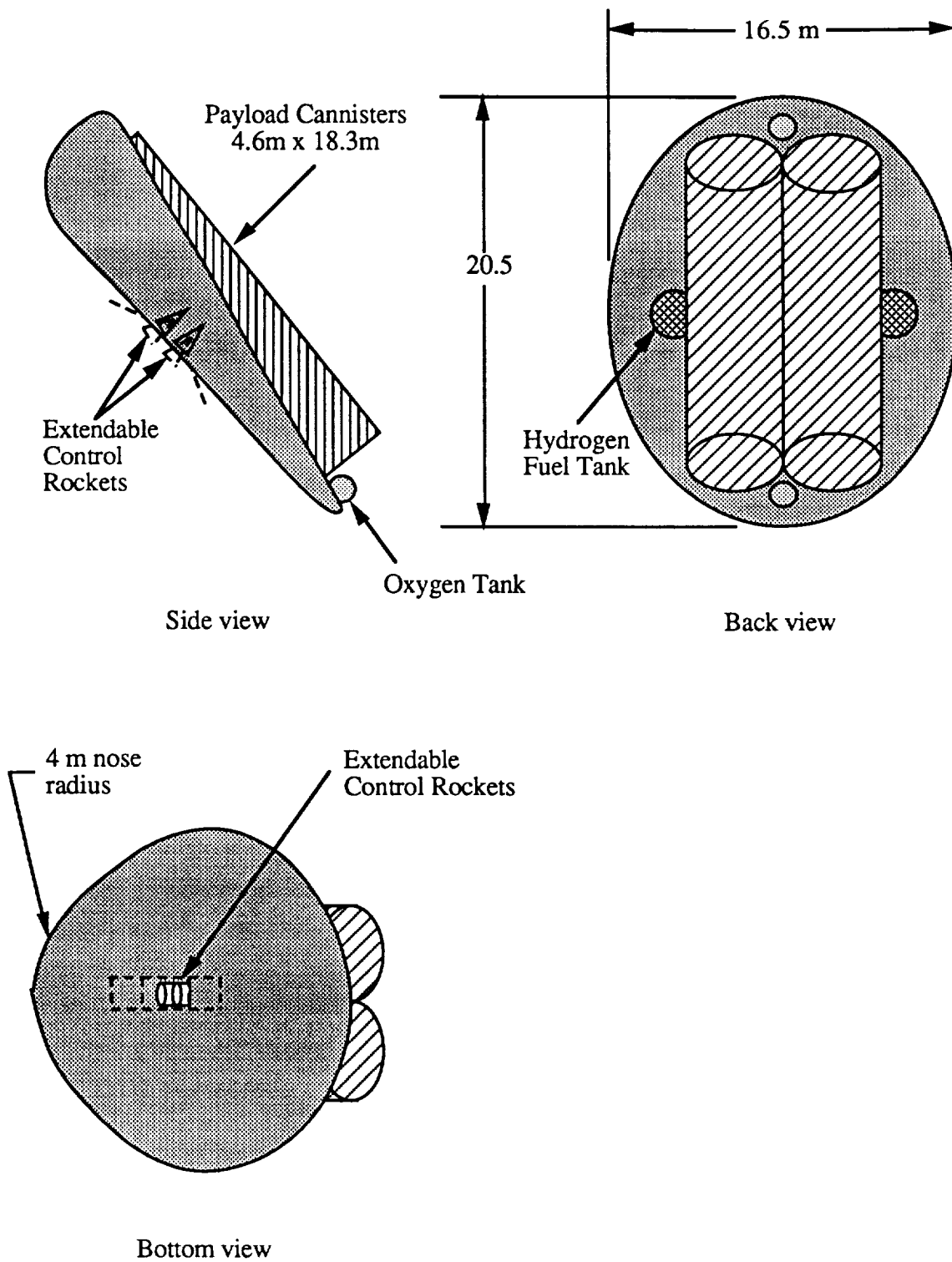


Figure A-1. Raked-off sphere cone ATV.

For the case of the solar thermal spacecraft, in which the mother craft never leaves the vicinity of earth orbit, an additional burn allows the payload to leave Earth orbit. This initial rocket system may be attached to the back of the cargo and released prior to the aerobrake maneuver into LMO.

Flight Path

Upon approach to Mars, the payload and its aerobraking system are released from the mother spacecraft to enter the upper atmosphere of Mars at an altitude of approximately 150 km [3]. The flight path angle of the vehicle as it enters the atmosphere must be sufficiently steep to avoid skipping out of the atmosphere, yet sufficiently shallow to achieve the desired apoapsis orbit. The entry corridor for a small range of entry velocities is shown in Fig. A-2 [5]. From this curve, the flight path angle must be between -13.5 and -14.5 degrees for an entry velocity of 6 km/s, which applies for a Hohmann transfer.

This ATV uses pitch control as well as a method known as roll modulation for control. The vehicle enters the atmosphere and begins to roll back and forth using small control rockets, which produce this oscillation throughout the aerobrake maneuver. This type of control was used in the Apollo missions and is commonly known as roll modulation [4]. During entry into the atmosphere, the ATV has its effective lift vector pointing up, away from Mars. Upon reaching the desired altitude, the vehicle rotates such that its effective lift vector points down, towards Mars, causing the vehicle to remain at this desired altitude. A high altitude proves beneficial since the atmospheric density is lower, resulting in lower heat transfer rates to the vehicle than at lower altitudes. After the desired amount of velocity change has occurred, the vehicle rotates again to exit the atmosphere. At the final orbiting altitude, the vehicle requires a small propulsive burn to circularize into this orbit. This propulsive burn requires 414 kg of H_2 and 3,316 kg of O_2 , which is discussed more in the component masses section later.

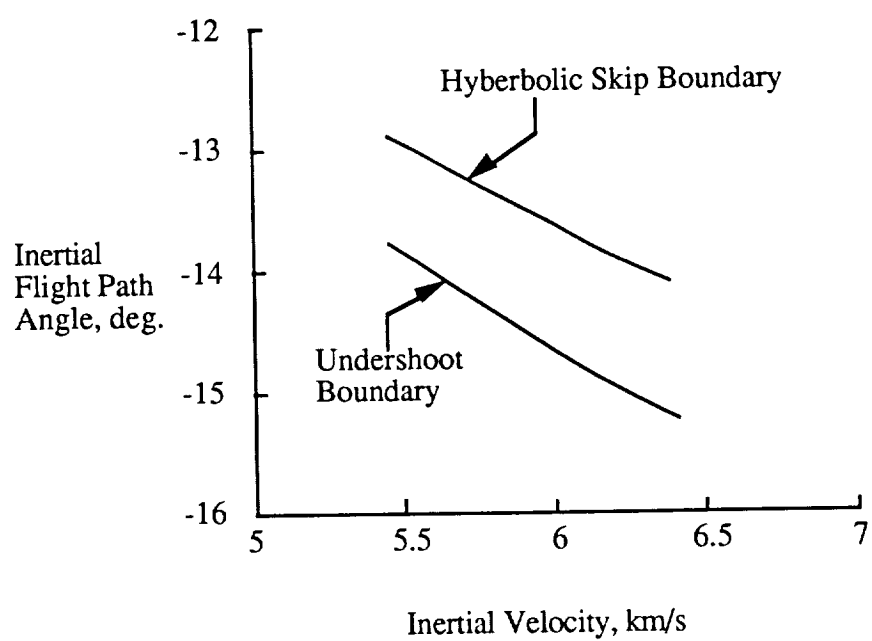


Figure A-2. Mars Entry Corridor.

For an ATV vehicle varying lift with roll modulation, the lift to drag ratio (L/D) of the vehicle must be twice that of its flight average L/D to account for unpredictable density variations in the Martian atmosphere [1]. Figure A-3 shows the L/D requirement for different entry velocities and a desired apoapsis of 15,000 km, accounting for a safety factor for density variations [5]. For the missions presented in this report, the desired apoapsis is 300 km. For a desired apoapsis lower than 15,000 km, the drag of the ATV must be larger, and therefore, the L/D requirement will be lower. Therefore, the L/D requirement of 0.55 for an apoapsis of 15,000 km is sufficient for the desired apoapsis of 300 km for our mission. The proposed raked-off sphere cone has a L/D of 0.6, making it an acceptable configuration [1].

Stability and Control

The stability of the vehicle is an important factor in the vehicle design. For the raked-off sphere cone, force lines originating from the center of pressure may be drawn rearward at each angle of attack (See Fig. A-4). These lines of force converge at a single point called the metacenter. The location of this point is about 60% of the diameter of the vehicle aft of the forward stagnation point [1,3]. The center of gravity, cg , of the ATV must be forward of the metacenter to provide stability. The design for this mission has a 25 m frustum diameter so the metacenter is 15 m aft of the forward stagnation point as shown in Fig. A-4. This is well aft of the cg location, thus the vehicle is quite stable. Referring again to Fig. A-2, the desired flight angle of attack, called the trim angle, is achieved by locating the cg of the ATV on one of the force lines drawn to the metacenter. The cg of the ATV for this mission will be positioned to give a trim angle of -5.0 degrees so the L/D is -0.55 without roll modulation [1].

Control is also required in addition to stability for the effectiveness of the vehicle. Control of the vehicle involves an efficient system that requires no surface deflection. Two methods to control lift are integrated to achieve satisfactory control in the unpredictable

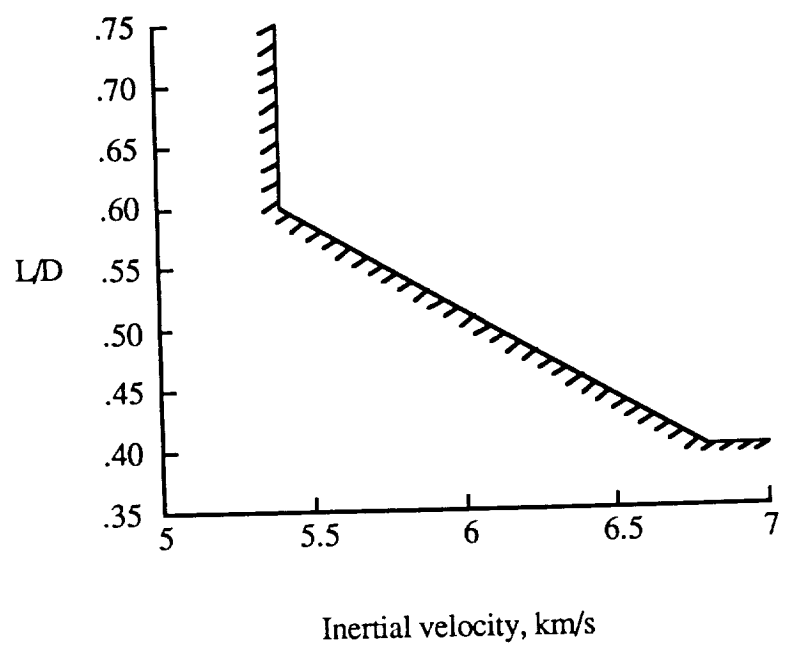


Figure A-3. Mars aerocapture L/D requirement.

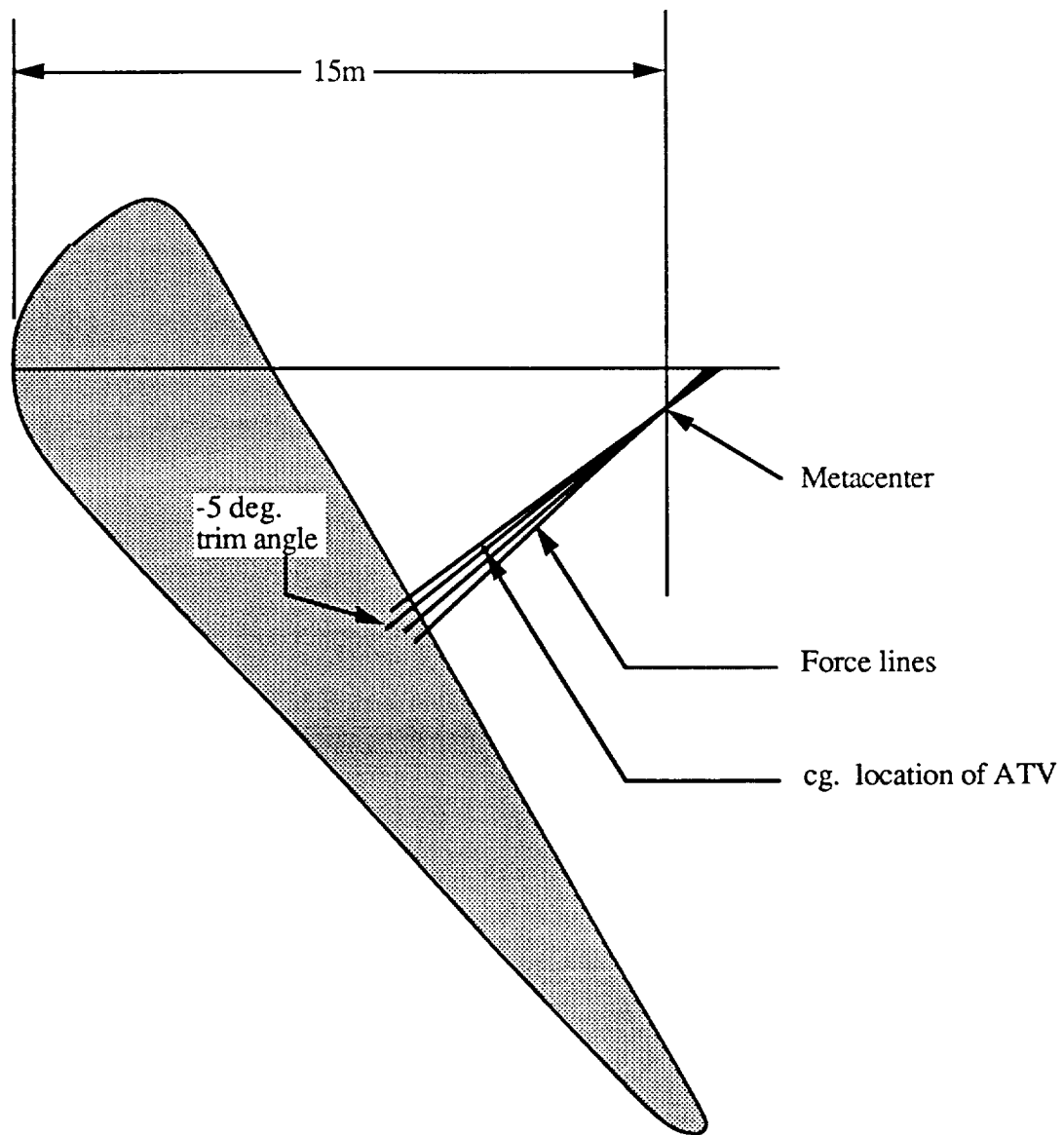


Figure A-4. Force lines and metacenter location on ATV.

Martian atmosphere. These methods include roll modulation, which was discussed previously, and pitch control to keep the angle of attack constant, as will be described later. With roll modulation, the calculations for the heat loading, drag, and lift of the vehicle are dependent only on height and velocity because of the fixed angle of attack. Therefore, the overall trajectory calculations will be much simpler than the calculations for a vehicle with variable trim angle of attack. Furthermore, roll modulation provides a safety margin in lift which allows for modifications should a density variation occur in the atmosphere.

In real gas flow, however, the angle of attack deviates from the desired angle of attack due to the changes in the flow temperature and the density caused by the dissociation of the gas. This effect was observed in the Space Shuttle and Apollo missions where the trim angle deviated up to 4° from the expected trim angle, which decreased the lift by 10% [3]. Some of this error may be accounted for with the location of the cg. However, it cannot be completely accounted for since the real gas variation of trim angle of attack varies with the specific heat ratio in non-equilibrium flow, which varies with the density and the velocity.

Rather than allow real gas effects to change the angle of attack and the aerodynamic characteristics as well, the pitch of the ATV is controlled such that the original -5° angle of attack is achieved and held constant. To accomplish a constant angle of attack, the cg of the vehicle is changed by shifting fuel between the tanks (See Fig. A-1). This method of control is known as pitch control where the oxygen can be shifted between tanks during flight so the constant angle of attack is achieved with real gas effects. This is the reason for the propellant tank configuration shown in Fig. A-1. By separating the propellant tanks, propellant may be transferred to change the vehicle center of gravity to the desired location.

The reason pitch control is not used alone is due to the complications in the trajectory calculations, as mentioned earlier. This type of control changes the aerodynamic characteristics with angle of attack. If the angle is increased more negatively, the lift will increase and the drag will decrease. Thus, to have the needed control and to drastically

reduce the complexity of the control calculations, both roll modulation and pitch control are needed.

Flow Impingement

Since the ATV flies in hypersonic flow, the flow actually turns as it flows over the edge of the aeroshell. For zero lift, this base turning angle is about 15° , and as angle of attack is increased more negatively, the lift increases and the base turning angle can become as much as 35° [3]. It is therefore necessary for the cargo on the back side of the ATV to have clearance such that the flow does not impinge on any after-body surface. The two reasons for this are thermal protection and steady flow requirements. If the flow impinged on a surface such as the cargo cannisters, the heat transfer rates on that surface would increase greatly, and additional thermal protection would be required to cover the surface. Furthermore, the location of the flow impingement would not be steady. Therefore, variable moments on the vehicle would result, causing the vehicle to shake violently. To avoid this, the cargo cannisters are positioned lying down with the forward portion deeper in the aeroshell as shown in Fig. A-1. This positioning eliminates the flow impingement problem and provides a very stable ATV, as described earlier.

Heat Transfer

There are three types of heat transfer that affect the design of the thermal protection system (TPS) of the ATV. The convective heat transfer to the ATV is dependent on the nose radius, r_n , the velocity, v , the density of the atmosphere, ρ , and the ratio of the wall enthalpy of the ATV to the total enthalpy, g_w . The convective heat transfer rate, q_c , (W/cm^2) is given as [6,7]:

$$q_c = 1.35 \times 10^{-8} \left(\frac{\rho}{R_e} \right)^{0.5} V^{3.04} (1 - g_w) \quad (\text{A-1})$$

This equation assumes a fully catalytic wall. The density at a given altitude, y , is determined by [4]

$$\rho = \rho_i e^{-\beta_i y} \quad (\text{A-2})$$

where, for altitudes above 36 km in the Martian atmosphere, the atmospheric density, ρ_i , is 0.03933 kg/m³ and the scaling constant, β_i , is 1.181x10⁻⁴ m⁻¹ [4,10].

For velocities in the Martian atmosphere above 8 km/s, there will be radiative heating of the aeroshell [6]. For velocities below this value, such as in the present mission, there will be radiation of heat away from the aeroshell. Not accounting for the dissociation of the atmospheric gas, the radiative heat transfer rate from the aeroshell, \dot{q}_r , is determined by

$$\dot{q}_r = \sigma \epsilon (T_w^4 - T_o^4) \quad (\text{A-3})$$

where σ is the Stefan-Boltzmann constant ($\sigma = 5.67 \times 10^{-8}$ W/m² K⁴), ϵ is the emissivity of the aeroshell material, T_w is the wall temperature, and T_o is the free stream temperature. The temperature variation in the Martian atmosphere is found from experimental data [8].

Assuming one-dimensional heat transfer, the conductive heat transfer rate \dot{q}_d , through the aeroshell material is given as

$$\dot{q}_d = \frac{k}{h} (T_w - T_b) \quad (\text{A-4})$$

where k is the thermal conductivity of the aeroshell material, T_b is the backface temperature, and h is the thickness of the aeroshell material.

The integrated heat load is determined from [9]

$$Q = m(V_e^2 - V_o^2) \frac{C_h S}{2 C_D A} \quad (\text{A-5})$$

where m is the mass of the ATV, v_e is the entry velocity, v_o is the exit velocity out of the atmosphere (which was assumed to be 3 km/s for the missions in this report), C_h is a non-dimensional heat transfer coefficient (the Stanton number), C_D is the drag coefficient, S is the surface area of the ATV, and A is the cross sectional area of the ATV. Before the integrated heat load can be calculated, C_h must be found from the heat transfer rate to the aeroshell, \dot{q} , by using the equation [9]

$$\dot{q} = C_h \rho V^3 \frac{S}{2} \quad (\text{A-6})$$

where q was determined using the previous equations.

Because the aeroshell material has a finite temperature range, the maximum wall temperature is determined for the worst possible flight condition for the ATV. For this extreme case, the ATV is assumed to be traveling with a velocity of 6 km/s at an altitude of 50 km. Assuming emissivity $\epsilon = 0.8$, the maximum T_w is 1,470 K for the extreme case, assuming a fully catalytic wall. Because this temperature is too low to cause a significant amount of dissociation, this approximation is reasonably accurate to within 10% error [6,7].

Shielding Materials

The aeroshell material is optimized according to several parameters. To minimize the ATV mass, a low density material is desired. The thickness of the material will be minimized for low thermal conductivities, high emissivities, and low catalycities of the material. The material must be able to support light structural loads and possess a low coefficient of thermal expansion to provide dimensional stability and rigidity. It is also desired that the aeroshell material be chemically inert with respect to the Martian and Earth

atmospheres, and cost efficient. Furthermore, the material must be capable of withstanding temperatures up to 1,470 K.

Several different types of heat shield materials have been developed for use on the Space Shuttle, as well as for proposed aeroassisted orbital transfer vehicles for Earth orbit transfers [10]. For the maximum wall temperature of 1,470 K, rigid, low density ceramics is determined to be the optimum heat shield material [10]. The most recently developed thermal protection system, TPS, using rigid, low density ceramics is Fibrous Refractory Composite Insulation (FRCI) developed by NASA [10,11]. FRCI is reusable and can withstand temperatures up to 1,750 K. It optimizes the parameters given in the previous paragraph and it is also chemically inert.

The TPS using FRCI contains a Reaction Cured Glass (RCG) coating over the FRCI tile which is bonded to a strain isolator pad using a room temperature vulcanizing (RTV 560) coating as shown in Fig. A-5 [10]. The total hemispherical emissivity of RCG is 0.8 for temperatures between 160 K and 1500 K, and the temperature limit for RTV is 315 K [10,11]. The thickness of the FRCI is dependent on the integrated heat load on the aeroshell, as shown in Fig. A-6 [10,11]. The integrated heat load is determined by integrating the heat transfer to the aeroshell over the total time in the aerobrake maneuver. This value is determined, using equations A-5 and A-6, to be 2230 J/cm^2 , thereby giving an insulation thickness of 1.8 cm.

Vehicle Mass

The total mass of the ATV is based on preliminary estimates for the size of the aeroshell for entry, the supporting structure for the aeroshell and components, the chemical rocket system, the propellant to recircularize the elliptical orbit, and the rocket system. The area density of the aeroshell is 3.5 kg/m^2 , as based on the TPS thickness of 1.8 cm [5].

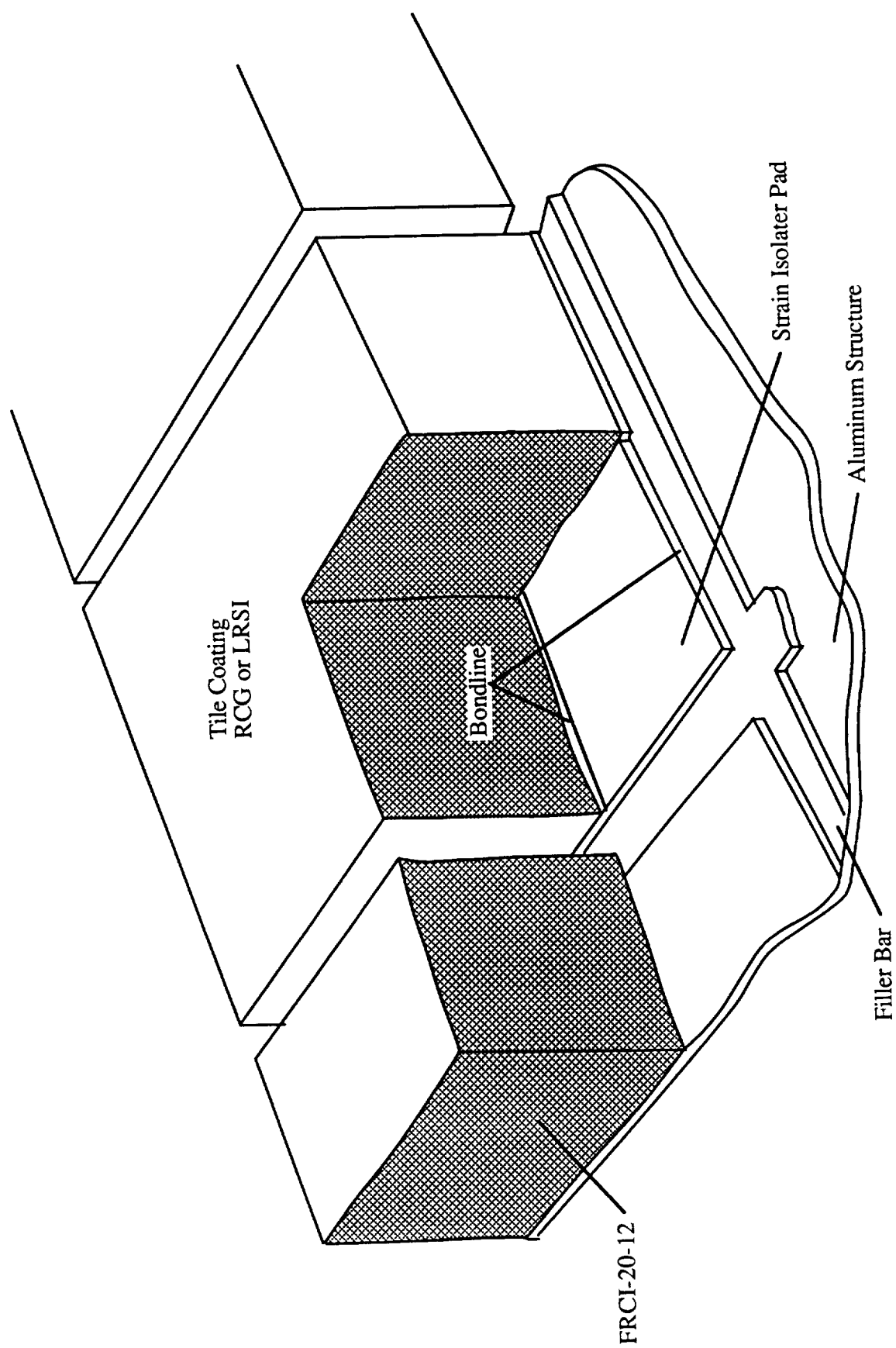


Figure A-5. RSI Tile System.

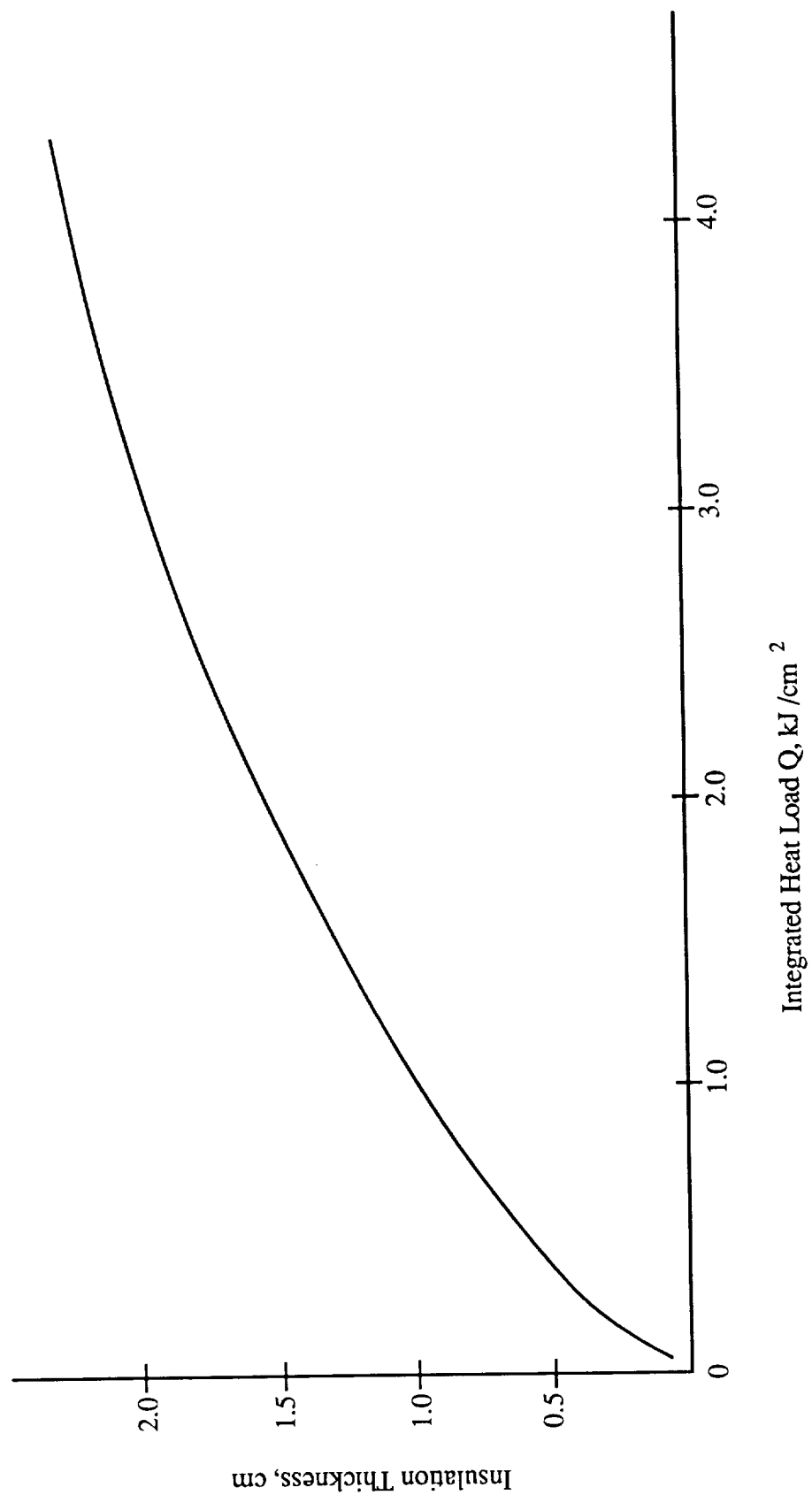


Figure A-6. Heat Shield Thickness for a Backwall Temperature of 315K.

The total surface area of the aeroshell is approximated by that of a circle having the major axis frustum diameter, d . The mass of the aeroshell, m_A , may be determined from:

$$m_A = 3.5\frac{\pi}{4}d^2 \quad (A-7)$$

Based on preliminary approximations for aerobrake component masses [12], the load bearing support structure mass, m_s , is given by:

$$m_s = 8.75(m_c)^{0.65} \quad (A-8)$$

where the component mass, m_c , is the ATV mass, m_T , less the payload mass. The mass of the secondary structure, m_{ss} , used to connect components to each other is given by:

$$m_{ss} = 0.2m_{ds} \quad (A-9)$$

where the dry stage mass, m_{ds} , is the ATV mass minus the payload and fuel masses. The mass of the propulsion system, m_{ps} , including propellant feed pipes, is given by:

$$m_{ps} = 0.0042m_T \quad (A-10)$$

The propellant required to recircularize the orbit cannot be accurately estimated, since for control and navigation reasons, the best trajectory, which will modulate its effective lift somewhat during flight, has not been specified for this vehicle design. However, Tauber estimates the velocity increment for recircularizing the orbit to be approximately 200-300 m/sec from a Hohmann transfer to an apogee height of 300 km and an L/D of -0.2 [13]. Therefore, a velocity increment of 300 m/s was assumed for the preliminary analysis. An integration of the equations of motion of the ATV, with a constant L/D of -0.2, a ballistic coefficient of 75 kg/m², and a C_D of 1.4 (the design of the ATV in this report [1,4]), indicates a velocity increment of 60 m/s was required at apogee

to recircularize the orbit. Since the actual trajectory will vary from this approximation, some pre-aerobraking attitude and trajectory adjustments will be needed before entry, and in the event of an unforeseen emergency abort mission on the first try, additional propellant must be carried. Thus, the conservative estimate of the 300 m/s velocity increment is considered for the propellant requirement calculations.

The propellant mass is determined from the mass fraction:

$$\frac{m_f}{m_i} = \exp\left(\frac{-\Delta v}{u_e}\right) \quad (A-11)$$

where m_f is the final mass, m_i is the initial mass, Δv is the velocity increment, and u_e is the exhaust velocity. The exhaust velocity assumed for the hydrogen oxygen propellant rocket system is 4,760 m/sec.

The total propellant mass required to circularize the orbit consists of 414 kg of hydrogen and 3,316 kg of oxygen. In a liquid state, the cryogenic densities at 100 kPa and 77.4 K are 1070 kg/m³ for oxygen and 70.8 kg/m³ for hydrogen. The radius of the storage tanks may be determined from:

$$r = \sqrt[3]{\frac{0.75m}{\pi\rho}} \quad (A-12)$$

where m and ρ refer to the mass and density of either hydrogen or oxygen. In this calculation, the mass of each tank is one half of the total value since there are two hydrogen tanks and two oxygen tanks for the vehicle. The mass of the propellant tanks, m_{pt} , may then be scaled from a 100 kg tank with a radius of 2.2 m which can withstand g loadings greater than our 1.5 g requirement [14]:

$$m_{pt} = 100\left(\frac{r}{2.2}\right)^2 \quad (A-13)$$

The multi-layer insulation is composed of both dacron and mylar, and has a density of 60 kg/m³. The mass of the required insulation, m_{ins} , is determined from:

$$m_{ins} = 80\rho(r_o^3 - r_i^3) \quad (A-14)$$

where the subscripts on the radii refer to the inner and exterior radii of the insulation. A vapor shield venting system keeps the tanks at the cryogenic temperature. A 1 cm thickness is assumed to account for the tank thickness and the venting shield thickness. Also, this vapor shield accrues a small loss of hydrogen propellant during the mission. This loss is proportional to surface area and inversely proportional to insulation thickness. The mass loss rate, m_{loss} , in kg/hr, is scaled from the mass loss rate of a given tank [14,15]:

$$m_{loss} = 0.0012667 \frac{r^2}{t} \quad (A-15)$$

where r is the tank radius, and t is the insulation thickness. An insulation thickness of 15 cm was chosen for the tanks by minimizing the total mass accounting for the hydrogen propellant lost during the transfer time to Mars and the mass of the insulation. This resulted in 130 kg total vented hydrogen during the trip to Mars. The oxygen mass loss was assumed to be negligible with this insulation thickness.

The above analysis indicates that the total mass of the ATV is 62,660 kg including the 50,000 kg payload yielding an aerobrake mass penalty of 20%. Table A-1 summarizes the component masses of the ATV.

Table A-1: Component Masses of the ATV

Component	Mass (kg)
Payload	50,000
Payload Canisters	2,000
Aeroshell	1,718
Support Structure	3,250
Secondary Structure	1,060
Rocket System	260
Propellant	3,870
Tanks	50
Insulation	340
Guidance and Control	112
TOTAL MASS	62,660

NOMENCLATURE

A	cross-sectional area of aeroshell
ATV	Aeroassisted transfer vehicle
cg	center of gravity
C_D	drag coefficient
C_h	heat transfer coefficient
d	freestream diameter (major axis)
FRCI	Fibrous Refractory Composite Insulation
g_w	wall to total enthalpy ratio
h	aeroshell thickness
I_{sp}	specific impulse
l	thermal conductivity
L/D	lift-to-drag ratio
m	mass of ATV
q	heat transfer rate
Q	integrated heat load
r	radius
r_i	inside radius of insulation
r_o	outside radius of insulation
RCG	reaction cured glass
RTV	room temperature vulcanizing
S	surface area of aeroshell
t	insulator thickness
T	temperature
T_o	freestream temperature
TPS	thermal protection system

u_e	exhaust velocity
v	vehicle velocity
y	altitude
Δv	velocity increment
ϵ	emissivity
ρ	density of atmosphere
σ	Stefan-Boltzman constant ($5.67 \times 10^{-8} \text{ W/m}^2 \text{ oK}^4$)

Subscripts

a	aeroshell
b	backface
c	convective
d	conductive
ds	dry stage
e	entry
f	final
i	initial
n	nose
o	exit
ps	propulsion system
pt	propellant tank
r	radiative
s	support structure
ss	secondary structure
t	tank
T	total
w	wall

REFERENCES

1. Park, C. and Davies, C. B., "Aerothermodynamics of Manned Mars Mission", AIAA Paper No. 89-0313, 1989.
2. Walberg, G. D., "A Survey of Aeroassisted Orbit Transfer", Journal of Spacecraft and Rockets, Vol. 22, pp. 3-18, Jan.-Feb. 1985.
3. Park, C., "A Survey of Aerobraking Orbital Transfer Vehicle Design Concepts", AIAA Paper No. 87-0514, 1987.
4. Davies, C. B. and Park, C., "Aerodynamics and Thermal Characteristics of Modified Raked-Off Blunted Cone", AIAA Paper 86-1309, June, 1986.
5. Hill, O. and Wallace, R. O., "Manned Mars Mission Vehicle Design Requirements for Aerocapture", NASA TM-89320, 89321, June, 1985.
6. Tauber, M. E. and Bowles, J. V., "Atmospheric Maneuvering During Martian Entry", AIAA Paper No. 88-4345, 1988.
7. Tauber, M. E., Menees, G., and Adelman, H., "Aerothermodynamics of Transatmospheric Vehicles", AIAA Paper No. 86-1257, 1986; also Journal of Aircraft, Vol. 24, pp. 594-602, March, 1987.
8. Kaplan, D., "Environment of Mars, 1988", NASA TM-100470, 1988.

9. Allen, H. J. and Eggers, A. J. Jr., "A Study of the Motion and Aerodynamic Heating of Missiles Entering the Earth's Atmosphere at High Supersonic Speeds", NACA Technical Note 4047, 1957.
10. Goldstein, H., "Development of Ceramic Thermal Protection Materials for Aerobraking Orbital Transfer Vehicles", 37th Pacific Coast Regional Meeting of the American Ceramic Society, Oct. 28-31, 1984.
11. Pitts, W. C. and Murbach, M. S., "Heatshield Design for Transatmospheric Vehicles", AIAA Paper No. 86-1258, 1986.
12. Kroll, K., NASA Johnson Space Center, Private Communication, Feb., 1989.
13. Tauber, M., NASA Ames Research Center, Moffett Field, CA, Private Communication, Feb., 1989.
14. Terre, C. N., "Low Pressure Light-Weight Cryogenic Propellant Tank Design for the Space-Based Orbital Transfer Vehicle", AIAA Paper No. 86-6916, 1986.
15. Eberhardt, R. N. and Fester, D. A., "Shuttle Compartment Cryogenic Liquid Storage and Supply Systems", AIAA Paper No. 89-1509, 1981.

APPENDIX B

Mathematical Model of Thermal Characteristics in Thruster Chamber

Melanie Miller

A computer code was generated in order to determine the shape and heat transfer characteristics of the plasma inside the laser thruster chamber. The mathematical model was developed by Keefer et al [1] and is a 2-D, steady state representation of a laser supported plasma in a circular cross-section channel. Two independent equations are used to describe the thermal flux upstream and downstream of the plasma center. The thermal flux, θ_1 , upstream of the plasma is given by:

$$\theta_1 = 8K_v S_0 (R_L/R_C) \sum A_n J_0 \left(x_{0n} \left(\frac{r}{R_C} \right) \right) e^{0.5\alpha(1 + \tau_n)x} \quad (B-1)$$

where r is the distance from the center of the cylinder and x is the distance upstream from the plasma center. S_0 is the intensity of the incident laser radiation into the working fluid, J_0 is a Bessel function of the first kind, and x_{0n} is the n^{th} zero of J_0 . K_v is the absorption coefficient of hydrogen, which is $2.0398 \times 10^{-2} \text{ cm}^{-1}$. This value was found from Fig. B-1, which is the absorption at a pressure of 10 atm. R_L is the radius of the laser beam in the fluid, and R_C is the radius of the chamber. The radius of the chamber is 13 cm. and α denotes the upstream conditions of the fluid:

$$\alpha = \rho_0 C_p \frac{u}{\lambda} \quad (B-2)$$

In Eq. B-2, ρ_0 is the upstream density of the fluid, taken to be $8.24 \times 10^{-4} \text{ g/cm}^3$ for 10 atm, and u is the upstream velocity, determined to be 0.133 cm/s for our mass flow rate.

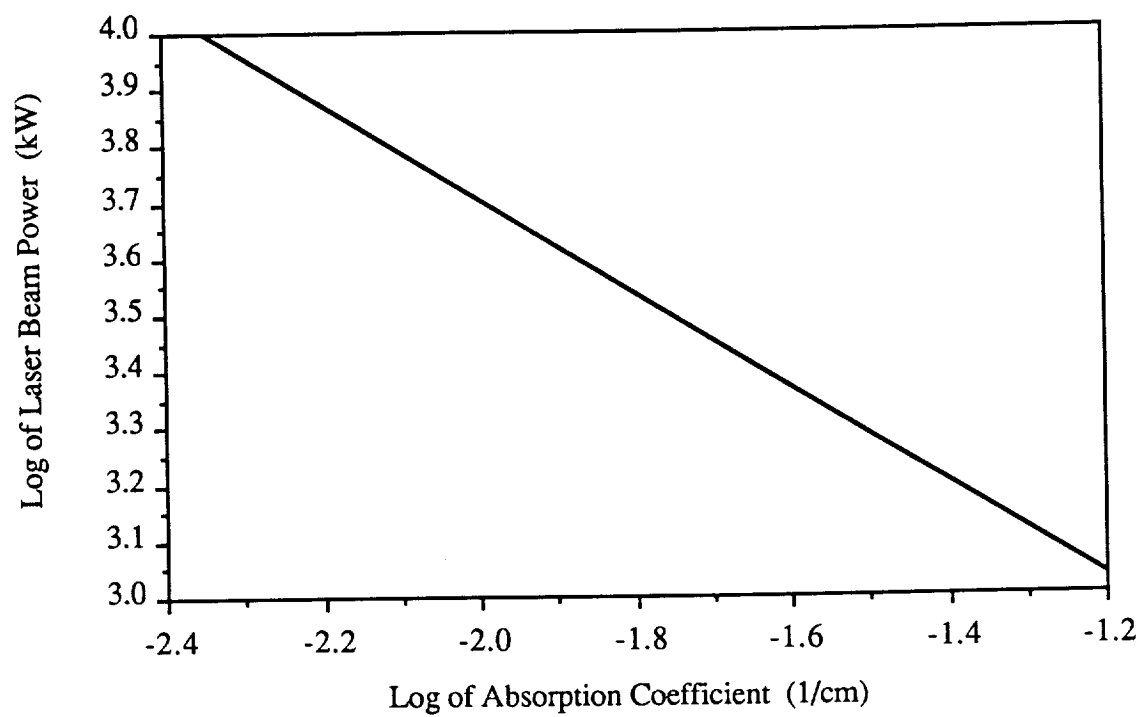


Figure B-1. Laser Beam Power as a Function of Absorption Coefficient.
(10 atm)

λ is the thermal conductivity, which is 0.0057 J/(cm K s) for hydrogen at 10 atm [1].

A_n is a coefficient determined from

$$A_n = J_1 \frac{(x_{on}(R_L/R_C))}{((2\alpha\tau'_n x_{on} J_1^2(x_{on}))[\alpha(\tau'_n - 1) + 2K_v])} \quad (B-3)$$

where J_1 is a Bessel function of the first kind. τ'_n is determined from

$$\tau'_n = \sqrt{1 + \left(\frac{4}{\alpha^2}\right)[(x_{on}/R_C)^2 + m]} \quad (B-4)$$

where m is the radiation loss coefficient, which is 875 cm⁻² at 10 atm [1]. The thermal flux downstream of the plasma center is given by:

$$\theta_2 = 8K_v S_o (R_L/R_C) \left[e^{-K_v} \sum B_n J_0 \left(x_{on} \left(\frac{r}{R_C} \right) \right) - \sum C_n J_0 \left(x_{on} \left(\frac{r}{R_C} \right) \right) e^{0.5\alpha(1 + \tau'_n)x} \right] \quad (B-5)$$

B_n and C_n are coefficients determined from

$$B_n = \left[\frac{(\alpha\tau'_n)}{(\alpha(\tau'_n - 1) - 2K_v)} \right] A_n \quad (B-6)$$

$$C_n = \left[\frac{(\alpha(\tau'_n + 1)) + 2K_v}{(\alpha(\tau'_n - 1) - 2K_v)} \right] A_n \quad (B-7)$$

The mathematical model above only calculates thermal flux values, θ , which need to be converted into temperatures. Keefer et al. [1] assumed that the thermal conductivity of the hydrogen was constant over the temperature gradients. A better approximation was determined using a linear approximation derived from thermal conductivity tables [2]. The increase in thermal conductivity as a function of temperature was approximated to be linear

for temperature values between 5,000 and 18,000 K. This assumption yields the following:

$$T = 1233.5 + 1.062 \times 10^6 [1.7161 \times 10^{-6} - 2.124 \times 10^{-6} \sqrt{0.393 - \theta}] \quad (\text{B-8})$$

where T is the temperature of the hydrogen gas in the absorption chamber. Temperatures evaluated using this program will tend to diverge from actual temperature values when the calculated temperature approaches 17,000 K. This is due to the linear assumption made about the thermal conductivity.

The functions J_0 and J_1 and the associated zeros used in equations B-1 and B-5 were attained from O'Neil [3].

NOMENCLATURE

A_n	constant coefficient
B_n	constant coefficient
C_n	constant coefficient
J_0	Bessel function of the zeroth order
J_1	Bessel function of the first order
K_v	absorption coefficient
r	radius
R	radius of absorption chamber
R_L	radius of laser beam
S_0	radiation intensity
T	temperature
u	upstream velocity
x_{on}	n^{th} zero of J_0
α	coefficient of upstream conditions
λ	absorption coefficient
ρ_0	upstream density
τ_n'	constant coefficient

REFERENCES

1. Keefer, D.R. and Crowder, H., "A Two-Dimensional Model of the Hydrogen Plasma for Laser Powered Rocket", AIAA Paper No. 82-0404, Jan., 1982.
2. Grier, N. T., "Calculation of the Transport Phenomena of Ionizing Atomic Hydrogen", NASA TN D-3186, April, 1966.
3. O'Neil, P. V., Advanced Engineering Mathematics, Wadsworth Publishing Company, Belmont, CA, pp. 302-305, 1987.

APPENDIX C

Analytical Methods Used in the Design of the MPD Propelled Spacecraft Structure

Tad A. Unger

Beam theory is a quick and easy way to analyze the truss beams that make up the array platform, and the payload and main body structure. Using this for a cantilever beam, the moment applied at the root of the truss is

$$M = \frac{p_o L^2}{2} \quad (C-1)$$

where p_o is the distributed load per length, and L is the length.

Reaction stresses in the elements provide the resistance to the applied moment. For the box beam the element stresses are found from statics to be

$$\sigma = \frac{M}{(wA_{\text{tube}})} \quad (C-2)$$

where M is the moment from Eq. C-1, w is the distance between the top and bottom elements of the mast, and A_{tube} is the cross sectional area of the tube element.

The critical buckling stress for a pinned element is found from Euler's equation

$$\sigma = C \left(\frac{\pi^2 E I_{\text{tube}}}{(l^2)} \right) \quad (C-3)$$

where C is 1 for the pinned boundary conditions, E is the modulus of elasticity, I_{tube} is the area moment of inertia of the tube element, and l is the length of the element.

To estimate the natural frequency, Rayleigh's method was used. The assumed mode shape was that for a distributed load on a cantilever beam. This gives an expression for the lowest frequency:

$$\omega_n^2 = 12.46 \frac{EI_{\text{truss}}}{(mL^3)} \quad (\text{C-4})$$

where I_{truss} is the area moment of inertia of the truss beam about its neutral axis and m is the mass distributed along the length.

To calculate the mass of the array structure the total length of the elements must be calculated.

From Fig. C-1, the following relations are apparent:

$$\begin{aligned} L &= \sqrt{\frac{A}{2}} \\ l &= \frac{(L - w)}{(2 C2)} \\ w &= \frac{L}{C2} \end{aligned}$$

where A is the total array area, among the two platforms, l is the horizontal length of a $C1$ cell, and $C2$ is the number of cells in the vertical direction.

The final equations are written in terms of L , $C1$, and $C2$, the input variables.

Length calculation of one side of the platform:

Σ length of longitudinals:

$$(C2 + 1) \left[C1 + C2 \right] (C1 - 1) = \frac{1}{2} \left(L - \frac{L}{C2} \right) (C2 + 1) + \left(\frac{C2}{2C1} \right) \left(L - \frac{L}{C2} \right) (C1 - 1)$$

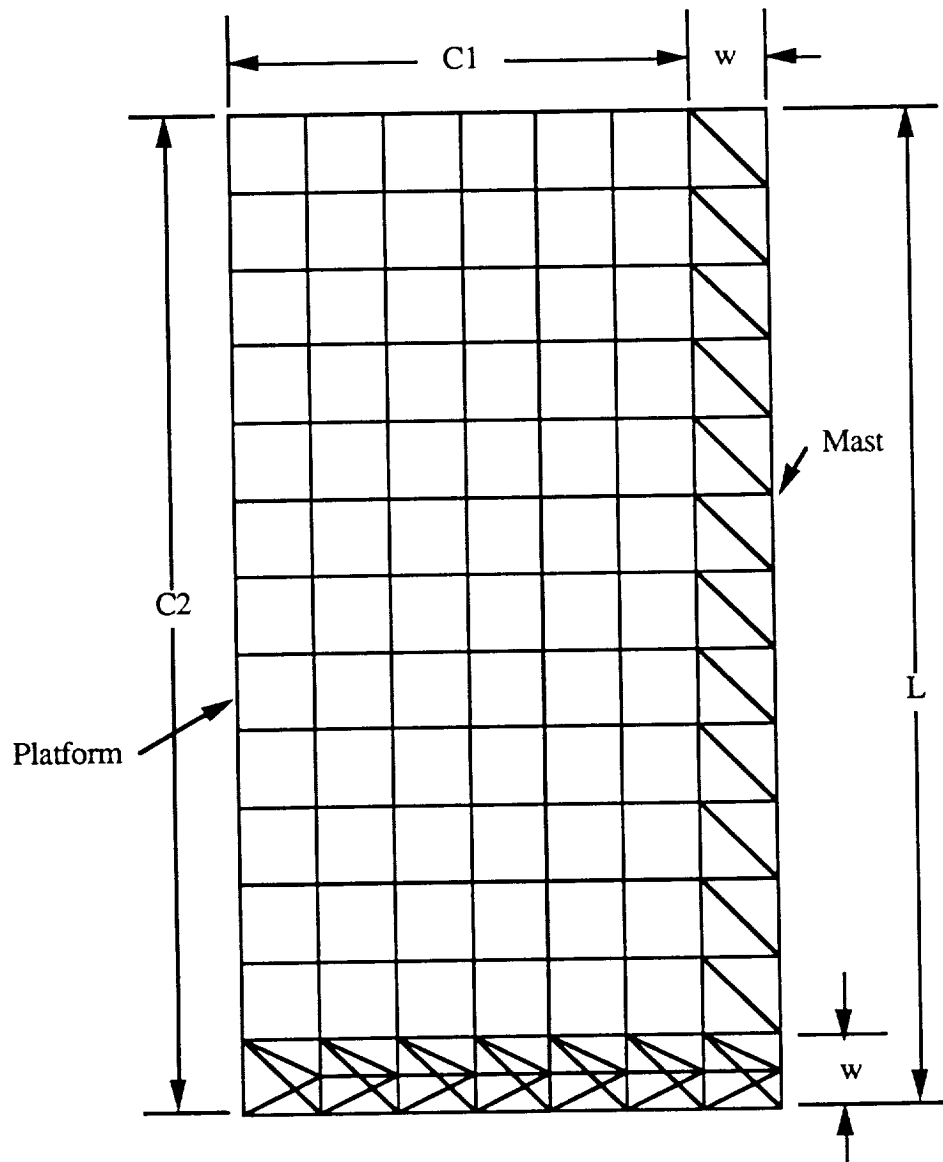


Figure C-1. Half of One Platform with the Notation Used to Calculate the Total Element Length.

Σ length of vert. cross:

$$(C1 - 1)(w\sqrt{5})C2 = \sqrt{5}\left(L - \frac{L}{C2}\right)(C1 - 1)L$$

Σ length of vert. diagonals:

$$2C1\left(\frac{3}{2}w\right)C2 = 3C1L$$

Σ length of horizontal cross:

$$C1wC2 + (C1 - 1)w(C2 - 1) = C1L + \left(\frac{L}{C2}\right)(C1 - 1)(C2 - 1)$$

Σ length of horizontal diagonals:

$$C1\sqrt{2}wC2 + (C1 - 1)\sqrt{2}w(C2 - 1) = \sqrt{2}C1L + \left(\frac{\sqrt{2}L}{C2}\right)(C1 - 1)(C2 - 1)$$

$$L_{\text{platf}} = \Sigma \text{ above}$$

Length calculation of the mast:

Σ length of the longitudinals:

$$2(L + 3) + 2\left(L - \frac{w}{2} + 3\right) = 4L - \frac{L}{C2} + 12$$

Σ length of vert. diagonals:

$$2\sqrt{5}wC2 + \sqrt{9 + w^2} = 2\sqrt{5}L + 2\sqrt{9 + \frac{L^2}{C2^2}}$$

Σ length of horizontal diag.:

$$\begin{aligned} \sqrt{2}wC2 + \sqrt{9 + w^2} + \sqrt{2}w(C2 - 1 + \sqrt{25 + w^2}) = \\ \sqrt{2}\left[L + \left(\frac{L}{C2}\right)(C2 - 1)\right] + \sqrt{9 + w^2} + \sqrt{25 + w^2} \end{aligned}$$

Σ length of horizontal cross:

$$w(2C2 + 1) = \left(\frac{L}{C2}\right)(2C2 + 1)$$

$$L_{\text{mast}} = \Sigma \text{ above}$$

$$\text{TOTAL LENGTH} = 4*L_{\text{platf}} + 2*L_{\text{mast}} \quad (\text{C-5})$$

The total mass is the Total Length multiplied by the density of the graphite/epoxy and the cross sectional area of the tube.

To calculate the number of nodes:

Σ of all platform nodes:

$$4 * \{ C1(C2 + 1) + (C1 - 1)C2 \}$$

Σ of all mast nodes:

$$2 * \{ 2 * C2 + 2 + 2 * C2 \}$$

$$\Sigma \text{ above} = 4 \{ C1(C2 + 1) + C2(C1 + 1) + 1 \} \quad (C-6)$$

The above equations were put into a spreadsheet program to simplify iteration and optimization.

NOMENCLATURE

A	Area of the solar array
A_{tube}	Cross sectional area of the tube elements
$C1$	Number of cells from the mast to the edge of the platform in the horizontal direction
$C2$	Number of cells in the vertical direction
E	Young's Modulus in the longitudinal direction
I_{truss}	The area moment of inertia of the truss beam
I_{tube}	The area moment of inertia of the tube elements
l	The length of a $C1$ cell in the horizontal direction
L	The overall length of one array platform
m	Mass distributed along the truss beam
M	Applied moment
p_0	Distributed load
w	Length of cells in the vertical direction
ω_n	Natural frequency

APPENDIX D

Numerical Trajectory Calculation Programs

Barbrina Dunmire
Jacqueline Auzias de Turenne
Neil Phelps

The following programs are those used to determine the orbital trajectories of the three solar-powered spacecraft. The computational technique used takes the equations of motion of the spacecraft and expresses them as first order differential equations using state variables. These differential equations are integrated using a standard fourth order Runge-Kutta numerical integration technique. The initial conditions, celestial body constants, and thrust program can be altered so that trajectories may be computed for a variety of primary bodies, starting orbits, and spacecraft configurations. Lift and drag terms may also be included in the governing equations of motion, making it possible to calculate the trajectory of the aerobraking payload system.

The programs also include an iterative method for determining the minimum amount of propellant necessary for the mission by calculating the amount of propellant required for an estimated initial spacecraft mass. If the final mass is less than the dry mass of the spacecraft, then the initial mass is increased. If the final mass is more than the dry mass of the spacecraft, then the initial mass is decreased. The final mass of the spacecraft is then recomputed, and the process is repeated until the final mass is nearly equal to the dry mass of the spacecraft. The propellant mass is then the initial mass minus the dry mass of the spacecraft.

The programs used in the analysis of the three solar-powered spacecraft are listed below and appear on the following pages.

- ELLIPSE: The geocentric, elliptical trajectory analysis used by the Solar Radiation Absorber propelled spacecraft to approximate finite apogee and perigee burns.
- SPIRAL: The geocentric trajectory analysis used by the Solar Pumped Laser and the MPD propelled spacecraft to approximate a constant, low thrust maneuver within the Earth's sphere of influence.
- HELIOCENTRIC: The heliocentric trajectory analysis used by the MPD propelled spacecraft to approximate a low thrust maneuver while under the gravitational influence of the sun.
- MSPIRAL: The Martian-centered trajectory analysis used by the MPD propelled spacecraft to approximate a constant, low thrust maneuver within Mars' sphere of influence.

PROGRAM ELLIPSE

```

      program ellipse
c
c *****
c * Ellipse is the main calling program for the integration of *
c * the equations of motion of the spacecraft while under the *
c * gravitational influence of the Earth. *
c *****
c
      implicit double precision(a-h,o-z)
      dimension xo(20),xx(20)
c
c *****
c * 'md' is the dry mass of the ship which includes everything *
c * except the propellant mass required for an individual *
c * maneuver. *
c * 'mp' is the estimated propellant mass required for a given *
c * maneuver. *
c * 'amin' *
c * 'amax' *
c * 'theta' *
c *****
c
      md=43814
      mp=24000
      amin=.6
      amax=1.2
      theta=5/180*3.14159
c
      open (file = 'escape', status = 'new', unit = 7)
c
      write (7,*) 'orbital trajectory data'
      write (7,*) 'data is in the following order'
      write (7,*) 'time      rdot      r      phidot      phi      velocity'
c
c *****
c * 'xo' is the array of the initial conditions where: x_(1) = rdot, *
c * x_(2) = r, x_(3) = phidot, x_(4) = phi, and x_(5) = mass. *
c *****
c
      50 xo(1)=0
         xo(2)=6878145
         xo(3)=0.00110678256
         xo(4)=0
         xo(5)=md+mp
c
c *****
c * The following are variables passed through to the integration *
c * subroutine. 'in' is a flag, 'nv' is the number of variables in *
c * the equations of motion, 'to' is the initial time, 'tp' is the *
c * final time (stopping the loop), and 'dtint' is the interval that *
c * the integration routine breaks each time loop down. *
c * *
c * 've' is the escape velocity of a given radius *
c * 'vv' is the instantaneous ship velocity *
c * 'vo' is the velocity required to undertake a hohmann transfer to *
c * mars *
c *****
c
      in=0
      nv=5
      to=0
      tp=43200000

```

```

      dtint=63
c
      do 200 t=5640,tp,100
      call ellrk4(to,t,dtint,xo,xx,nv,in)
      vv=(xx(1)**2+(xx(2)*xx(3))**2)**0.5/1000
      vo=(2.94**2+(2*3.986*10**5/xx(2)*1000))**.5
c      write (7,100) t,xx(1),xx(2),xx(3),xx(4),vv
c 100 format (e11.5,1x,d11.5,1x,d11.5,1x,d11.5,1x,d11.5,1x,d11.5)
c
      150 ve=(2000*3.986012e05/xx(2))**.5
      if (vv.gt.(vo-.75)) go to 250
      200 continue
c
c *****
c * This next scheme is a method to check that the final      *
c * propellant consumption, as determined from the burn time, *
c * is equal to the initial estimate. If not, the              *
c * process is repeated with a new estimate.                   *
c *****
c
      250 mpr=xo(5)-xx(5)
      if (abs(mpr-mp).lt.100) go to 350
      if (mpr.gt.mp) go to 300
      if (mpr.lt.mp) go to 325
c
      300 mp=mp+(mpr-mp)
      go to 50
c
      325 mp=mp-(mp-mpr)
      go to 50
c
      350 write (7,*) 'congratulations you have escaped earth orbit'
      write (7,*) 'vesc, v, and vo',ve,vv,vo
      write (7,*) 'total time of spiral (days)',t/3600/24
      write (7,*) 'mass of propellant consumed',xo(5)-xx(5)
      write (7,*) 'total number of revolutions',xx(4)/2/3.14159
      write (7,*) 'orbital radius at escape (km)',xx(2)/1000
      write (7,*) 'mp',mp
      write (7,*) 'vo',vo
c
      end

```

```

      subroutine ellrk4(to,tp,dtint,xo,xx,nv,in)
c
c *****
c * This is a fourth order runge-kutta numerical integration      *
c * subroutine courtesy of Stephen Paris, flight mechanics      *
c * specialist, Boeing Aerospace Division of the Boeing Company. *
c *
c * Ellrk4 integrates a set of 'nv' 1st order ordinary differential *
c * equations from xo(to) to xo(tp) with step size 'dtint'. The *
c * differential equations are contained in subroutine fcn, and *
c * the values computed are returned to ellipse. *
c *****
c
      implicit double precision(a-h,o-z)
      common/nwvcl/time,xv(100),d(100)
      common/rkblk/vs(20),ds(20),xs(20)
      dimension xo(20),xx(20)
      external ellfcn
c
      if (in.eq.0) time=to
      900 continue
c
c *****
c * This step checks to see if a fractional step is required. *
c *****
c
      h=tp-time
      if (abs(h).gt.dtint)h=sign(1.0d0,h)*dtint
      h2=h/2
      h6=h/6
c
c *****
c * This routine initializes the variables. If the variables *
c * have already been initialized, this routine is overlooked. *
c *****
c
      if (in.eq.1) go to 1300
      in=1
      do 1100 i=1,nv
      xv(i)=xo(i)
1100 continue
      tn=to
c
      do 1200 i=1,nv
      ds(i)=d(i)
      xs(i)=xv(i)
1200 continue
c
      1300 continue
c
c *****
c * Make first estimate of canter state. *
c *****
c
      do 1400 i=1,nv
      xv(i)=xs(i)+h2*ds(i)
1400 continue
      time=tn+h2
c
      call ellfcn
c
c *****

```

```

c * Revise estimate with derivative at center. *
c *****
c
      do 1600 i=1,nv
        vs(i)=ds(i)+2.00*d(i)
        xv(i)=xs(i)+h2*d(i)
1600 continue
c
      call ellfcn
c
c *****
c * Make first estimate of state at end of step. *
c *****
c
      do 1800 i=1,nv
        vs(i)=vs(i)+2.00*d(i)
        xv(i)=xs(i)+h*d(i)
1800 continue
      time=tn+h
c
      call ellfcn
c
c *****
c * Final estimate based on derivative at center and both ends, *
c * with double weight on the center estimates. *
c *****
c
      do 1810 i=1,nv
        vss=h6*(vs(i)+d(i))
        xs(i)=xs(i)+vss
        xv(i)=xs(i)
1810 continue
c
      call ellfcn
c
      do 1820 i=1,nv
        ds(i)=d(i)
1820 continue
c
c *****
c * Update the time for the next step. *
c *****
c
      tn=time
c
c *****
c * End: copy state ot 'xx' *
c *****
c
      if(time.ne.tp) go to 900
c
      do 2000 i=1,nv
        xx(i)=xv(i)
2000 continue
c
      return
      end

```

```

      subroutine ellfcn
c
c *****
c * Ellfcn is the derivative evaluation routine for runge-kutta *
c * numerical integration routine. The values of t,x,and d *
c * are passed thru the common block. *
c * *
c * The differential equations are of the following form: *
c *  $d(n) = dx(n)/dt = f(x(1), x(2), \dots x(nv))$ . *
c *****
c
      implicit double precision (a-h,o-z)
      common/nwvcl/t,x(100),d(100)
c
c *****
c * The constans defined below are as follows: *
c * g = acceleration due to gravity at the planet's surface *
c * ro = radius of the Earth *
c * f = thrust of the spacecraft *
c * pmdot = propellant mass flow rate *
c *****
c
      g=9.80665
      ro=6378145
c
c *****
c * The following determines the angular position of the *
c * spacecraft between 0 and 360 degrees. *
c *****
c
      s=x(4)
      rev=0.0
      if (s.lt.6.283) go to 200
      rev=s/2/3.14159
      s=s-int(rev)*2*3.14159
c
c *****
c * The following is a sequence of steps which determines the *
c * firing angle about the perigee of the ellipse and checks *
c * to see if the spacecraft is within this range. *
c *****
c
      200 ang=amin+(amax-amin)/60*int(rev)
         if (s.lt.(3.14159-.6458)) go to 300
         if (s.gt.(3.14159+.6458)) go to 300
         f=100
         pmdot=-0.004
         go to 400
c
      300 f=0.0
         pmdot=0.0
c
c *****
c * State Dictionary: *
c * r = radius of the spacecraft's orbit *
c * phi = true anomaly measured from initiation of maneuver *
c * m = instantaneous mass of the spacecraft *
c * x(1) = dr/dt *
c * x(2) = dr *
c * x(3) = d(phi)/dt *
c * x(4) = phi *

```



```

c * x(5) = m *
c *****
c
400 temp=x(2)*x(3)**2-g*ro**2/(x(2))**2+f/x(5)*sin(theta)
    d(1)=f*cos(theta)*x(1)/x(5)/(x(1)**2+(x(2)*x(3))**2)**0.5+temp
c
    d(2)=x(1)
c
    temp=2*x(1)*x(3)/x(2)
    d(3)=f*cos(theta)*x(3)/x(5)/(x(1)**2+(x(2)*x(3))**2)**0.5-temp
c
    d(4)=x(3)
c
    d(5)=pmdot
c
    return
end

```

PROGRAM SPIRAL

```

      program spiral
c
c *****
c * Spiral is the main calling program for the integration of *
c * the equations of motion of our spacecraft while under the *
c * gravitational influence of the Earth. *
c *****
c
c      implicit double precision(a-h,o-z)
c      dimension xo(20),xx(20)
c
c *****
c * 'md' is the dry mass of the ship which includes everything *
c * except the propellant mass required for an individual *
c * maneuver. *
c * 'mp' is the estimated propellant mass required for a given *
c * maneuver. *
c * 'sphereofi' is the sphere of influence for the planet *
c * The values are entered interactively. *
c * 'hexcess' is the required hyperbolic excess velocity *
c * for the transfer orbit. *
c *****
c
c      write(*,*) 'dry mass of the ship in kg'
c      read(*,*) md
c      write(*,*) 'estimate of the propellant mass in kg'
c      read(*,*) mp
c      write(*,*) 'sphere of influence of the Earth in meters'
c      read(*,*) sphereofi
c      write(*,*) 'desired hyperbolic excess in km/sec'
c      read(*,*) hexcess
c
c      open (file = 'escape', status = 'new', unit = 7)
c
c      write (7,*) 'orbital trajectory data'
c      write (7,*) 'data is in the following order'
c      write (7,*) 'time      rdot      r      phidot      phi      velocity'
c
c *****
c * 'xo' is the array of the initial conditions where: x_(1) = rdot *
c * x_(2) = r, x_(3) = phidot, x_(4) = phi, x_(5) = mass. *
c *****
c
c      50 xo(1)=0
c         xo(2)=6878145
c         xo(3)=0.0011393
c         xo(4)=0
c         xo(5)=md+mp
c
c *****
c * The following are variables passed through to the integration *
c * subroutine. 'in' is a flag, 'nv' is the number of variables in *
c * the equations of motion, 'to' is the initial time, 'tp' is the *
c * final time (stopping the loop), and 'dtint' is the interval that *
c * the integration routine breaks each time loop down. *
c *****
c
c      in=0
c      nv=5
c      to=0
c      tp=50000000
c      dtint=63

```

```

c
do 200 t=500,tp,500
ts=t-500
call rk4(ts,t,dtint,xo,xx,nv,in)
vv=(xx(1)**2+(xx(2)*xx(3))**2)**0.5/1000
c
write (7,100) t,xx(1),xx(2),xx(3),xx(4),vv
c 100 format (e11.5,1x,d11.5,1x,d11.5,1x,d11.5,1x,d11.5,1x,d11.5)
c
c *****
c * 've' is the escape velocity at a given radius; 'vv' is the ship *
c * velocity at a given radius. The exit condition is designated *
c * as when the spacecraft velocity exceeds the hyperbolic excess *
c * velocity, or when the spacecraft has passed the sphere of *
c * influence of the Earth. *
c *****
c
ve=(2000*3.986012e05/xx(2))**0.5
if ((vv.gt.ve) .AND. (vv.gt.hexcess)) go to 250
c
if (vv.gt.ve) go to 250
if (xx(2).gt.sphereofi) go to 250
200 continue
c
c *****
c * This next scheme is a method to check that the final *
c * propellant consumption, as determined from the time of *
c * spiral, is equal to the initial estimate. If not, the *
c * process is repeated with a new estimation. *
c *****
c
250 mpr=xo(5)-xx(5)
if (abs(mpr-mp).lt.100) go to 350
if (mpr.gt.mp) go to 300
if (mpr.lt.mp) go to 325
c
300 mp=mp+(mpr-mp)
go to 50
c
325 mp=mp-(mp-mpr)
go to 50
c
350 write (7,*) 'congratulations you have escaped earth orbit'
write (7,*) 'vesc and v',ve,vv
write (7,*) 'total time of spiral (days)',t/3600/24
write (7,*) 'mass of propellant consumed',xo(5)-xx(5)
write (7,*) 'total number of revolutions',xx(4)/2/3.14159
write (7,*) 'orbital radius at escape (km)',xx(2)/1000
write (7,*) 'mp',mp
write (7,*) 'rdot',xx(1)
write (7,*) 'phidot',xx(3)
c
end

```

```

      subroutine rk4(to,tp,dtint,xo,xx,nv,in)
c
c *****
c * This is a fourth order runge-kutta numerical integration *
c * subroutine courtesy of Stephen Paris, flight mechanics *
c * specialist, Boeing Aerospace Division of the Boeing Company. *
c *
c * Rk4 integrates a set of 'nv' 1st order ordinary differential *
c * equations from xo(to) to xo(tp) with step size 'dtint'. The *
c * differential equations are contained in subroutine fcn, and *
c * the values computed are returned to spiral. *
c *****
c
      implicit double precision(a-h,o-z)
      common/nwvcl/time,xv(100),d(100)
      common/rkblk/vs(20),ds(20),xs(20)
      dimension xo(20),xx(20)
      external fcn
c
      if (in.eq.o) time=to
      900 continue
c
c *****
c * This step checks to see if a fractional step is required. *
c *****
c
      h=tp-time
      if (abs(h).gt.dtint)h=sign(1.0d0,h)*dtint
      h2=h/2
      h6=h/6
c
c *****
c * This routine initializes the variables. If the variables *
c * have already been intialized, this routine is overlooked. *
c *****
c
      if (in.eq.1) go to 1300
      in=1
      do 1100 i=1,nv
      xv(i)=xo(i)
      1100 continue
      tn=to
c
      do 1200 i=1,nv
      ds(i)=d(i)
      xs(i)=xv(i)
      1200 continue
c
      1300 continue
c
c *****
c * Make first estimate of canter state. *
c *****
c
      do 1400 i=1,nv
      xv(i)=xs(i)+h2*ds(i)
      1400 continue
      time=tn+h2
c
c
c
      call fcn
c
c *****

```

```

c * Revise estimate with derivative at center. *
c *****
c
c      do 1600 i=1,nv
c          vs(i)=ds(i)+2.00*d(i)
c          xv(i)=xs(i)+h2*d(i)
c      1600 continue
c
c          call fcn
c
c *****
c * Make first estimate of state at end of step. *
c *****
c
c      do 1800 i=1,nv
c          vs(i)=vs(i)+2.00*d(i)
c          xv(i)=xs(i)+h*d(i)
c      1800 continue
c          time=tn+h
c
c          call fcn
c
c *****
c * Final estimate based on derivative at center and both ends, *
c * with double weight on the center estimates. *
c *****
c
c      do 1810 i=1,nv
c          vss=h6*(vs(i)+d(i))
c          xs(i)=xs(i)+vss
c          xv(i)=xs(i)
c      1810 continue
c
c          call fcn
c
c      do 1820 i=1,nv
c          ds(i)=d(i)
c      1820 continue
c
c *****
c * Update the time for the next step. *
c *****
c
c          tn=time
c
c *****
c * End: copy state to 'xx'. *
c *****
c
c          if(time.ne.tp) go to 900
c
c          do 2000 i=1,nv
c              xx(i)=xv(i)
c          2000 continue
c
c          return
c          end

```

```

      subroutine fcn
c
c *****
c * Fcn is the derivative evaluation routine for runge-kutta *
c * numerical integration routine. The values of t,x, and d *
c * are passed thru the common block. *
c * *
c * The differential equations are of the following form: *
c *  $d(n) = dx(n)/dt = f(x(1), x(2), \dots, x(nv))$ . *
c *****
c
      implicit double precision (a-h,o-z)
      common/nwvcl/t,x(100),d(100)
c
c *****
c * The constants defined below are as follows: *
c * *
c * g = acceleration due to gravity at the planet's surface *
c * ro = radius of the Earth *
c * f = the thrust of the spacecraft *
c * pmdot = propellant mass flow rate *
c * rs = the radius of the sun *
c * dse = the distance from the center of the sun to the Earth *
c *****
c
      g=9.80665
      ro=6378145
      rs=696000000
      dse=149.5*(10**9)
c
c *****
c * The following sequence of steps incorporates the effect *
c * of the shadow of the planet. *
c *****
c
      s=x(4)
      de=ro*dse/(rs-ro)
      if (x(2).gt.de) go to 300
      beta=ro/de
      gamma=atan((de-x(2))/x(2)*tan(beta))
c
      if (s.lt.6.283) go to 200
      rev=S/2/3.14159
      s=s-int(rev)*2*3.14159
100 continue
c
200 if (s.lt.(3.14159-gamma)) go to 300
   if (s.gt.(3.14159+gamma)) go to 300
   f=0
   pmdot=0
   go to 400

300 f=100
   pmdot=-.00409
c
c *****
c * State Dictionary: *
c * r = radius of the spacecraft's orbit *
c * phi = true anomaly measured from initiation of maneuver *
c * m = mass of the spacecraft *
c * x(1) = dr/dt *
c * x(2) = r

```

```

c * x(3) = d(phi)/dt *
c * x(4) = phi *
c * x(5) = m *
c *****
c
400 d(1)=f*x(1)/x(5)/(x(1)**2+(x(2)*x(3))**2)**0.5+x(2)*x(3)**2-
lg*ro**2/x(2)**2
c
d(2)=x(1)
c
d(3)=f*x(3)/x(5)/(x(1)**2+(x(2)*x(3))**2)**0.5-2*x(1)*x(3)/x(2)
c
d(4)=x(3)
c
d(5)=pmdot
c
return
end

```


PROGRAM HELIOCENTRIC

```

      program heliocentric
c
c *****
c * Heliocentric is the main calling program for the integration *
c * of the equations of motion of our spacecraft while under the *
c * gravitational influence of the sun. *
c *****
c
      implicit double precision(a-h,o-z)
      dimension xo(20),xx(20)
      common/blhfcn/theta
c
c *****
c * 'md' is the dry mass of the ship which includes everything *
c * except the propellant mass required for an individual *
c * maneuver. *
c * 'mp' is the estimated propellant mass required for a given *
c * maneuver. *
c * 'phidoti' is the initial angular velocity and 'rdoti' is *
c * initial radial velocity of the spacecraft around the sun. *
c * 'degrees' is the direction of thrust. *
c * 'ri' is the starting radius and 'rf' is the final radial *
c * position. *
c *****
c
      write(*,*) 'dry mass of the ship in kg'
      read(*,*) md
      write(*,*) 'estimate of propellant usage in kg'
      read(*,*) mp
      write(*,*) 'initial phi dot in rad/sec'
      read(*,*) phidoti
      write(*,*) 'initial rdot in meters/sec'
      read(*,*) rdoti
      write(*,*) 'thrusting angle in degrees'
      read(*,*) degrees
      write(*,*) 'final radius in meters'
      read(*,*) rf
      write(*,*) 'initial radius in meters'
      read(*,*) ri
c
      theta=degrees/180*3.1415926
c
      open (file = 'escape', status = 'new', unit = 7)
c
      write (7,*) 'orbital trajectory data'
      write (7,*) 'data is in the following order'
      write (7,*) 'time      rdot      r      phidot      phi      velocity'
c
c *****
c * 'xo' is the array of the initial conditions where: x_(1) = rdot *
c * x_(2) = r, x_(3) = phidot, x_(4) = phi, x_(5) = mass. *
c *****
c
      50 xo(1)=rdoti
         xo(2)=ri
         xo(3)=phidoti
         xo(4)=0
         xo(5)=md+mp
c
c *****
c * The following are variables passed through to the integration *
c * subroutine. 'in' is a flag, 'nv' is the number of variables in *

```

```

c * the equations of motion, 'to' is the initial time, 'tp' is the      *
c * final time (stopping the loop), and 'dtint' is the interval that    *
c * the integration routine breaks each time loop down.                  *
c *****                                                                *
c
c      in=0
c      nv=5
c      to=0
c      tp=43200000
c      dtint=63
c
c      do 200 t=1000,tp,1000
c          ts=t-1000
c          call hrk4(ts,t,dtint,xo,xx,nv,in)
c          vv=(xx(1)**2+(xx(2)*xx(3))**2)**0.5/1000
c      write (7,100) t,xx(1),xx(2),xx(3),xx(4),vv
c 100 format (e11.5,1x,d11.5,1x,d11.5,1x,d11.5,1x,d11.5,1x,d11.5)
c
c *****                                                                *
c * The exit condition is met when the spacecraft achieves the final    *
c * radius.                                                              *
c *****                                                                *
c
c      if (xx(2).gt.rf) go to 250
c 200 continue
c
c *****                                                                *
c * This next scheme is a method to check that the final                *
c * propellant consumption, as determined from the time of              *
c * spiral, is equal to the initial estimate. If not, the                *
c * process is repeated with a new estimation.                          *
c *****                                                                *
c
c 250 mpr=xo(5)-xx(5)
c      if (abs(mpr-mp).lt.100) go to 350
c      if (mpr.gt.mp) go to 300
c      if (mpr.lt.mp) go to 325
c
c 300 mp=mp+(mpr-mp)
c      go to 50
c
c 325 mp=mp-(mp-mpr)
c      go to 50
c
c 350 write (7,*) 'This segment of the orbit is complete.'
c      write (7,*) 'Beam me up Scottie.'
c      write (7,*) 'v',vv
c      write (7,*) 'total time of spiral (days)',t/3600/24
c      write (7,*) 'mass of propellant consumed',xo(5)-xx(5)
c      write (7,*) 'total number of revolutions',xx(4)/2/3.14159
c      write (7,*) 'orbital radius at escape (km)',xx(2)/1000
c      write (7,*) 'mp',mp
c      write (7,*) 'rdot',xx(1)
c      write (7,*) 'phidot',xx(3)
c      write (7,*) 'theta',theta*180/3.14159
c      write (7,*) 'degrees',degrees
c
c      end

```

```

      subroutine hrk4(to,tp,dtint,xo,xx,nv,in)
c
c *****
c * This is a fourth order runge-kutta numerical integration *
c * subroutine courtesy of Stephen Paris, flight mechanics *
c * specialist, Boeing Aerospace Division of the Boeing Company. *
c *
c * Rk4 integrates a set of 'nv' 1st order ordinary differential *
c * equations from xo(to) to xo(tp) with step size 'dtint'. The *
c * differential equations are contained in subroutine fcn, and *
c * the values computed are returned to spiral. *
c *****
c
      implicit double precision(a-h,o-z)
      common/nwvcl/time,xv(100),d(100)
      common/rkblk/vs(20),ds(20),xs(20)
      dimension xo(20),xx(20)
      external hfcn
c
      if (in.eq.o) time=to
      900 continue
c
c *****
c * This step checks to see if a fractional step is required. *
c *****
c
      h=tp-time
      if (abs(h).gt.dtint)h=sign(1.0d0,h)*dtint
      h2=h/2
      h6=h/6
c
c *****
c * This routine initializes the variables. If the variables *
c * have already been intialized, this routine is overlooked. *
c *****
c
      if (in.eq.1) go to 1300
      in=1
      do 1100 i=1,nv
      xv(i)=xo(i)
1100 continue
      tn=to
c
      do 1200 i=1,nv
      ds(i)=d(i)
      xs(i)=xv(i)
1200 continue
c
      1300 continue
c
c *****
c * Make first estimate of canter state. *
c *****
c
      do 1400 i=1,nv
      xv(i)=xs(i)+h2*ds(i)
1400 continue
      time=tn+h2
c
      call hfcn
c
c *****

```

```

c * Revise estimate with derivative at center. *
c *****
c
      do 1600 i=1,nv
        vs(i)=ds(i)+2.00*d(i)
        xv(i)=xs(i)+h2*d(i)
1600 continue
c
      call hfcn
c
c *****
c * Make first estimate of state at end of step. *
c *****
c
      do 1800 i=1,nv
        vs(i)=vs(i)+2.00*d(i)
        xv(i)=xs(i)+h*d(i)
1800 continue
      time=tn+h
c
      call hfcn
c
c *****
c * Final estimate based on derivative at center and both ends, *
c * with double weight on the center estimates. *
c *****
c
      do 1810 i=1,nv
        vss=h6*(vs(i)+d(i))
        xs(i)=xs(i)+vss
        xv(i)=xs(i)
1810 continue
c
      call hfcn
c
      do 1820 i=1,nv
        ds(i)=d(i)
1820 continue
c
c *****
c * Update the time for the next step. *
c *****
c
      tn=time
c
c *****
c * End: copy state to 'xx'. *
c *****
c
      if(time.ne.tp) go to 900
c
      do 2000 i=1,nv
        xx(i)=xv(i)
2000 continue
c
      return
      end

```

```

      subroutine hfcn
c
c *****
c * Fcn is the derivative evaluation routine for runge-kutta *
c * numerical integration routine. The values of t,x, and d *
c * are passed thru the common block. *
c * *
c * The differential equations are of the following form: *
c *  $d(n) = dx(n)/dt = f(x(1), x(2), \dots, x(nv))$ . *
c *****
c
      implicit double precision (a-h,o-z)
      common/nwvcl/t,x(100),d(100)
      common/blhfcn/theta

c
c *****
c * The constants defined below are as follows: *
c * *
c * g      = acceleration due to gravity at the planet's surface *
c * ro     = radius of the planet *
c * f      = the thrust of the spacecraft *
c * pmdot  = propellant mass flow rate *
c *****
c
      g=274
      rs=696000000

c
      f=0
      pmdot=0

c
c *****
c * State Dictionary: *
c * *
c * r      = radius of the spacecraft's orbit *
c * phi    = true anomaly measured from initiation of maneuver *
c * m      = mass of the spacecraft *
c * x(1)   = dr/dt *
c * x(2)   = r *
c * x(3)   = d(phi)/dt *
c * x(4)   = phi *
c * x(5)   = m *
c *****
c
      temp1=x(2)*x(3)**2-g*rs**2/(x(2))**2+f/x(5)*sin(theta)
      d(1)=f*cos(theta)*x(1)/x(5)/(x(1)**2+(x(2)*x(3))**2)**0.5
1      +temp1
c      d(1)=f*x(1)/x(5)/(x(1)**2+(x(2)*x(3))**2)**0.5+x(2)*x(3)**2-
c      lg*ro**2/x(2)**2
c
      d(2)=x(1)

c
      temp2=2*x(1)*x(3)/x(2)
      d(3)=f*cos(theta)*x(3)/x(5)/(x(1)**2+(x(2)*x(3))**2)**0.5
1      -temp2
c      d(3)=f*x(3)/x(5)/(x(1)**2+(x(2)*x(3))**2)**0.5-2*x(1)*x(3)/x(2)
c
      d(4)=x(3)

c
      d(5)=pmdot

c
      return
      end

```

PROGRAM MSPIRAL

```

      program mspiral

c
c *****
c * Spiral is the main calling program for the integration of *
c * the equations of motion of our spacecraft while under the *
c * gravitational influence of a Mars. *
c *****
c
      implicit double precision(a-h,o-z)
      dimension xo(20),xx(20)

c
c *****
c * 'md' is the dry mass of the ship which includes everything *
c * except the propellant mass required for an individual *
c * maneuver. *
c * 'mp' is the estimated propellant mass required for a given *
c * maneuver. *
c * 'sphereofi' is the sphere of influence for the planet *
c * These values are entered interactively. *
c *****
c
      write(*,*) 'dry mass of the ship in kg'
      read(*,*) md
      write(*,*) 'estimate of the propellant mass in kg'
      read(*,*) mp
      write(*,*) 'the sphere of influence of Mars'
      read(*,*) sphereofi

c
      open (file = 'escape', status = 'new', unit = 7)

c
      write (7,*) 'orbital trajectory data'
      write (7,*) 'data is in the following order'
      write (7,*) 'time      rdot      r      phidot      phi      velocity'

c
c *****
c * 'xo' is the array of the initial conditions where: x_(1) = rdot *
c * x_(2) = r, x_(3) = phidot, x_(4) = phi, x_(5) = mass. *
c *****
c
      50 xo(1)=0
         xo(2)=4000000
         xo(3)=0.0001340166
         xo(4)=0
         xo(5)=md+mp

c
c *****
c * The following are variables passed through to the integration *
c * subroutine. 'in' is a flag, 'nv' is the number of variables in *
c * the equations of motion, 'to' is the initial time, 'tp' is the *
c * final time (stopping the loop), and 'dtint' is the interval that *
c * the integration routine breaks each time loop down. *
c *****
c
      in=0
      nv=5
      to=0
      tp=5000000
      dtint=63

c
      do 200 t=500,tp,500
         ts=t-500
         call mrk4(ts,t,dtint,xo,xx,nv,in)

```



```

      vv=(xx(1)**2+(xx(2)*xx(3))**2)**0.5/1000
c      write (7,100) t,xx(1),xx(2),xx(3),xx(4),vv
c 100 format (e11.5,1x,d11.5,1x,d11.5,1x,d11.5,1x,d11.5,1x,d11.5)
c
c *****
c * 've' is the escape velocity at a given radius; 'vv' is the ship *
c * velocity at a given radius. The exit condition is designated *
c * as when the spacecraft velocity exceeds the hyperbolic excess *
c * velocity or achieves the sphere of influence. *
c *****
c
      ve=(2000*3.986012e05/xx(2))**0.5
      if ((vv.gt.ve).AND. (vv.gt.hexcess)) go to 250
      if (xx(2).gt.sphereofi) go to 250
200 continue
c
c *****
c * This next scheme is a method to check that the final *
c * propellant consumption, as determined from the time of *
c * spiral, is equal to the initial estimate. If not, the *
c * process is repeated with a new estimation. *
c *****
c
250 mpr=xo(5)-xx(5)
      if (abs(mpr-mp).lt.100) go to 350
      if (mpr.gt.mp) go to 300
      if (mpr.lt.mp) go to 325
c
300 mp=mp+(mpr-mp)
      go to 50
c
325 mp=mp-(mp-mpr)
      go to 50
c
350 write (7,*) 'congratulations you have escaped Mars orbit'
      write (7,*) 'vesc and v',ve,vv
      write (7,*) 'total time of spiral (days)',t/3600/24
      write (7,*) 'mass of propellant consumed',xo(5)-xx(5)
      write (7,*) 'total number of revolutions',xx(4)/2/3.14159
      write (7,*) 'orbital radius at escape (km)',xx(2)/1000
      write (7,*) 'mp',mp
      write (7,*) 'rdot',xx(1)
      write (7,*) 'phidot',xx(3)
c
      end

```

```

      subroutine mrk4(to,tp,dtint,xo,xx,nv,in)
c
c *****
c * This is a fourth order runge-kutta numerical integration *
c * subroutine courtesy of Stephen Paris, flight mechanics *
c * specialist, Boeing Aerospace Division of the Boeing Company. *
c *
c * Rk4 integrates a set of 'nv' 1st order ordinary differential *
c * equations from xo(to) to xo(tp) with step size 'dtint'. The *
c * differential equations are contained in subroutine fcn, and *
c * the values computed are returned to spiral. *
c *****
c
      implicit double precision(a-h,o-z)
      common/nwvcl/time,xv(100),d(100)
      common/rkblk/vs(20),ds(20),xs(20)
      dimension xo(20),xx(20)
      external mfcn
c
      if (in.eq.o) time=to
1900 continue
c
c *****
c * This step checks to see if a fractional step is required. *
c *****
c
      h=tp-time
      if (abs(h).gt.dtint)h=sign(1.0d0,h)*dtint
      h2=h/2
      h6=h/6
c
c *****
c * This routine initializes the variables. If the variables *
c * have already been intialized, this routine is overlooked. *
c *****
c
      if (in.eq.1) go to 1300
      in=1
      do 1100 i=1,nv
      xv(i)=xo(i)
1100 continue
      tn=to
c
      do 1200 i=1,nv
      ds(i)=d(i)
      xs(i)=xv(i)
1200 continue
c
1300 continue
c
c *****
c * Make first estimate of canter state. *
c *****
c
      do 1400 i=1,nv
      xv(i)=xs(i)+h2*ds(i)
1400 continue
      time=tn+h2
c
      call mfcn
c
c *****

```

```

c * Revise estimate with derivative at center. *
c *****
c
c      do 1600 i=1,nv
c        vs(i)=ds(i)+2.00*d(i)
c        xv(i)=xs(i)+h2*d(i)
c      1600 continue
c
c          call mfcn
c
c *****
c * Make first estimate of state at end of step. *
c *****
c
c      do 1800 i=1,nv
c        vs(i)=vs(i)+2.00*d(i)
c        xv(i)=xs(i)+h*d(i)
c      1800 continue
c        time=tn+h
c
c          call mfcn
c
c *****
c * Final estimate based on derivative at center and both ends, *
c * with double weight on the center estimates. *
c *****
c
c      do 1810 i=1,nv
c        vss=h6*(vs(i)+d(i))
c        xs(i)=xs(i)+vss
c        xv(i)=xs(i)
c      1810 continue
c
c          call mfcn
c
c      do 1820 i=1,nv
c        ds(i)=d(i)
c      1820 continue
c
c *****
c * Update the time for the next step. *
c *****
c
c        tn=time
c
c *****
c * End: copy state to 'xx'. *
c *****
c
c        if(time.ne.tp) go to 900
c
c      do 2000 i=1,nv
c        xx(i)=xv(i)
c      2000 continue
c
c      return
c      end

```

```

      subroutine mfcn
c
c *****
c * Fcn is the derivative evaluation routine for runge-kutta *
c * numerical integration routine. The values of t,x, and d *
c * are passed thru the common block. *
c * *
c * The differential equations are of the following form: *
c *  $d(n) = dx(n)/dt = f(x(1), x(2), \dots, x(nv))$ . *
c *****
c
      implicit double precision (a-h,o-z)
      common/nwvcl/t,x(100),d(100)
c
c *****
c * The constants defined below are as follows: *
c * *
c * g      = acceleration due to gravity at the planet's surface *
c * ro     = radius of the planet *
c * f      = the thrust of the spacecraft *
c * pmdot  = propellant mass flow rate *
c * rs     = radius of the sun *
c * dsm    = distance from the center of the sun to the center *
c *         of Mars *
c *****
c
      g=3.768
      ro=3380000
      rs=696000000
      dsm=2.4e11
c
c *****
c * The following sequence of steps incorporates the effect *
c * of the shadow of the planet. This analysis is clarified *
c * within the text of the corresponding appendix. *
c *****
c
      s=x(4)
      dm=ro*dsm/(rs-ro)
      if (x(2).gt.dm) go to 300
      beta=ro/dm
      gamma=atan((dm-x(2))/x(2)*tan(beta))
c
      if (s.lt.6.283) go to 200
      rev=S/2/3.14159
      s=s-int(rev)*2*3.14159
100 continue
c
200 if (s.lt.(3.14159-gamma)) go to 300
   if (s.gt.(3.14159+gamma)) go to 300
   f=0
   pmdot=0
   go to 400
c
300 f=40
   pmdot=-.001638001638
c
c *****
c * State Dictionary: *
c * r      = radius of the spacecraft's orbit *
c * phi    = true anomaly measured from initiation of maneuver *
c * m      = mass of the spacecraft *

```

```

c * x(1) = dr/dt *
c * x(2) = r *
c * x(3) = d(phi)/dt *
c * x(4) = phi *
c * x(5) = m *
c *****
c
c 400 d(1)=f*x(1)/x(5)/(x(1)**2+(x(2)*x(3))**2)**0.5+x(2)*x(3)**2-
      lg*ro**2/x(2)**2
c
c      d(2)=x(1)
c
c      d(3)=f*x(3)/x(5)/(x(1)**2+(x(2)*x(3))**2)**0.5-2*x(1)*x(3)/x(2)
c
c      d(4)=x(3)
c
c      d(5)=pmdot
c
c      return
c      end

```